

Mechanisms in Biological Electron Transfer: Raman Spectroscopic Investigations of Cytochrome *c* and CoFeSP

vorgelegt von
Diplom-Chemikerin
Wiebke Meister
geboren in Hannover

Von der Fakultät II – Mathematik und Naturwissenschaften der
Technischen Universität Berlin zur Erlangung des akademischen
Grades Doktor der Naturwissenschaften
– Dr. rer. nat. –

genehmigte Dissertation

Promotionsausschuss:

- Vorsitzender: Prof. Dr. Nediljko Budisa
1. Bericht: Prof. Dr. Peter Hildebrandt
2. Bericht: Prof. Dr. Holger Dobbek

Tag der wissenschaftlichen Aussprache: 19.09.2014

Berlin 2014
D 83

Abstract

Proteins involved in biological electron transfer (ET) can be divided into two groups. These are proteins that solely transfer electrons between electron donors and acceptors, and redox proteins that link ET with other processes. In these two cases the extent of coupling between ET and protein dynamics is qualitatively different. To contribute to a general understanding of underlying principles, representatives of both groups are investigated in this thesis. A representative of the second group is the cobalamin-containing protein CoFeSP, an essential component in the acetyl-CoA pathway. It is reductively activated by the [FeS] protein RACo. Using resonance Raman (RR) spectroscopy it is shown that complex formation is accompanied by a conformational change that affects the axial coordination of the cobalt in CoFeSP leading to the perturbation of the electronic structure of the corrin. This change supposedly alters the redox potential of the corrinoid to facilitate the otherwise uphill reduction by the [2Fe2S] cluster of RACo. With investigations on deletion mutants of both proteins it was possible to identify the interacting domains of the partner proteins, consistent with recent crystallographic data. As an example for a “simple” ET protein, cytochrome *c* (Cyt*c*) and its ET reactions were studied by (time-resolved) surface enhanced resonance Raman spectroscopy [(TR) SERR]. Cyt*c* primarily serves as an ET shuttle in the respiratory chain interacting with membrane-bound proteins. Cyt*c* wild type (WT) and selected variants with lysines-to-cysteine substitutions in and remote from the binding domain were electrostatically immobilized onto Ag electrodes coated with carboxyl-terminated self-assembled monolayers (SAMs) of different length. The determination of the apparent rate constants of the interfacial ET of the heme were analysed to elucidate the interplay between the rotational reorientation and the electron tunneling. The experimental data, complemented by theoretical calculations (in collaboration) demonstrate the crucial role of the electrostatic field in the electrode/SAM/protein interface for controlling the gated electron transfer process.

In its second function Cyt*c* acts as a peroxidase catalyzing the peroxidation of cardiolipin (CL). Thus, this function involves a coupling of the redox process with internal conformational changes of the protein to allow CL binding and generation of a catalytic center via the removal

of the 6th axial Fe-ligand. This function which is assumed to be promoted by post-translational modifications of internal tyrosine residues was studied by RR spectroscopy. Comparing WT and “phosphomimetic” tyrosine mutants potential structural changes at the redox site were analysed. However, the results do not provide a distinct and unambiguous indication for alterations of the heme center due to the modification of nearby tyrosines.

As SERR spectroscopy of ET proteins immobilized on SAM-coated electrodes is a key approach for studying interfacial biological ET, this methodology was critically assessed. To examine the transferability of conclusions derived from spectroelectrochemical experiments on simple model systems to physiological conditions, the experiments on Cyt_c, bound to SAM-coated electrodes, were extended to significantly higher ionic strengths that are close to those in cellular systems. While the ET kinetics were slowed down at higher ionic strength, the redox potential was found to be positively shifted. It was shown that the slower ET kinetics were therefore not an electric field effect but the result of a change in the orientation distribution of Cyt_c due to the higher ionic strength.

A drawback of TR SERR spectroscopy is the relative large scattering of kinetic data, the origin of which was systematically explored in this thesis. The analysis revealed an unexpected and relatively strong “personal” effect on the kinetic data. A possible explanation is based on different pressures applied upon surface polishing that could lead to differing surface morphologies. This in turn might influence the formation of the SAM and the SAM structure and thus may result in different electronic couplings between the redox center of the immobilised protein and the electrode.

Zusammenfassung

Proteine, die Elektronen übertragen können, lassen sich in zwei Gruppen einteilen. Die eine Gruppe bezieht sich auf Proteine, deren Funktion ausschließlich der Elektronentransfer (ET) zwischen Donor und Akzeptor ist, während bei Proteinen der zweiten Gruppe der ET mit weiteren Prozessen verbunden ist. Das Ausmaß der Kopplung zwischen ET und Proteindynamik ist in beiden Gruppen qualitativ unterschiedlich. Um zum allgemeinen Verständnis der zugrundeliegenden Prinzipien beizutragen, wurden in dieser Arbeit Vertreter beider Gruppen untersucht. Ein Vertreter der zweiten Gruppe ist das CoFeSP Protein, das einen Cobalamin Kofaktor enthält. CoFeSP, das eine wichtige Rolle im Stoffwechsel anaerober Mikroorganismen spielt, wird reduktiv vom [FeS]-Protein RACo aktiviert. Mithilfe von Resonanz-Raman (RR) Spektroskopie wurde gezeigt, dass die Komplexbildung von einer Konformationsänderung begleitet wird, die die axiale Koordination des Kobalts im CoFeSP und damit auch die elektronische Struktur des Corrins verändert. Dies führt vermutlich zu einer Verschiebung des Redoxpotentials des Corrinoids, so dass die reduktive Reaktivierung durch den [2Fe2S]-Cluster des RACo ermöglicht wird. Die wechselwirkenden Domänen der Partnerproteine konnten anhand von Untersuchungen an Deletionsmutanten identifiziert werden. Diese Ergebnisse wurden durch jüngste kristallographische Ergebnisse bestätigt. Als Beispiel für ein „einfaches“ ET-Protein der ersten Gruppe wurden das Hämprotein Cytochrome *c* (Cyt_c) und seine ET-Reaktionen mit (zeitaufgelöster) oberflächenverstärkter Resonanz-Raman [(TR)-SERR] Spektroskopie untersucht. Cyt_c dient primär als Elektronentransporter zwischen membrangebundenen Reaktionspartnern in der Atmungskette aerober Organismen. Der Wildtyp (WT) und Lysin→Cystein Proteinvarianten, mit Mutationen innerhalb und außerhalb der Bindungsdomäne, wurden elektrostatisch auf Ag-Elektroden immobilisiert, die zuvor mit negativ geladenen selbstorganisierten Monolagen (SAMs) bedeckt wurden. Die aus den TR-SERR Experimenten gewonnenen Kinetiken des heterogenen ET ermöglichten die Analyse der Zusammenhänge zwischen Elektronentunneln und Orientierungsdynamik des adsorbierten Proteins. Die experimentellen Ergebnisse, zusammen mit in Kooperation durchgeführten Rechnungen, zeigen die entscheidende Rolle lokaler elektrostatischer Felder in der Elektrode / SAM / Protein-Grenzschicht

für den Redoxprozess.

In seiner zweiten Funktion wirkt Cyt_c als Cardiolipin(CL)-Peroxidase. Dabei ist der Redoxprozess mit internen Konformationsänderungen gekoppelt, die die CL-Bindung erlauben und durch die Abtrennung des sechsten axialen Fe-Liganden ein katalytisches Zentrum generieren. Es wird angenommen, dass diese Funktion durch post-translationale Modifikationen von Tyrosinresten unterstützt wird. Um die potentiellen strukturellen Änderungen am Redoxzentrum zu identifizieren, wurden der WT und „phosphomimetische“ Tyrosin-Mutanten RR spektroskopisch untersucht. Allerdings lieferten die Ergebnisse keine eindeutigen Hinweise auf Strukturänderungen des Hämzentrums aufgrund der Modifikationen an benachbarten Tyrosinen.

Die SERR-Spektroskopie von ET-Proteinen auf SAM-beschichteten Elektroden ist eine Schlüsseltechnik zur Untersuchung des biologischen ET an Grenzflächen. Deshalb wurde diese Methode in dieser Arbeit kritisch begutachtet. Um die Übertragbarkeit der spektroelektrochemischen Ergebnisse auf physiologische Bedingungen zu überprüfen, wurden die SERR-Experimente an immobilisiertem Cyt_c bei deutlich höherer und den intrazellulären Bedingungen vergleichbarer Ionenstärke ausgeweitet. Während die ET-Kinetik bei höherer Ionenstärke langsamer wurde, wurde das Redoxpotential positiv verschoben. Es wurde gezeigt, dass der langsamere ET primär auf eine veränderte Orientierungsverteilung des Cyt_c zurückzuführen ist.

Ein Nachteil der TR-SERR Spektroskopie ist die relativ hohe Streuung der kinetischen Daten. Die in dieser Arbeit vorgenommene Untersuchung ergab einen unerwarteten, relativ starken „personenbezogenen“ Effekt. Dies kann letztlich auf den je nach Experimentator unterschiedlichen Druck zurückgeführt werden, mit dem die Elektrode im ersten Schritt der Oberflächenmodifikation „poliert“ wird. Daraus können unterschiedliche Oberflächenmorphologien resultieren, die die Bildung und die Struktur der SAMs und damit auch die elektronische Kopplung zwischen der Elektrode und dem immobilisierten Protein beeinflussen können.

Publications

Parts of this work have been already published in:

1. D. Alvarez-Paggi, W. Meister, U. Kuhlmann, I. Weidinger, K. Tenger, L. Zimányi, G. Rákhely, P. Hildebrandt and D. Murgida, *Disentangling Electron Tunneling and Protein Dynamics of Cytochrome c through a Rationally Designed Surface Mutation* The Journal of Physical Chemistry, Part B, **117**, 6061-6068 (2013)

Damián Alvarez-Paggi and myself have contributed equally to the publication. It is part of Chapter 6 and 9. Supplements were added and small changes applied. It is “adapted with permission from [D. Alvarez-Paggi, W. Meister, U. Kuhlmann, I. Weidinger, K. Tenger, L. Zimányi, G. Rákhely, P. Hildebrandt and D. Murgida, *Disentangling Electron Tunneling and Protein Dynamics of Cytochrome c through a Rationally Designed Surface Mutation* The Journal of Physical Chemistry, Part B, **117**, 6061–6068 (2013)] Copyright(2013) American Chemical Society”

2. W. Meister, S. E. Hennig, J. Jeoung, F. Lenzian, H. Dobbek and P. Hildebrandt, *Complex Formation with the Activator RACo Affects the Corrinoid Structure of CoFeSP* Biochemistry, **51**, 7040-7042 (2012)

This publication is part of Chapter 6, 13 and 14. Supplements were added and small changes applied. It is “adapted with permission from [W. Meister, S. E. Hennig, J. Jeoung, F. Lenzian, H. Dobbek and P. Hildebrandt, *Complex Formation with the Activator RACo Affects the Corrinoid Structure of CoFeSP* Biochemistry, **51**, 7040–7042 (2012)] Copyright (2012) American Chemical Society.”

Notes

When using direct quotes, all abbreviations and the case sensitivity were adopted to the pattern of this work. The references for the quoted literature and figures have been matched to the works internal numbering. All other changes in quotes have been indicated in each case by using squared brackets following the conventions of quotation. Copyright for figures, if necessary, is given in the figure captions individually. The publications mentioned above are used without explicit quotation but the individual contributions are clearly indicated.

Similar summaries of the theoretical background can be found in related theses,^{6,59,85,87,103,118,141} which will not be specifically mentioned as source.

The protein figures were prepared with either PyMol or VMD software.

Contents

Abstract	I
Zusammenfassung	III
Publications	V
Notes	VII
List of Abbreviations	XV
I. Introduction	1
II. Theoretical Background	5
1. Electron Transfer	7
1.1. Homogeneous electron transfer	8
1.1.1. Classical Marcus theory	8
1.1.2. Non-adiabatic ET and QM approach	11
1.2. Heterogeneous electron transfer	12
1.2.1. Biological ET	14
1.2.2. Gated ET	14
2. Electrochemical Interfaces	15
2.1. Electrode-solution interface	15
2.2. SAM and interfacial potential distribution	16
3. Raman Spectroscopy	21
3.1. Vibrational spectroscopy	21
3.2. The Raman effect	22
3.2.1. QM description of the Raman effect	23
3.3. The resonance Raman effect	25
3.4. Surface enhancement of radiation on metal surfaces	27
3.4.1. SER spectroscopy	28

4. Investigation of Cytochrome <i>c</i>, CoFeSP, and RACo with Resonance Raman Spectroscopy	29
4.1. RR spectroscopy of the different chromophores	31
4.1.1. RR spectra of Cyt <i>c</i>	31
4.1.2. RR spectra of CoFeSP and RACo	33
III. Experimental Details, Setup and Material	35
5. RR and SERR Spectroscopy	37
5.1. Electrode preparation for SERR spectroscopy	37
5.2. Spectroscopic setup	37
5.2.1. Electrochemical cell for SERR spectroscopy . .	37
5.2.2. Cell for RR spectroscopy	38
5.2.3. Experimental parameters and spectrometer . . .	38
5.2.4. RR measurements	39
5.2.5. Stationary SERR measurements	39
5.2.6. TR SERR measurements	39
5.3. Spectra analysis of Cyt <i>c</i>	40
5.3.1. Component analysis	40
6. Proteins and Experimental Details	41
6.1. Horse heart cytochrome <i>c</i>	41
6.2. Human heart cytochrome <i>c</i>	43
6.3. CoFeSP and RACo	45
IV. SERRs as Tool for Studying Electron Transfer Kinetics	47
7. Statistical Investigation of the Method of TR SERR Spectroscopy for Studying the ET of Cyt<i>c</i>	49
7.1. Why undertaking this effort for a well established method?	49
7.2. Approach to the problem of varying TR SERR results . .	49
7.3. Results of the comparative TR SERR experiments	51
7.4. A “personal” effect in TR SERR experiments	53
V. Cytochrome <i>c</i>—Interplay Between Protein Dynamics and Electron Transfer	55
8. Introduction of the Role of Cyt<i>c</i> in Cell ET	57
8.1. Native Cyt <i>c</i>	57
8.2. Cyt <i>c</i> in eukariotic aerobic respiration	57

9. ET of Lysine to Cysteine Mutants of hh Cytc	59
9.1. Background to the approach of surface mutations of hh Cytc	59
9.2. The K87C mutant of hh Cytc	62
9.2.1. MD characterization of the K87C mutant	62
9.2.2. Pathways analysis of the Cytc/SAM complexes	66
9.2.3. Structural and redox equilibria of immobilized Cytc	68
9.2.4. ET dynamics	71
9.2.5. Conclusions from results concerning the ET of the K87C mutant	75
9.2.6. Q-Band excitation in TR SE(R)Rs experiments with the K87C mutant	76
9.3. The K39C and K8C mutants of hh Cytc	80
9.3.1. Stationary SERR experiments with the K39C and K8C mutants	80
9.3.2. Kinetics of K39C and K8C mutants	82
9.4. Conclusions—rational designed surface mutations of hh Cytc	86
10. Effect of Ionic Strength on the Redox Potential and ET Kinetics of hh Cytc	87
10.1. Implications of increased ionic strength on the SERR spectra of Cytc	87
10.2. Stationary SERR experiments with different ionic strength	89
10.3. Kinetics of the ET of Cytc at high ionic strength	89
10.4. The effect of the ionic strength on the electric field	91
10.5. The effect of ionic strength on Cytc in the literature	93
10.5.1. Shift of the redox potential upon immobilization of Cytc	93
10.5.2. The influence of the ionic strength on the redox potential of Cytc in solution	93
10.5.3. The influence of the ionic strength on the redox potential of immobilized Cytc	94
10.5.4. ET kinetics in relation to ionic strength	94
10.6. Interpretation of the effect of increased ion concentration in solution on Cytc	95
VI. Cytochrome <i>c</i>—Changing Function from Electron Transfer to Apoptosis	99
11. The Role of Cytc in Apoptosis	101
11.1. Programmed cell death—Apoptosis	101

11.2. Cytochrome <i>c</i> and cardiolipin	102
11.3. Regulatory instruments for Cyt <i>c</i> tuning	104
11.3.1. Alkaline Transition	104
11.3.2. Posttranslational modifications of Cyt <i>c</i> tyrosines	105
12. Tyrosine Phosphomimetic-Mutations of huh Cyt<i>c</i>	107
12.1. Tyrosine mutations of Cyt <i>c</i> in the literature and func- tional data	107
12.2. RR results of the Y-Mutants of Cyt <i>c</i>	109
12.2.1. Reduced species	110
12.2.2. Oxidized species	111
12.3. The Y48pCMF variant vs. the WT	116
12.3.1. Conclusive picture of structure-property correla- tion in the Y48pCMF variant?	122
12.4. Incorporation of the Cyt <i>c</i> variants into liposomes	123
VII. CoFeSP—Electron Transfer and Conformational Gat- ing	125
13. Introduction of CoFeSP	127
13.1. The reductive acetyl-CoA pathway	127
13.2. Structure and function of CoFeSP	128
13.3. Structure and function of RACo	129
13.4. Reactivation of CoFeSP by RACo	130
14. Conformational Gating by Complex Formation of CoFeSP and RACo	133
14.1. The RR corrinoid marker region	134
14.2. The RR marker region of the [FeS] clusters	136
14.3. Interpretation of the RR spectra	137
14.4. EPR measurements	139
15. The Crystal Structure of the Complex of CoFeSP and RACo	141
15.1. Mechanistic model for the regeneration of active CoFeSP	142
VIII. Concluding Discussion	145
Acknowledgements	151
Bibliography	172

List of Abbreviations

5c	five coordinated
6c	six coordinated
acetyl-CoA	acetyl coenzyme A
ADP	adenosine diphosphate
Apaf	apoptotic protease activating factor
Arg	arginine - R
ATP	adenosine triphosphate
BD	binding domain
C10	11-mercaptoundecanoic acid
C15	16-mercaptohexadecanoic acid
C5	6-mercaptohexanoic acid
CcO	cytochrome c oxidase
CGS	Gouy-Chapman-Stern
CL	cardiolipin
CoFeSP	corrinoid-, iron-, sulfur containing protein
CV	cyclic voltammetry
CW	continuous wave
Cys	cysteine - C
Cytc	cytochrome <i>c</i>
dATP	desoxyadenosine triphosphate
e.g.	exempli gratia (for example)
EF	electric field
EPR	electron paramagnetic resonance
ET	electron transfer
ferric	Fe ⁺³
ferrous	Fe ⁺²
Glu	glutamic acid - E
HF	high frequency
hh Cytc	horse heart cytochrome <i>c</i>
His	histidine - H
HOMO	highest occupied molecule orbital
HS	high spin
huh Cytc	human heart cytochrome <i>c</i>

i.a.	inter alia (among other things)
i.e.	id est (that is)
IMM	inner mitochondrial membrane
IR	infrared
LF	low frequency
LS	low spin
LUMO	lowest unoccupied molecule orbital
Lys	lysine - K
MD	molecular dynamics
Met	methionine - M
MM/GBSA	molecular mechanics/generalized Born surface area
MO	molecule orbital
MOMP	mitochondrial outer membrane permeabilization
MUA	11-mercaptoundecanoic acid
MZ	main zone
NHE	normal hydrogen electrode
NMR	nuclear magnetic resonance
OMM	outer mitochondrial membrane
PBC	periodic boundary conditions
pCMF	p-carboxymethyl-L-phenylalanine
PDB	protein data bank
Phe	phenylalanine - F
POPE	1-palmitoyl-2-oleoyl-sn-glycero-3-phospho-ethanolamine
PS	pulse time
PZC	potential of zero charge
QCR	ubiquinol/cytochrome c oxidoreductase
RACE	reductive activases for corrinoid enzymes
RACo	reductive activator of CoFeSP
RC	reaction coordinate
RR	resonance Raman
RT	recovery time
SAM	self-assembled monolayer
SDS-PAGE	sodium dodecyl sulfate polyacrylamide gel
SEIRA	surface-enhanced infrared absorption
SER	surface-enhanced Raman
Ser	serine - S
SERR	surface-enhanced resonance Raman

SMD	steered MD
Thr	threonine - T
TR	time-resolved
TR SERR	time-resolved surface-enhanced resonance Raman
Tyr	tyrosine - Y
UV / vis	ultra violet / visible
WT	wild type

List of Symbols

δ	delay time
Δ	measuring time
δ'	real delay time
E_i	initial potential
E_f	final potential
D^H	electronic coupling decay
$ H_{DA} $	electronic coupling matrix
β	tunneling decay parameter
I	ionic strength
E^0	redox potential of the adsorbed Cytc species
E_F	electric field
κ	inverse Debye length
d_C	chain length of the SAM or thickness of Stern layer
E_{RC}	potential drop at redox center; $E_{RC} = E^0 - E_S^0$
E_S^0	redox potential of the Cytc in solution
ϵ_C	dielectric constant in SAM
ϵ_S	dielectric constant in water
σ_C	charge density at carboxylate / protein interface
σ_{RC}	charge density at redox center
Γ_{prot}	surface coverage of the protein
T	temperature
N_A	Avogadro constant; $6.02214 \times 10^{23} \frac{1}{mol}$
k_B	Boltzmann constant; $1.38065 \times 10^{-23} \frac{J}{K}$
e	elementary charge; $1.60218 \times 10^{-19} C$
F	Faraday constant; $9.64853 \times 10^4 \frac{C}{mol}$
R	universal gas constant; $8.31446 \frac{J}{K \cdot mol}$
ϵ_0	vacuum permittivity; $8.85419 \times 10^{-12} \frac{F}{m}$

Part I.

Introduction

MECHANISMS IN BIOLOGICAL ELECTRON TRANSFER is the title of my work. These mechanisms addressed in the title involve “simple” electron transfer (ET) as well as coupled reactions where the ET is accompanied by structural changes of a protein, proton transfer, or catalytic reactions. Proteins working as “simple” electron carriers are often smaller proteins with well defined interaction domains for the reactions with the respective partner proteins. Usually, the redox center is located in the vicinity of this domain. The group of “ET enzymes”, which execute different tasks and couple the ET with other reactions are in general more complex.^{198,199} All biological ET reactions have in common, that specific protein-protein interactions are required, governed by recognition reactions. Many of the proteins involved in ET are membrane-bound so that also their partner proteins are affected by parameters specific for interfacial processes. The consequences on the proteins can be severe, e.g. the potential distribution across the membrane can lead to high local electric fields at the redox site which can influence the structures and kinetics of the interacting system.

There are many methods for the investigation of redox proteins and their reactions in vitro including NMR and EPR spectroscopic techniques, optical spectroscopy, and electrochemistry. Especially interesting for the investigation of structural changes of these proteins are vibrational spectroscopic methods. In Raman spectroscopy the appropriate choice of the excitation wavelength provides a resonance enhancement of the chromophore signals due to coupling to an electronic transition. As a result resonance Raman (RR) spectroscopy gains sensitivity and selectivity only for the redox-center.

For the investigation of integral and peripheral membrane proteins often simplified model systems are used, in which the proteins are immobilized on electrodes coated with biocompatible films, which mimic the membrane. Surface enhanced resonance Raman (SERR) spectroscopy uses nanostructured electrodes which provide an enhancement of the signal of the protein molecules in the vicinity of the surface. With this method, thermodynamics and kinetics of interfacial ET reactions can be studied.

The main task of this work was the investigation of key parameters of biological ET. For this purpose two different systems were chosen which are representatives for both groups of ET proteins as described above. (1) The RR investigation of structural changes in CoFeSP that are necessary to accomplish reductive reactivation by its partner protein RACo represents the study of a system in which ET is coupled to large intramolecular structural changes. Such protein structural changes are a prerequisite for adjusting the redox potential of the enzyme. (2) As an example for an electron shuttle, the small protein cytochrome *c* (Cyt*c*) was investi-

gated with SERR spectroscopy. Cyt c , which transfers electrons in the respiratory chain between membrane bound proteins in the intermembrane space in the mitochondrion, was electrostatically immobilized on a model system consisting of a rough Ag electrode coated with carboxyl-terminated self-assembled monolayers (SAMs) of different length. Prior to this work an electric field strength dependent gated ET mechanism was found, that is based on a rotational diffusion of the bound proteins to sample for the optimum ET orientation.^{88,89} Here, in this work, single amino acid surface mutants of Cyt c , with altered electrostatics, were used to further test this hypothesis.

Preoccupied with the role of Cyt c in cellular ET another function of Cyt c gained focus in this work. Cyt c takes part in the apoptotic route of the cell.^{73,75,147} To carry out this function, the ET function is impaired and the Cyt c gains peroxidase activity towards cardiolipin (CL), a lipid exclusively found in the mitochondrial membrane. As a consequence Cyt c is released into the cytosol acting as pre-apoptotic factor. There are indications for a posttranslational phosphorylation of internal tyrosines as the origin of the change in function.^{48,94,126,149,206} In this work phosphomimetic tyrosine mutants of Cyt c were investigated with RR spectroscopy to test the implications on the heme structure and the consequence of the interaction towards CL.

SERR spectroscopy of ET proteins immobilized on SAM-coated electrodes is a key approach for studying interfacial biological ET. However, it is associated with two central questions: (i) Why do kinetic data obtained from time-resolved SERR spectroscopy partly deviate quite substantially even if the same setup is used? To address this findings a comparative approach was chosen to test the statistical distribution of results of the same experiment carried out by different experimenters. (ii) Can the conclusions derived from investigations of the model systems be extended to physiological conditions? Here the focus was laid on one aspect that was not yet considered so far, i.e. the effect of the ionic strength. The ionic strength deviate in the standard SERR experiments from physiological ionic strength due to the optimization of the experimental parameters for good spectroscopic visibility.

Altogether, the goal of this thesis was to contribute to a general understanding of the underlying mechanisms in biological ET as well as to assess the potential of SERR spectroscopy as tool for studying interfacial ET.

Part II.

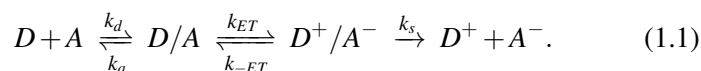
Theoretical Background

1. Electron Transfer

The main focus in this work is on the elucidation of electron transfer (ET) mechanisms in proteins i.e. Cyt c and CoFeSP, a subject that is widely explored and has solid theoretical basis. A sound theoretical approach was developed by R. A. Marcus, first published in 1956,¹⁰⁷ and further refined over many years,^{104,106,108–111,113} where a relationship between the thermodynamic driving force (ΔG^0) and the reaction rate (k_{ET}) was established for reactions with little overlap between the electronic wavefunctions of the reacting species in the activated complex. Detailed overviews can be found elsewhere.^{19,58,105,114,128}

The potential energy surfaces of the reactant (R) and product (P) states (including the environment) intersect if there is no electronic coupling. Electronic coupling leads to a splitting into two energy surfaces and enables ET as depicted in Figure 1.1.¹¹⁴

An ET reaction between a donor D and an acceptor A can be written as^{19,107}



First, D and A diffuse together and form a complex which reorganizes

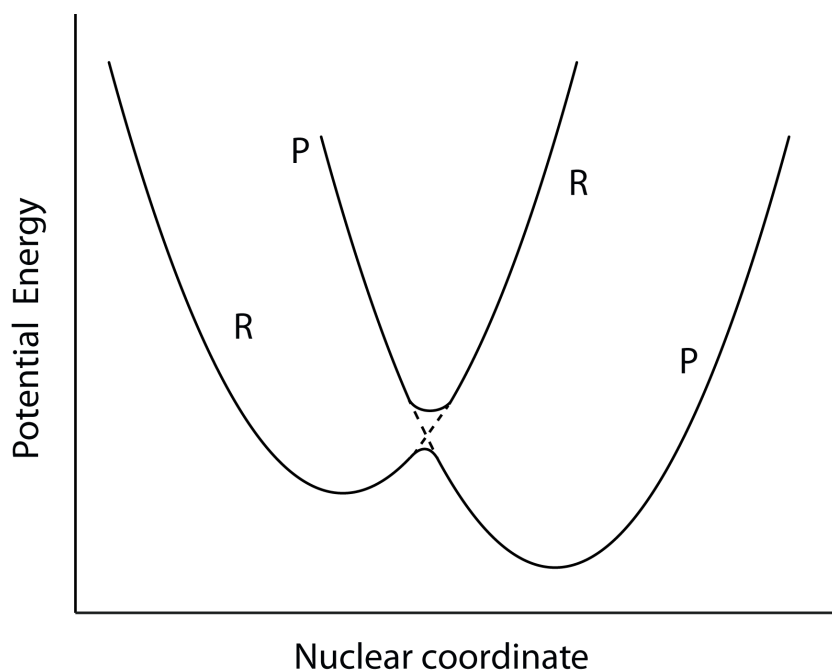


Figure 1.1.: Profile of the potential energy surface of reactants (R) and products (P) against the nuclear configuration of the system. The dashed lines indicate the surface for zero electronic interaction of the reacting species while the solid surface gives the adiabatic reaction surface. (The schematic reaction depicted here is accompanied by an decrease in potential energy.)¹¹²

to an activated state D/A which enables the ET. After the electronic transition the products D^+ and A^- move apart.

The observed rate constant k_{obs} of the overall ET reaction ($D + A \xrightarrow{k_{obs}} D^+ + A^-$) can be derived from a steady-state approximation as

$$\frac{1}{k_{obs}} = \frac{1}{k_a} + \frac{1}{K_A k_{-ET}} \left(1 + \frac{k_{-ET}}{k_s} \right) \quad (1.2)$$

with $K_A = k_a/k_d$.

Two extreme cases can be distinguished:

$$\begin{aligned} k_s \gg k_{-ET} \text{ and } k_d \gg k_{ET} &\rightarrow k_{obs} = K_A k_{ET} \\ k_d \ll k_{ET} &\rightarrow k_{obs} = k_A \end{aligned}$$

The second case will not give any information about the ET rate constant and since the reaction it is controlled only by the first reaction step and therefore the ET is “gated”.

The difference in the Gibbs energy between the initial and final state of the reaction can be approximated as

$$\Delta G^0 = e(E_D^0 - E_A^0 + w^P - w^R) \quad (1.3)$$

where E_D^0 and E_A^0 represent the standard redox potentials of the redox couples D/D^+ and A/A^- . w^P and w^R denote the work necessary to form the D/A complex (reactant) and to induce the separation of D^+/A^- (product), respectively.¹⁰⁴

1.1. Homogeneous electron transfer

1.1.1. Classical Marcus theory

The homogeneous ET, i.e. the electron transfer between two chemical species in solution was described extensively within the classical Marcus theory.^{104,105,107,112,114} The potential energy surface (Figure 1.1) of the system is simplified and replaced by free Gibbs energy curves along a reaction coordinate as depicted in Figure 1.2. The free Gibbs energy of the reactant (D/A) and product (D^+/A^-) state is approximated with the same but shifted parabolas, which is justified since the energies and internal coordinates of the complexes change only slightly upon the ET (Franck-Condon principle). The ET occurs when the D/A system energetically reaches the intersection point of the parabolas by thermal fluctuation. The “activation” Gibbs energy (ΔG^\ddagger) is related to the stan-

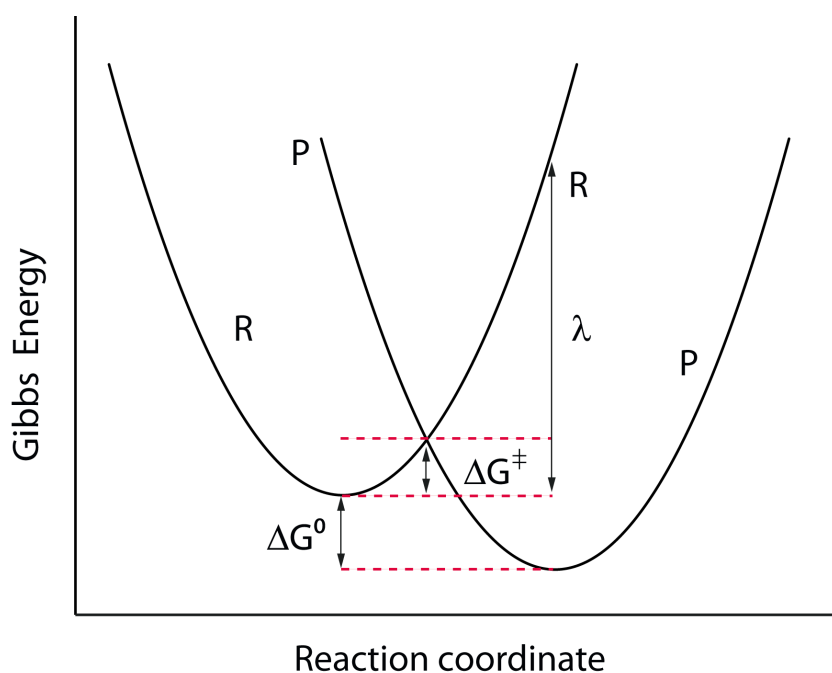


Figure 1.2.: Gibbs energy profiles of reactants (R) and products (P) versus the reaction coordinate with the standard reaction Gibbs energy ΔG^0 , the “activation” Gibbs energy ΔG^\ddagger and the reorganization energy λ for an ET reaction.¹¹⁴

standard reaction Gibbs energy (ΔG^0) and the reorganization energy λ , which is the change in Gibbs energy that would be required to bring the reactants to the equilibrium configuration of the product state without the transfer of an electron.

$$\Delta G^\ddagger = \frac{(\lambda + \Delta G^0)^2}{4\lambda}. \quad (1.4)$$

The reorganisation energy λ consists of two components which account for (1) the structural differences between the equilibrium configurations of the initial and final states and (2) changes in orientation and polarisation of the surrounding solvent molecules.^{104,105,114}

The ET rate constant can be described by

$$k_{ET} = \kappa_{el} \nu_n \exp\left(\frac{-\Delta G^\ddagger}{k_B T}\right) = \kappa_{el} \nu_n \exp\left(\frac{-(\lambda + \Delta G^0)^2}{4\lambda k_B T}\right). \quad (1.5)$$

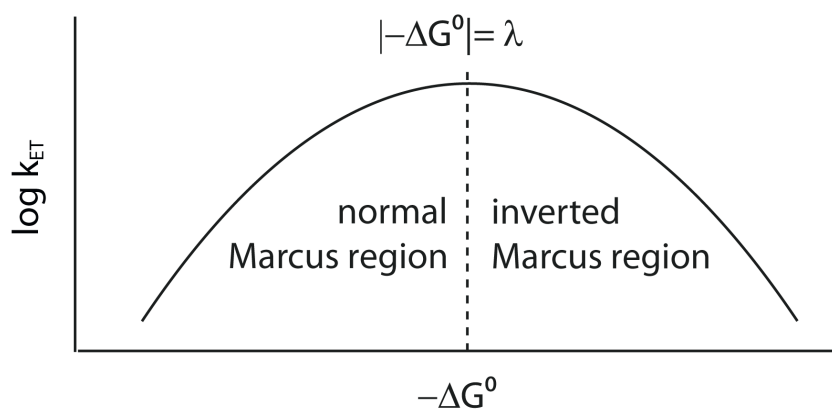
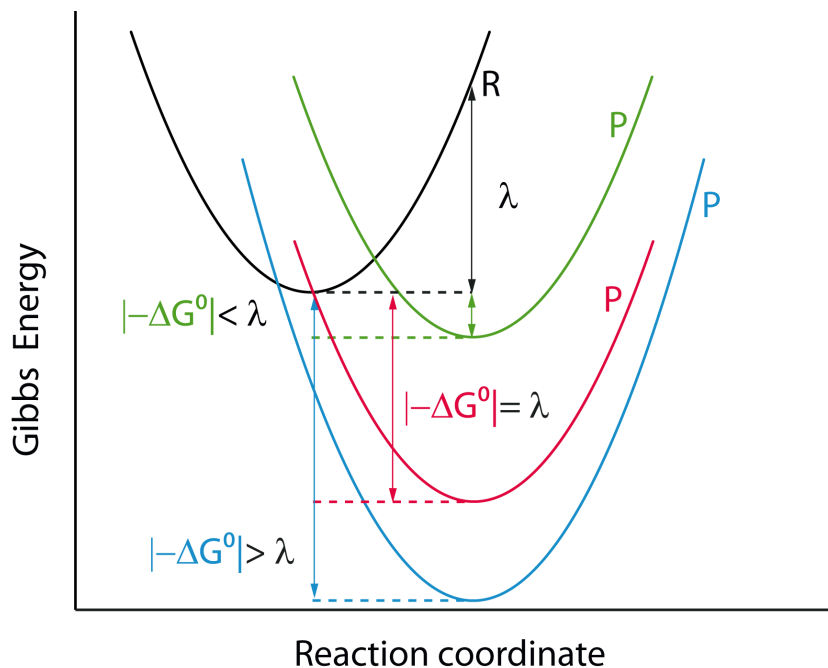


Figure 1.3.: Scheme of the dependency of $\log k_{ET}$ vs. the standard reaction Gibbs energy ΔG^0 in the normal and inverted Marcus region predicted by classical description.

Figure 1.4.: Gibbs energy profile of reactants (R) and products (P) versus the reaction coordinate for different values of the standard reaction Gibbs energy ΔG^0 : The reactant state is depicted in black, the normal Marcus region with $|\Delta G^0| > \lambda$ in green, in red a profile with $|\Delta G^0| = \lambda$ so that $G^\ddagger = 0$ and k_{ET} reaches a maximum, and in blue the inverted Marcus region with $|\Delta G^0| < \lambda$.¹¹⁴



κ_{el} denotes the electronic transition coefficient and ν_n is the vibrational frequency of the activated complex D/A necessary for reaching the transition state.¹¹⁴

According to Equation (1.5) k_{ET} reaches a maximum for $|\Delta G^0| = \lambda$ (with $G^\ddagger = 0$) and the ET rate will decrease again when $|\Delta G^0| < \lambda$ in the so-called Marcus inverted region (see Figure 1.4 and 1.3). This effect was experimentally confirmed.^{28,124,194}

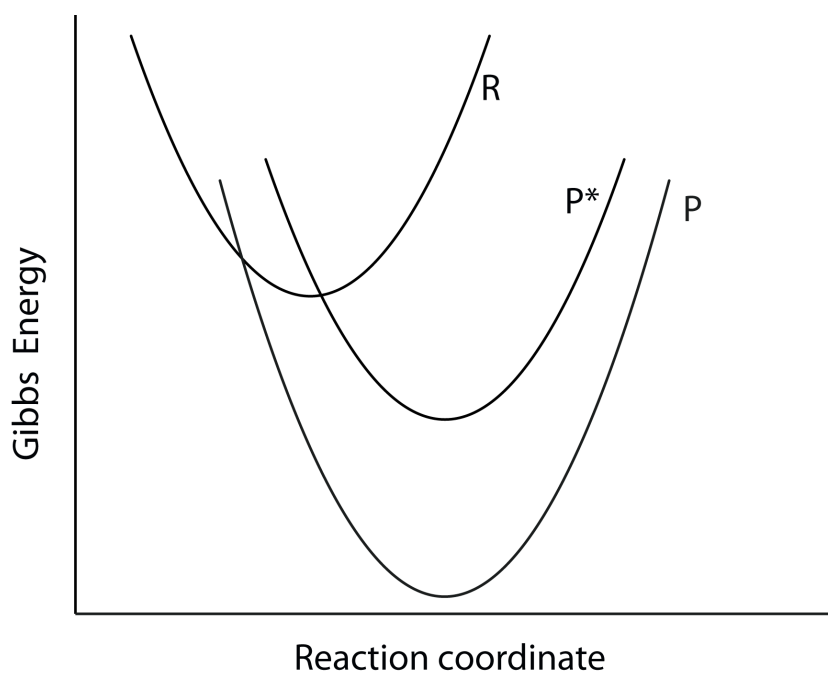


Figure 1.5.: Gibbs energy profile of the reactant (R), the product (P) with a very negative ΔG^0 , and an electronically excited product state (P^*) versus the reaction coordinate. The formation of the electronically excited product state is favoured. This results in chemiluminescence which is an indirect evidence for the so-called Marcus inverted region.^{114,194}

1.1.2. Non-adiabatic ET and quantum mechanical approach

The classical Marcus theory is able to predict ET rates very well for adiabatic reactions, i.e. reactions with electronic transition coefficients $\kappa_{el} = 1$, which means that the ET definitively occurs when the system reaches the transition state. The probability for an electron to cross the intersection to the product state not always equals 1 and is reflected by smaller electronic transition coefficients ($\kappa_{el} \ll 1$), which is termed non-adiabatic regime.¹¹²

A qualitative picture of adiabatic and non-adiabatic processes can be described by the potential energy surfaces of the reactant / product system as depicted in Figure 1.1 on page 7. When the system passes the intersection of the potential energy curves with high velocity, there is little time for ET and the system will usually jump from the lower R surface to the upper R surface and only cross to the product surface occasionally, which is a “non-adiabatic process”. At low velocity the system will usually remain on the lower solid “adiabatic” surface during the passage of the intersection.¹¹² Adiabatic processes are generally found for systems where A and D are close together.¹⁹

Non-adiabatic reactions have to be addressed quantum mechanically where tunneling effects are considered.^{74,79,191} The quantum model allows ET below the intersection point (nuclear tunneling) of the free Gibbs energy profiles of the initial (R) and final state (P). For the non classical approach an electronic-coupling matrix element, H_{DA} is introduced, which is defined as the overlap of the electronic wave functions of the equilibrium reactant and product states, ψ_R^0 and ψ_P^0 , respectively.

$$H_{DA} = \langle \psi_R^0 | \hat{H}_{el} | \psi_P^0 \rangle \quad (1.6)$$

The electronic Hamilton operator \hat{H}_{el} is part of the Born-Oppenheimer approximation, which separates a wavefunction into its electronic and nuclear components ($\Psi_{total} = \psi_{electronic} \times \psi_{nuclear}$). The electronic coupling decays exponentially with the separation r of the electronic wave functions according to

$$|H_{DA}(r)|^2 = |H_0|^2 \exp(-\beta(r - r_0)), \quad (1.7)$$

with H_0 as the maximum electronic coupling at the Van-der-Waals distance r_0 . The tunneling parameter β depends on the separating medium.¹⁰⁵

When considering the electronic coupling, a semi-classical Marcus equation can be expressed, where only the electronic part is treated quantum

mechanically, while the nuclear part is treated classically. The derivation can be found elsewhere.^{79,105} Here only the high-temperature approximation is given

$$k_{ET} = \frac{2\pi}{\hbar} |H_{DA}|^2 \frac{1}{\sqrt{4\pi\lambda k_B T}} \exp\left(\frac{-(\lambda + \Delta G^0)^2}{4\lambda k_B T}\right). \quad (1.8)$$

This is equivalent to Equation (1.5) with

$$\kappa_{el} \nu_n = \frac{2\pi}{\hbar} |H_{DA}|^2 \frac{1}{\sqrt{4\pi\lambda k_B T}}. \quad (1.9)$$

1.2. Heterogeneous electron transfer

So far only the electron transfer between two chemical species is discussed. For the ET between proteins and electrodes, as studied in this work, further considerations have to be made. In heterogeneous ET reactions the electron is transferred at an electrode/solution interface (interfacial ET) to or from a localized state from or to a delocalized state. In general, the same theoretical framework as for homogeneous ET can be applied.^{104,105,112} The overall reaction can be described as in Equation (1.1) but the first and last step has to be replaced by a diffusion of the reactant to and from the electrode surface or the reorientation or conformational change of the reactant. The main difference of the heterogeneous ET, in contrast to homogeneous ET, is the “delocalized electron” in the electrode metal. It is described by the Fermi-Dirac distribution function $f(\varepsilon)$ which accounts, in analogy to the Boltzmann distribution, for the different occupation probabilities of the different energy levels ε by an electron.

$$f(\varepsilon) = \frac{1}{1 + \exp\left(\frac{\varepsilon - \varepsilon_f}{k_B T}\right)}, \quad (1.10)$$

in which ε_f denotes the Fermi level (level with the highest possible energy of the system in the ground state at $T = 0$ K). The density of states theory which describes the number of states per interval of energy at each energy level is represented by the state density function $\rho(\varepsilon)$.⁴⁶

The driving force ΔG^0 of an ET reaction is proportional to the applied overpotential η in an electrochemical process, which is the difference between the applied electrode potential E and the redox potential E^0 of the redox active species at the electrode.^{104,105,112}

$$\eta = E - E^0 \quad (1.11)$$

E^0 is defined by the Nernst equation with the equilibrium concentrations of the reduced and oxidized species c_{red} and c_{ox} , k_B is the Boltzmann constant, F is the Faraday constant, R is the universal gas constant, e is the elementary charge, and n is the formal number of transferred electrons.

$$E = E^0 - \frac{k_B T}{ne} \ln \left(\frac{c_{ox}}{c_{red}} \right) = E^0 - \frac{RT}{nF} \ln \left(\frac{c_{ox}}{c_{red}} \right) \quad (1.12)$$

lead to

$$\Delta G^0 = |F\eta|. \quad (1.13)$$

In analogy to the homogeneous non-adiabatic ET reaction an ET rate constant (Equation (1.5) and (1.8)) can be expressed as⁵³

$$k_{ET} = \frac{2\pi}{\hbar} \frac{1}{\sqrt{4\pi\lambda k_B T}} \times \int d\varepsilon f(\varepsilon) \rho(\varepsilon) |H_{DA}(\varepsilon)|^2 \exp \left(\frac{-(\lambda + \Delta G^0(\varepsilon, \rho))^2}{4\lambda k_B T} \right), \quad (1.14)$$

with the integration over all occupied electronic levels of the electrode. $\rho(\varepsilon) |H_{DA}(\varepsilon)|^2$ yields the electronic coupling strength between the electrochemical active species and the electrode $|H_{DA}|^2$.⁴⁶

Under the assumptions (1) that a step function can replace the Fermi-Dirac distribution, (2) that the density of state function is independent of the energy, and (3) that contributions of the high and low energy levels, far from the Fermi level, can be neglected, relatively simple expressions for the ET rates can be derived.^{26,138,139}

$$k_{red} = A \frac{\sqrt{\pi\lambda k_B T}}{e} \left(1 - \operatorname{erf} \frac{e\eta + \lambda}{2\sqrt{\lambda k_B T}} \right) \\ k_{ox} = A \frac{\sqrt{\pi\lambda k_B T}}{e} \left(1 + \operatorname{erf} \frac{e\eta - \lambda}{2\sqrt{\lambda k_B T}} \right), \quad (1.15)$$

with the error function defined as

$$\operatorname{erf}(x) = \frac{2}{\sqrt{\pi}} \int_0^x \exp(-t^2) dt. \quad (1.16)$$

A is a constant related to the electronic coupling term $|H_{DA}(\varepsilon)|^2$ which decays exponentially with the distance between the weakly coupled electron donor and acceptor.

For heterogeneous ET reactions no inverted Marcus region is found. With increasing overpotential η , i.e. with increasingly negative ΔG^0 , k_{ET} is reaching a plateau. This effect is due to the possibility of the electron to be transferred into a high excitation level of the product state, far from

the Fermi level, which intersects at the energetic minimum of the reactant state.

1.2.1. Biological electron transfer

The reactants in biological ET are expected to undergo vibrational and solvation / environmental changes during the reaction, as it is true for the ET of small molecules. For biological ET reactions one has to account also for electric field effects on ΔG^0 which is discussed in Chapter 2.¹⁰⁵ Biological ET usually occurs in the non-adiabatic regime.

1.2.2. Gated ET

In interfacial electron transfer reactions often a gated mechanism is found.^{12,78,117,138,143} A rate-limiting non-ET step, like reorientation of the redox-active species or of solvent molecules, is required to activate or optimize the system for ET. These gated mechanisms will be discussed in Chapter 9 and 10.

2. Electrochemical Interfaces

2.1. Electrode-solution interface

The insertion of a bare metal electrode into an aqueous solution leads to the immediate adsorption of ions onto the electrode surface, constituting an electrical double layer. A classical description of the electrical double layer is based on the Gouy-Chapman-Stern (CGS) model^{11,179} and considers a densely packed, rigid layer of ions without a hydration shell at the electrode surface which is called the Helmholtz or Stern layer while outside this layer the ions are distributed in a diffuse double layer.

The electrode with the Stern layer is treated as capacitor and therefore the potential ϕ drops linearly from the electrode surface at d_0 (ϕ_M) to d_C , which is the thickness of the Stern layer (ϕ_C). Outside the Stern layer the potential drops exponentially with increasing distance from the electrode until it reaches the solution potential ϕ_S . The charge densities σ at the interface can be quantified using the approach of Smith and White.¹⁷³ The charge density of the metal (σ_M) is given by

$$\sigma_M = \frac{\epsilon_0 \epsilon_C}{d_C} (\phi_M - \phi_C) \quad (2.1)$$

where ϵ_0 is the permittivity and ϵ_C the dielectric constant of the Stern layer. The charge density in solution can be derived from the Gouy-Chapman distribution with an exponential potential decay of the potential with increasing distance from the Stern layer.

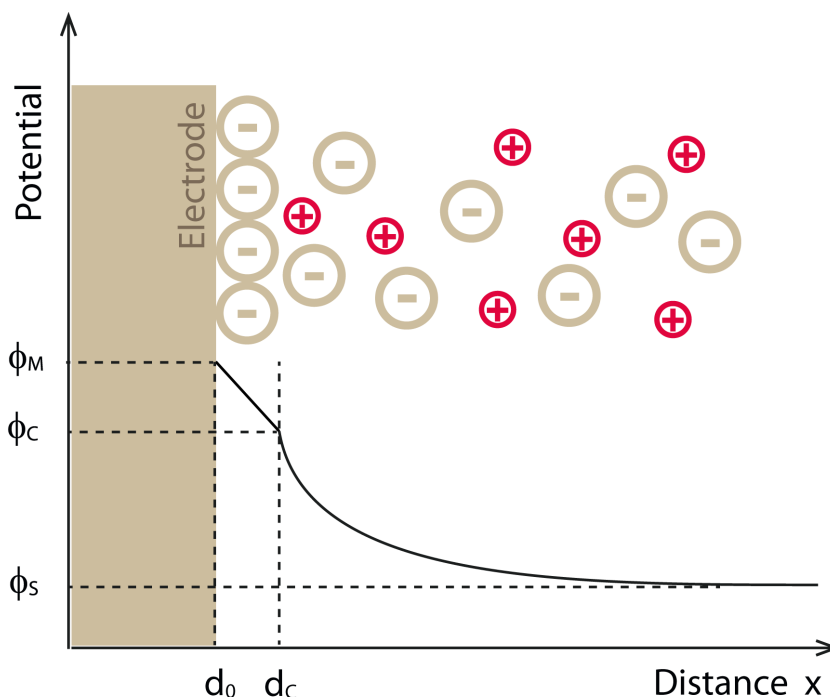
$$\sigma_S = -\epsilon_0 \epsilon_s \kappa \frac{2k_B T}{e} \sinh \left(\frac{e}{2k_B T} (\phi_C - \phi_S) \right) \quad (2.2)$$

with the inverse Debye length κ , which is defined as

$$\kappa = \frac{1}{\sqrt{\frac{\epsilon_0 \epsilon_C k_B T}{2N_A e^2 I}}} \quad (2.3)$$

The inverse Debye length describes the charge density of the solution dependent of the electrolyte ionic strength I . The Debye length κ^{-1} decreases with increasing concentration of the electrolyte.

Figure 2.1.: Schematic representation of the Gouy-Chapman-Stern model of the electrical double layer at the electrode-solution interface.



The requirement of charge neutrality of the complete system then gives the charge density at the Stern layer (σ_C).

$$\sigma_M + \sigma_C + \sigma_S = 0 \quad (2.4)$$

The charge densities vary with the electrode potential (ϕ_M). In the special case that ϕ_M equals ϕ_S the absolute charge density (σ_M) on the metal surface and the effective electric field (E_F) perturbing the solution becomes zero. This is called the potential of zero charge of the metal (E_{PZC}). For $\phi_M \neq \phi_C$, the potential drop at the Stern layer causes an electric field.

$$E_F = \frac{\phi_M - \phi_C}{d_C} = \frac{\sigma_M}{\epsilon_0 \epsilon_C} \quad (2.5)$$

The CGS model was further developed to take into account the different probabilities of ions to build hydration shells or adsorb directly to the surface, depending on charge and size.^{34,55–57}

2.2. Self-assembled monolayer and interfacial potential distribution

The adsorption of proteins on bare metal surfaces may cause denaturation or distortion of the native structure.¹⁷⁴ Moreover, when using silver as electrode material one has to keep in mind the high chemical activity of Ag^+ that inter alia may attack disulfate bridges in proteins. To avoid

the degradation of molecules often bio-compatible coatings are used to shield the species from direct contact with the metal.⁴³

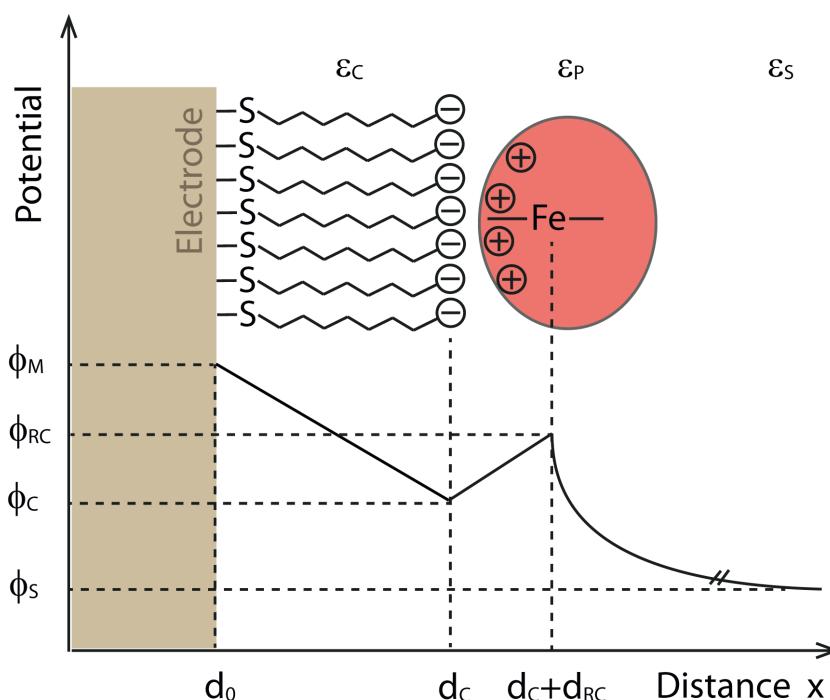
A commonly used strategy is the coating of the electrode with SAMs (self-assembled monolayers).^{10,20,42,98,132,165,192} SAMs are formed by alkanethiols of the type $R - (CH)_n - SH$ with a variable alkyl chain length. The sulfur group binds with high affinity to a variety of metals (Au, Ag, Cu, Pd, Pt) and the chains assemble together, forming a highly ordered monolayer, stabilized by Van-der-Waals interactions. These kind of monolayers are quite stable over a wide potential range and desorb at negative potentials ($E < -1.0$ V vs. Ag/AgCl (3M)).^{13,77} The structure of the SAM, including the tilt angle of the chains with respect to the surface, depends on the metal, the chain length, and the headgroup.^{78,98}

Proteins can be immobilized electrostatically, covalently, hydrophobically, or by other strategies.^{43,98} In this work cytochrome *c* (Cyt*c*) was immobilized via electrostatic interactions between negatively charged carboxyl-terminated SAM and the positively charged, lysine-rich patch on the Cyt*c* surface.^{9,43}

SAMs do not only constitute tunable biocompatible interfaces but also allow controlling the electric field strength. Since a SAM is well ordered it can be assumed that the potential drops linearly in the SAM chains, so that the electric field strength can be controlled by varying chain lengths, the tail functional group of the SAM, pH, ionic strength of the solution, and the electrode potential.¹³²

The interfacial potential distribution across the different interfaces (electrode / SAM / (redox-)protein / solution interface) can be described, in analogy to the considerations made above,¹⁷³ with the charge densities σ at different interfaces (σ_M -metal, σ_C -SAM, σ_{RC} -redox center, σ_S -solution). The corresponding potentials are ϕ_M , ϕ_C , ϕ_{RC} , and ϕ_S . The thickness of the SAM is given by d_C , while the protein redox center (RC) is located at a distance of $d_C + d_{RC}$ from the electrode. The dielectric constants of the SAM, protein, and solution are ϵ_C , ϵ_P , and ϵ_S , respectively. The electrostatic potential vary linearly from ϕ_M to ϕ_C and linearly from ϕ_C to ϕ_{RC} . In the solution phase the potential decays exponentially till it reaches ϕ_S .

Figure 2.2.: Schematic representation of the interfacial potential distribution for a redox protein immobilized at an electrode/SAM surface, here the specific case of cytochrome *c* electrostatically adsorbed on an Ag electrode coated with a COOH-terminated SAM.



The electric field can be described by

$$E_F = \begin{cases} 0 & x < 0 \\ \left(\frac{\phi_M - \phi_C}{d_C} \right) & 0 < x < d_C \\ \left(\frac{\phi_C - \phi_{RC}}{d_{RC}} \right) & d_C < x < (d_C + d_{RC}) \\ \kappa \left(\frac{2k_B T}{ze} \right) \sinh \left(ze \frac{\phi_x - \phi_S}{2k_B T} \right) & x > (d_C + d_{RC}) \\ 0 & x \rightarrow \infty \end{cases}$$

with ϕ_x representing the potential in the solution at position x , and z as the charge of the electrolyte ions.

ET reactions of immobilized proteins are influenced by the potential distribution.⁹³ The potential experienced by the redox center (E_{exp}) is different from the applied electrode potential (E).

$$E_{exp} = E - E_{RC} \quad (2.6)$$

The potential drop at the redox center (E_{RC}) is given by

$$E_{RC} = \phi_{RC} - \phi_S \quad (2.7)$$

and the charge densities can be obtained (analogous to Equation (2.1)) by

$$\begin{aligned} \sigma_M &= \frac{\epsilon_0 \epsilon_C}{d_C} (\phi_M - \phi_C), \\ \sigma_M + \sigma_C &= \frac{\epsilon_0 \epsilon_P}{d_C + d_{RC}} (\phi_C - \phi_{RC}) \end{aligned} \quad (2.8)$$

and for small E_{RC}

$$\sigma_S = -\epsilon_0 \epsilon_S \kappa E_{RC} \quad (2.9)$$

with the requirement of charge neutrality in mind ($\sigma_M + \sigma_C + \sigma_{RC} + \sigma_S = 0$) the potential drop at the redox center can be derived as

$$E_{RC} = \frac{\sigma_C \epsilon_P d_C + \epsilon_0 \epsilon_P \epsilon_C (E - E_{PZC}) + (d_C \epsilon_P + d_{RC} \epsilon_C) \sigma_{RC}}{\epsilon_0 [\epsilon_C \epsilon_P + (d_C \epsilon_P + d_{RC} \epsilon_C) \epsilon_S \kappa]} \quad (2.10)$$

where E denotes the electrode potential and E_{PZC} the potential of zero charge with $E = \phi_M - \phi_{ref}$ and $E_{PZC} = \phi_s - \phi_{ref}$ where ϕ_{ref} denotes the reference potential.

Experimentally the E_{RC} is accessible through

$$E_{RC} = E^0 - E_S^0. \quad (2.11)$$

E_S^0 is the redox potential of the protein in solution and E^0 is that of the adsorbed protein. The resulting electric field strength at the protein binding site is

$$E_F = \frac{\epsilon_0 \epsilon_S \kappa E_{RC} - \sigma_C - \sigma_{RC}}{\epsilon_0 \epsilon_C}. \quad (2.12)$$

For studies on proteins associated with membranes the SAM monolayer might represent a suitable model for the natural system and the potential distribution across the SAM is able to account for the transmembrane potential in cell membranes. Predictions for the electric field strength at carboxyl-terminated SAMs at Ag electrodes yield 10^9 V/m,^{133,135} which is comparable to the values expected in the vicinity of charged phospholipid head groups of biological membranes.²⁷ A detailed review of the potential distribution at phospholipid membranes can be found elsewhere.²⁷

3. Raman Spectroscopy

3.1. Vibrational spectroscopy

There are $3N - 6$ normal modes (vibrational degrees of freedom) for any non-linear molecule with N atoms and $3N - 5$ normal modes for a linear molecule. Each atom possesses 3 translational degrees of freedom which is reduced by 3 degrees of freedom for simultaneous translation of all atoms along the three axes and further by three degrees of freedom (two for linear molecules) for the rotation around the three (two) axes. Each normal mode is assigned to a single normal coordinate, Q_k , which describes the position of the atoms deflected from their equilibrium position and the relation to each other. Q_k can be described by summation over the Cartesian coordinates of the atomic positions in the molecule.¹⁶⁷

Vibrational transitions between the initial and final vibrational levels $|i\rangle$ and $|f\rangle$ can either be induced by direct absorption of a photon (IR spectroscopy) or by inelastic scattering of light of energy higher than the transition from $|i\rangle$ to $|f\rangle$. The latter effect is called the Raman effect, named after C. V. Raman who experimentally observed this phenomenon 1928 for the first time,^{156,157} which was theoretically predicted by A. Smekal five years earlier.¹⁷²

The intensity in an IR or Raman band $I_{Raman/IR}$ resulting from a transition from $|i\rangle$ to $|f\rangle$ is proportional to the transition probability P_{if} and therefore to the square of the integral

$$I_{Raman/IR} \propto P_{if} \propto |\langle \psi_f^* | \hat{\Omega} | \psi_i \rangle|^2, \quad (3.1)$$

where ψ_i and ψ_f are the wavefunctions of the vibrational states $|i\rangle$ and $|f\rangle$ and $\hat{\Omega}$ denotes the operator that describes the perturbation of the molecule by the electromagnetic radiation.¹⁶⁷ The perturbation operator is different for absorption (IR) and scattering (Raman) processes.¹⁶⁷

IR The absorption of light is determined by the effective coupling of the vibrational state to the electromagnetic radiation and therefore by

the transition dipole moment, which is related to the electrical dipole moment operator $\hat{\mu}_q$, defined by

$$\hat{\mu}_q = \sum_{\alpha} e_{\alpha} \cdot q_{\alpha} \quad (3.2)$$

with the effective charge e_{α} at atom α and the distance to the center of gravity q_{α} in Cartesian coordinates ($q = x, y, z$). A non-zero transition probability is only possible for a mode when the dipole moment varies with the respective normal coordinate and when additionally the quantum numbers of the states $|i\rangle$ and $|f\rangle$ differ by one.¹⁶⁷

Raman Scattering processes occur upon interactions of the electric field of electromagnetic radiation with matter.^{86,158} The electric field vector \vec{E} of the incident electromagnetic wave with the frequency ν_0 can induce an electric dipole moment μ_{ind} .

$$\vec{\mu}_{ind} = \alpha(\nu) \cdot \vec{E}(\nu_0) = \alpha(\nu) \cdot \vec{E}_0 \cdot \cos(2\pi\nu_0 t), \quad (3.3)$$

where $\alpha(\nu)$ is the frequency(ν)-dependent polarizability and ν_0 is the frequency of the incident radiation.^{31,167} Inelastic/Raman scattering (scattering with energy transfer) only occurs when the α changes with a normal mode.

3.2. The Raman effect

If the nuclei oscillate with the normal mode frequency ν_k , $\alpha(\nu)$ is expressible as

$$\alpha(\nu) = \alpha_0(\nu_0) + \left(\frac{\delta\alpha}{\delta Q_k} \right)_0 (2\pi\nu_k t). \quad (3.4)$$

From Equation (3.3) and (3.4) follows that

$$\begin{aligned} \vec{\mu}_{ind} = & \vec{E}_0 \alpha_0 \cos(2\pi\nu_0 t) \\ & + \vec{E}_0 \left(\frac{\delta\alpha}{\delta Q_k} \right)_0 Q_k \cos[2\pi(\nu_0 + \nu_k)t] \\ & - \vec{E}_0 \left(\frac{\delta\alpha}{\delta Q_k} \right)_0 Q_k \cos[2\pi(\nu_0 - \nu_k)t]. \end{aligned} \quad (3.5)$$

Inelastic scattering leads to frequency shifts of the incident radiation ν_0 . For $|i\rangle \rightarrow |f\rangle$ with $|i\rangle < |f\rangle$ the frequency shifts to $\nu_r = \nu_0 - \nu_k$ which is denoted as Stokes scattering and with $|i\rangle > |f\rangle$ the frequency shifts to $\nu_r = \nu_0 + \nu_k$ which is denoted as anti-Stokes scattering. At ambient or low temperatures the Stokes scattering (middle term in Equation (3.5))

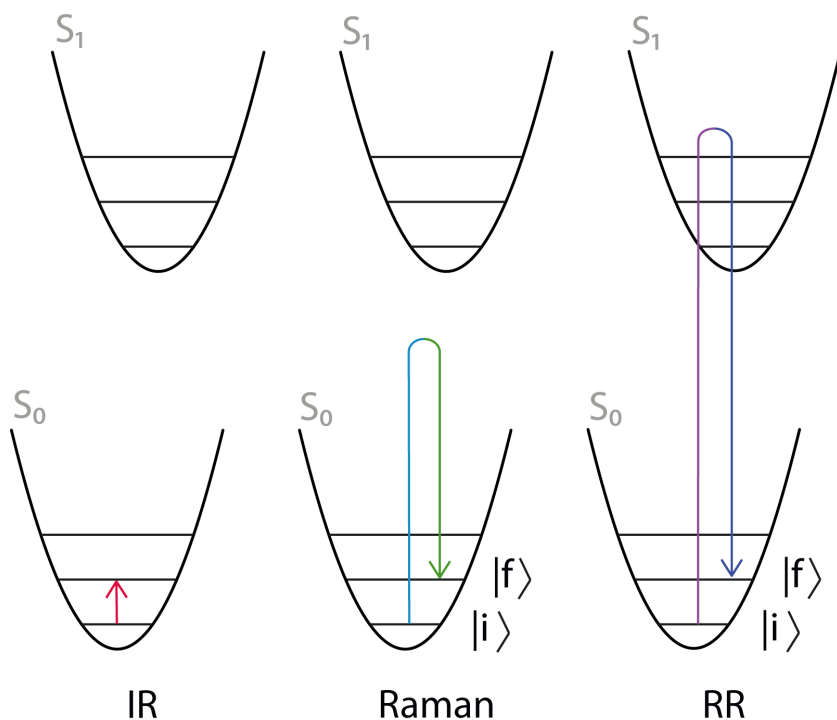


Figure 3.1: Schematic energy diagram of different vibrational transitions induced by IR absorption, Stokes-Raman photon scattering, and resonance Stokes-Raman scattering within the harmonic approximation. S_0 and S_1 denote the electronic ground and the first excited singlet state, respectively. The energy levels in the electronic states are the vibrational states. The initial and final vibrational state of the ground state are denoted as $|i\rangle$ and $|f\rangle$ respectively. Here only the case of Stokes scattering is shown with $|i\rangle < |f\rangle$. $|i\rangle > |f\rangle$ would lead to anti-Stokes scattering and $|i\rangle = |f\rangle$ to Rayleigh scattering. The colour code of the arrows is matching schematically the electromagnetic spectrum, with radiation of different energies needed for excitation.

represents the main Raman scattering since the thermal energy is lower than the energy of most normal modes and therefore mainly the ground state is populated (Boltzmann distribution).¹⁶⁷ However, the quantum yield of Raman scattering is very low and the first term in Equation (3.5), due to elastic scattering (Rayleigh scattering), is highly dominant.^{86,158}

3.2.1. Quantum mechanical description of the Raman effect

The probability of the Raman transition between the vibrational states $|i\rangle \rightarrow |f\rangle$, is determined by the polarizability operator $\hat{\alpha}$ and can be described by a Taylor series along the normal coordinates Q_k .

$$\hat{\alpha} = \alpha_0 + \sum_{k=1}^{3N-6} \left(\frac{\delta\alpha}{\delta Q_k} \right)_0 Q_k + \dots \quad (3.6)$$

α_0 is the dominant term which is responsible for the elastic scattering, where state $|i\rangle$ equals $|f\rangle$ (Rayleigh scattering).¹⁵⁸ As already mentioned above, Raman intensity ($|i\rangle \neq |f\rangle$) is observed for a vibrational mode when the molecular polarizability changes along the normal coordinate so that Equation (3.1) can be written as

$$I_{Raman} \propto |\langle \psi_f^* | \hat{\alpha} | \psi_i \rangle|^2 \propto \left(\left(\frac{\delta\alpha}{\delta Q_k} \right)_0 Q_k \right)^2. \quad (3.7)$$

A Raman cross section $\sigma_{i \rightarrow f}$, that is the ratio between the scattered intensity integrated overall scattering angles and polarisation directions

for a non oriented sample $I_{i \rightarrow f}$ and the incident radiation intensity I_0 , for the vibrational transition from $|i\rangle$ to $|f\rangle$ can be expressed by

$$\sigma_{i \rightarrow f} = \frac{I_{i \rightarrow f}}{I_0} \propto (v_0 \pm v_k)^4 \cdot \sum_{\rho\sigma} |\alpha_{\rho,\sigma}|^2, \quad (3.8)$$

with the sum over the polarizabilities for the molecule-fixed coordinates ρ and σ . The scattered intensity scales with the fourth power of to the frequency of the scattered light.¹⁶⁷

For Raman spectroscopy usually polarized laser light is used. The intensity of the scattered Raman radiation consists of two components which are polarized parallel (I_{para}) and perpendicular (I_{perp}) to the electric field \vec{E} of the incident radiation. They are only dependent on the matrix elements of the polarisation which refer to the respective direction and determine the Raman activity of a normal mode.¹⁶⁷

The depolarization ratio

$$\rho = \frac{I_{perp}}{I_{para}} \quad (3.9)$$

can be used for the vibrational band assignment of symmetric molecules and to gain information of the orientation of ordered structures.^{31,167,201} For $\rho = 0.75$ a band is called depolarized which are due to non-totally symmetric vibration, while totally symmetric vibrations give rise to polarized bands with $\rho < 0.75$. The higher the symmetry of a molecule, the smaller is ρ ($0.75 > \rho > 0$) for a totally symmetric vibration.³¹

Photon scattering can be described by the Kramers-Heisenberg-Dirac dispersion formula which is based on the classical dispersion theory of light.^{36,86} Since two photons are involved in Raman scattering second-order perturbation theory is required.^{3,4,30,97,167} The polarizability tensor for the transition from the vibrational state $|i\rangle$ to $|f\rangle$ can be expressed as

$$[\alpha_{\rho\sigma}]_{if} = \frac{1}{h} \sum_{r \neq i,f} \left(\frac{\langle f | M_\rho | r \rangle \langle r | M_\sigma | i \rangle}{v_r - v_i - v_0 - i\Gamma_r} + \frac{\langle r | M_\rho | i \rangle \langle f | M_\sigma | r \rangle}{v_r - v_f + v_0 + i\Gamma_r} \right) \quad (3.10)$$

where M_σ and M_ρ are the transition dipole moments in directions ρ, σ , for the molecule-fixed non-rotating coordinate system where $\rho, \sigma = x, y, z$.^{4,31,196} The vibrational states $|i\rangle$ and $|f\rangle$ refer to the electronic ground state, where $|r\rangle$ refers to all vibronic states of the molecule. $h(v_r - v_i)$ and $h(v_r - v_f)$ represent the energy necessary for the transition from $|i\rangle$ to $|r\rangle$ and $|r\rangle$ to $|f\rangle$ and $h\nu_0$ is the energy of the incident radiation. Equation (3.10) represent a sum of Dirac integrals that describe the transitions from $|i\rangle \rightarrow |r\rangle$ and $|r\rangle \rightarrow |f\rangle$. The summation in the

polarizability tensor run over all vibronic states $|r\rangle$, where the transition dipole moment between the states $|r\rangle$ to both $|i\rangle$ and $|f\rangle$ is non-zero. The contribution of any state $|r\rangle$ is dependent of the energetic distance from the incident radiation and has individual effect on the Raman transition probability.^{167,175} The so-called damping constant Γ_r is a correction term which is related to the finite natural lifetime of the different vibronic states $|r\rangle$.

3.3. The resonance Raman effect

For normal Raman scattering the summation in the polarizability tensor run over all vibronic states $|r\rangle$. If ν_0 approaches the frequency of an electronic transition to an electronically excited state $|e\rangle$ ($\nu_0 \approx \nu_e - \nu_i$) the transition polarizability tensor $[\alpha_{\rho\sigma}]_{if}$ is dominated by one term of the sum of Equation (3.10), $\nu_e - \nu_i - \nu_0$ becomes very small and the denominator of the first term is $\approx -i\Gamma_r$ which is small (low damping for the excited electronic state). This term is called resonant, and constitutes the resonance effect in Raman spectroscopy. Equation (3.10) is then simplified to

$$[\alpha_{\rho\sigma}]_{if} \cong \frac{1}{h} \sum_r \left(\frac{\langle f | M_\rho | r \rangle \langle r | M_\sigma | i \rangle}{\nu_r - \nu_i - \nu_0 - i\Gamma_r} \right) \quad (3.11)$$

where the summation is now restricted to vibrational states of the resonant electronically excited state $|e\rangle$.^{4,167,185,196}

As an electronic transition is involved, nuclear coordinates change. The separation of the wavefunction into its electronic and nuclear components is applicable, using the Born-Oppenheimer approximation. The wavefunctions $|i\rangle$, $|f\rangle$, and $|r\rangle$ of the integrals in Equation (3.11) depend on electronic and nuclear coordinates, which can be separated.

$$|i\rangle = |g\rangle |m_i\rangle \quad |f\rangle = |g\rangle |m_f\rangle \quad |r\rangle = |e\rangle |n\rangle \quad (3.12)$$

$|g\rangle$ and $|e\rangle$ are the ground and excited electronic state, where $|m_i\rangle$ and $|m_f\rangle$ are the initial and final vibrational states of the electronic ground state and $|n\rangle$ denote all vibrational states of the excited electronic state, respectively. With $\langle f | M_\rho | r \rangle = \langle m_f n | \langle g | M_\rho | e \rangle = \langle m_f n | M_{ge,\rho} \dots$, where $M_{ge,\rho}$ and $M_{ge,\sigma}$ denote the electronic transition dipole moments for the transition from g to e . The integrals of type $\langle m_f n |$ are the integrals

over the products of two vibrational wavefunctions represent the so-called Franck-Condon factors. The Equation (3.11) can be further simplified to

$$[\alpha_{\rho\sigma}]_{if} \cong \frac{1}{h} \sum_n \left(\frac{\langle m_f n \rangle M_{ge,\rho} \langle n m_i \rangle M_{ge,\sigma}}{\nu_n - \nu_i - \nu_0 - i\Gamma_n} \right) \quad (3.13)$$

The electronic transition dipole moments can be expanded in a Taylor series with respect to the normal coordinates Q_k around the displacement from the equilibrium position $Q_k^{(0)}$.

$$M_{ge,\rho}(Q_k) = M_{ge,\rho}(Q_k^{(0)}) + \sum_k \left(\frac{\delta M_{ge,\rho}}{\delta Q_k} \right)_0 Q_k + \dots \quad (3.14)$$

Neglecting higher order terms, which is reasonable within the harmonic approximation, an expression for the transition polarizability tensor as a sum of two terms is obtained, the so-called Albrecht's A- and B-terms.^{4,185}

$$[\alpha_{if}]_{\rho\sigma} \cong A_{\rho\sigma} + B_{\rho\sigma} \quad (3.15)$$

with

$$A_{\rho\sigma} \cong \frac{1}{h} \sum_n \left(\frac{\langle m_f n \rangle M_{ge,\rho}^0 \langle n m_i \rangle M_{ge,\sigma}^0}{\nu_n - \nu_i - \nu_0 - i\Gamma_n} \right) \quad (3.16)$$

and

$$B_{\rho\sigma} \cong \frac{1}{h} \sum_n \left(\frac{\langle m_f | Q_k | n \rangle \langle n m_i \rangle \left(\frac{\delta M_{ge,\rho}}{\delta Q_k} \right)_0 M_{ge,\sigma}^0}{\nu_n - \nu_i - \nu_0 - i\Gamma_n} \right) + \frac{1}{h} \sum_n \left(\frac{\langle m_f n \rangle \langle n | Q_k | m_i \rangle \left(\frac{\delta M_{ge,\sigma}}{\delta Q_k} \right)_0 M_{ge,\rho}^0}{\nu_n - \nu_i - \nu_0 - i\Gamma_n} \right) \quad (3.17)$$

In both terms the denominators decrease rapidly when the exciting frequency matches an electronic transition and thus the resonance Raman (RR) intensity increase. Nevertheless the two terms represent different enhancement mechanisms.^{4,167,185,196}

The enhancement via the A-term (Equation (3.16)) is strong when the electronic transition dipole moment M_{ge}^0 is large, since it scales with $|M_{ge}^0|^2$. Additionally the enhancement in the A-term depends strongly on the Franck-Condon overlap integral products $\langle m_f n \rangle$ and $\langle n m_i \rangle$. Therefore, the displacement of the potential energy curve in the electronic excited state is determining whether a normal mode is resonance enhanced. This can be understood, when considering a transition from state $\langle m_i |$ in the electronic ground state to $\langle n |$ in the electronic excited state. If $\langle m_i |$ and $\langle n |$ are similar in symmetry the Franck-Condon factor $\langle n m_i \rangle$ will be zero if the origin of the potential curve is unchanged upon transi-

tion. However, if there is a displacement of the potential energy curve of the electronic excited state leads to a non-zero Franck-Condon factor is obtained regardless of the symmetry of the vibrational states.^{4,95,167}

The B-term enhancement (Equation (3.17)) arises from vibronic coupling between different nearby excited states. This effect is called Herzberg-Teller vibronic coupling.^{37,63,95,159} It is most pronounced when the incident radiation matches a weakly allowed electronic transition that is vibronically mixed with a nearby strong one. The transition dipole moment of the transition from the electronic state $|g\rangle$ to $|e\rangle$ contains contributions from transitions from the state $|g\rangle$ to another nearby excited state if the energy difference of the coupled excited states is sufficiently small. For vibration k the amount of the “borrowed” contribution is proportional to the appropriate coupling integral and the displacement Q_k . Mostly the B-term scattering accounts for RR enhancement of non-totally symmetric modes.^{4,31}

Since A-term enhancement is stronger than B-term enhancement, totally symmetric vibrations almost always exhibit significantly higher intensity than non-totally symmetric vibrations.¹⁸⁵

In general, resonance enhancement not necessarily requires an exact frequency match of the incident radiation and the electronic transition. The frequencies measured in RR spectroscopy refer to the molecular structure in the initial electronic state, usually the ground state, although the RR intensities are sensitively controlled by the properties of the electronically excited state(s).¹⁶⁷ While in Raman spectroscopy only polarized and non-polarized bands appear in resonant enhanced Raman spectroscopy also anomalous polarized bands may occur with $\rho > 0.75$.³¹

3.4. Surface enhancement of radiation on metal surfaces

The free electrons in a metal particle can effectively couple to the electromagnetic field of incident light $\vec{E}_0(\nu_0)$, if the particle size is small with respect to the wavelength. The coupling lead to collective vibrations of the free electrons with respect to the metal nuclei, oscillating parallel to the surface. The resulting so-called surface plasmons cause an additional electric field component $\vec{E}_{ind}(\nu_0)$, normal to the surface in the near-field of the sphere. The total electric field of the radiation with frequency ν_0 is expressed by

$$\vec{E}_{total}(\nu_0) = \vec{E}_0(\nu_0) + \vec{E}_{ind}(\nu_0). \quad (3.18)$$

The induced electric field component $\vec{E}_{ind}(\nu_0)$ depends on the dielectric properties of the metal. For a spherical particle the electrostatic approximation yields

$$E_{ind} = \frac{\varepsilon(\nu_0) - \varepsilon_S}{\varepsilon(\nu_0) + 2\varepsilon_S} E_0 \quad (3.19)$$

where $\varepsilon(\nu_0)$ is the frequency-dependent dielectric constant of the metal and ε_S is the complex dielectric constant of the surrounding medium. For $\varepsilon(\nu_0) = -2\varepsilon_S$ the induced electric field and therefore \vec{E}_{total} becomes greatly enhanced. This simple model can be applied successfully to different shapes and surface morphologies. The shape and size of metal particles, or the surface roughness characteristics, determine the wavelength that induce the surface plasmon oscillations. The resonance condition is met by several coinage metals in the visible spectral region, which make them candidates for use in vibrational spectroscopy where the signal intensity can greatly be enhanced by the interaction of the incident light with a rough metal surface. To get surface enhancement the optimal dimension of the surface roughness or nanostructures ranges from 5–100 nm.^{24,130,131}

3.4.1. Surface enhanced Raman spectroscopy

Not only the incident electromagnetic field but also the scattered Raman electromagnetic field can be enhanced by the interaction with a rough metal surface.^{5,47,72} This surface enhanced Raman (SER) effect is found to be up to 10^6 -fold stronger than the normal Raman scattering and can be combined with the resonance Raman (RR) effect. It is applicable for molecules in the vicinity of rough Ag and Au surfaces. Conveniently, the support metal can be used as electrode to probe redox processes.

The enhancement factor F_{SER} decrease with the distance d from the surface. For a spherical colloid of the radius a_0 it is given by

$$F_{SER} = F_{SER}(0) \cdot \left(\frac{a_0}{a_0 + d} \right)^{12} \quad (3.20)$$

with $F_{SER}(0)$ as the enhancement factor for molecules directly adsorbed onto the metal surface. Even with this distance dependence, one gets distinct signal enhancements when the molecules are kept several nm (1–5 nm) apart from the enhancing metal surface, by e.g. biocompatible coatings like SAMs.^{24,130} Detailed descriptions of the field enhancement mechanisms at certain metal surfaces and SER-scattering can be found elsewhere.^{24,68,70,81,123,129–131,189}

4. Investigation of Cytochrome *c*, CoFeSP, and RACo with Resonance Raman Spectroscopy

The proteins studied in this work possess different metal containing cofactors for which electronic transitions can be induced in the UV / visible region and therefore can be investigated by resonance Raman (RR) spectroscopy where only the cofactors are probed.

Cytochrome *c* (Cyt*c*) harbours an iron porphyrin cofactor, the heme *c*. The corrinoid iron-sulphur protein (CoFeSP) includes two cofactors which are a corrin macrocycle with a cobalt center, which is structurally related to the porphyrin in Cyt*c*, and a [4Fe4S] cluster. The reductive activator of CoFeSP (RACo) harbours a [2Fe2S] cluster.

Heme *c* The heme *c* in Cyt*c* is covalently linked via thioether bridges to two cysteine residues (Cys14/Cys17). The iron in the heme center, coordinated by the four pyrrole nitrogens, additionally exhibits two axial coordination sites, from which one can remain unoccupied so that either a fivefold (5c) or a sixfold (6c) coordination of the iron occur. Depending on the axial ligands a high (HS) or low spin (LS) state of the iron is formed. In the octahedral ligand field of the iron the five d-orbitals split into two degenerate e_g orbitals (from $d_{z^2}, d_{x^2-y^2}$) with higher and three degenerate t_{2g} orbitals (from d_{xy}, d_{xz}, d_{yz}) with lower energy. Strong ligands lead to a large separation of the two orbital levels and therefore a LS state is formed. Weak ligands, in contrast, lead to a small separation of the orbital levels which is smaller than the spin pairing energy and

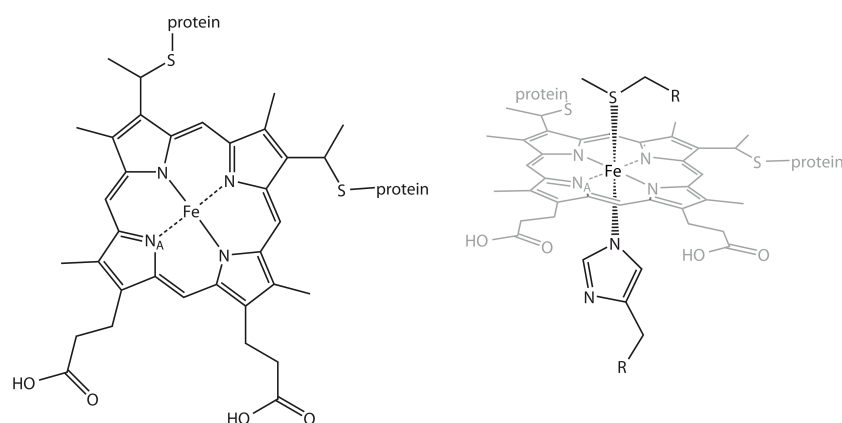
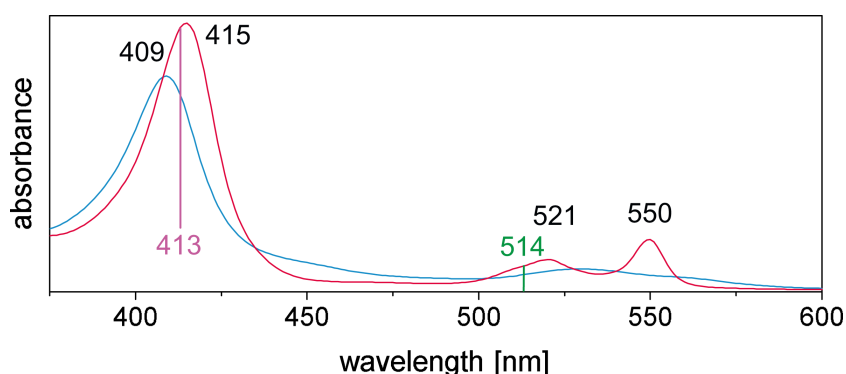


Figure 4.1.: Chemical constitution of the heme *c* chromophore in Cyt*c*, with a conjugated tetrapyrrole macrocycle coordinating an iron atom. The heme *c* is covalently attached via two thioether bridges to cysteine residues. View from the top on the left side and the axial coordination with a methionine coordinating the iron from the top and a histidine from the bottom side depicted on the right side.

Figure 4.2.: UV/Vis absorption spectrum of oxidized (blue) and reduced (red) Cyt c . In RR experiments, a laser excitation line at 413 nm (purple) is used to obtain strong resonantly scattered signals, which are even stronger for the reduced Cyt c in comparison with the oxidized form. Excitation with 514 nm (green) causes a so-called pre-resonance enhancement.



favour the formation of a HS state. The iron center can change the formal oxidation state between Fe^{3+} (ferric, $3d^5$) and Fe^{2+} (ferrous, $3d^6$).

The UV/vis spectra of hemes display broad bands in two regions of the spectrum. Both regions are more pronounced for an reduced iron center than for an oxidized one. The strong band in the near UV region around 410 nm is the so-called Soret-band. The weaker bands between 500 and 550 nm are the Q-bands. The absorption in both regions results from $\pi - \pi^*$ electronic transitions from the porphyrin ring and can be understood on the basis of the molecule orbital (MO) theory.⁵⁴ In a first approximation, the porphyrin ring may be considered as a two dimensional system of conjugated π bonds with D_{4h} symmetry. The highest occupied MOs (HOMOs) have a_{1u} and a_{2u} symmetry and are close in energy,^{35,178} whereas the lowest unoccupied MO (LUMO) is double degenerated and shows e_g symmetry. The two resulting electronic (HOMO to LUMO) transitions are both of the same E_u -symmetry so that the electronic transitions are strongly interacting. Additive and subtractive combination of the transition dipole moments lead to the intense Soret-band and the Q-band, respectively. The Q-band is split into two bands due to a (0, 0) and (0, 1) vibronic transition.^{54,167}

Corrinoid The Co β -aqua-(5,6-dimethylbenzimidazolcobamide) cofactor in CoFeSP is depicted in Figure 4.3. Analogous to the iron porphyrin the cobalt in the corrin frame is coordinated by the nitrogen atoms of the four pyrrole rings. Also cobalt exhibits two additional axial coordination sites. In general the same rules apply for cobalt as for the iron in the heme *c*, as discussed above, but cobalt can exhibit three different formal oxidation states (Co^{1+} , Co^{2+} , and $\text{Co}^{3+} - \text{CH}_3$).

In the UV/vis spectra of a corrinoid contains absorption bands similar to the porphyrin resulting from $\pi - \pi^*$ electronic transitions.

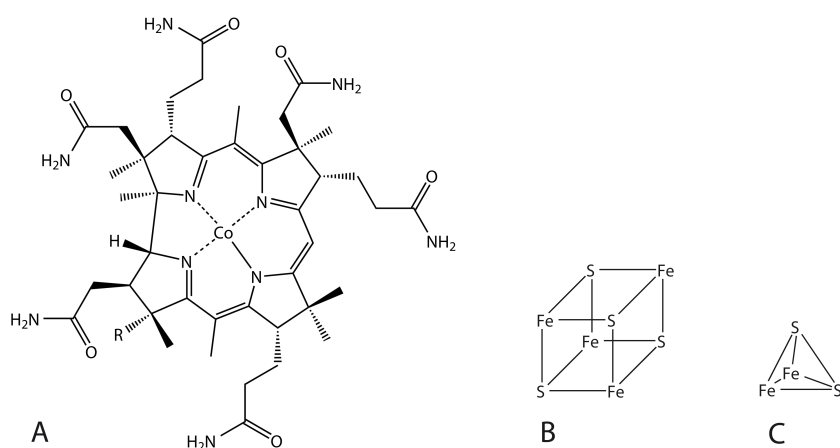


Figure 4.3.: Chemical constitution of the different chromophores in CoFeSP and RACo. (A) The corrinoid cofactor of CoFeSP, (B) the [4Fe4S] cluster of CoFeSP, and (C) the [2Fe2S] cluster of RACo.

[FeS] cluster [FeS] cluster normally function as electron donor or acceptor in proteins. The [2Fe2S] cluster in RACo varies the oxidation state between $[2Fe_2S]^{+2}$ and $[2Fe_2S]^{+1}$ while the [4Fe4S] cluster in CoFeSP only is found in the oxidation state $[4Fe_4S]^{+2}$.

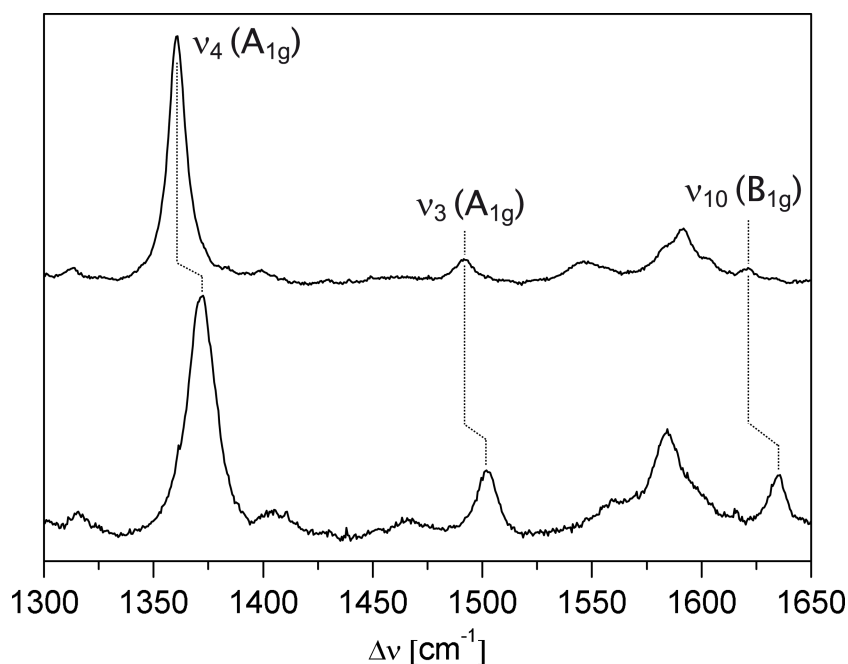
Typical UV / vis absorption spectra of [FeS] clusters show broad unresolved sulfur-to-iron charge transfer bands with more or less distinct maxima around 400 nm.

4.1. Resonance Raman spectroscopy of the different chromophores

4.1.1. RR spectra of Cyt_c

Due to the complex interactions of the electronic states the RR spectra depend on the excitation wavelength. The symmetry of the normal mode determines which enhancement term comes into effect. For the ideal D_{4h} symmetry only in-plane modes should be enhanced since the transition dipole vector lies in the x, y-plane for both transitions. This is not true anymore for the heme with lower symmetry, but still the in-plane modes are much stronger enhanced than other modes.¹ The totally symmetric A_{1g} bands dominate the RR spectrum under Soret-band excitation, due to A-term resonance enhancement. Pronounced B-term enhancement comes into play at Q-band excitation where the non-totally symmetric B_{1g} , A_{2g} , and B_{2g} modes gain intensity in the RR spectrum. Due to the deviation from planarity of the heme (symmetry lower than D_{4h}) out-of-plane coordinates can couple with in-plane coordinates and thus may gain resonance enhancement as well.¹⁷⁶ There are RR active modes which are Raman inactive under non-resonant conditions, e.g. the modes with A_{2g} , which are anomalously polarized.^{167,177}

Figure 4.4.: Resonance Raman spectra of the reduced (top) and oxidized (bottom) Cyt c obtained with 413 nm excitation. The significant marker bands ν_4 , ν_3 and ν_{10} are highlighted to track their frequency and intensity changes upon the redox transition.



Cyt c is extensively studied and the vibrational bands are completely assigned.^{1,33,65,176,177} The band pattern in the so-called marker band region, 1200–1700 cm^{-1} , originates from modes which include C–C and C–N stretching vibrations of the porphyrin and reflects the core size of the macrocycle and thus the oxidation, spin, and ligation state of the heme iron.^{145,178} The oxidation state marker bands shift upon a change in the oxidation state. The most important among them are the intense ν_4 (A_{1g}), ν_3 (A_{1g}), and ν_{10} (B_{1g}) modes. These bands shift to lower wavenumbers upon reduction. The additional negative charge at the iron increases the electron density in the anti-bonding π^* orbitals of the porphyrin ring and as a consequence the C–N / C–C bond strength is weakened. Also the electron density at axial ligands of the iron determine the core size and therefore also the positions of bands resulting from the porphyrin in-plane modes. The core size increases in the order 6cLS < 5cHS < 6cHS axial ligation and the corresponding marker band frequencies decrease accordingly.¹⁶⁷

In the low frequency region of the RR spectrum of Cyt c between 300 and 450 cm^{-1} additional spectroscopic features are found which arise from bending and out-of-plane modes of the porphyrin macrocycle and the substituents. These modes are sensitive to changes in the ligation pattern of the iron. This region is called the fingerprint region due to the fact that substituents and axial ligands can be identified by their fingerprint, i.e. the relative band intensities and the position pattern.^{15,64,65,144,146,167,193}

4.1.2. RR spectra of CoFeSP and RACo

Due to the structural similarity of a porphyrin and a corrin the RR spectrum of CoFeSP has similar properties to Cyt c in the marker band region, where the bands arise mainly from the in-plane C–C and C–N stretching modes. Bands in this region reflect the oxidation, spin, and ligation state of the cobalt in the center of the macrocycle. In the low frequency fingerprint region of CoFeSP, out-of-plane modes of the corrin ring appear. In this spectral region also the RR-active fundamentals of Fe-S clusters are expected which involve Fe-S stretching and bending coordinates.^{29,38,39,162,180}

Part III.

Experimental Details, Setup and Material

5. Resonance Raman (RR) and Surface Enhanced Resonance Raman (SERR) Spectroscopy

Note All reported potentials in this work refer to the Ag / AgCl (3 M KCl) electrode, with a potential of -210 mV vs. the normal hydrogen electrode (NHE).

5.1. Electrode preparation for SERR spectroscopy

Silver ring electrodes (≈ 8 mm diameter and 2.5 mm height) were mechanically polished consecutively with several 3MTM polishing paper from 30 to 1 μ m grade. After washing and sonication in water and ethanol, electrodes were subjected to several oxidation-reduction cycles in 0.1 M KCl to create a SER-active nanostructured surface (for details see page 50). Subsequently, the electrodes were incubated in about 1.5 mM ethanolic solutions of the alkanethiol for ca. 20 h, and then rinsed and transferred to the spectroelectrochemical cell (see Section 5.2.1).⁹⁹

The alkanethiol compounds used for SAM (self-assembled monolayer) formation on the electrochemically roughened Ag ring electrode were 6-mercaptohexanoic acid (C5), 11-mercaptoundecanoic acid (C10) and 16-mercaptohexadecanoic acid (C15). C5 was purchased from Dojindo whereas C10 and C15 were purchased from Sigma-Aldrich. The compounds were used without further purification.⁹⁹

For electrostatic adsorption the protein was added to the electrochemical cell from a stock solution to a final concentration of 0.2 – 0.4 μ M in an electrolyte buffer solution (as specified in Chapter 6) and allowed to incubate at room temperature 30 – 60 min at -100 mV before starting the experiments.⁹⁹

5.2. Spectroscopic setup

5.2.1. Electrochemical cell for SERR spectroscopy

A Pt wire and an Ag / AgCl (Dri-Ref, World Precision Instruments) electrode were used as counter- and reference electrodes, respectively. The

working electrode was a silver ring, roughened and coated as described above, mounted on a shaft that was rotated at about 5 Hz to avoid laser-induced sample degradation. The electrode potentials were controlled via a potentiostat (Model 263A, Princeton Applied Research). As electrolyte a buffer solution was used.⁹⁹ The measuring cell fabricated from POM (Polyoxymethylen) with a volume of about 10 mL was fixed to the shaft holder. It was equipped with a quartz window for the incident laser beam which was focused onto the rotating electrode surface. All experiments were executed at room temperature and under atmospheric conditions if not specified otherwise. No heating of the cell solution could be detected but the local temperature at the laser beam on the sample could not directly be measured.

5.2.2. Cell for RR spectroscopy

For RR spectroscopy either a rotating quartz cuvette with a maximum volume of 0.5 mL (usable in the range of 0.1 – 0.5 mL), an aluminium chip with a ring-shaped vat with a sample volume of 20 – 50 μL or a small quartz cuvette with a volume of about 20 μL was used. In case of the aluminium chip and the small quartz cuvette the sample could be moved under the laser beam by a constantly moving table. Both devices could be used in- and outside of a cryostat which allowed to control the surrounding atmosphere and the temperature.

5.2.3. Experimental parameters and spectrometer

RR and SERR spectra were acquired with the 413 nm line of a Krypton (Coherent Innova 300c) or the 514 nm line of an Argon (Coherent Innova 70c) ion laser in backscattering (180°) geometry by using a confocal microscope coupled to a single-stage spectrograph (Jobin Yvon, LabRam 800 HR or XY 800) equipped with a liquid-nitrogen-cooled back-illuminated CCD detector (dimension of the CCD chip are 2048×512). Elastic scattering was rejected with notch or edge filters. The laser beam was focused using a long-working-distance objective (Nikon $20\times$, N.A. 0.35) with a working distance of 20 mm.⁹⁹

The scattered light collected by the objective was focused onto a confocal hole of 1000 μm and through an additional lens onto a slit (100 μm) placed at the entrance of the spectrograph. The grating of the spectrograph, which dispersed the scattered light, included 2400 lines / mm.^{87,99}

Usually the spectra were acquired with a binning factor of 2, i.e. the intensities of two adjacent pixels are summed up. This setting implies

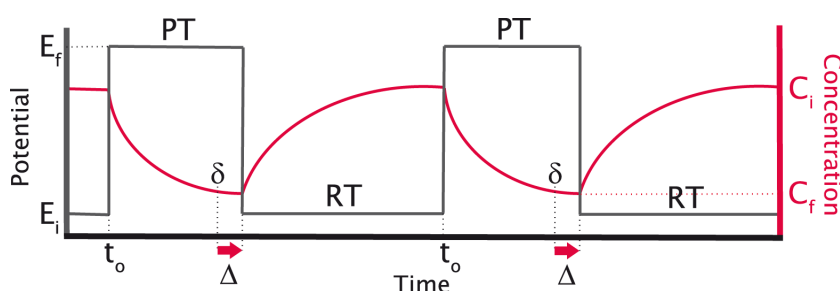


Figure 5.1: Schematic representation of the sequence of potential jumps and laser gating for TR SERR measurements and the concentration of the studied redox species. For explanation see text in Subsection 5.2.6.

a spectral resolution of ca. 2 cm^{-1} .⁸⁷ The spectrometer is controlled by the LabSpec software (Version 4.07) and was calibrated before and often after each experiment with a standard mercury lamp. The reported frequencies are accurate within approximately 0.5 cm^{-1} .⁸⁷

5.2.4. RR measurements

Details of the RR measurements are given in Chapter 6 for the different proteins.

5.2.5. Stationary SERR measurements

For determination of the redox equilibria of Cyt c stationary SERR spectra at different potentials were measured in the potential range from -400 mV to $+150\text{ mV}$. Spectra only were recorded after equilibrium times of 20 s to 60 s, depending on the monolayer used.

5.2.6. Time resolved SERR measurements

For time-resolved (TR) SERR experiments, potential jumps of variable height and duration were applied to trigger the reaction. The pulse time (PS) is the time span in which the final potential (E_f) is applied to the working electrode while the following recovering time (RT) is the time where the initial potential E_i is applied after the potential jump, in order to recover initial equilibrium. The SERR spectra were recorded at different delay times (δ) following the potential jump (E_i to E_f) by “switching” on the laser for a certain time window, the measuring time Δ . Thus, each TR SERR spectrum refers, at average, to a delay time of $\delta' = \delta + \frac{\Delta}{2}$. This series of events had to be repeated until the overall collected signal led to a good signal-to-noise ratio.

Synchronization of potential jumps and probe laser pulses was achieved by a home-built pulse-delay generator. The probe pulses were generated by passing the cw laser beam through two consecutive laser intensity modulators (Linos), which exhibit a total extinction better than 1:50000

and a time response of ca. 20 ns. Details of the TR SERR measurements are described elsewhere^{99,134,136} and are depicted in Figure 5.1.

5.3. Spectra analysis of Cytc

After background subtraction the spectra of Cytc were treated by single band (514 nm) or component analysis (413 nm)⁴⁰ in which the spectra of the individual species were fitted to the measured spectra by using a home-made analysis software based on Matlab or using GNU Octave Software. The time-dependent or potential-dependent spectral changes were converted into changes of the relative concentrations of the species involved (413 nm) or of the relative contribution of modes of different symmetry (514 nm). These data were subsequently analyzed in terms of redox equilibria or relaxation kinetics.^{99,134}

5.3.1. Component analysis

The spectral components present in a particular SERR spectrum of Cytc can be determined on the basis of RR measurements under conditions that lead to only one of the species.

The relative solution (RR) or surface (SERR) concentrations c_i of species i can be calculated according to Equation (5.1) where f_i is a factor proportional to the reciprocal RR cross section (which describes the visibility of a species in comparison to an other species) and I_i is the relative intensity of the individual spectral component.

$$c_i = \frac{I_i f_i}{\sum_i I_i f_i} \quad (5.1)$$

Since also the RR cross sections of the different oxidation states differ, one can define the ratio of the proportionality factors f_i in which f_{red} and f_{ox} denote the factor of the reduced and oxidized species, respectively.⁸⁷

$$R_f = \frac{f_{red}}{f_{ox}} \quad (5.2)$$

6. Proteins and Experimental Details

All purified proteins were stored at -80°C in aliquots with small volume until they were used for experiments. A protein sample was always used immediately after taking it from the -80°C freezer. No protein was refrozen (only after preparing the aliquots) or kept longer times at more than -80°C . No sample was used over different days only if it is noted specifically otherwise. Each experiment was carried out with fresh protein sample.

All experiments were executed at room temperature and under air, if not noted otherwise. No heating of the cell solution could be detected but the local temperature at the laser beam on the sample could not directly be measured.

6.1. Horse heart cytochrome *c*

Wild type horse heart cytochrome *c* (WT hh Cyt*c*) was obtained from Sigma-Aldrich and purified by HPLC. The water used in all experiments was purified by a Millipore system and its resistance was greater than $18\text{ M}\Omega$. The purification was done by my colleague Claudia Schulz.

The K87C, K39C and K8C mutants of hh Cyt*c* were provided by Katalin Tenger from the group of László Zimányi from the *Biological Research Center* in Szeged, Hungary. All three mutants were produced by site-directed mutagenesis and co-expression with the yeast Cyt*c* heme lyase in the BL21-AI (Invitrogen) *E. coli* strain, according to procedures previously described by Tenger et al.^{9,186,187}

As standard electrolyte and if not noted otherwise a 30 mM phosphate buffer, pH 7 (413 nm measurements) or a 12.5 mM phosphate / 12.5 mM sulfate buffer, pH 7 (514 nm measurements) was used. For the investigation of the influence of the ionic strength on the ET of hh Cyt*c* a high ionic strength buffer consisting of 30 mM phosphate and 120 mM potassium chloride at pH 7 was used.

SERR and TR SERR experiments with 413 nm excitation wavelength were performed with laser powers of about 1 mW for all measurements with 25 / 30 mM electrolyte solution and about 1.5 mW for measurements

in 150 mM electrolyte solution. For the experiments with 514 nm excitation wavelength laser powers of about 12 mW at the sample were applied. The laser powers were chosen in such a way that laser induced degradation of the protein would be reduced to a minimum.¹¹⁸ Effective acquisition times were between 3 and 10 s for standard ionic strength and about 30 s for high ionic strength to get a good signal to noise ratio. All experiments were repeated several times to ensure reproducibility.

The computational work and calculations concerning the K87C mutant and the WT of hh Cyt_c were done by Damián Alvarez-Paggi from the group of Daniel H. Murgida at the *Universidad de Buenos Aires*. The computational methods have been described in detail previously by Alvarez-Paggi et al.^{7,9} Briefly, the initial structure of ferric hh Cyt_c (Fe⁺³) was obtained from the PDB database (1HRC).²³ Molecular dynamic (MD) simulations were performed using the AMBER 2005 package, with the f99 force field implementation and heme parameters adopted from previous work. To simulate the SAMs, an infinite array of fixed Au atoms with lattice structure 111 was built in silico. Each of the Au atoms was linked to a HS-(CH₂)₅-COOH molecule (C5) through the S atom. SAM and lattice parameters were adopted from the literature.¹⁵⁵ Adsorption of hh Cyt_c to C5 SAMs was investigated using steered MD simulations (SMD) starting from 26 different configurations that differ solely in the rotational orientation of the protein with respect to the SAM. For each starting configuration hh Cyt_c was pulled towards the surface at constant velocity, while computing the applied force. The pulling reaction coordinate (RC) is defined as the distance between the fixed central Au atom and the center of mass of the C_α atoms of the protein. Integration of the force applied for moving the protein towards the surface yields the work performed along the RC. From the 26 starting orientations that extensively sample possible hh Cyt_c / SAM complex structures, those showing a minimum in the work-versus-RC profiles at contact distances were selected as stable electrostatic complexes and each subjected to 20 ns periodic boundary conditions (PBC) simulations in explicit TIP3P water molecules. From these simulations, binding energies were estimated using Molecular Mechanics/Generalized Born Surface Area (MM/GBSA), while the electronic coupling matrix elements were calculated using the pathways algorithm developed by Beratan et al.¹⁶ The orientation of hh Cyt_c with respect to the Au/SAM surface is defined by the relative heme orientation using two angles, α and φ (see Figure 9.4 and Figure 9.5 and description in the text on page 64). The protein dipole moment was computed with respect to the center of charge of the protein, as reported by Margoliash et al.⁸⁴ and its relative orientation is defined as the angle between the dipole vector and the Z axis normal to

the SAM plane. In order to improve sampling of the possible hh Cyt c /SAM complexes for the K87C mutant, three additional 20 ns MD simulations were performed with starting orientations adapted from those found in our previous work for WT hh Cyt c .^{7,9}

6.2. Human heart cytochrome *c*

The human heart cytochrome *c* (huh Cyt c) wild type (WT) and the mutants Y48E, Y97E (tyrosine to glutamic acid) and Y48F, Y97F (tyrosine to phenylalanine) as well as Y48pCMF (tyrosine to non-natural amino acid para-carboxymethyl-L-phenylalanine) were provided by the group of Prof. Miguel A. De la Rosa from the *Institute of Plant Biochemistry and Photosynthesis* (IBVF), joint center of the *National Research Council Spain* (CSIC) and the *University of Seville*.

Site-directed mutagenesis, protein expression, and purification procedure description for the Y48E, Y97E, Y48F and Y97F can be found elsewhere.⁴⁸

The unpublished description for the production of the Y48pCMF mutant was provided by Alejandra Guerra who produced this mutant. The plasmid that encoded WT huh Cyt c was mutated by replacing the TAT triplet coding Tyr48 with TAG, the AMBER STOP signal. The new plasmid, containing the mutated sequence, was called pCcY48AMBER. In order to obtain Y48pCMF Cyt c , *Escherichia coli* BL-21 (DE3) cells were co-transformed with the plasmids pCcY48AMBER and pEVOL/pCMF/tRNA, a gift from Professor P. G. Schultz (Scripps Research Institute of California), encoding the orthogonal Amber-suppressor tRNA / aminoacyl-tRNA synthetase (aaRS) pair. Cells were grown during 20 h at 30 °C and 150 rpm in minimal media M9 supplemented with ampicillin and chloramphenicol and induced at DO 0.6 with 0.02 % of arabinose and 1 mM of IPTG (isopropyl β -D-1-thiogalactopyranoside). The non-canonical aminoacid p-carboxymethylphenylalanine (pCMF) and δ -aminolevulinic acid were added after induction at a final concentration of 1 mM and 0.1 mM, respectively. Cells were collected by centrifugation, and then resuspended in lysis buffer to extract the periplasm fraction by sonication. The raw extract was centrifuged at 20000 g for 15 min. The supernatant was collected and loaded onto a carboxymethyl-cellulose column pre-equilibrated with 1.5 mM borate buffer, pH 8.5. Y48pCMF Cyt c was eluted from the column with a 36 – 360 mM NaCl gradient and tested by UV-Vis spectrometry. The A278 / A549 ratio of the resulting Cyt c preparations in the reduced state was ca. 1:1, as previously described.⁴⁹

Two WT protein samples were sent in 5 mM sodium phosphate buffer at pH 6.0 and 10 mM at pH 6.5 respectively. The Y48E, Y48F, Y97E and Y97F mutants were delivered in 5 mM sodium phosphate at pH 6.5 (one sample each), and two Y48pCMF samples were provided in 10 mM sodium phosphate at pH 5.5 and pH 5.8 respectively. The RR experiments with the free protein variants were carried out in fresh 10 mM potassium phosphate buffer at different pH values. For pH values outside the buffer-range the buffer was titrated to the desired pH value by adding potassium hydroxide or hydrogen chloride. For experiments with the Cyt_c variants incorporated in liposomes the used buffer consisted of 20 mM HEPES (4-(2-hydroxyethyl)-1-piperazineethanesulfonic acid), 150 mM sodium chloride and 5 mM EDTA (ethylenediaminetetraacetic acid) at pH 7.4 and pH 5.8.

For all Cyt_c variants the RR experiments were carried out with an excitation wavelength of 413 nm, in a cryostat at 4°C under constant N₂ stream at laser powers about 1.5 – 2 mW. The sample volume was 20 – 30 μL (quartz cuvette) and the sample was constantly moved under the laser beam. The accumulation time was between 30 and 180 s and 2 to 20 single spectra were averaged to improve the signal to noise ratio. The protein concentrations for the RR measurements of the free proteins varied between 10 and 100 μM. For the RR measurements with the liposomes the protein-lipid ratio (v/v) was kept at 1:125; with for example 100 μM Cyt_c:12.5 mM liposomes for the Y48pCMF mutant.

The liposomes consisting of POPE (1-palmitoyl-2-oleoyl-sn-glycero-3-phosphoethanolamine) and CL (cardiolipin from bovine heart), 4:1 were produced following the protocol below adopted from the protein providing group of Prof. Miguel A. De la Rosa, University of Seville, Spain. The lipids were purchased from Avanti Polar Lipids in chloroform. The liposomes were synthesized by mixing POPE and CL in a molar relation of 4:1. The lipids were dissolved in a chloroform / methanol 3:1 (vol) stock solution (1 mM total lipid concentration) at ≈ 30°C (melting point of POPE 25°C). The solution was dried under constant N₂ stream with constant rotation. The thin lipid film was then rehydrated in 20 mM HEPES, 150 mM sodium chloride and 5 mM EDTA at pH 7.4 / pH 5.8 and was sonicated for 10 min. The liposomes were incubated with (pre-oxidized or -reduced) Cyt_c for ≈ 30 min. The final lipid and Cyt_c concentration was 6 – 12.5 mM and 48 – 100 μM respectively. The solution was used immediately and not longer than for a few hours. For each experiment fresh liposomes were produced.

Note: The real pH of the sample could of cause not be checked because of the small volume.

The reduced or oxidized form of the Y48E, Y48F, Y97E and Y97F Cyt_c variants were produced by adding small amounts of dithionite or peroxydisulfate to the solution in the measuring cuvette ignoring the possible influence on the pH value of the solution. The chemical reduction and oxidation of the WT Cyt_c and the Y48pCMF variant was accomplished by adding chemicals already to the buffer solution. For reduction we used ascorbat in a concentration of 1 mM (10:1 Cyt_c), and for the oxidation potassium ferricyanide in a concentration of 900 μ M (9:1 Cyt_c) was used. The pH value of the buffer solution was checked and adjusted after adding the reduction- and oxidation-chemical, respectively.

6.3. CoFeSP and RACo

All CoFeSP and RACo protein variants were produced from the hydrogenogenic bacterium *Carboxydotherrnus hydrogenoformans* by Sandra Hennig from the group of Holger Dobbek at the *Humboldt-Universität zu Berlin*.

RACo and the N-terminal domain lacking variant RACo Δ 100 were purified according to a published protocol.⁶² Three chromatography steps were applied using DEAE (diethylaminoethanol) and phenylsepharose materials followed by a SuperdexTM 200 prep-grade gel-filtration column. Except for RACo Δ 100 all purification steps were carried out under anoxic conditions inside a glove box under an atmosphere of 95% N₂ and 5% H₂ at room temperature.¹¹⁹

CoFeSP, CoFeSP_MC lacking the [4Fe4S] cluster binding domain, and CoFeSP_NM, lacking the corrinoid binding C-terminal domain, were prepared as described previously.⁵¹ After DEAE, phenylsepharose and gel-filtration using a SuperdexTM 200 prep-grade column, the protein was reconstituted by incubation with hydroxocobalamin overnight. As a last step, reconstituted CoFeSP was loaded on a Source 30Q column.¹¹⁹

The samples for RR spectroscopy were prepared inside a glove box by concentrating the stock protein solutions (in 50 mM Tris/HCl, pH 8.0 containing 150 mM NaCl) to a final concentration of 1 mM using Vivaspin 500 concentrators (30 000 MW for the CoFeSP variants and 50 000 MW for the RACo variants, respectively). When CoFeSP variants and RACo variants were mixed, the samples were incubated for 15 minutes at room temperature prior to concentration (Vivaspin 500, 100 000 MW).¹¹⁹

RR spectra were measured in a (Linkam Cryostage THMS600) cryostat at approximately 80 K under constant nitrogen stream on the sample.

The samples were prepared as follows: A 3 μ l drop of a 1 mM protein solution (50 mM Tris-buffer and 150 mM NaCl) was placed on a quartz holder, anaerobically shock-frozen by direct immersion in liquid nitrogen, and subsequently transferred into the cryostat. Co(II)FeSP was reduced chemically using sodium dithionite.¹¹⁹

The laser power on the sample was 5 mW. Acquisition times ranged from 60 to 150 s depending on spectral quality of the sample. 4–30 single spectra were averaged to improve the signal to noise ratio.¹¹⁹

The electron paramagnetic resonance spectroscopy (EPR) and the EPR data analysis were done by Friedhelm Lenzian. The 9.3 GHz X-Band EPR spectra were acquired using a Bruker “EMX Plus” spectrometer equipped with a high sensitivity Bruker Super-high-Q-cavity (ER 4122 SHQE). For low temperature measurements the sample was kept in an Oxford ESR 900 helium flow cryostat that allows for temperature control between 5 K and 200 K (Oxford ITC4). The EPR spectra shown in Figure 14.7 on page 139 were measured at 100 K. Baseline corrections, if required, were performed by subtracting a background spectrum, obtained under the same experimental conditions from a sample containing only a buffer solution.¹¹⁹

Part IV.

Surface Enhanced Resonance Raman
Spectroscopy as Tool for Studying Electron
Transfer Kinetics—A Statistical Case Study

7. Statistical Investigation of the Method of Time Resolved SERR Spectroscopy for Studying the Electron Transfer of Cytochrome *c*

7.1. Why undertaking this effort for a well established method?

The published electron transfer (ET) rates of immobilized hh Cyt c (on SAM coated metal electrodes) vary considerably, even the rates from our group (research group of Prof. Hildebrandt).^{9,88,99,102,135,136} The aim of this chapter is to elucidate the variance of experimental results with our experimental setup and the origin of differences in the results. It is to take a closer look on the strong and weak points of the method and should give a tool for the experimentalists to judge about the comparability of results. It is not to compare different setups and the corresponding results but to find out about the intrinsic variance of results from the same setup and to assess the accuracy of the kinetic constants. Additionally, it had to be checked if all the individual devices were working properly.

7.2. Approach to the problem of varying TR SERR results

The general TR SERR setup is described in Chapter 5 of this work. In short: A roughened silver ring electrode coated with a SAM is mounted on a rotating electrode holder. The electrode is contacted via the holder to the electrical circuit and used as working electrode. The holder is mounted on a cell with a counter platinum electrode and a AgCl reference electrode, filled with a buffer solution containing the Cyt c . The potential is controlled by a potentiostat. The laser enters the cell via a quartz window and is focused on the electrode surface, so that only Cyt c adsorbed on the surface contributes to a SERR signal.

For a TR SERR measurement that is designed to probe a redox process, a potential jump from an initial potential (E_i) to the final potential (E_f) have to be applied to the system. The spectrum then is recorded for a time window (Δ) after a defined delay time δ beginning with the jump. Further details of the data acquisition are given in Chapter 5 on page 39.

Table 7.1.: Preparation protocol and experimental setup for the comparative SERR measurements of Cytc.

Electrode Roughening	
Polishing	mechanically (grain size: 30, 9, 5 μm)
Sonication	5 min in water, then 5 min in ethanol
Electrode cleaning	in 0.1 M KCl at -2 V for 40 s under rotation, then open cell and take the electrode out of the solution until the remaining hydrogen bubbles on the surface of the electrode are vanished
Electrochemical roughening	+0.5 V (40 s) / -0.5 V (40 s) +0.5 V (15 s) / -0.5 V (15 s) +0.5 V (30 s) / -0.4 V (300 s)
Electrode functionalisation	
SAM	C_{10}COOH , 1–2 mM in ethanol
Incubation time	12–16 h in SAM solution, then 2 h in pure ethanol
Cell setup	
Cytc concentration	0.3 μM
Cytc incubation	45 min at open circuit
Buffer	30 mM phosphate at pH 7
Remarks	Check of 3 M AgCl reference electrode before and after measurements Protein stays in solution during measurement All measurements are done under air
Raman setup	
Laser power	1 mW
Binning / grating	2 / 2400
Slit / hole	100 / 1000
central wave number	1400 cm^{-1}
Laser	413.138 nm
Alignment	
Position Mercury line at 435.83 nm (binning 1)	
Intensity of the silicium signal at about 519 cm (binning 1)	

The comparative measurements were supported by my colleagues Khoa Ly and Jacek Kozuch. We agreed on an exact protocol referring to the buffers, reference electrode, batch of protein, silver electrodes, holders, cells, other equipment, potential jumps, procedures and analysis (see Table 7.1 for experimental details). The experiments done by one person were evaluated by him or herself and in addition I analyzed all experiments independently, not knowing the results of the other experimentalists, for comparison.

I will refer to the three persons in this part of my work as experimentalist 1,2 and 3. For our measurements we used three different electrode holders (A, B, C) and four cells (a, b, c, d). The holders and cells can be combined as follows: Aa, Ab, Ba, Bb, Cc, Cd. Each person carried out two different experiments with each possible holder / cell combination. The first one was a TR SERR experiment with a potential jump from an initial potential of -80 mV to the final potential of $+20$ mV, which is around the redox potential of Cyt c , so it will be called “redox potential jump”. The second experiment was the TR SERR measurement with a potential jump from $+40$ mV to -200 mV which equals to an overpotential of 220 mV, this was called the “overpotential jump”. The exact scheme for the delay times is given in Table 7.2. Both experiments were done always with one electrode. Four silver electrodes were used randomly for the individual experiments.

We used similar recovering-to-pulse-time ratios as well as measuring-to-delay time ratios for every spectrum of one experiment. Moreover we tried, for each spectrum, to achieve the same quality by comparable total accumulation times. For spectra analysis we used the same fitting procedure and only the native B1 oxidized and reduced species were considered (in fact no other species were found in appreciable amounts).

7.3. Results of the comparative TR SERR experiments

The first important outcome was the fact that the determined rate constants of the analysis done by each person were identical to those found by myself when evaluating all experiments. This indicates that there is no personal bias in the data analysis. It has to be mentioned that for the “overpotential jump” measurements a monoexponential fit to the concentration changes of the oxidized species required the neglect of the data for delay times smaller than 2 ms. It may be that these deviations originate from the response time of the electrical double layer on the electrochemical cell. The apparent rate constants are listed Table 7.3.

Table 7.2.: Design of the TR SERR experiment, data points.

Potential jump –80 mV to +20 mV				
Recovering time in ms	Pulse time in ms	Delay time in ms	Measuring time in ms	Accumulation time
5	0.5	0.4	0.1	2*60 s
10	1	0.8	0.2	2*60 s
20	2	1.6	0.4	2*60 s
40	4	3.2	0.8	2*60 s
80	8	6.4	1.6	2*60 s
160	16	12.8	3.2	2*60 s
320	32	25.6	6.4	2*60 s
640	64	51.2	12.8	2*60 s
1280	128	102	26	2*60 s
Potential jump +40 mV to –200 mV				
Recovering time in ms	Pulse time in ms	Delay time in ms	Measuring time in ms	Accumulation time
2.5	0.22	0.2	0.02	2*80 s
4	0.675	0.6	0.075	2*80 s
7	1.35	1.2	0.15	2*80 s
15	2.2	2	0.2	2*80 s
25	4	3.6	0.4	2*80 s
40	5.8	5.2	0.6	2*80 s
70	10.2	9.4	0.8	2*80 s
160	15	14	1	2*80 s
200	18	16.4	1.6	2*80 s

Potential jump –80 mV to +20 mV Taking into account the relatively low standard deviation, the average rate constants obtained by the individual experimentalists point to a “personal” factor. (Table 7.3). This could be also shown in an ANOVA (Analysis of variance) statistical test done by Robert Götz. Indicating a significant difference between the single persons it shows no difference between the different holder / cell systems based on a significance of 5 %. The ANOVA test in principle needs a larger data set but can be taken as an additional support for the “personal” effect.

Potential jump +40 mV to –200 mV The results for the “overpotential jump” display a different picture since the scattering of the rate constants obtained by each experimentalist is larger than the difference between the average values for the rate constants of each person. To prove or disprove a personal effect here a larger number of experiments per person would be needed. But also here no significant difference between the holder / cell systems can be found.

It seem to be that for the faster processes in the overpotential experiments the response time of the system interferes more strongly with the ET

	−80 mV to +20 mV				+40 mV to −200 mV			
	1	2	3	Σ	1	2	3	Σ
Aa	58	53	47	158	188	107	200	495
Ab	55	61	42	158	232	308	290	830
Ba	44	63	45	152	188	155	195	588
Bb	58	71	45	174	270	211	265	746
Cc	58	55	43	156	280	227	144	651
Cd	50	61	42	153	158	225	270	653
Average	54	61	44	154	219	206	227	652
Std.-Dev.	5.7	6.4	2.0		49.3	68.8	56	

Table 7.3.: Apparent rate constants k in s^{-1} of hh Cyt c on a C11 SAM, determined by the persons 1, 2, 3 for all holder (ABC)/cell (abcd) systems for the “redox potential jump” (−80 mV to +20 mV) and for the “overpotential jump” (+40 mV to −200 mV).

processes. This means that the accuracy of the fast rates is much smaller than for slower rates.

7.4. A “personal” effect in TR SERR experiments

The experiments were in all steps controlled by physical equipment and chemical composition that did not involve direct interaction with the experimentalist except for one: The polishing of the electrode demands physical interaction with the electrode. The electrode surface structure depends strongly on the applied strength and polishing approach. Consequences arising from different surface morphologies can be severe. Different surface roughness and structure lead to differently organized SAMs which effect the surface enhancement of the Raman signal, the electrical double layer and therefore the response time, the electron transfer behaviour and reorientation behaviour of the Cyt c . To quantify this finding one can compare the found ET rates for the “redox potential jump”. The average rates in descending order relate directly to the physical strength of the experimentalists: $2 > 1 > 3$. The stronger the person the faster the rate constant.

The equipment, meaning all cell/holder systems, seem to function properly and give comparable results. Also a “time” effect, meaning a slow change in the equipment that could effect the results over time (month, years) can be ruled out when comparing the rates presented here with the rate constants for comparable experiments which were conducted by me, later in time. This apparent rate constants are quite similar compared to the rates presented here. The comparison shows that the setup of the experiments is stable and supports the conclusion that only experiments done by the same person should directly be compared. In Table 9.1 on page 74, one can find the rate $45 s^{-1}$ for the “redox potential jump” and $221 s^{-1}$ for the “overpotential jump”, in Table 10.1 on page 90 for similar

measurements one finds the rates 42.5 s^{-1} and 242 s^{-1} and in this chapter it was 44 s^{-1} and 227 s^{-1} respectively (Table 7.3).

It can be concluded that even if everything is seemingly done the same, it does not mean that a personal influence on the experiment can be ruled out. But despite this “personal” effect on the TR SERR experiments, the results of the different experimentalists are in the same order and hence it is indeed possible to conclude that the effect is not too large to compare the results with each other and to conclude a “true” rate, but it has to be kept in mind that the error is somewhat bigger than the standard deviation suggests.

Note: Since all experimentalists had to write down all details of their experiments we could control that everything was done the same way to the possible level of control. We also assisted each other to be able to see possible differences in the experimental approach. Only a subtle detail was different. Person 1 had applied a slightly different initial potential of -100 mV at the “redox potential jump”. In theory, this should not change the rate constant, which should only be dependent at the final potential. In fact, this difference cannot be the origin for the detected personal effect since the average rate constants of the other two are both higher (2) and lower (3) than that of person 1.

Part V.

Cytochrome *c*—Interplay Between Protein
Dynamics and Electron Transfer

8. Introduction of the Role of Cytochrome *c* in cell Electron Transfer

8.1. Native Cyt c

Cytochrome *c* is a small soluble protein which is highly conserved in eukaryotes (103–115 amino acids).¹⁴ Detailed descriptions of the structure and function can be found elsewhere.^{127,152,166} The chromophore of Cyt c is an iron porphyrin, the heme *c* (see also Chapter 4). The heme iron is axially coordinated by His18 and Met80.^{23,169} This coordination results in 6cLS species for the oxidized (Fe³⁺) and reduced (Fe²⁺) iron which are called B1 state. The chromophore structure is only changing slightly upon a redox transition.^{183,184} For immobilized Cyt c , “non-native” B2 states are found where the Met80 is lost as an axial ligand which results in either a 5cHS or, upon ligation of another histidine, in a 6cLS species. In the B2 state, the redox potential is shifted to negative values such that it cannot serve as an electron carrier in the respiratory chain anymore.¹⁶⁷

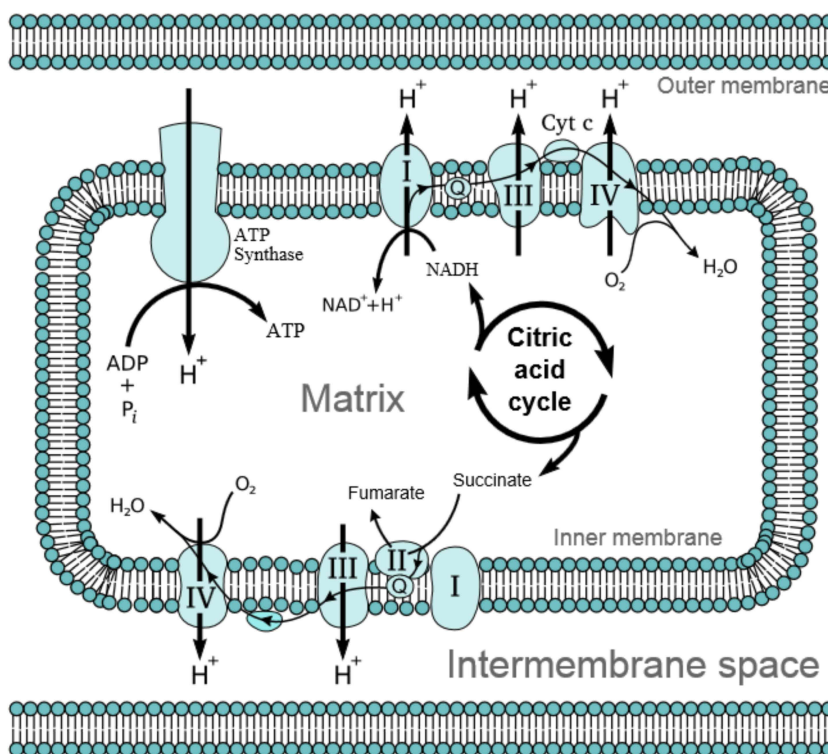
The essential role of Cyt c is that of an electron transfer protein involved in aerobic and anaerobic energy transfer processes throughout all organisms, like eukaryotes, (gram-negative and gram-positive) bacteria and archaea.¹⁸ Dependent on the organism other functions may include hydrogen peroxide scavenging¹⁵² or involvement in apoptosis in eukaryotes (see detailed information in Chapter 11 from page 101).

8.2. Cyt c in eukariotic aerobic respiration

In eukaryotes, Cyt c is located in the intermembrane space of the mitochondrion where it shuttles electrons between inner-membrane bound complexes III and IV.¹⁸

Complex III is also called bc₁ complex or ubiquinol/cytochrome *c* oxidoreductase (QCR) and consists of many subunits, among them a cytochrome *c*₁ and a cytochrome *b*.¹⁸ It is a transmembrane protein complex that transfer electrons from a quinol with relatively low redox potential in the lipid phase to an acceptor protein in the aqueous phase. The electron transfer is coupled to the generation of a proton gradient across the membrane, which drives the synthesis of ATP.¹⁸ The

Figure 8.1.: Mitochondrial electron transport (respiratory) chain. Cytochrome *c* is located in the intermembrane space of the mitochondrion. *Fvasconcellos (2007)*. This picture is licensed under the Creative Commons Attribution-ShareAlike 3.0 Unported License. To view a copy of this license, visit <http://creativecommons.org/licenses/by-sa/3.0/> or send a letter to Creative Commons, 444 Castro Street, Suite 900, Mountain View, California, 94041, USA.



crystal structure of the yeast cytochrome *bc*₁ complex with its bound substrate *Cytc* suggests that the electron transfer occur through direct heme-heme contact.^{18,91} Even though the electron transfer partners are complementarily charged at neutral pH (the *bc*₁ complex is negatively charged whereas *Cytc* is positively charged), the most stable configuration seem to be determined by nonpolar contacts.^{18,91} With the uptake of an electron from complex III, *Cytc* is reduced.

The reduced *Cytc* transfers an electron to cytochrome *c* oxidase (CcO) where four electrons are used to reduce oxygen to water.¹²² This process is coupled to the pumping of protons into the intermembrane space.^{121,122} The CcO consists of two hemes, a cytochrome *a* and a cytochrome *a*₃ and two copper centers, Cu_A and Cu_B.^{121,190} *Cytc* delivers the electron to the Cu_A center close to the membrane surface,¹²¹ and the electron is internally transferred then to the heme *a* and finally to the heme *a*₃-Cu_B binuclear center, where the oxygen reduction takes place.¹²¹ The interaction between CcO and *Cytc* is facilitated by electrostatic interactions between the positive charged lysine patch of the *Cytc* and the negatively charged region of the subunit II which contains the Cu_A site.^{18,83,195}

The proton gradient across the inner membrane is used to drive the production of ATP from ADP by a ATP-synthase.¹²²

9. Electron transfer of Lysine to Cysteine Mutants of Horse Heart Cytochrome *c*

The experimental part of Chapter 9 is entirely my work. All reported experiments were done in our laboratories by myself.

All hh Cyt c mutants were provided by Katalin Tenger from the group of László Zimányi from the *Biological Research Center* in Szeged, Hungary (see page 41 for details).

The computational work was done by Damián Alvarez-Paggi at the *Universidad de Buenos Aires* from the group of Daniel H. Murgida.

The experimental data concerning the hh Cyt c mutant K87C and the corresponding WT experiments as well as the computational work (for details see page 42) for this mutant and the WT is in great parts and only with slight changes taken from the joint paper Alvarez-Paggi et al., 2013.⁹

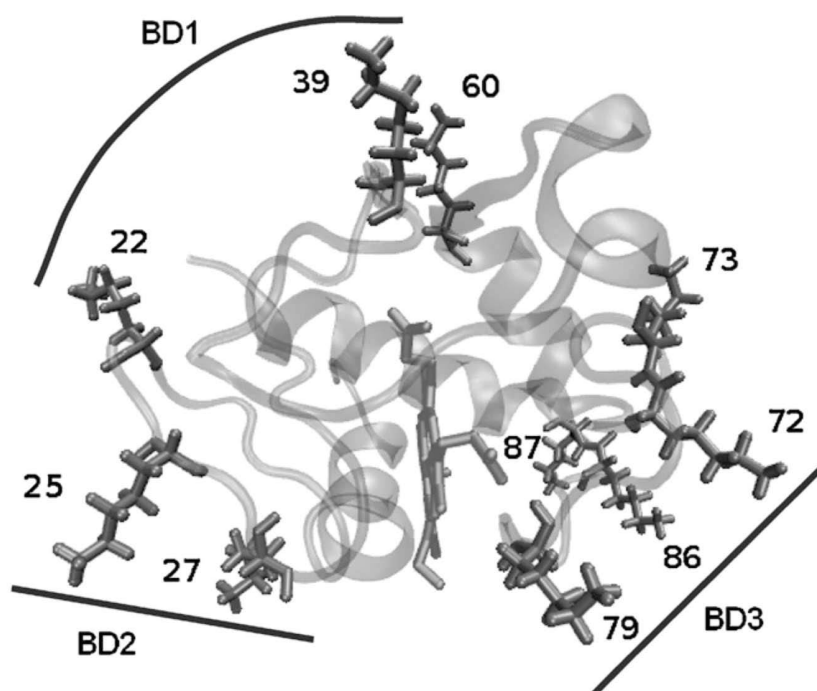
9.1. Background to the approach of rational designed surface mutations of hh Cyt c for investigations on the ET mechanism

Electron transfer proteins present a structural and dynamical complexity that poses several challenges to the well-established theoretical frame of (bio)electrochemistry. For instance, the reigning theory of long-range redox reactions predicts an exponential decay of the ET rate constants with the distance between electron donor and acceptor that has been readily verified for a large number of experimental systems.⁵⁸ However, such dependency breaks down for several different ET proteins adsorbed on electrodes coated with SAMs of variable chain length. These phenomena have spurred an active research field while hinting at a possible role in the regulation of ET reactions in vivo.^{12,25,32,78,88,125,134,142,197,202}

A mechanism involving electric field controlled protein reorientation to rationalize the anomalous distance-dependence of k_{ET} for hh Cyt c electrostatically adsorbed on SAMs of carboxyl-terminated alkanethiols and related systems have been recently proposed.^{7,88} Using molecular dynamics (MD) simulations, it was shown that hh Cyt c may interact

Figure 9.1.: Schematic representation of the three binding domains (BD) of hh Cyt_c for binding to a C5-SAM with 10% ionization.

“Reprinted from *Electrochimica Acta*, 54, D. Alvarez Paggi, D. F. Martin, A. Kranich, P. Hildebrandt, M. A. Marti and D. H. Murgida, Computer simulation and SERR detection of cytochrome c dynamics at SAM-coated electrodes 4963–4970, Copyright (2009), with permission from Elsevir.”⁸



electrostatically with the COOH-terminated SAMs through four different protein surface regions as depicted in Figure 9.2, thus leading to a distribution of orientations.^{7,8} This distribution, however, is relatively narrow as one of the regions that has been designated as the interaction main zone (MZ) exhibits significantly higher binding energies and a largely perpendicular orientation of the dipole moment of the protein with respect to the surface. The electrostatic contacts of the MZ with the SAM involve lysine residues 13, 72, 73, 79, 86 and 87 (constituting the binding domain 3 (BD3) in Figure 9.1) both for ferric (Fe^{3+}) and ferrous (Fe^{2+}) hh Cyt_c, thus resulting in a heme group oriented roughly perpendicular with respect to the surface and with its exposed edge in direct contact with the SAM. In addition to the above-mentioned residues, ferrous hh Cyt_c exhibits additional contacts with the SAM through lysines 22, 25 and 27 (constituting the BD2 in Figure 9.1), which forces the heme into a more perpendicular orientation compared with the ferric form (125°). Remarkably, altogether the same residues have been implicated in the interactions of hh Cyt_c with natural redox partners such as CcO, cytochrome *c* peroxidase and the *bc*₁ complex.^{7,91,150,160}

Pathways analysis shows that the preferred orientation of ferrous hh Cyt_c in electrostatic complexes leads to nearly optimal electronic coupling with the SAM-coated metal. In contrast, the most favourable orientation of ferric hh Cyt_c establishes a relatively weak electronic coupling, thus requiring transient protein reorientation as a prerequisite for fast heterogeneous ET. This gating step, in turn, is predicted to be controlled by the charge density of the SAM and by the interfacial electric field.⁷ In

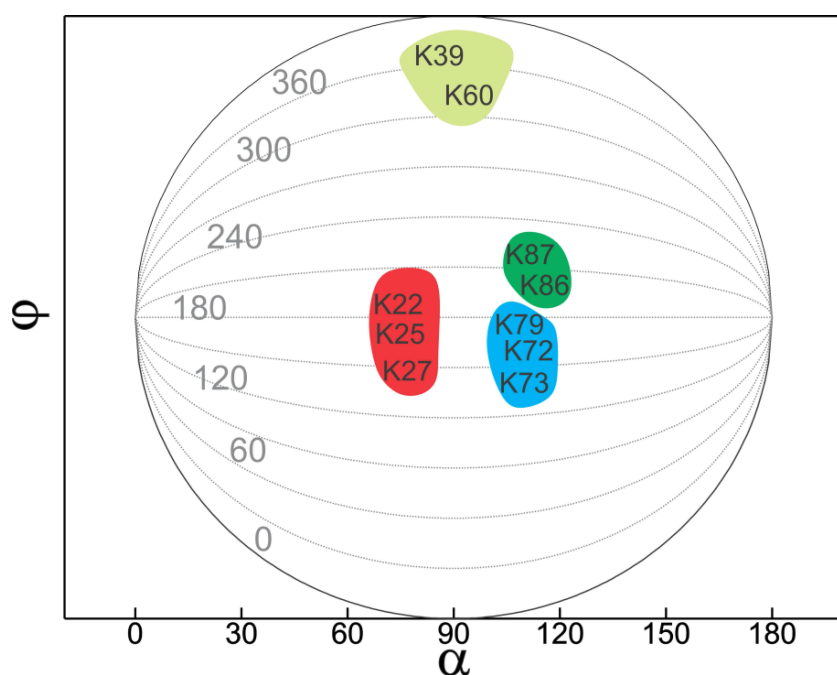


Figure 9.2.: Representation of the key lysine (K) residues that establish hh Cytc/SAM contacts in the different orientations defined by the α and φ angles. Comparison with Figure 9.7 shows that K87 stabilizes hh Cytc in orientations that exhibit a low average electronic coupling. Further details regarding lysine residues and their role in the complex formation may be found elsewhere.^{7,8}

“Reprinted with permission from [D. Alvarez-Paggi, W. Meister, U. Kuhlmann, I. Weidinger, K. Tenger, L. Zimányi, G. Rákhely, P. Hildebrandt and D. Murgida, Disentangling Electron Tunneling and Protein Dynamics of Cytochrome c through a Rationally Designed Surface Mutation *The Journal of Physical Chemistry, Part B*, **117**, 6061–6068 (2013)] Copyright (2013) American Chemical Society.”⁹

agreement with these computational results, TR SERR spectroelectrochemical experiments demonstrated that, for thick SAMs, corresponding to weak electric fields, reorientation is much faster than ET, whereas for thinner films (stronger fields) both processes occur at the same rate, thus suggesting reorientation as the rate-limiting event.⁸⁸

Establishing the validity of this hypothesis unambiguously is motivated by its implications both for fundamental and applied science. The electric field control of protein dynamics in electrostatic complexes might constitute the basis of a general feedback mechanism for the regulation of electron-proton energy transduction in respiration and photosynthesis exerted by variations of the membrane potential.^{2,7,80,92,153} Moreover, it may afford a consistent explanation to the unusual distance-dependences of k_{ET} often observed in bioelectrochemistry,^{12,25,32,78,88,125,134,142,197,202} thereby inspiring new strategies for the development of efficient bioelectronic devices.^{44,200}

This chapter (Chapter 9) is dedicated to further test the above-mentioned hypothesis both experimentally and theoretically by altering protein binding, dynamics and electronic coupling through a surface mutation. Careful inspection of our previous results reveals six key lysines (K8, K13, K72, K73, K86, K87) residues that may be crucial in determining interfacial ET.⁷ Among them, K87 is particularly interesting as the replacement of this residue by a neutral amino acid would in principle abolish contacts that stabilize low electronic coupling orientations (over binding domain 3 (BD3) depicted in Figure 9.1, see also Figure 9.7 on page 66). Indeed, MD simulations and pathways calculations reported

here for the *in silico* K87C mutant predict an enhanced average electronic coupling for this protein variant, thus constituting a rational choice for experimental studies. Therefore, we have produced the K87C variant and studied its heterogeneous ET reaction in protein/SAM electrostatic complexes. TR SERR spectroelectrochemical experiments show an excellent agreement with the theoretical predictions, thus unveiling the role of protein dynamics behind the anomalous distance-dependences in biological ET reactions.

9.2. The K87C mutant of hh Cytc

9.2.1. MD characterization of the K87C hh Cytc mutant in electrostatic complexes

Previous experimental and computational studies of WT hh Cytc electrostatically adsorbed on SAM-coated electrodes indicate that heterogeneous ET dynamics in these complexes are largely determined by protein reorientation.^{7,88} To further test this hypothesis, we considered abolishing key hh Cytc/SAM contacts that stabilize low coupling orientations, while preserving the average coarse orientation.

The results obtained from previous MD simulations^{7,8} suggest that contacts involving K72 and 73 are ubiquitous in hh Cytc/SAM complexes. In addition, K22 and 25 stabilize orientations with high electronic coupling, while K86 and 87 participate in orientations that yield a low electronic coupling. These results suggest K87 as a good candidate for being replaced by a neutral residue for this purpose. Therefore, the K87C variant of ferric hh Cytc was created *in silico* by replacement of the corresponding amino acid in the PDBID 1HRC structure,²³ followed by 10 ns thermalization. Root-mean-square deviations (RMSD) of the backbone atoms of the mutant from the reference structure remained largely constant along the simulation, with an average value of 1.5 Å, suggestive of a well preserved and stable native folding.⁹

Adsorption of K87C on electrodes coated with C5-SAMs was investigated by steered MD (SMD) simulations following the procedures described previously.⁷ As described in Section 6.1 we computed work-vs-distance profiles obtained by pulling the protein towards the SAM, starting from 26 different orientations that span a comprehensive range of possible hh Cytc/SAM complexes. Five of these orientations resulted in protein binding, as determined by the appearance of minima at contact distances in the profiles (Figure 9.3). The dynamics of hh Cytc in these five stable complexes were explored by performing 20 ns MD simulations

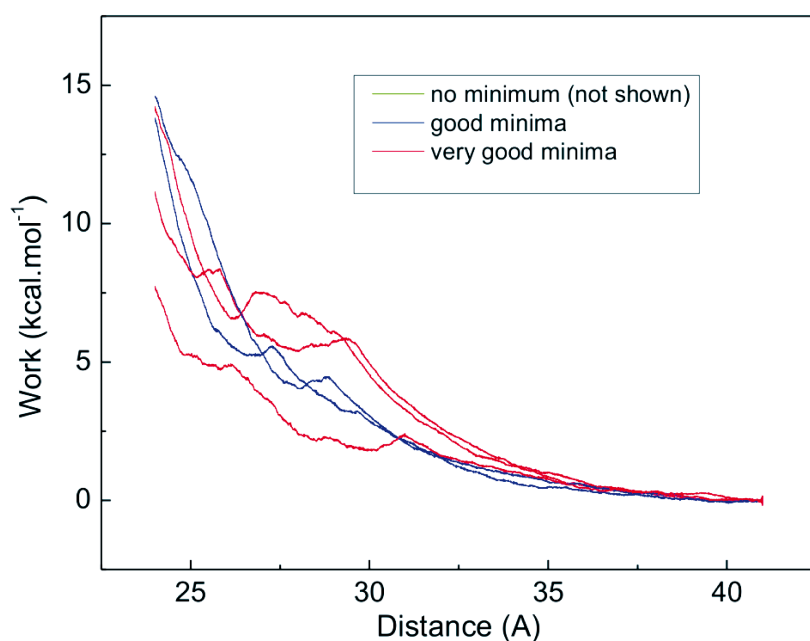


Figure 9.3.: Work-vs-distance profiles from the SMD simulations of K87C. The trajectories that yielded an energy minimum are displayed. The structures corresponding to said minima were employed as starting point for the MD simulations in explicit solvent.

“Reprinted with permission from [D. Alvarez-Paggi, W. Meister, U. Kuhlmann, I. Weidinger, K. Tenger, L. Zimányi, G. Rákhely, P. Hildebrandt and D. Murgida, Disentangling Electron Tunneling and Protein Dynamics of Cytochrome c through a Rationally Designed Surface Mutation *The Journal of Physical Chemistry, Part B*, **117**, 6061–6068 (2013)] Copyright (2013) American Chemical Society.”⁹

in explicit solvent for each starting orientation. RMSD values of the adsorbed K87C from the initial structure remained below 2.5 Å along the simulations,⁹ thereby indicating that the native folding is preserved.

The protein orientation is represented in terms of the angles α and φ as defined below and in Figure 9.4, with constant φ values indicated in Figure 9.2 and 9.6 as dotted isolines.

α is the angle between the vector of the Fe–S (Met80) bond, which is perpendicular to the heme plane, and the Z-axis, normal to the SAM surface. Thus, values of α close to 0° or 180° imply that the heme lies parallel to the SAM, whereas values close to 90° indicate a perpendicularly oriented heme. φ is the angle between the vector defined by the Fe–N_A (pyrrole A) bond and the vector pointing towards the SAM which lies in the heme plane. The Fe–S vector is pointing towards the reader and the φ angle is measured counter clockwise from the vector pointing towards the SAM to the Fe–N_A vector.⁸ Values of φ between 270° and 360° correspond to

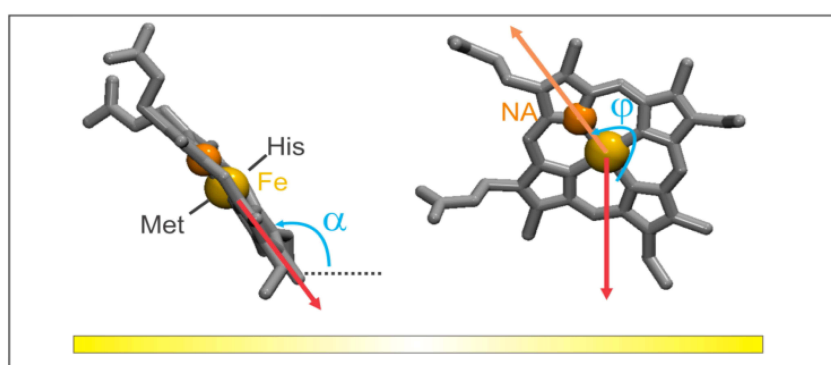


Figure 9.4.: Representation of the rotational angles α (left) and φ (right).

“Reprinted with permission from [D. Alvarez-Paggi, W. Meister, U. Kuhlmann, I. Weidinger, K. Tenger, L. Zimányi, G. Rákhely, P. Hildebrandt and D. Murgida, Disentangling Electron Tunneling and Protein Dynamics of Cytochrome c through a Rationally Designed Surface Mutation *The Journal of Physical Chemistry, Part B*, **117**, 6061–6068 (2013)] Copyright (2013) American Chemical Society.”⁹

protein orientations with the heme propionates pointing toward the SAM, whereas for values in the range from 90° to 180° the propionates point in the opposite direction. Note that, for α values close to 0° or 180° , changes in the φ do not correspond to significant variations of protein orientation since the heme remains parallel to the SAM surface.

Figure 9.6 summarizes the orientations explored by K87C along the different 20 ns simulations starting from the five initial K87C/SAM structures identified by SMD as stable electrostatic complexes (depicted in Figure 9.3). The complexes denoted as o4 and o5 present φ values close to 0° or to 360° , while for o2 this value is close to 240° , implying that in these three cases the partially exposed heme edge remains apart

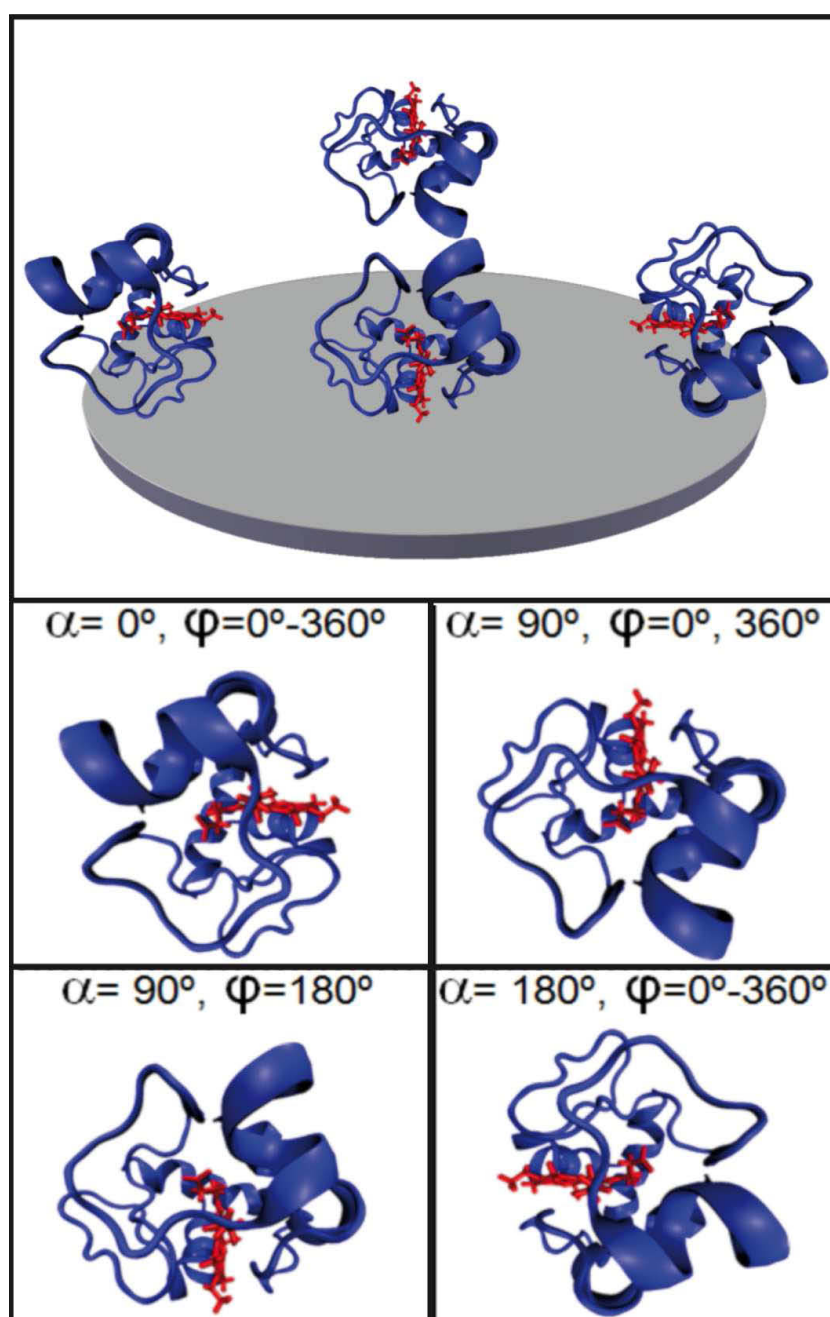


Figure 9.5.: Representation of the different orientations of the hh Cytc/SAM complexes for key α and φ values (bottom) and their corresponding positions in the α vs. φ plots (top).

“Adapted with permission from [D. Alvarez-Paggi, W. Meister, U. Kuhlmann, I. Weidinger, K. Tenger, L. Zimányi, G. Rákhely, P. Hildebrandt and D. Murgida, Disentangling Electron Tunneling and Protein Dynamics of Cytochrome c through a Rationally Designed Surface Mutation *The Journal of Physical Chemistry, Part B*, **117**, 6061–6068 (2013)] Copyright (2013) American Chemical Society.”⁹

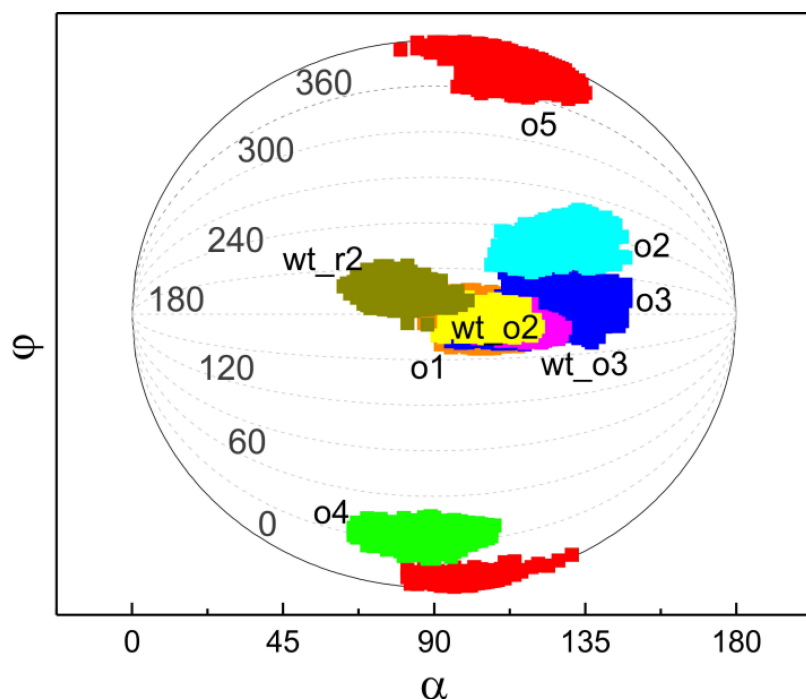


Figure 9.6.: Conformations of the K87C⁺³/SAM complex defined by the orientational angles α and φ obtained from all equilibrium MD simulations in explicit solvent. Each point represents a snapshot from the corresponding MD, which are represented in different colours. Snapshots were taken every 10 ps. “wt” refers to starting orientations adopted from WT hh Cytc either in the oxidized (o) or reduced (r) state.⁷ The dotted lines represent isovalues of φ . For a description of the lysine residues that establish hh Cytc/SAM contacts in each orientation see Figure 9.2.

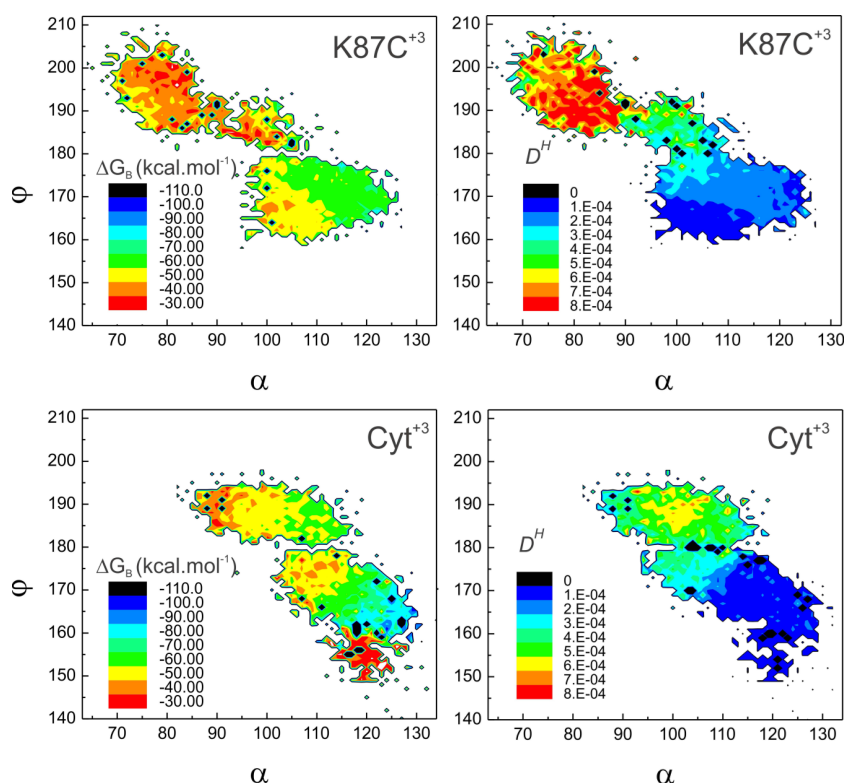
“Reprinted with permission from [D. Alvarez-Paggi, W. Meister, U. Kuhlmann, I. Weidinger, K. Tenger, L. Zimányi, G. Rákhely, P. Hildebrandt and D. Murgida, Disentangling Electron Tunneling and Protein Dynamics of Cytochrome c through a Rationally Designed Surface Mutation *The Journal of Physical Chemistry, Part B*, **117**, 6061–6068 (2013)] Copyright (2013) American Chemical Society.”⁹

from the SAM surface. As the electronic coupling decays exponentially with distance, the k_{ET} from these orientations would be orders of magnitude slower and not experimentally detectable under conditions that allow for the detection of well oriented molecules. In addition, binding energies from these complexes are small (Figure 9.3). Altogether, these results render direct ET from these orientations quite unlikely. Therefore, these structures are regarded as not relevant for the reaction and were not considered further. For the remaining initial complexes (o1, o3) the protein explores the central region shown in Figure 9.6, which corresponds to a heme group perpendicularly oriented and in close contact to the SAM such that, a priori, they can be regarded as electrochemically competent. In order to improve sampling of this region, we also performed 20 ns MD simulations of K87C using three additional starting complexes that were adopted from previous work⁷ and correspond to regions of high electronic coupling found for ferrous (WT_r2) and ferric (WT_o2, WT_o3) wild type hh Cytc.

The regions explored in the latter five dynamics (wt_o2, wt_o3, wt_r2, o1, o3) present significant overlap and, taken together, constitute the main zone (MZ) to be considered for analyzing protein and ET dynamics. Figure 9.7 compares the MZ explored for the K87C mutant obtained in the present work with that found previously for WT hh Cytc.⁷ Note that

Figure 9.7.: Binding energies (left) and average electronic coupling decays D^H (right) as a function of the orientational angles for the MZ orientations of ferri K87C (top panel) and WT (bottom panel) hh Cytc variants. The colour code indicates increasing binding energies from $-110 \text{ kcal} \cdot \text{mol}^{-1}$ (black, stronger binding) to $-30 \text{ kcal} \cdot \text{mol}^{-1}$ (red, weaker binding) and respectively the increasing electronic coupling decays, from $1 \times 10^{-4} \text{ eV}$ (blue, weak) to $8 \times 10^{-4} \text{ eV}$ (red, strong).

“Adapted with permission from [D. Alvarez-Paggi, W. Meister, U. Kuhlmann, I. Weidinger, K. Tenger, L. Zimányi, G. Rákhely, P. Hildebrandt and D. Murgida, Disentangling Electron Tunneling and Protein Dynamics of Cytochrome c through a Rationally Designed Surface Mutation *The Journal of Physical Chemistry, Part B*, **117**, 6061–6068 (2013)] Copyright (2013) American Chemical Society.”⁹



K87C explores a broader range of α angles and, in average, presents slightly higher ϕ values and lower α values.

The data in Figure 9.7 (left side) are presented employing a colour code that represents a scale of binding free energies obtained by the MM/GBSA method. In the MZ, these energies vary between -30 and $-60 \text{ kcal} \cdot \text{mol}^{-1}$ for K87C, whereas for the WT protein they cover the range from -30 to $-110 \text{ kcal} \cdot \text{mol}^{-1}$. Thus, simulations predict that upon abolishing the K87–SAM electrostatic contact, the protein exhibits weaker binding and is able to explore a broader range of orientations with respect to the electrode surface.

9.2.2. Pathways analysis of the Cytc/SAM complexes

The electronic matrix elements of the protein/SAM electrostatic complexes were evaluated semi-quantitatively by employing the pathways algorithm.¹⁶ To that end, electronic coupling decays (D^H) between the heme iron and the metal surface were calculated for K87C and WT hh Cytc along the five 20 ns trajectories that define the main zone represented in Figure 9.7 (left). The results are summarized in Figure 9.7 (right) in terms of the orientational angles α and ϕ .

The stronger electronic couplings are achieved for protein orientations with $\alpha < 95^\circ$, which are only explored by the K87C mutant, thus suggesting faster heterogeneous ET for this variant. Note that coupling

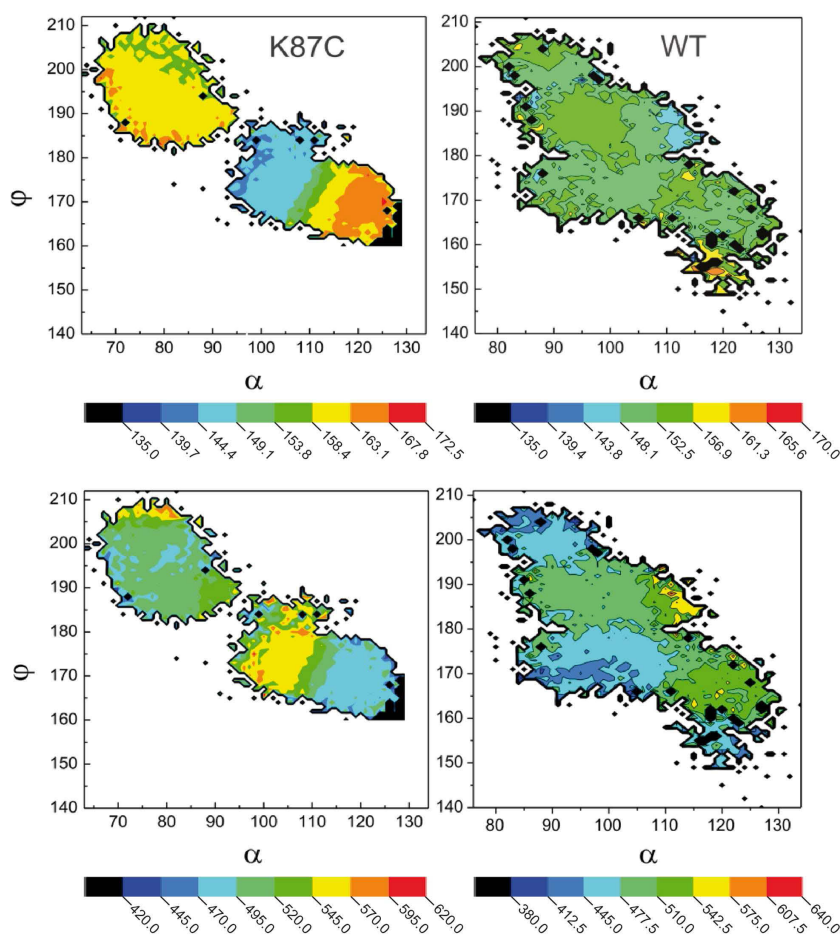


Figure 9.8.: Top: Dipole moment angular orientation as a function of the protein orientation vs. the Z axis (the colour code indicates increasing perpendicularity of the dipole moment with respect to the Au/SAM surface from blue to red). Bottom: The total protein dipole moment (modulus) as a function of the orientation (the colour code indicates increasing dipole moments from blue to red in Debye (D)).

The ferric forms of K87C (left) and WT hh Cytc (right) are shown. The orientation of the protein is defined by the angles α and ϕ .

“Adapted with permission from [D. Alvarez-Paggi, W. Meister, U. Kuhlmann, I. Weidinger, K. Tenger, L. Zimányi, G. Rákhely, P. Hildebrandt and D. Murgida, Disentangling Electron Tunneling and Protein Dynamics of Cytochrome c through a Rationally Designed Surface Mutation *The Journal of Physical Chemistry, Part B*, **117**, 6061–6068 (2013)] Copyright (2013) American Chemical Society.”⁹

decays adopt values between 7×10^{-4} eV and 8×10^{-4} eV for $\alpha < 95^\circ$ and between 2×10^{-4} eV and 3×10^{-4} eV for $\alpha > 95^\circ$. Therefore, ET of K87C in the low affinity orientations ($\alpha < 95^\circ$) is predicted to be between 16 and 36 times faster than in the high affinity orientations ($\alpha > 95^\circ$), because the k_{ET} is proportional to the square of the electronic coupling matrix ($|H_{DA}|$).

Evaluation of the protein dipole moment in the adsorbed state as a function of the orientation shows that the modulus (absolute value) is not significantly affected upon mutation (Figure 9.8). However, while WT hh Cytc does not exhibit a preferential orientation for dipole alignment with the vector normal to the surface, i.e. with the interfacial electric field,⁷ K87C presents better alignment in the high affinity orientations ($\alpha < 110^\circ$) with a nearly perpendicular orientation. Variations of the modulus of the dipole moment mainly arise from the movement of charged residues during the MD simulation, while the direction of the dipole moment varies in response to both the movement of charged residues and concerted rotations of the protein⁷.

In summary, MD simulations and pathways calculations predict that replacement of K87 by a neutral amino acid should exert a strong impact

on the interplay of protein dynamics and electronic coupling of hh Cytc in electrostatic complexes. Therefore we produced the K87C mutant and investigated its heterogeneous ET dynamics experimentally.

9.2.3. Structural and redox equilibria of the immobilized hh Cytc obtained by SERR spectroscopy

WT hh Cytc and the single mutant K87C were electrostatically adsorbed on nanostructured Ag electrodes coated with negatively charged SAMs of HS-(CH₂)_n-COOH with n = 5, 10 and 15 (C5, C10 and C15, respectively) (for procedures see Part III). The structure of the adsorbed

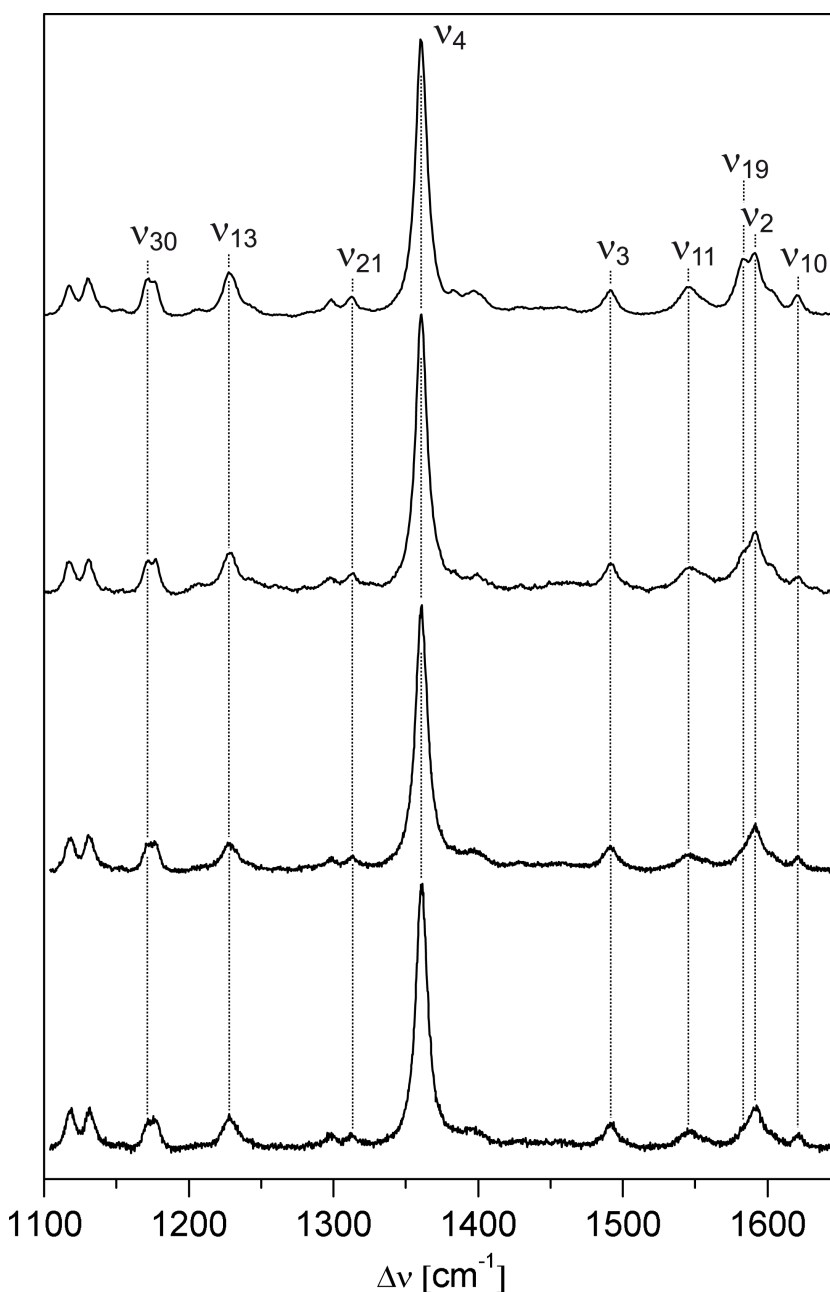


Figure 9.9.: Comparison of SERR spectra of ferrous hh Cytc on a C10 SAM coated Ag electrode at -0.4 V with the RR spectra of ferrous WT hh Cytc and K87C. From top to bottom: RR spectrum of the WT hh Cytc, RR spectrum of K87C, SERR spectrum of the WT hh Cytc, SERR spectrum of K87C. Spectra were measured with 413 nm excitation. Reduction of the proteins in solution was achieved chemically by adding dithionite. Potentials refer to the Ag/AgCl (3M KCl) reference electrode.

“Adapted with permission from [D. Alvarez-Paggi, W. Meister, U. Kuhlmann, I. Weidinger, K. Tenger, L. Zimányi, G. Rákhely, P. Hildebrandt and D. Murgida, Disentangling Electron Tunneling and Protein Dynamics of Cytochrome c through a Rationally Designed Surface Mutation *The Journal of Physical Chemistry, Part B*, **117**, 6061–6068 (2013)] Copyright (2013) American Chemical Society.”⁹

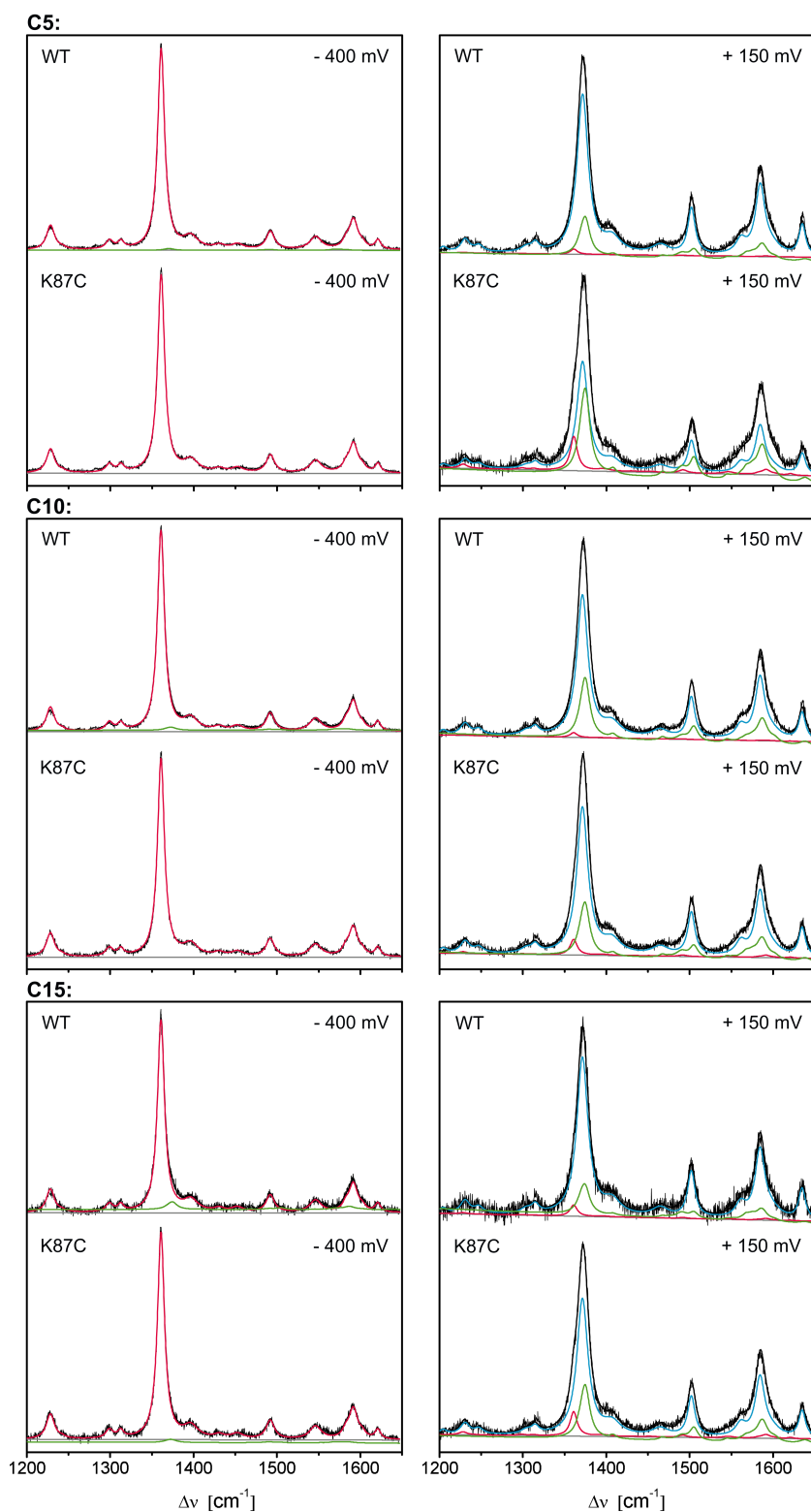


Figure 9.10.: SERR experimental spectra of WT and K87C hh Cytc on a C5, C10 and C15 coated electrode measured at -400 mV and $+150$ mV with 413 nm excitation. The component spectra of ferric B1, ferrous B1, and ferric B2 (HS and LS) are represented by the blue, red, and green lines. The baseline is displayed in grey and the overall fit (sum of the component spectra) is shown on black. “Adapted with permission from [D. Alvarez-Paggi, W. Meister, U. Kuhlmann, I. Weidinger, K. Tenger, L. Zimányi, G. Rákhely, P. Hildebrandt and D. Murgida, Disentangling Electron Tunneling and Protein Dynamics of Cytochrome c through a Rationally Designed Surface Mutation *The Journal of Physical Chemistry, Part B*, **117**, 6061–6068 (2013)] Copyright (2013) American Chemical Society.”⁹

proteins at the level of the redox sites was monitored by SERR spectro-electrochemistry under Soret-band excitation with 413 nm.

In agreement with previous reports,^{133–135} SERR spectra of WT hh Cytc adsorbed on C10 and C15-SAMs recorded at oxidizing and reducing potentials are essentially identical to the RR spectra of the chemically oxidized and reduced native protein in solution, respectively, thus indicating a conserved heme pocket structure (Figure 9.9).

Moreover, SERR spectra recorded at variable electrode potentials could be quantitatively simulated by superposition of the RR spectra of native WT hh Cytc (also called B1 state, see Chapter 8 on page 57) with variable contributions of the ferrous (Fe^{2+}) and ferric (Fe^{3+}) forms adsorbed on all three SAMs (Figure 9.10). Only for very positive electrode potentials, the component analysis of the SERR spectra reveals minor contributions of the so-called B2 species of hh Cytc,¹³⁵ in which the axial ligand Met80 is displaced from the heme iron, resulting in a five-coordinated high-spin heme species (B2oxHS) in equilibrium with a non-native six-coordinated low-spin form (B2oxLS) with a histidine residue bound to the sixth axial position (Figure 9.10).

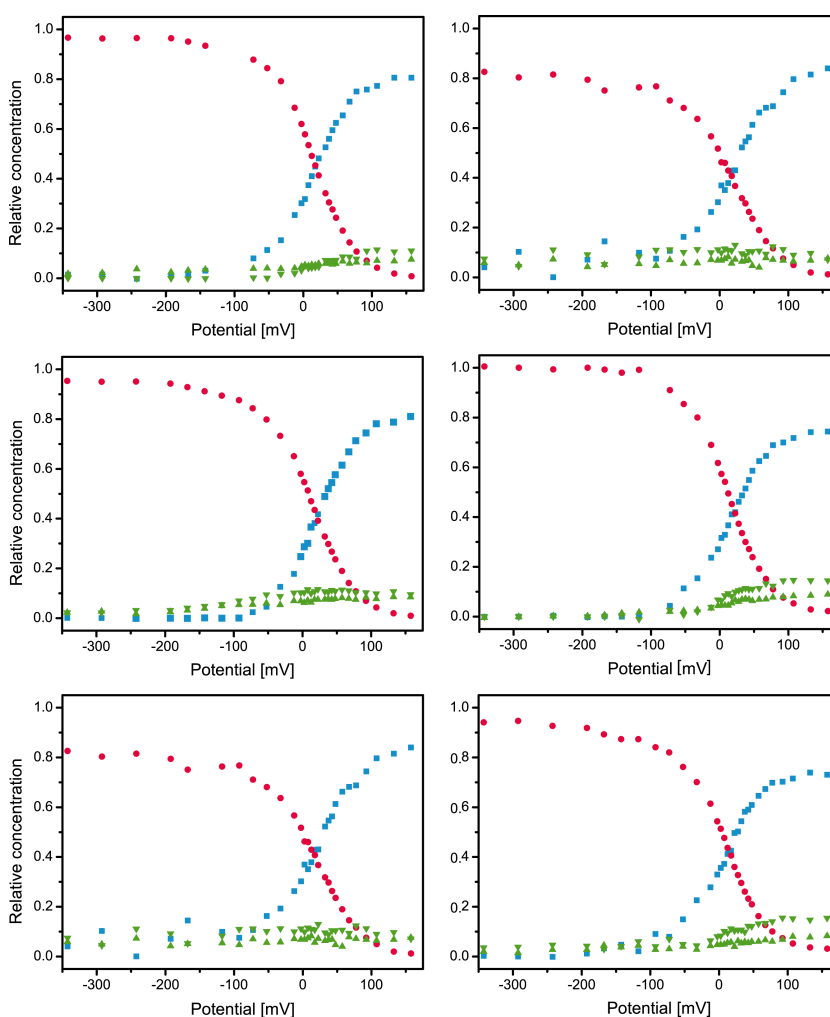


Figure 9.11.: Potential dependence of the relative concentrations of the various hh Cytc species as derived from the component analysis of the experimental SERR spectra of WT hh Cytc (left) and K87C (right) on C5 (top), C10 (middle) and C15 (bottom) SAMs. The red circles and blue squares refer to the reduced and oxidized B1 species, respectively. The non-native oxidized B2 species are presented by green triangles (high spin - upright; low spin - reversed). “Adapted with permission from [D. Alvarez-Paggi, W. Meister, U. Kuhlmann, I. Weidinger, K. Tenger, L. Zimányi, G. Rákhely, P. Hildebrandt and D. Murgida, Disentangling Electron Tunneling and Protein Dynamics of Cytochrome c through a Rationally Designed Surface Mutation *The Journal of Physical Chemistry, Part B*, **117**, 6061–6068 (2013)] Copyright (2013) American Chemical Society.”⁹

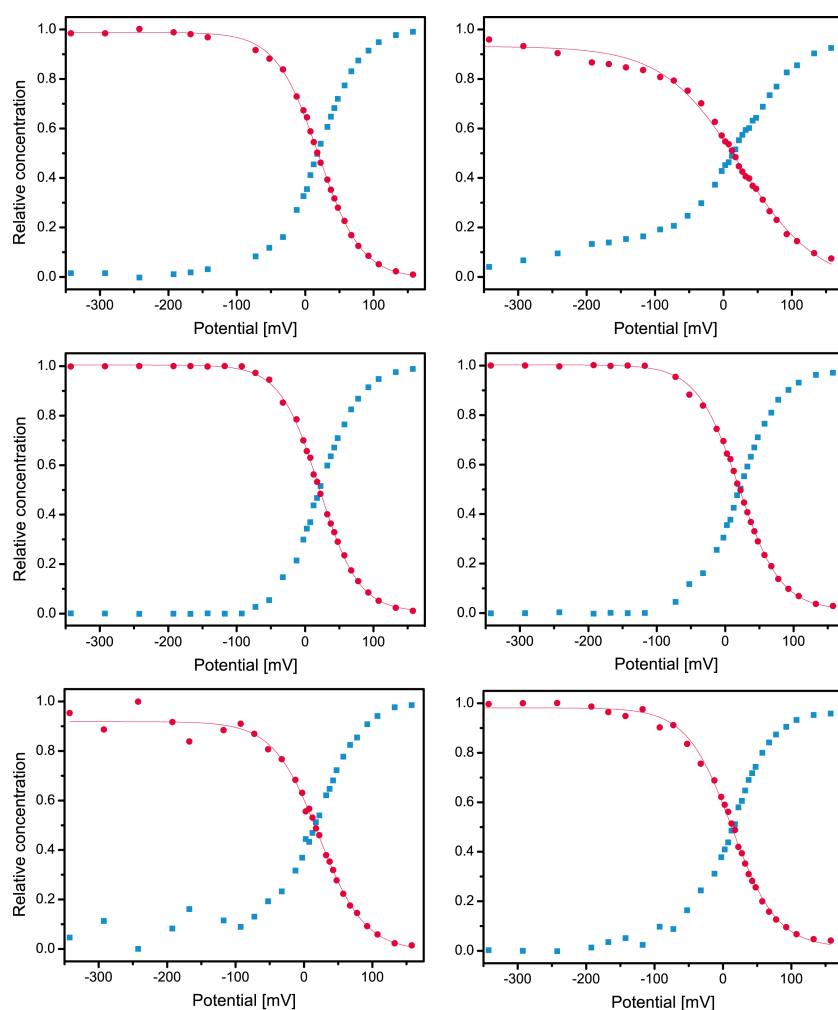


Figure 9.12.: Nernst plots (red trace) derived from the component analysis of the stationary experimental SERR spectra of the WT hh Cytc (left) and K87C (right) on C5 (top), C10 (middle) and C15 (bottom) SAMs. The red circles and blue squares refer to the reduced and oxidized B1 species, respectively.) “Adapted with permission from [D. Alvarez-Paggi, W. Meister, U. Kuhlmann, I. Weidinger, K. Tenger, L. Zimányi, G. Rákhely, P. Hildebrandt and D. Murgida, Disentangling Electron Tunneling and Protein Dynamics of Cytochrome c through a Rationally Designed Surface Mutation *The Journal of Physical Chemistry, Part B*, **117**, 6061–6068 (2013)] Copyright (2013) American Chemical Society.”⁹

The structural transition to the B2 state is only observed for the ferric protein, whereas upon electrochemical reduction the B1 form is fully recovered. Similar results were obtained for the K87C mutant, except that in this case the amounts of B2 species can reach total spectral contributions of up to 20% (Figure 9.11) which, as for the WT protein, remain constant within the time window of the experiments.

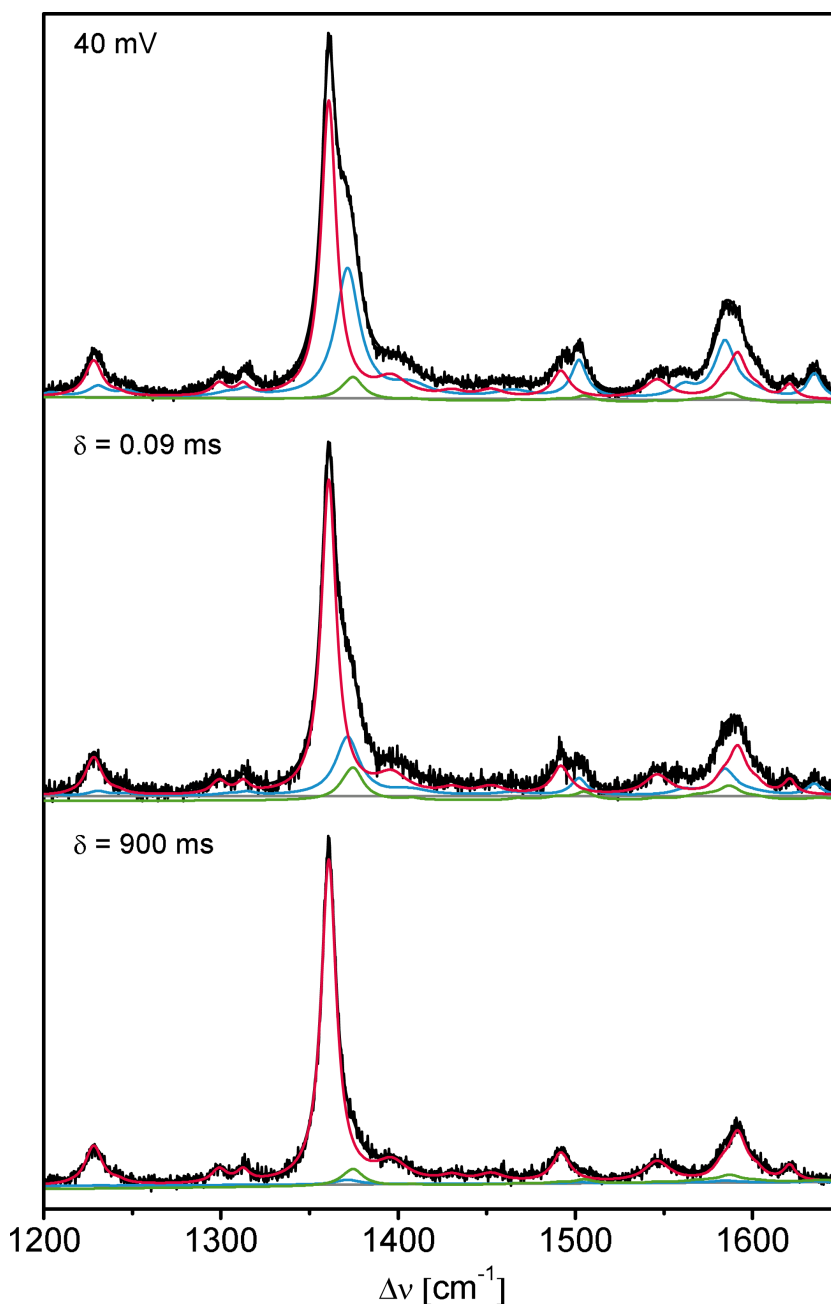
Component analysis of the potential dependent SERR spectra for both protein variants on the different SAMs affords nearly ideal Nernst plots (Figure 9.12) with reduction potentials close to 20 mV for the corresponding B1 states (Table 9.1).

9.2.4. ET dynamics investigated by TR SERR spectroscopy

The kinetics of heterogeneous ET of the hh Cytc/SAM electrostatic complexes was investigated by TR SERR spectroelectrochemistry. In these experiments the redox equilibrium of immobilized hh Cytc is perturbed by applying steps from an initial (E_i) to a final (E_f) electrode potential, while recording SERR spectra at variable delay times along

Figure 9.13.: SERR and TR SERR spectra of K87C immobilized on an Ag electrode coated by a C10 SAM, measured with 413 nm excitation, prior to a potential jump from 40 mV (top) to -200 mV after delay times of 0.09 ms (middle) and 900 ms (bottom). The component spectra of the ferrous B1, ferric B1, and the ferric B2 (HS and LS) states are represented by red, blue, and green lines, respectively.

“Adapted with permission from [D. Alvarez-Paggi, W. Meister, U. Kuhlmann, I. Weidinger, K. Tenger, L. Zimányi, G. Rákhely, P. Hildebrandt and D. Murgida, Disentangling Electron Tunneling and Protein Dynamics of Cytochrome c through a Rationally Designed Surface Mutation *The Journal of Physical Chemistry, Part B*, **117**, 6061–6068 (2013)] Copyright (2013) American Chemical Society.”



the perturbation. Two types of experiments were performed for both protein variants: (i) in the oxidative direction at nearly zero driving force with $E_i = -80$ mV and $E_f = +20$ mV ($\approx E^0$) and (ii) in the reductive direction from $E_i = +40$ mV to $E_f = -200$ mV, corresponding to a ca. -220 mV over-potential for the ET reaction. In all cases TR SERR spectra could be quantitatively reproduced using variable contributions of the same spectral components found in stationary experiments, i.e. the ferrous and ferric (native) state B1 of hh Cytc and additional small contributions from the B2oxHS and B2oxLS species. As the reduction potentials of the B2 species are below -300 mV,¹³⁵ these species do not undergo redox chemistry within the potential windows of the experiments

and, moreover, their spectral contributions remained invariant. Typical TR SERR spectra obtained for K87C are shown in Figure 9.13, along with the corresponding spectral components.

The spectral component contributions were converted into relative surface concentrations by employing relative reciprocal cross sections (Equation (5.1) on page 40) determined previously.¹⁴⁵ Time-concentration profiles obtained from this analysis for the B1 state of WT hh Cytc adsorbed on the various SAMs can be well described as one-step relaxation processes (Figure 9.14), characterized by apparent ET rate constants (k_{ET}^{app}) (Table

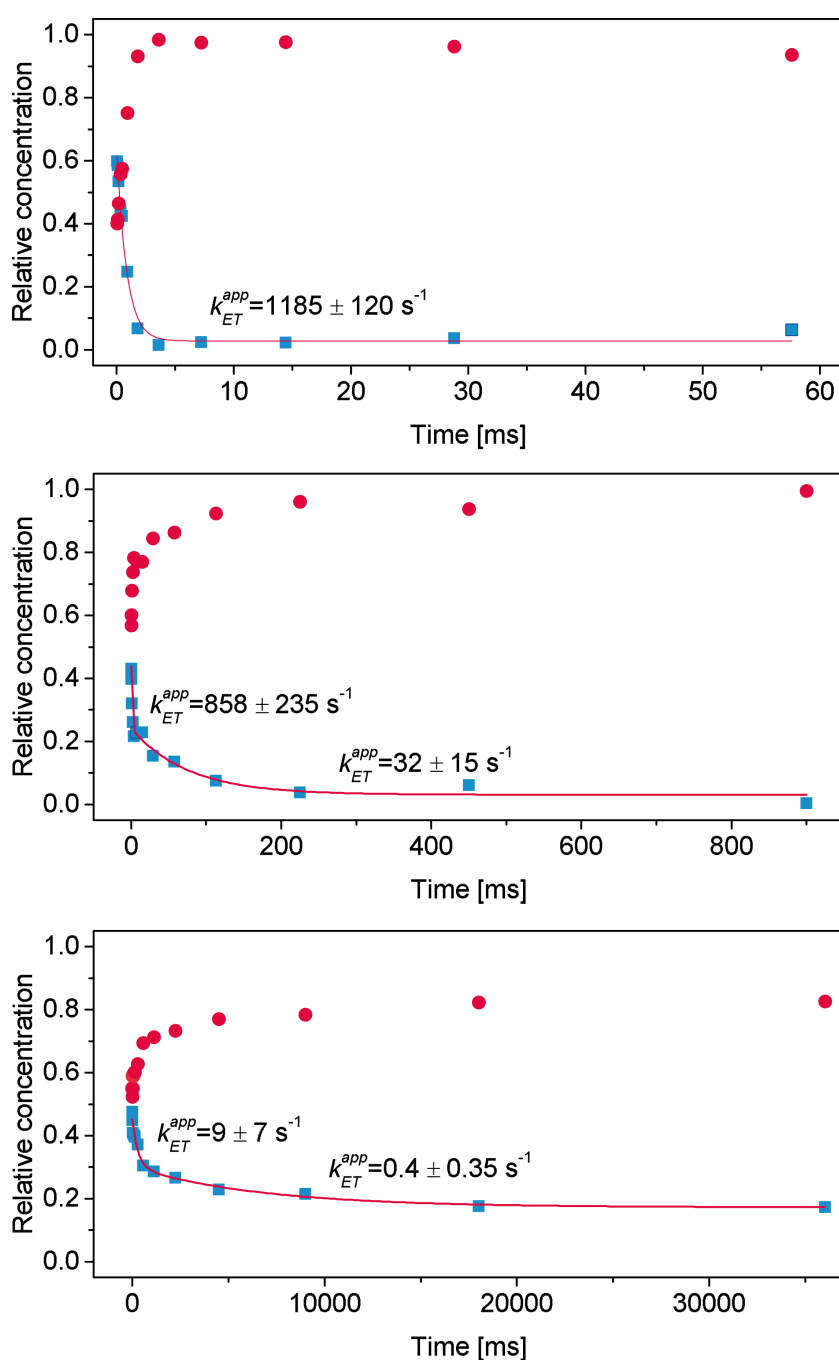


Figure 9.14.: Representative kinetics of the reduction of the hh Cytc mutant K87C (+40 → −200 mV) adsorbed on C5 (top), C10 (middle) and C15 (bottom) SAMs as monitored by TR SERR. The relative concentrations of ferrous and ferric hh Cytc are shown in red and blue, respectively. While monophasic kinetics are observed on C5, reproducible biphasic curves are obtained for both C10 and C15. Fitting to biexponential functions allow for disentanglement of the fast and slow contributions to the of the ET rate. “Adapted with permission from [D. Alvarez-Paggi, W. Meister, U. Kuhlmann, I. Weidinger, K. Tenger, L. Zimányi, G. Rákhely, P. Hildebrandt and D. Murgida, Disentangling Electron Tunneling and Protein Dynamics of Cytochrome c through a Rationally Designed Surface Mutation *The Journal of Physical Chemistry, Part B*, **117**, 6061–6068 (2013)] Copyright (2013) American Chemical Society.”⁹

Table 9.1.: Thermodynamic (E^0) and kinetic (k_{ET}^{app}) values for the hh Cytc WT and K87C mutant determined by TR SERR for protein samples adsorbed on C5, C10 and C15 SAMs. The potential step applied is indicated in each case. n is the number of transferred electrons derived from the Nernst equation.

“Adapted with permission from [D. Alvarez-Paggi, W. Meister, U. Kuhlmann, I. Weidinger, K. Tenger, L. Zimányi, G. Rákhely, P. Hildebrandt and D. Murgida, Disentangling Electron Tunneling and Protein Dynamics of Cytochrome c through a Rationally Designed Surface Mutation *The Journal of Physical Chemistry, Part B*, **117**, 6061–6068 (2013)] Copyright (2013) American Chemical Society.”⁹

WT				
	E^0 (mV)	n	k_{ET}^{app} (s^{-1})	
			$-80 \rightarrow +20$ mV	$+40 \rightarrow -200$ mV
C5	19	0.82	308 ± 20	735 ± 80
C10	20	0.9	45 ± 4	221 ± 69
C15	21	0.77	0.3 ± 0.2	1.2 ± 0.35
K87C				
	E^0 (mV)	n	k_{ET}^{app} (s^{-1})	
			$-80 \rightarrow +20$ mV	$+40 \rightarrow -200$ mV
C5	23	0.51	317 ± 17	1185 ± 120
C10	20	0.85	$238 \pm 146/11 \pm 7$	$858 \pm 235/32 \pm 15$
C15	13	0.78	$5.2 \pm 0.3/0.3 \pm 0.3$	$9 \pm 7/0.4 \pm 0.35$

9.1) very close to values reported previously for comparable experimental conditions.⁸⁸

Monophasic heterogeneous ET kinetics were also observed for the K87C protein adsorbed on C5 SAMs, with k_{ET}^{app} very similar to those determined for the WT protein at equivalent chain lengths and over potentials. In sharp contrast, however, time traces recorded for K87C adsorbed on C10 and C15 SAMs exhibit reproducible biphasic kinetics (see Figure 9.14 and Table 9.1). Partial protein dimerization through sulphur bridge formation between cysteine residues is ruled out as it is not observed for C5 SAMs and, on the other hand, TR SERR experiments performed with K87C freshly reduced with tris(2-carboxyethyl)phosphine⁵⁰ yield identical results.

For both reduction and oxidation, when considering the fast kinetic component of K87C from C10 and C15 along with the single component from C5, the observed distance-dependence is characterized by an exponential variation of k_{ET}^{app} at the thicker films, followed by a plateau at thinner films (Figure 9.15), similar to hh Cytc WT.^{12,134,135}

Notably, grouping the slow kinetic component decays from C10 and C15 together with the C5 component yields an exponential decay in the entire range of chain lengths explored (Figure 9.15). The tunnelling decay parameter β , from Equation (1.7), determined from this variation is ca. 0.8 per $-CH_2-$ group which, considering the errors involved in the measurements and data processing, is compatible with the average value of 1.1 reported in the literature for electron tunnelling across SAMs of alkanethiols.^{45,171,203}

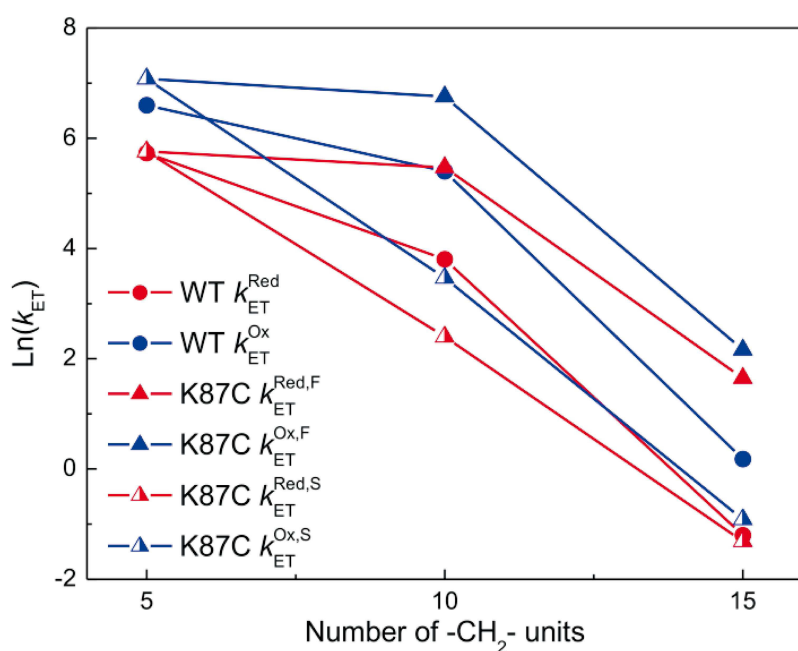


Figure 9.15.: Distance-dependence of k_{ET}^{app} for both the oxidation (red) and reduction (blue) processes of hh Cytc WT (circles) and K87C (triangles). Full and half-filled triangles represent the fast and slow component of k_{ET}^{app} for K87C, respectively.

“Reprinted with permission from [D. Alvarez-Paggi, W. Meister, U. Kuhlmann, I. Weidinger, K. Tenger, L. Zimányi, G. Rákhely, P. Hildebrandt and D. Murgida, Disentangling Electron Tunneling and Protein Dynamics of Cytochrome c through a Rationally Designed Surface Mutation *The Journal of Physical Chemistry, Part B*, **117**, 6061–6068 (2013)] Copyright (2013) American Chemical Society.”⁹

Note that, on average, the experimentally determined fast and slow ET kinetic components differ by about a factor of 22 (see Table 9.1), in excellent agreement with the differences predicted from MD simulations and pathways calculations between high and low affinity K87C/SAM electrostatic complexes (see page 67).

9.2.5. Conclusions from experimental and computational results concerning the ET of the K87C hh Cytc mutant

Experimental and computational results obtained here display a consistent overall picture. At thicker SAMs (C10, C15), which also correspond to weaker interfacial electric fields^{133,135,173} low and high amplitude motions of adsorbed ferric WT hh Cytc and of interfacial water molecules are expected to be significantly faster than electron tunneling. Indeed, rotational diffusion of WT hh Cytc on C15 SAMs has been estimated at least 4 orders of magnitude faster than ET.⁸⁸ Therefore, as a result of the interplay between fast reorientation dynamics and weak electronic coupling, redox reactions are expected to occur almost exclusively from a narrow range of high coupling orientations, thus leading to monophasic kinetics. In contrast, the biphasic kinetics of K87C at lower electric fields (C15 and C10) indicates that ET takes place from both the high affinity ($\alpha > 95^\circ$, strong binding, low coupling, slower rates) and the low affinity ($\alpha < 95^\circ$, weak binding, strong coupling, faster rates) orientations. This behaviour can be rationalized in terms of the factors that control the strength of hh Cytc binding to the SAM-coated electrode, which are the local binding energy in the absence of an external electric

field as it is estimated by the MD simulations, and the contributions due to the external electric field that are determined by the electrode potential and, thus, are not directly accessible by the present theoretical approach. However, some insight about the importance of the latter contribution is gained when considering the alignment of protein dipole moments with the interfacial electric fields, which are nearly parallel to the Z-axis for the orientations of K87C in the high affinity binding zone. Consequently, transitions from this binding zone, associated with weak electronic couplings, to the low affinity binding zone with strong coupling might be slower than reorientation dynamics of the WT hh Cytc resulting in a biphasic ET kinetics for thick SAMs (C10 and C15). As the strength of the interfacial electric field increases, those orientations that lead to a good alignment of the dipole moment but relatively weak coupling are strongly favoured, as reflected by the monophasic kinetics on thin films (C5). This interpretation suggests that on C5, only the slow kinetic component is probed experimentally, which is supported by the recovery of the exponential distance dependence when only considering such component in the entire length range explored.

9.2.6. Q-Band excitation in TR SE(R)Rs experiments with the K87C hh Cytc mutant

Theory predicts that the comparison of Raman modes of different symmetry in SER spectroscopy of symmetric molecules can provide information about the orientation of the molecules in respect to the surface, “because for modes of different symmetry the individual components of the scattering tensor are modified to different extents depending on their relative orientation with respect to the electric field vector. [...] it can be shown that the totally symmetric A_{1g} modes will experience preferential enhancement when the heme plane is parallel to the surface, while for a perpendicular orientation the A_{1g} modes as well as the non-totally symmetric A_{2g} , B_{1g} and B_{2g} modes will be enhanced to the same extent. [...] This is strictly true under non-resonant excitation conditions [...]” (Ly et al., 2010)⁹⁹ More informations on the theoretical background can be found in Chapter 3 and 4.

It was shown in TR SE(R)R experiments with WT hh Cytc using Q-band excitation (514 nm, pre resonance) that the time evolution of the intensity ratio between the non-totally symmetric mode $\nu_{10}(B_{1g})$ (for ferric hh Cytc at 1636 cm^{-1}) and the totally symmetric $\nu_4(A_{1g})$ (for ferric hh Cytc at 1372 cm^{-1}) after e.g. a potential jump, is suitable to follow the reorientation process of the protein (heme plane) on the surface of the electrode/SAM system.^{88,100,137} The reported $\nu_{10}(B_{1g})/\nu_4(A_{1g})$ ratios

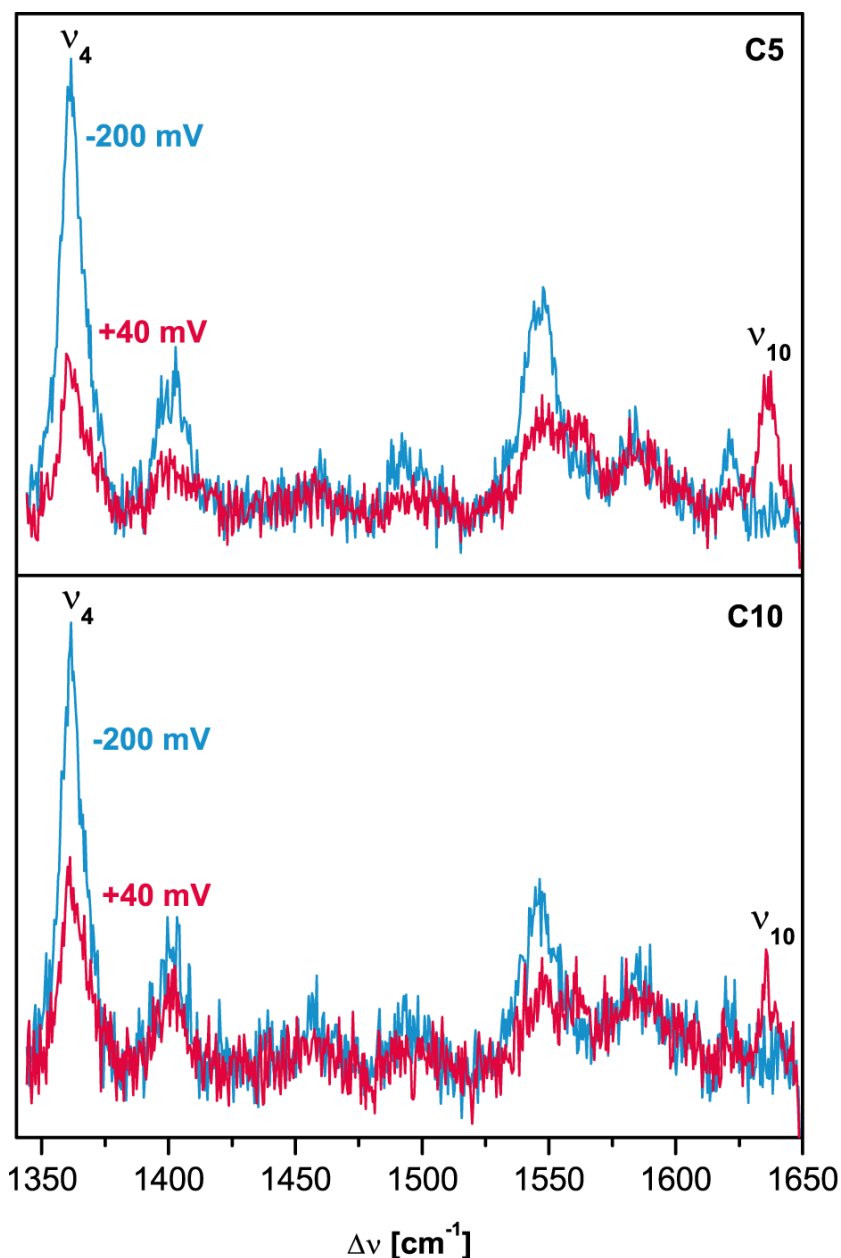


Figure 9.16.: Stationary spectra of the K87C hh Cyt_c mutant adsorbed on C5 (top) and C10 (bottom) SAMs at a potential of +40 mV (red) to −200 mV (blue) using 514 nm excitation.

of the 514 nm TR SER experiments for C5 SAMs vary between ≈ 5.5 for the initial potential of +50 mV and ≈ 2.5 for very long delay times at the final potential of −50 mV. The reorientation rates k_{reor}^{app} derived from these data suggested that reorientation becomes ET rate limiting for short SAMs (C5) and is much faster than ET for longer SAMs (C15). For short SAMs the measured rate of the ratio $\nu_{10}(B_{1g})/\nu_4(A_{1g})$ with 514 nm lead to the same ET rate detected under resonance excitation conditions at 413 nm.⁸⁸

Similar TR SE(R)R experiments with 514 nm excitation were carried out with the K87C mutant of hh Cyt_c. The results are summarized in Table 9.2. The first impression of the outcome is somehow irritating since the apparent rate constants for the development of the ν_{10}/ν_4

Table 9.2.: Apparent rate constants for the development of the $v_{10}(B_{1g})/v_4(A_{1g})$ intensity ratio under 514 nm excitation k_{514}^{app} and the reduction of K87C hh Cytc probed with 413 nm excitation $k_{ET,413}^{app}$ both for the potential jump from +40 mV to -200 mV on different SAM length. Values for 413 nm excitation were taken from Table 9.1 on page 74.

	k_{514}^{app} (s ⁻¹)	$k_{ET,413}^{app}$ (s ⁻¹)
C5	840 ± 270	1185 ± 120
C10	430 ± 240	858 ± 235/32 ± 15

intensity ratio with time after a potential jump, that is associated with the reorientation, is faster on a short SAM (C5) than on a medium length SAM (C10). This seems to contradict the findings presented in this work, that K87C protein reorientation is hindered on short SAMs (high fields).

A closer look reveals that the two, under different excitation wavelength, detected rate constants exhibit the same distance dependence. For the C5 SAM $k_{ET,413}^{app}$ is reproduced by the apparent rate constant (k_{514}^{app}) for development of the v_{10}/v_4 intensity ratio under 514 nm excitation.

514 nm excitation is still in pre resonance with an electronic transition of the heme cofactor, consequently not only the reorientation but also the redox-transition changes the v_{10}/v_4 intensity ratio in the spectra obtained with 514 nm excitation. The rate constant k_{514}^{app} reflects both, reorientation and ET.

Since for the K87C mutant $k_{514}^{app}(C5) > k_{514}^{app}(C10)$, and k_{514}^{app} is only slightly smaller than $k_{ET,413}^{app}$ for both cases (C5, C10), it is evident that reorientation does not play a strong role for the ET rate of the K87C mutant, unlike for the WT. This supports the previous findings of this

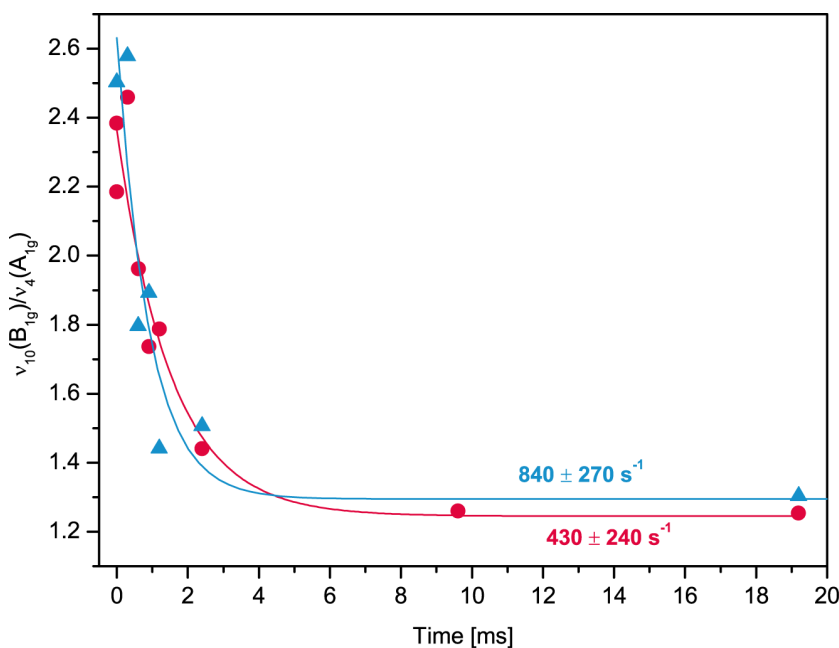


Figure 9.17.: Time evolution of the $v_{10}(B_{1g})/v_4(A_{1g})$ intensity ratio for the ferric hh Cytc mutant K87C adsorbed on C5 (blue trace, triangles) and C10 (red trace, spheres) SAMs after a potential jump from +40 mV to -200 mV using 514 nm excitation.

work that the reorientation of this mutant is strongly hindered on the short C5 SAM, but also on C10 not much reorientation is detectable.

Note: The error associated with k_{514}^{app} is much larger than for $k_{ET,413}^{app}$ due to poorer spectral quality.

As shown in Figure 9.17 the alteration and the absolute value of the k_{514}^{app} rates for the K87C mutant on both probed SAMs are quite similar. They change from ≈ 2.5 at +40 mV (initial potential) to ≈ 1.3 at long delay times (final potential; -200 mV). The variance of the v_{10}/v_4 ratio is much smaller than that reported for the WT hh Cytc.⁸⁸ Smaller ratios predict a more parallel orientation of the heme in respect to the surface for the K87C mutant, at least at C5 SAMs (C10 SAMs have not been shown for the WT in the literature) which further supports the conclusions previously made in Subsection 9.2.5. On the other hand, a broader orientation distribution, which is predicted for the K87C mutant in comparison to the WT, would lead to a unpredictable overall intensity ratio between the v_{10} and the v_4 .

9.3. The K39C and K8C mutants of hh Cytc

It was shown that K87 of hh Cytc lies in the area of the domains which interact directly with negatively charged surfaces as the carboxyl-terminated SAMs. The changes of the ET of the K87C mutant vs. the WT protein are a result of changes in the direct interactions between the Cytc and the SAM surface as well as an effect of the overall electrostatics and dipole interplay with the electric field. For the reason of differentiation between the two effects we choose also the K39C and K8C mutants of hh Cytc for SERR spectroscopic experiments.

As the mutations on position 39 and 8 should not alter the direct interactions since they both do not lie in the assumed ET pathway, only the charge distribution of the hh Cytc is altered by these substitutions. The effect of the resulting electrostatics is studied in the following section. The position of the mutations are depicted below.

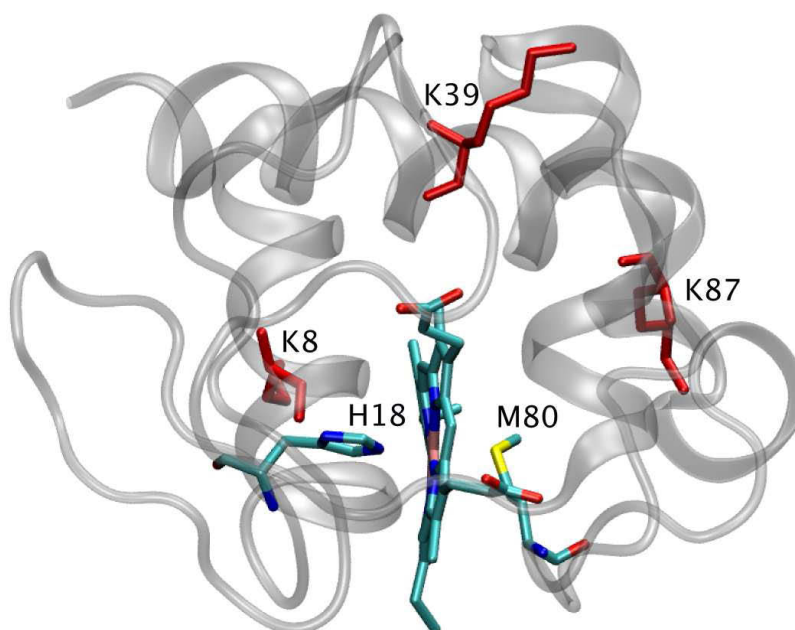


Figure 9.18.: Crystal structure of oxidized hh Cytc (Protein Data BankID code 1HRC) with the heme center and the three lysines that has been mutated for our experiments (depicted in red). The view was chosen for comparison with figure 9.1 on page 60.

9.3.1. Stationary SERR experiments with the K39C and K8C hh Cytc mutants

The SERR spectra of the hh Cytc mutants K39C and K8C could be fitted and described by the B1 and B2 species known for the WT without any changes in the component spectra. The component analysis of potential dependent SERR measurements of K39C and K8C immobilized electrostatically on carboxyl-terminated SAMs of different chain length show significantly higher spectral contributions of the non native B2 species at

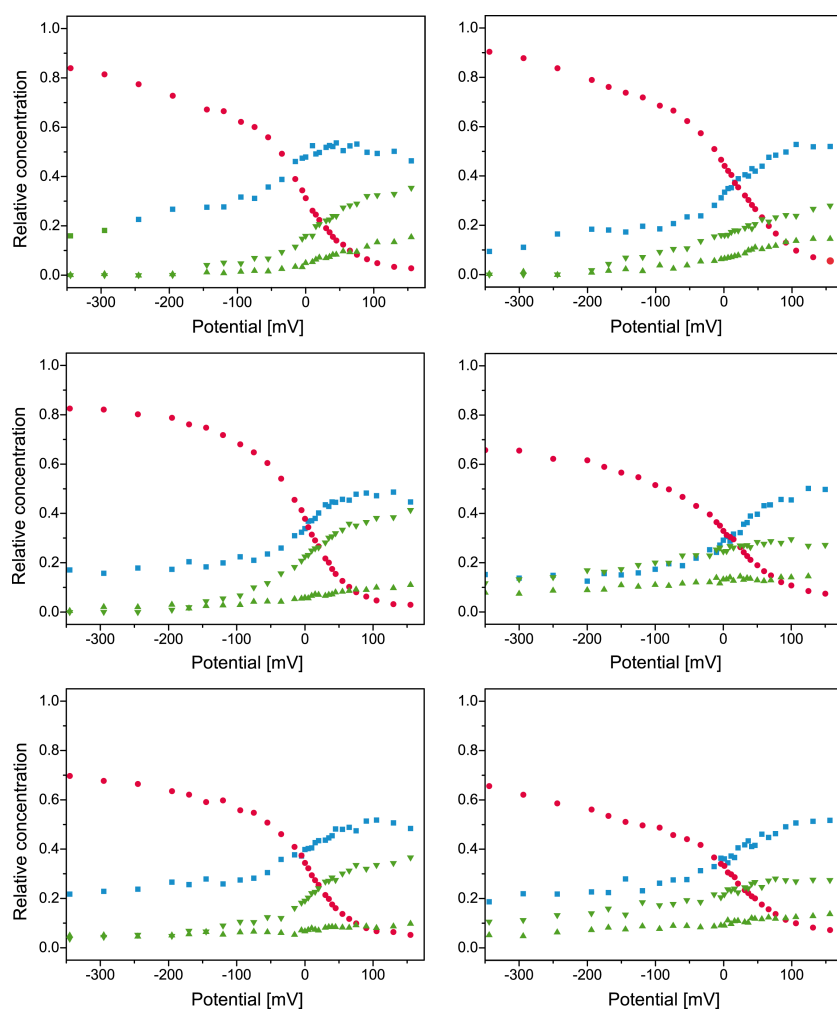
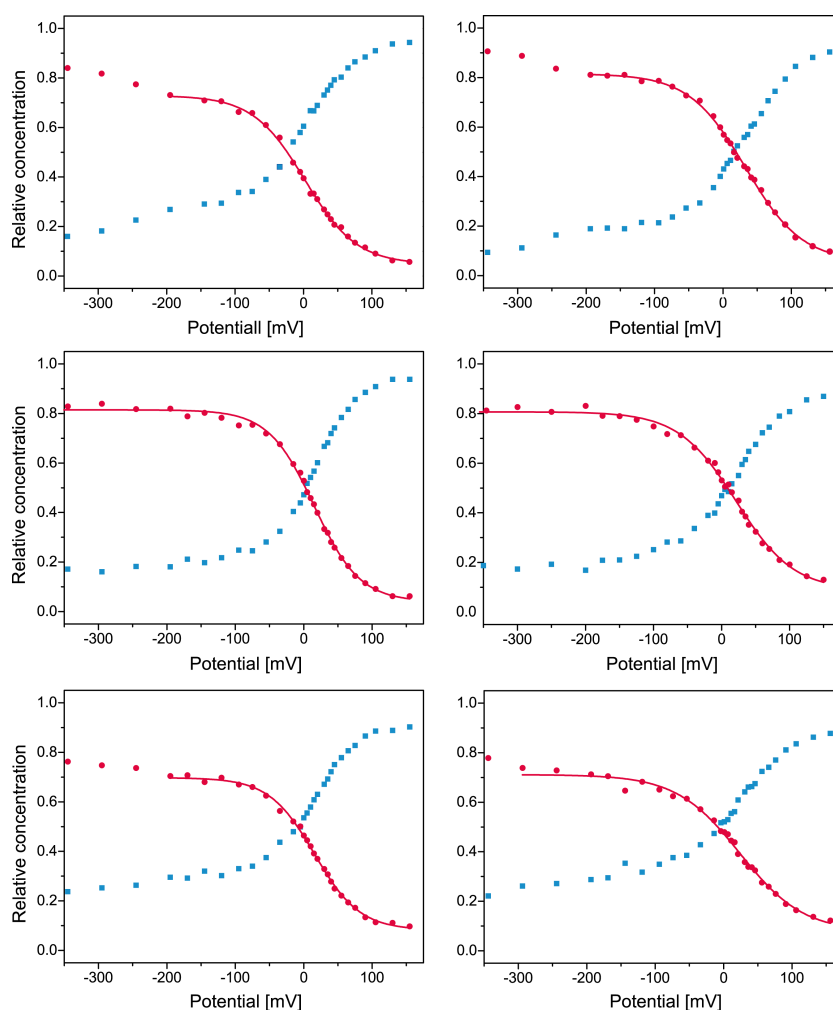


Figure 9.19.: Potential dependence of the relative concentrations of the various hh Cytc species of the K39C and K8C mutants of hh Cytc as derived from the component analysis of the experimental SERR spectra of K39C (left) and K8C (right) on C5 (top), C10 (middle) and C15 (bottom) SAMs. The red circles and blue squares refer to the reduced and oxidized B1 species, respectively. The non-native oxidized B2 species are presented by green triangles (high spin - upright; low spin - reversed).

positive electrode potentials, than the WT. This is especially true for the K39C mutant of hh Cytc, see Figure 9.19 (compare with Figure 9.11 on page 70). Furthermore it seems to be impossible to completely reduce the proteins. This suggests that a fraction of the protein is immobilized in a orientation which impairs ET. To account only for the ET active protein the B1 species were normalized, as for the WT and K87C before, to 100%.

The Nernst plots, shown in Figure 9.20, derived from the spectral normalized B1 contributions show a slightly different trend for both examined mutants than the WT (compare with Figure 9.12 on page 71). As summarized in Table 9.3 on page 83 the redox potential E^0 of the K39C mutant is increasing while that of the K8C mutant is decreasing with chain length. E^0 of the K39C variant is lower, whereas that of the K8C mutant is higher than that of the WT protein. The number of transferred electrons n is in both cases much lower as the expected number for the WT of 1, which means that the ET is less effective for these mutants.

Figure 9.20.: Nernst (red trace) plots derived from the component analysis of the stationary experimental SERR spectra of the *hh*Cyt K39C (left) and K8C (right) on C5 (top), C10 (middle) and C15 (bottom) SAMs. The red circles and blue squares refer to the reduced and oxidized B1 species, respectively.



9.3.2. TR SERR experiments—kinetics of the K39C and K8C mutants of *hh* Cyt c

The redox potential of the B2 species known for the WT Cyt c are much more negative than the E^0 of the B1 species.^{136,137} Also the kinetics of the B2 species are expected to be different from the kinetics of the B1 species. To check potential irreversible accumulation of (B2) species during the TR SERR experiments, spectra were first measured at negative delay times with respect to the potential jumps. A representative example (K39C immobilized on a C10 SAM with potential jumps from $-80 \rightarrow +20$ mV) is shown in Figure 9.21. It was shown that the jump start conditions are stable and the lower instability of the two mutants does not interfere with the TR SERR experiment.

The TR SERR measurements confirmed the relatively high B2 concentrations particularly for the K39C mutant, as well as a portion of the protein that does not participate in the ET process (see Figure 9.22 and 9.23). The kinetics of the K39C and K8C mutants of *hh* Cyt c are slowed down by a factor of 3.5–10 for K39C and 12–16 for K8C (when only consider-

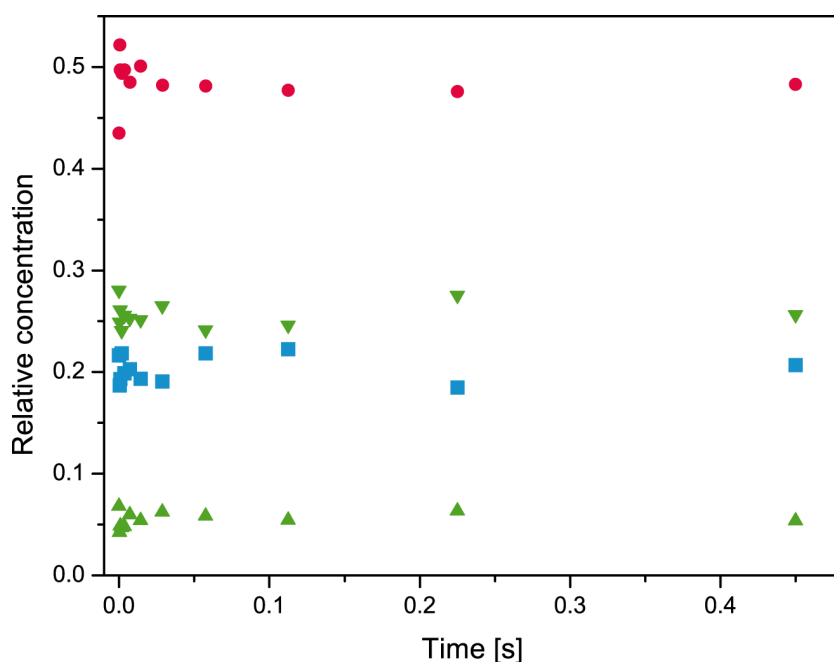


Figure 9.21.: Spectral component composition at the start of each applied potential jump (x-axis give the delay time of each jump) for the K39C mutant immobilized on a C10 SAM for a potential jump from $-80 \rightarrow +20$ mV derived from the component analysis of the experimental SERR spectra. The red circles and blue squares refer to the reduced and oxidized B1 species, respectively. The non-native oxidized B2 species are presented by green triangles (high spin - upright; low spin - reversed)

ing the monoexponential rate constant) compared to the WT protein. The results are summarized in Table 9.3. The kinetics of the B1 species of the K39C mutant can in each case be fitted by a monoexponential function, while for the K8C mutant for the C10 SAM a biexponential fit is possible. In this case one rate is close to the one of the monoexponential fit while the other is much slower for the oxidation ($-80 \rightarrow +20$ mV) and much faster for the reduction ($+40 \rightarrow -200$ mV). The kinetic of the K8C variant might also be biphasic for longer SAMs (C15) but the rates would then lie below the detection limit. The biphasic behaviour may result from different orientations of the K8C mutant.

In contrast to the hh Cytc mutant K87C, the K39C and the K8C mutants exhibit lower stability (high B2 fraction) and a less uniform orientation, since part of the protein is ET inactive. This points to a role of all

K39C				
	E^0 (mV)	n	k_{ET}^{app} (s^{-1})	
			$-80 \rightarrow +20$ mV	$+40 \rightarrow -200$ mV
C5	3	0.68		
C10	16	0.77	8 ± 3	60 ± 10
C15	17	0.77	0.03 ± 0.01	0.11 ± 0.06
K8C				
	E^0 (mV)	n	k_{ET}^{app} (s^{-1})	
			$-80 \rightarrow +20$ mV	$+40 \rightarrow -200$ mV
C5	34	0.62		
C10	28	0.61	2.8 ± 0.2 (0.074/5.5)	17 ± 1 (16/1050)
C15	25	0.55	0.022 ± 0.008	0.1 ± 0.02

Table 9.3.: Thermodynamic (E^0) and kinetic (k_{ET}^{app}) values for the K39C and K8C mutants of hh Cytc determined by TR SERR for protein samples adsorbed on C5, C10 and C15 SAMs. The potential step applied is indicated in each case. n is the number of transferred electrons derived from the Nernst equation. The two rates given in brackets for K8C/C10 indicate that a biexponential fit could be applied at least in some measurements.

surface lysines of Cytc for ideal immobilisation and recognition of the redox partner even if the lysine is not part of the direct interactions. The overall charge of the Cytc is reduced (also true for the K87C) by changing a positive charged lysine to a neutral cysteine and this new charge distribution lead to a change in direction and magnitude of the dipole moment.

The slower ET rates allow two interpretations. On the one hand, one may assume different ET pathways. On the other hand, it may be possible that the orientational distribution is altered by the substitution at position 39 and 8.

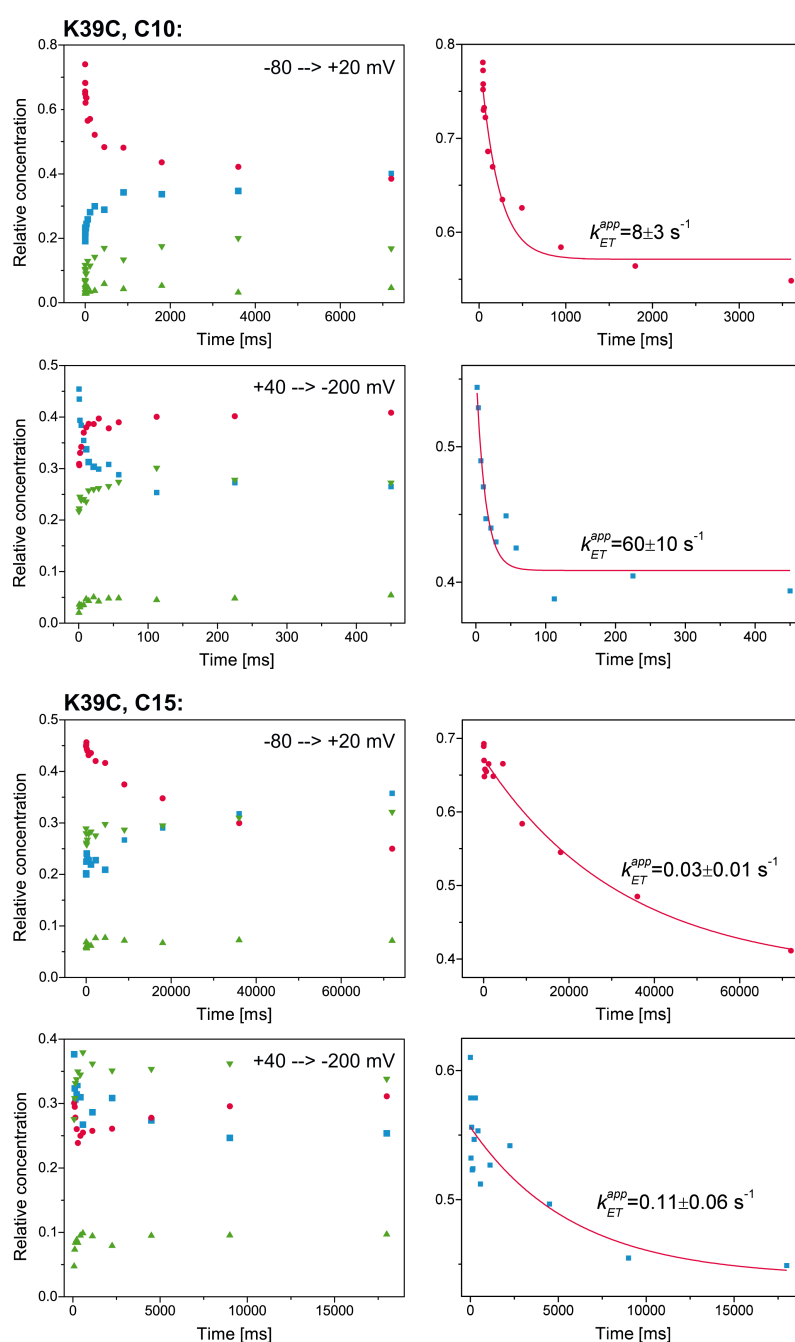


Figure 9.22.: Potential dependence of the relative concentrations of the various hh Cytc species (left) and representative kinetics (right) as derived from the component analysis of the experimental SERR spectra relative concentration of K39C adsorbed on C10 and C15 SAMs for the oxidation ($-80 \rightarrow +20 \text{ mV}$) and reduction ($+40 \rightarrow -200 \text{ mV}$) as monitored by TR SERR. The relative concentrations of ferrous and ferric hh Cytc are shown in red cycles or blue squares, respectively. The B2 species are labelled in green.

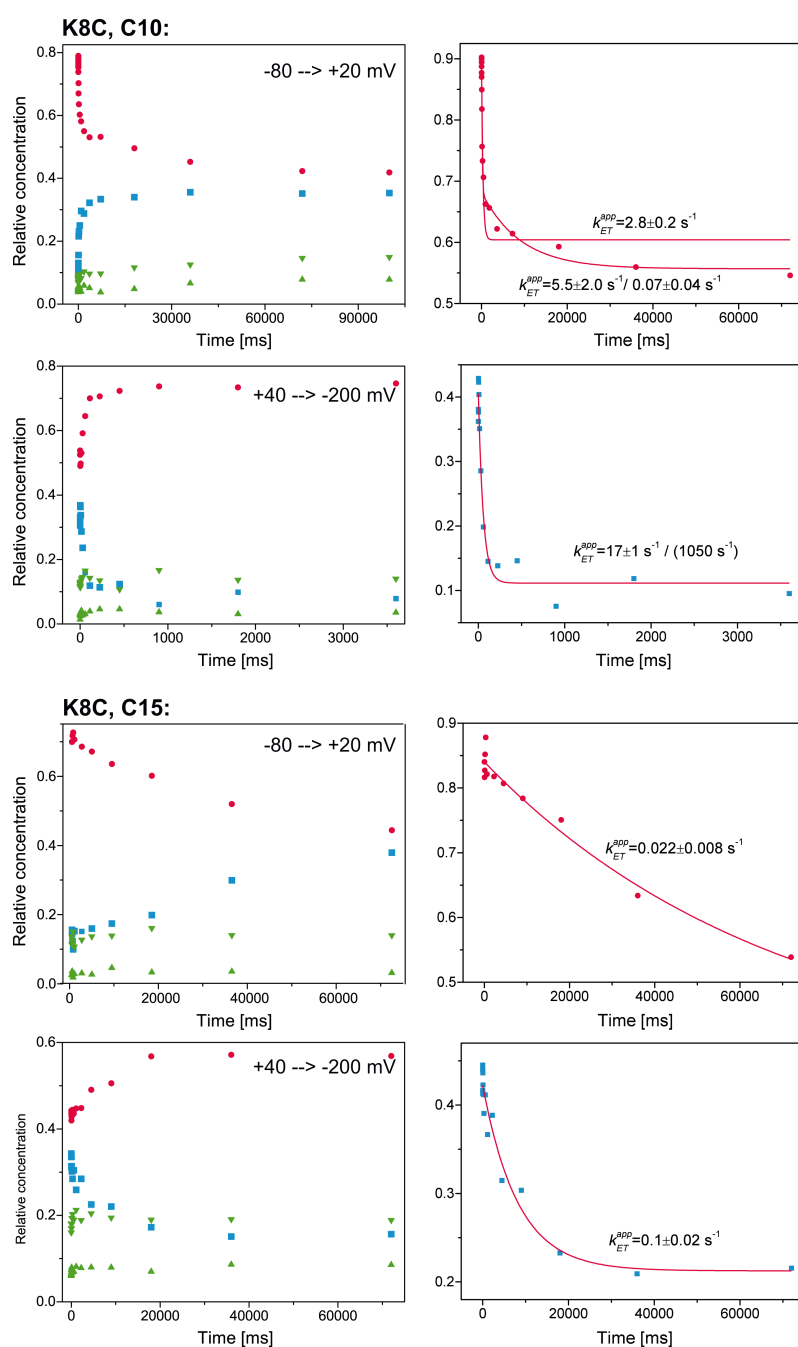


Figure 9.23.: Potential dependence of the relative concentrations of the various hh Cytc species (left) and representative kinetics (right) as derived from the component analysis of the experimental SERR spectra relative concentration of K8C adsorbed on C10 and C15 SAMs for the oxidation ($-80 \rightarrow +20 \text{ mV}$) and reduction ($+40 \rightarrow -200 \text{ mV}$) as monitored by TR SERR. The relative concentrations of ferrous and ferric hh Cytc are shown in red cycles or blue squares, respectively. The B2 species are labelled in green.

Preliminary MD simulation studies with the three hh Cytc mutants, done by Tillman Utesch, suggest that for the K87C mutant stable protein / SAM contacts are established over the so-called BD2 (containing amongst others Lys25 and 27) and BD3 (containing amongst others Lys72, 73, 79, 86 and 87), depicted in Figure 9.1 on page 60. For the K39C and K8C mutant only BD3 is predicted to be involved in stable protein / SAM electrostatic interactions, but in a different manner. If one consider the kinetics of the K39C and K8C mutant as monophasic a consistent picture emerges since the slow component of the K87C mutant is ascribed to the ET via the high affinity domain BD3 with low coupling efficiency. One could conclude that the comparable ET rates of the K87C (slow

trace), K39C and K8C mutants point to a ET pathway through BD3. It may be that protein reorientation is slowed down in these mutants such that, unlike to the WT, (slow) ET via the high affinity binding domain represents the preferred ET mechanism.

9.4. Conclusions from the results of the investigations of rational designed surface mutations of hh Cytc

The exploration of anomalous distance dependencies of protein ET on SAM-coated electrodes is of interest for a very long time. Rational surface mutation of the protein allowed us to further support a gating mechanism involving protein reorientation.^{7,88,99}

Of great significance, the exponential distance dependence of k_{ET} was recovered by disentangling protein dynamics from ET kinetics. This was achieved by rational surface mutations that change the energetic balance of the hh Cytc/SAM complexes allowing us to confirm here our previous hypothesis, thus emphasizing the role of interfacial electric field in modulating the interplay between protein dynamics and electron tunnelling.⁹

10. The Effect of the Ionic Strength on the Redox Potential and the Electron Transfer Kinetics of Horse Heart Cytochrome *c*

In chemical reactions the ionic strength can be a crucial parameter, especially if ions are involved.

The SERR experiments conducted not only in this work but also in our working group are designed to meet the optimal parameters to get good signals as well as keeping the proteins in their native state. In SERR spectroscopy with Cyt*c* the distance of the heme center from the electrode surface is critical and high ion concentrations are known to cause desorption of the Cyt*c*. Usually, a concentration of 30 mM phosphate buffer is used for experiments with COOH-SAMs. This leads to stable Cyt*c* signals of good quality within acceptable acquisition times. However, in this respect these conditions do not mimic the cellular environment where the ionic strength is usually distinctly higher.

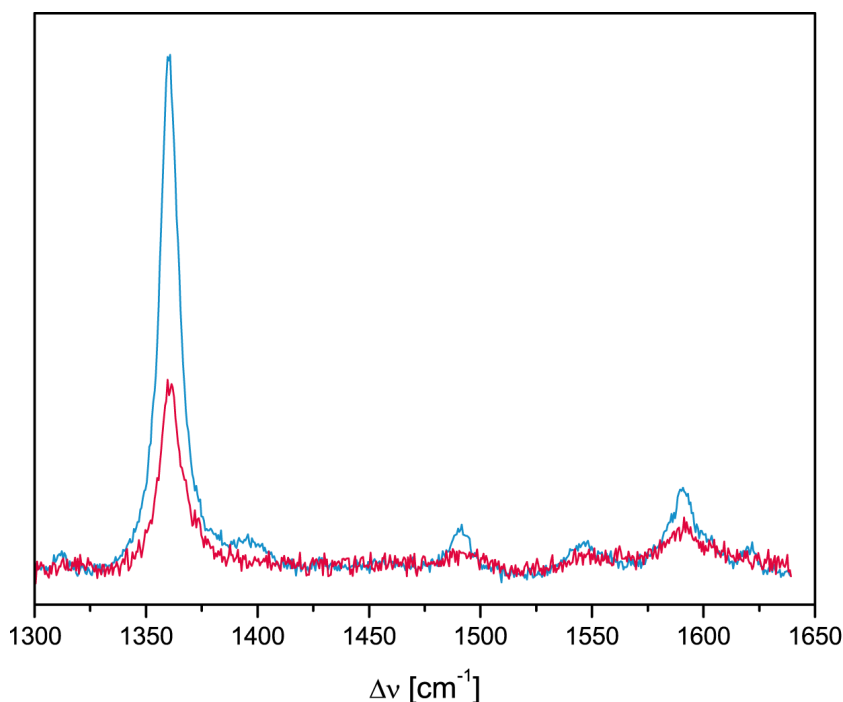
In this chapter, the effect of ionic strength on the ET behaviour of Cyt*c* was investigated with SERR spectroscopy. All experiments reported here were done by myself and by Robert Götz under my supervision. Some of the results are already presented in his bachelor thesis.

10.1. Implications of increased ionic strength on the SERR spectra of hh Cyt*c*

For all experiments (SERR, 413 nm excitation) the hh Cyt*c* was electrostatically immobilized on a C10 SAM. The protein stayed in the buffer solution during the measurements. For the immobilisation we used two systems. The so-called “low ionic strength” buffer was the standard buffer of 30 mM phosphate, pH 7 with a protein concentration of approximately 0.7 μM (laser power ≈ 1 mW). The “high ionic strength” system was a 30 mM phosphate / 120 mM potassium chloride buffer at pH 7 with a protein concentration of about 1.4 μM (laser power ≈ 1.5 mW).

The ionic strength is given as $I = \frac{1}{2} \sum c_i z_i^2$. A phosphate buffer at pH 7 consists of a $\approx 1:1$ ratio of $K^+ / H_2PO_4^-$ and $2K^+ / HPO_4^{2-}$. So the ionic strength of the “low ionic strength” buffer equal to $I = 60$ mM and of

Figure 10.1.: SERR spectra of WT hh Cyt_c immobilized on an Ag electrode coated by a C10 SAM at different ionic strength and at an applied potential of -350 mV, measured with 413 nm excitation. The blue spectrum was measured with a concentration of $0.74 \mu\text{M}$ in 30 mM phosphate buffer at pH 7 and an acquisition time of 3 s with 1 mW laser power, the red spectrum was measured with a concentration of $1.4 \mu\text{M}$ in 30 mM phosphate buffer +120 mM KCl at pH 7 and an acquisition time of 30 s with 1.5 mW.



the “high ionic strength” buffer to $I = 180$ mM. The physiological ionic strength in cell environment is given in literature and is about 100 mM.¹⁵¹

It is important to note that we could not achieve spectra of the same spectral quality for the high ionic strength measurements as with low ionic strength albeit we increased the laser power by the factor of 1.5 and the acquisition time by a factor of 10 (Figure 10.1). The overall signal intensity per milliwatt and second for the high ionic strength system was only 1 % of that of the low ionic strength system. The implications of the poorer spectra quality are that the data analysis is not as reliable for high ionic strength as for the low ionic strength. The error of each

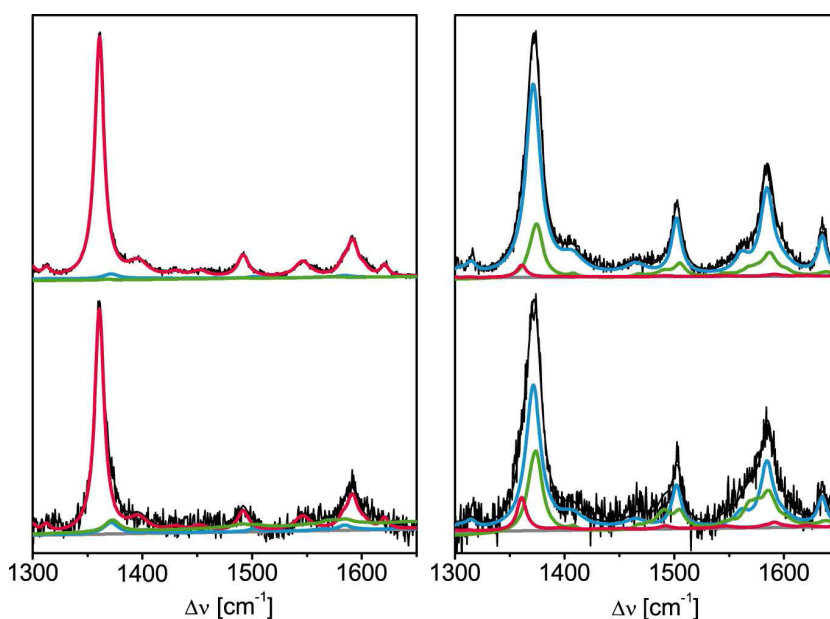


Figure 10.2.: SERR experimental spectra of WT hh Cyt_c immobilized on a C10-SAM at 60 mM (left) and 180 mM (right) ionic strength at -350 mV (top) and $+150$ mV (bottom) with 413 nm excitation. The component spectra of ferric B1, ferrous B1, and ferric B2 (HS and LS) are represented by the blue, red, and green lines. The baseline is displayed in grey and the overall fit (sum of the component spectra) is shown on black.

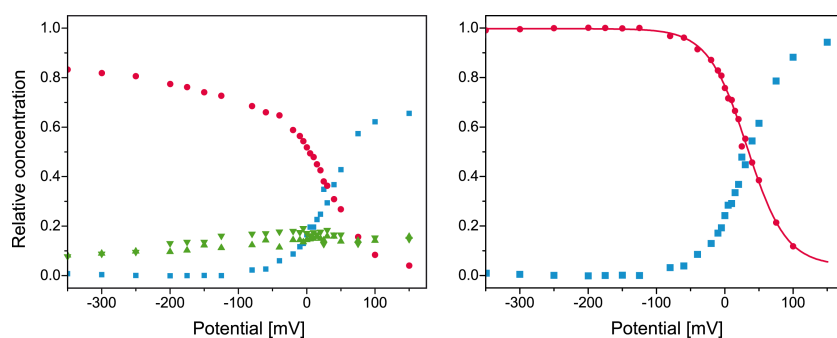


Figure 10.3.: Potential dependence of the relative concentrations of the various hh Cyt c species (left) and nernst plot for normalized B1 species (right, red trace) as derived from the component analysis of the experimental SERR spectra of WT hh Cyt c on a C10 SAM at 180 mM ionic strength. The red circles and blue squares refer to the reduced and oxidized B1 species, respectively. The non-native oxidized B2 species are presented by green triangles (high spin - upright; low spin - reversed).

data point in the component analysis is somewhat greater. Moreover the longer acquisition times together with the increased laser power may have induced protein damage. In fact, we found higher contributions of the B2 species in the high ionic strength spectra which, however, may also originate from the altered local field strength due to the increased ionic strength. Compare Figure and 10.2 with Figure 9.10 on page 69.

10.2. Stationary SERR experiments with different ionic strength—Redox potential and composition

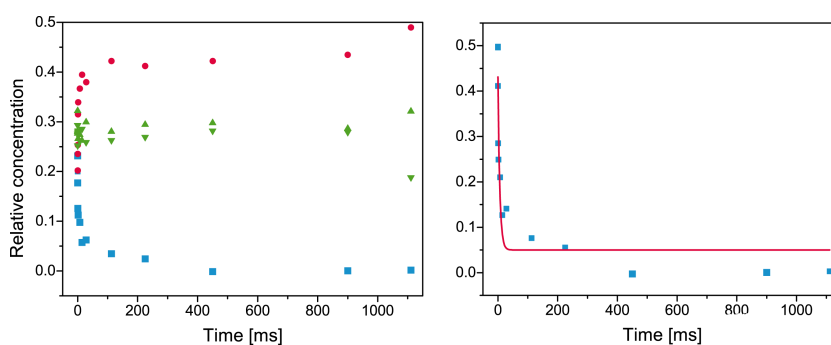
For low ionic strength, previous findings were reproduced (Chapter 9, results for the WT hh Cyt c and Chapter 7). The portion of B2 species is very low and only increase over 10–20 % for positive electrode potentials (see Figure 9.11 on page 70 and Figure 10.2 top). The redox potential E^0 of 20 mV was confirmed (Table 10.1).

For stationary measurements with high ionic strength we observe slightly higher B2 concentrations up to 30 % (Figure 10.2 and 10.3). The Nernst plot of the redox titration gives a positively shifted redox potential E^0 of 29 mV for high ionic strength (see Table 10.1). Note that the redox potential of unbound hh Cyt c is ≈ 50 mV vs. a Ag/AgCl (3M) in solution, relatively independent of the ionic strength.^{52,115,133,136,151}

10.3. Kinetics of the ET of hh Cyt c at high ionic strength

To ensure that the low and high ionic strength experiments were carried out in the same manner without a different “personal” influence on the outcome (see Chapter 7 of this work from page 49) we repeated the low ionic strength experiments (see Chapter 7 and 9). For reason of comparability the same two types of time-resolved experiments were performed for both ionic strength: (i) in the oxidative direction at nearly

Figure 10.4.: Exemplary relative concentrations evolution of the various hh Cytc species (left) and ET kinetics of the normalized oxidized B1 species(right, red trace) as derived from the component analysis of the experimental TR SERR spectra of WT hh Cytc on a C10 SAM at 180 mM ionic strength for the applied potential jump of $+40 \rightarrow -200$ mV. The red circles and blue squares refer to the reduced and oxidized B1 species, respectively. The non-native oxidized B2 species are presented by green triangles (high spin - upright; low spin - reversed).



zero driving force with $E_i = -80$ mV and $E_f = 20$ mV ($\approx E^0$) and (ii) in the reductive direction from $E_i = 40$ mV to $E_f = -200$ mV, corresponding to a ca. -220 mV or -230 mV overpotential for the ET reaction, respectively.

For low ionic strength the kinetics of the previous experiments were well reproduced (Table 7.3 on page 53 and Table 9.1 on page 74). The high ionic strength kinetics show a slight decrease of a factor of about 1.5 in comparison to the low ionic strength kinetics for both potential jumps. The results are summarized in Table 10.1.

Whereas in the TR SERR experiments with low ionic strength very low contributions of the B2 species were detectable, we saw much higher B2 contributions in the TR SERR experiments with high ionic strength up to a total spectral portion of 60 % (example in Figure 10.4, other measurements were qualitatively the same). The B2 concentration was also much higher than of the high ionic strength stationary SERR measurements, indicating stress of the immobilized Cytc in the TR experiments due to the sequence of potential jumps.

A resulting problem was that the high B2 contribution lowered the accuracy of the B1 component analysis. The scattering of the time dependent relative concentration was much higher for the high ionic strength mea-

Table 10.1.: Kinetic (k_{ET}^{app}) ET values for the WT hh Cytc electrostatically immobilized on a C10 SAM at different ionic strength for different potential jumps at pH 7. The ionic strength and the potential step applied is indicated in each case. (Average value out of * two, ** three or *** four measurements). The electric field values are calculated on page 92.

Buffer	30 mM phosphate	30 mM phosphate +120 mM KCl
I	60 mM	180 mM
E^0 (mV)	20	29
n	0.9	0.9
k_{ET}^{app} ($-80 \rightarrow +20$ mV) (s^{-1})	42.5 *	28 **
k_{ET}^{app} ($+40 \rightarrow -200$ mV) (s^{-1})	242 ***	170 ***
E_F^{calc}	$1.51 \times 10^9 \frac{V}{m}$	$1.47 \times 10^9 \frac{V}{m}$

measurements and therefore the apparent rate constants k_{ET}^{app} are associated with a larger error. In this respect I will only discuss the qualitative outcome of the analysis.

10.4. The effect of the ionic strength on the electric field

In the course of this work it was argued and shown that the electric field has influence on the ET of Cyt c . It is now important to find out about the impact of the ionic strength on the electric field of the electrode/SAM/Cyt c system to further discuss the effect of the ionic strength on the electron transfer.

To calculate the electric field E_F the following equation taken from Murgida and Hildebrandt¹³³ was used, which is derived in the Chapter 2 on page 19 (Equation (2.12)).

$$E_F(d_C) = \frac{\epsilon_0 \epsilon_S \kappa E_{RC} - \sigma_C - \sigma_{RC}}{\epsilon_0 \epsilon_C}$$

with the inverse Debye length κ (Equation (2.3) on page 15) given as

$$\kappa^{-1} = \sqrt{\frac{\epsilon_0 \epsilon_C k_B T}{2 N_A e^2 I}}$$

as a function of the ionic strength (I).

The model is based on the work of Smith and White.¹⁷³ They trace back the change of the redox potential of an immobilized redox center to the potential drop at the SAM surface such that it “experiences” a different potential than the applied one.

The electric field is a function of the chain length of the SAM (d_C) as well as of the ionic strength ($E_F(d_C, I)$) of the system. The potential drop at the redox site is E_{RC} , the difference between E^0 of the adsorbed B1 species and the redox potential of the Cyt c in solution E_S^0 ($E_{RC} = E^0 - E_S^0$),¹³³ with the redox potential of the hh Cyt c in solution of $E_S^0 \approx 50$ mV vs. a Ag/AgCl (3M), which is nearly independent of the ionic strength.¹¹⁵ The negative shift of the redox potential for increasing ionic strength in solution is quantitatively so small (see Subsection 10.5.2) that we take this value as invariant for the calculation of the electric field. The redox potential of the Cyt c adsorbed on a C10 SAM are $E^0(60mM) = 20$ mV and $E^0(180mM) = 29$ mV and result in $E_{RC}(60mM) \approx -30$ mV and $E_{RC}(180mM) \approx -21$ mV (Table 10.1 on page 90). Note that the change in the redox potential here is quantitatively in the same order as measured elsewhere.¹⁵¹

The following values have been adopted from previous work.¹³³ ϵ describes the dielectric constants (index S stands for the value in solution/water ($\epsilon_S = 78$), C for the SAM ($\epsilon_C = 2.26$)) and σ are charge densities (index C describe the charge density at the carboxylate/protein interface and RC for the charge density on the redox center). The maximum value for σ_C is $\sigma_C^{max} = -0.816 \frac{C}{m^2}$ in the case for all carboxylate groups being effectively deprotonated and is therefore the lower limit of σ_C . At this point we assume σ_C to be $\approx -0.05 \frac{C}{m^2}$ at pH 7 and to be largely invariant with respect to the ionic strength, the potential and the SAM length. The value σ_{RC} (60 mM) is set to be $0.00287 \frac{C}{m^2}$ following the literature.¹³³ Since σ_{RC} is proportional to the surface coverage of the protein Γ_{prot} and the SERR spectroscopic signal in our experiments dropped with change to high ionic strength to $\approx 1\%$ of the signal at low ionic strength we can assume that the surface coverage also is only 1% of that of low ionic strength so that $\sigma_{RC}(180 mM) = 0.000287 \frac{C}{m^2}$. The other constants and values have the usual meaning (ϵ_0 – vacuum permittivity, k_B – Boltzmann constant, N_A – Avogadro constant, e – elementary charge, T – temperature).

Equation (2.12) is based on the model for the interfacial potential distribution described in Chapter 2.^{93,133} Since the Debye length is used, the limitations of the Debye-Hückel theory are coming into effect here. The protonation state and σ_C of the SAM at pH 7 (or any pH) may also change with ionic strength since counter ions can somehow compensate the effective charge density of the SAM. One should also keep in mind that the resulting E_F value is that on the SAM/solution interface and not that experienced at the heme center of the Cytc. But nevertheless the results should give a magnitude of the electric field and how it changes with changing ionic strength.

The total electric field at the interface was determined to be $E_F(60 mM) = 1.51 \times 10^9 \frac{V}{m}$ and $E_F(180 mM) = 1.47 \times 10^9 \frac{V}{m}$ which reveal a decrease in the electric field with higher ionic strength.

$$\Delta E_F = E_F(180 mM) - E_F(60 mM) = -4.18 \times 10^7 \frac{V}{m}$$

The change in the redox potential for the different ionic strength somehow compensates the effect the ionic strength has on the Debye length.

10.5. The effect of ionic strength on Cyt_c in the literature

10.5.1. Shift of the redox potential upon immobilization of hh Cyt_c

The negative shift of the redox potential of Cyt_c upon electrostatic binding to electrodes coated with negatively charged SAMs was well studied.^{93,133,151,173} Smith and White developed the theory of the interfacial potential distribution (see also Chapter 2 for further details, also used above for investigating the electric field effect in Section 10.4 on page 91).¹⁷³ It is argued that across the SAM monolayer a potential drop occurs, so that the immobilized protein exhibits a different potential than that applied to the electrode as reason for the negative shift of the redox potential of the Cyt_c.^{93,133,173} Accordingly, the potential experienced by the protein is therefore strongly dependent on the potential of zero charge of the metal (PZC).

A shift of the redox potential can on the other hand be understood as a differential stabilization of one of the redox states and a shift upon binding can only occur when there is differential binding of the different redox species.¹⁵¹ The negative shift of the redox potential of Cyt_c upon binding to anionic surfaces like carboxyl-terminated SAM indicate that the ferric Cyt_c binds more strongly than the ferrous form to the surface.^{96,151} This is logical since the ferric form displays a more positive net charge than the ferrous form of hh Cyt_c.

10.5.2. The influence of the ionic strength on the redox potential of Cyt_c in solution

In binding media, i.e. in buffer solutions with ions like phosphate and chloride that are able to bind to positive surface charges of Cyt_c, an increasing number of binding ions (with increasing ionic strength) in solution lead to a small decrease in the formal redox potential as shown by Gopal et al. They could further demonstrate, that chloride and phosphate bind more strongly to oxidized hh Cyt_c than to the reduced form, which has a stabilizing effect on the oxidized form over the reduced and therefore led to the small negative shift in the redox potential with increasing ionic strength.⁵² Also the opposite effect, i.e. an increasing redox potential with increasing ionic strength, has been found before.¹¹⁵

10.5.3. The influence of the ionic strength on the redox potential of immobilized Cytc

The opposite effect to the negative shift of the redox potential in hh Cytc in solution with increasing ionic strength (and more distinct) was found by Petrović et al. for the immobilized protein on electrodes coated with negative carboxylate-terminated SAM.¹⁵¹ This would mean an increasing stability of the reduced form in comparison to the oxidized form of hh Cytc. It was argued that upon binding to the negative charges of the SAM the net charge of the Cytc is reversed from positive to negative and therefore the effect of the ionic strength on the redox potential is also reversed in comparison to the protein in solution.

10.5.4. ET kinetics in relation to ionic strength

Yue et al. have shown that the standard electron exchange rate constant of hh Cytc decreased with increasing ionic strength of the solution.²⁰⁷

The explanation of the authors is that: "...The inhomogeneity of electrostatically immobilized Cytc increases with the increase of the solution's ionic strength [...]. A comparison of these different ET behaviours suggests that the thermodynamically stable geometry of Cytc in the electrostatic assemblies is also an electron transfer favourable one. It suggests that the surface charges of Cytc are capable of guiding it into geometries in which its front surface faces the electron-transfer partner. The inhomogeneity observed in this study indicates that a distribution of Cytc orientations and thus a distribution of ET rate constants exists." (Yue et al., 2006)²⁰⁷

It was argued that, since the apparent rate constants of covalently bound Cytc as measured in comparison was not affected by the changing ionic strength, "ionic strength changes the effective distance between the electrode and the protein for electrostatic assemblies [...]. If small buffer ions lodge between the protein and the electrode, then increasing the ionic strength will increase the percentage of Cytc molecules that have ions lodged between them and the negatively charged monolayer. Such ions could screen the electrostatic interaction and decrease the electronic coupling between Cytc and the SAM by increasing the effective distance." (Yue et al., 2006)²⁰⁷

Furthermore the authors²⁰⁷ compared their findings and that of Avila et al.¹² to those of other groups who studied the effect of the ionic strength on protein-protein complexes.^{60,66,161} "In all these cases, the redox partners form a stable ET complex whose geometry is not favourable for

ET so that a conformational gating step is a prerequisite for the ET. In this model, the gating step becomes easier as the ionic strength increases because it weakens their electrostatic attraction [...]. The [...] ionic strength dependence observed for the carboxylic acid-terminated SAMs suggests that the stable binding geometry of Cyt_c on the surface is also the favourable ET geometry. [...] The decrease in k^0 values with the increase in ionic strength likely results from increasing the effective distance between Cyt_c and the film. If the distance change causes a decrease in the rate because of the increased tunnelling distance, then the distance would need to increase by about 1.5 Å for an increase in ionic strength from 10 to 80 mM, assuming that the tunnelling probability decreases as $\exp(-1.1n)$ where n is the number of methylene groups.” (Yue et al., 2006)²⁰⁷

An additional finding of the authors is a voltammetric peak broadening with rising ionic strength for hh Cyt_c that is ascribed to “Cyt_c molecules in films that have different environments, leading to a range of k^0 values.” (Yue et al., 2006)²⁰⁷ The apparent rate constant would be then the conglomerate of the rate constants of Cyt_c molecules in different orientations.

10.6. Effect of increased ion concentration in solution on Cyt_c—Interpretation of the experimental findings

The experimental conditions under which the present results have been obtained are comparable to those of the experiments presented in the cited literature above. Petrović et al.¹⁵¹ and Yue et al.²⁰⁷ did cyclic voltammetry studies with hh Cyt_c electrostatically immobilized on a C15 SAM covered Au electrode in different ionic strength buffer solutions. In their work a 4.4 mM phosphate buffer, pH 7, was used and for higher ionic strength KCl was added. This is basically the same approach as in our measurements. The ionic strength varied between 10 mM and 80 mM while for our work we used 60 mM and 180 mM. The main differences between your experimental setup and the setup of Yue et al. and Petrović et al. were the electrode material, the SAM-length and the different ionic strength in our system. Furthermore, for the CV measurements the protein was not allowed to stay in the solution (as in our study), what could effect the dissociation and association behaviour of the Cyt_c in a different way. Regardless of the differences in the setup we obtained qualitatively the same results. Petrović et al. even reported quantitatively the same positively shifted redox potentials with increasing ionic strength as we found in our experiments.¹⁵¹ Yue et al. have shown

that the standard electron exchange rate constant decreased with the ionic strength of the solution.²⁰⁷

Our experimental findings presented in this chapter are in line with these results.^{151,207} The ET rates of electrostatically immobilized hh Cytc at carboxyl-terminated SAMs (C10) decreased with increasing ionic strength while the redox potential was positively shifted. The change in the apparent rate constants were small but clearly detectable. For our TR SERR measurements with applied overpotential the rate at higher ionic strength corresponds to a higher driving force than the rate at lower ionic strength since the redox potential is shifted to more positive values. Therefore the effect of smaller rate constants would be more pronounced at the same driving force.

Following the arguments discussed above we can explain our results of the upshifted redox potential and the slower rates for higher ionic strength accordingly. The shifted redox potential upon immobilization was explained as (I) an effect due to the potential drop across the SAM^{93,133,173} and as (II) a stronger binding of the ferric form to anionic surfaces.¹⁵¹ Both explanations have shown to be reasonable and therefore the shift of the redox potential upon immobilization is considered to be a combination of both effects.

The positive shift of the redox potential of hh Cytc with increasing ionic strength is ascribed to the specific binding of ions to the protein and therefore to a change in the protein's effective charge.¹⁵¹ Using the model of the interfacial potential distribution^{133,173} for the calculation of the electric field and taking the experimentally found shift in the redox potential at different ionic strength we evaluate a lower field strength at higher ionic strength. When ignoring the shifted redox potential the outcome would be reversed. As stated above, the change of the redox potential for the different ionic strength compensates the effect the ionic strength has on the Debye length and therefore on the electric field in the calculation. Here it is important to mention that the Debye-Hückel theory is valid for very diluted solutions and might not describe the present system properly. But nevertheless, it might be that the compensatory effect of the redox potential shift reduces consequences of electric field changes that are, for instance, brought about by changes of the transmembrane potential.

As shown above, the slower apparent rate constants for the "higher" ionic strength cannot be an effect of higher electric field restricting the reorientation of the Cytc in the system as it applies e.g. for shorter SAM length in comparison to longer ones (see Chapter 9).^{9,88,99} Even more, the fact that we obtain slower rates at higher ionic strength is remarkable since the effect of decreasing electric field is effectively compensated.

Previous findings in this work (Chapter 9) and other studies have shown that reorientation must take place for fast ET of Cyt_c and that the immobilisation of hh Cyt_c do not lead to a good orientation for direct ET. A change in electric field was found to be the reason for changing speed of reorientation and therefore changing ET rates. The view of a reorientation process of the Cyt_c being rate-limiting (at least for hh Cyt_c immobilized C5 SAMs) and a prerequisite for the effective electron transfer in the electrode/SAM/Cyt_c system is supported by experiments with covalently bound Cyt_c. Previous findings have shown that also in covalent SAM/Cyt_c complexes reorientation is not totally suppressed, and slower ET rates in these complexes are due to restricted movement. Also in covalent complexes the electron transfer takes place as a result of reorientation processes, low amplitude motions of the Cyt_c are enough to lead to effective ET. Reorientation occurs and is rate limiting also in covalent systems.⁹⁹

Using theoretical methods Alvarez-Paggi et al.⁸ could show that the surface domain of hh Cyt_c with the highest binding energies to SAMs with carboxylate headgroups is not the area with the highest electronic couplings. Therefore, Cyt_c is expected to bind strongly to the SAM surface over the so-called BD3 (binding domain 3) (see Figure 9.1 on page 60) and needs to reorient to high coupling orientations where additional lysines-SAM contacts over BD2 are established.⁷⁻⁹ Taking into account the different binding energies it is possible to argue that stronger binding interactions are not as easy to disturb as weaker binding interactions. If the ionic strength is now increased and thus the number of ions that compete with the surface lysines of the Cyt_c. Screening the electrostatic Cyt_c/SAM interactions is more efficient in the low affinity binding domain. In the case of Cyt_c it would mean that the reorientation is slowed down because the protein/SAM contacts of the lysines which are involved in the fast ET are weakened.

Part VI.

Cytochrome *c*—Changing Function from
Electron Transfer to Apoptosis

11. The Role of Cytochrome *c* in Apoptosis

11.1. Programmed cell death—Apoptosis

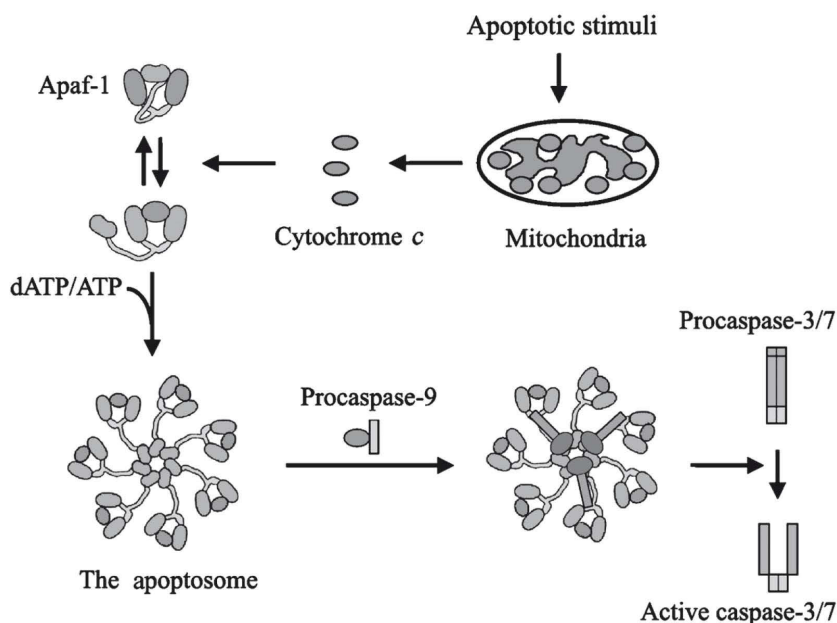
There are different mechanisms to terminate the life of cells, among them necrosis, senescence, and apoptosis. Apoptosis or programmed cell death enables a damaged or unwanted cell to self elimination and shows very unique and dynamic morphological features with a complex signalling pathway. In the end the so-called apoptotic body is formed which is then processed by the phagocytes and so possible inflammation reaction of the tissue is avoided.^{73,76}

A subfamily of cysteine proteases, known as caspases, is executing the apoptotic route. “Caspases are normally inactive [...]. During apoptosis, a procaspase is proteolytically cleaved to generate a small subunit and a large subunit, and two cleaved caspase molecules form a heterotetramer, which is the active form of the enzyme. [...] The proteolytic cleavage of a caspase can induce a dramatic conformational change that exposes the catalytic pocket of the enzyme, and therefore results in its activation. [...] [T]he activated executioner caspases cleave numerous cellular targets to destroy normal cellular functions, activate other apoptotic factors, inactivate anti-apoptotic proteins, and eventually lead to apoptotic cell death.”^{22,188} (Jiang & Wang, 2004)⁷³

There are different caspase activation pathways known in mammals. For one there is the cell surface death receptor mediated pathway which is initiated by extracellular hormones or antagonists like members of the tumour necrosis factor superfamily.⁷³ But also a dATP / ATP triggered caspase activation was found inside the cell in the cytosol. Two crucial components necessary for the dATP / ATP initiated caspase activation were identified as Apaf-1 (apoptotic protease activating factor 1) and cytochrome *c*.⁷³ From Apaf-1, Cyt c and dATP / ATP a large complex is formed, the apoptosome. “[A] model illustrating the detailed biochemical mechanism of Cyt c -induced caspase activation is presented in Figure [11.1] [...]. Upon sensing a variety of apoptotic stimuli, Cyt c is released from mitochondria and associates with the apoptotic mediator Apaf-1 [...]. After association with Cyt c , Apaf-1 switches from a rigid conformation to a more flexible one such that the nucleotide dATP / ATP

Figure 11.1.: The mechanisms of apoptosome formation and caspase activation initiated by cytochrome c release.

“Reprinted from *Annu. Rev. Biochem.*, 73, Cytochrome C-mediated apoptosis, X. Jiang and X. Wang, 87–106, Copyright (2004) *Annual Reviews.*”⁷³



binding activity [...] is greatly facilitated. Binding of dATP/ATP in turn triggers formation of the active, seven-span symmetrical complex, the apoptosome, via interaction among the N-terminal [...] domains of the individual Apaf-1 molecules. The apoptosome subsequently recruits procaspase-9 into its central [...] region [...], and a conformational change of the enzyme is induced. Therefore caspase-9 and the apoptosome form an active holoenzyme to activate downstream executioner caspases, such as caspase-3 and caspase-7, which eventually lead to programmed cell death.” (Jiang & Wang, 2004)⁷³

There are many proteins known to take part in the inhibition or activation of caspase activity inside and outside the mitochondrion but it is until now not well understood how exactly the change in the function of Cyt c is triggered and what changes the protein undergoes in the process. A prerequisite to promote apoptosis is the release of Cyt c from the mitochondrion where it carries out its normal ET function in the respiratory chain (see Figure 8.1 on page 58). The protein release has to be precisely regulated. Pore forming proteins interacting and being regulated by mitochondria specific lipids, as cardiolipin, and proteins are found to be in charge of the Cyt c release into the cytosol.^{73,182}

11.2. Cytochrome c and cardiolipin

Many heme proteins exhibit peroxidase activity. Very effective heme peroxidases like horseradish peroxidase depend on histidine and arginine residues in the distal heme pocket and on the presence of a histidine as fifth iron ligand. The histidine and arginine participate in the so

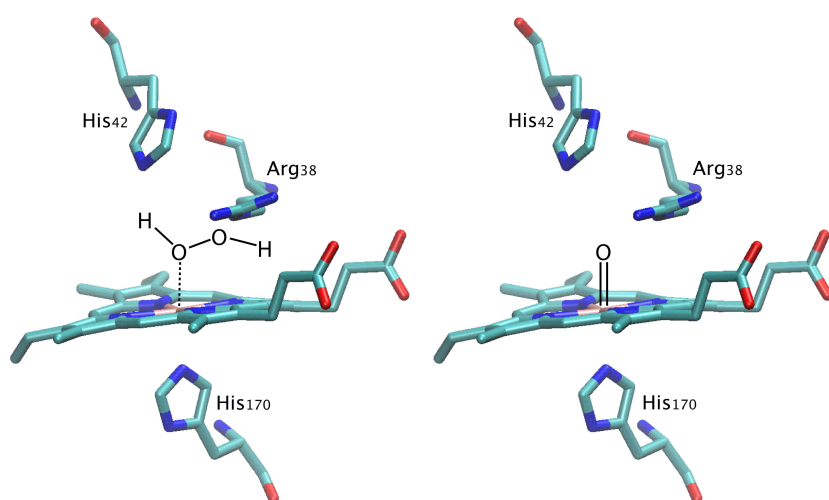


Figure 11.2.: Catalytic mechanism of horseradish peroxidase. Left: Ferric heme (Fe^{3+}) with H_2O_2 bound as a ligand in the sixth coordination position of iron. Right: Oxoferryl iron and porphyrin-centered radical ($\bullet Fe^{4+}$, compound I). Protein Data Bank ID code 1h5m. Similar to figure from Kagan et al., 2009.⁷⁵

called “push-pull” mechanism for the catalytic cleavage of H_2O_2 (Figure 11.2).^{17,75}

Mammalian Cyt c has a potential peroxidase activity but the compact tertiary structure of Cyt c in solution, in its hexacoordinated low spin configuration, prevent the catalytic activation of the heme iron by peroxides.¹⁵ Furthermore the “lack of Arg and His residues in close proximity to the heme [...] [and the] remote location of electron-accepting Trp or Tyr residues [...] decrease the occurrence of peroxidase functions in native [...] [Cyt c].” (Kagan et al., 2009)⁷⁵

Interactions of Cyt c with the anionic phospholipid cardiolipin (CL), induces changes in the structure of the Cyt c where H_2O_2 , which is generated in the early stages of apoptosis, or other peroxides have access to the heme center and triggers the peroxidase activity.^{15,76} About 15 % of the mitochondrial Cyt c is bound tightly to CL and does not participate in ET.^{67,169} Probably two acyl chains of CL intruding in Cyt c ¹⁶⁹ but also other binding situations have been proposed.^{67,75,147} The weakening of the Fe-Met80 bond upon CL binding is concordantly approved

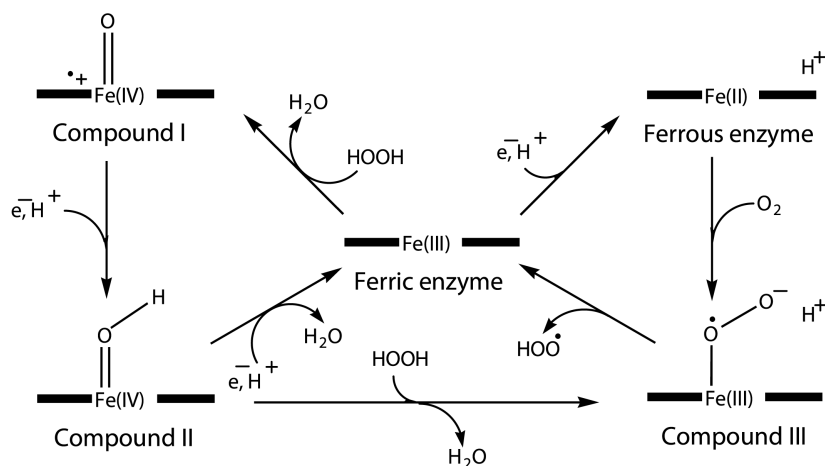


Figure 11.3.: The five oxidation states of horseradish peroxidase. Similar to figure from Berglund et al., 2002.¹⁷

by many^{75,76,140,169} and indicate an opening of the heme crevice with enlarged accessibility for small molecules. It was suggested by Sinibaldi et al. that this methionine is replaced by a lysine residue like it is found in the alkaline transition (see Subsection 11.3.1).^{169,170} Upon breaking the Fe-Met80 bond the redox potential of the Cyt c in the complex with CL is enormously negatively shifted (≈ -400 mV) and the ET in the respiratory chain becomes unfeasible.^{15,75}

Cyt c bound to cardiolipin functions as a CL specific peroxidase.⁷⁶ The peroxidation products of CL interacting with specific proteins leading to a permeabilization of the mitochondrial membrane, called mitochondrial outer membrane permeabilization (MOMP).¹⁸² Moreover the affinity of Cyt c to nonoxidized CL is much higher than for the oxidized form.^{76,147} The oxidation of CL is therefore required for release of the mitochondrial Cyt c into the cytosol and consequently Cyt c regulates its own release.⁷⁶ “CL oxidation is required for both [...] [Cyt c] detachment from the inner mitochondrial membrane and for permeabilization of the outer membrane followed by the release of [...] [Cyt c] into the cytosol.” (Kagan et al., 2005)⁷⁶ CL is the only mitochondrial phospholipid known that undergo peroxidation during apoptosis.⁷⁶

CL accounts for 25 % of all phospholipids in the inner mitochondrial membrane (IMM) and is almost exclusively found there in normal functioning cells. 60 % of it is confined to the inner leaflet (matrix side) of the IMM. The CL content in the outer mitochondrial membrane (OMM) in apoptotic cells is largely increased (up to 40 %) and also the distribution of CL in the IMM is changed. 70 % of the CL in the IMM is located in the outer leaflet (facing the intermembrane space). More CL becomes available for Cyt c due to the redistribution of CL during apoptosis. The reorganisation of CL seem to be important for the apoptotic pathway.^{15,75,76}

11.3. Regulatory instruments for Cyt c tuning

The molecular circumstances that push Cyt c to change function and the exact mechanisms of the transition are unknown. But a few possible regulatory instruments have been found in Cyt c .

11.3.1. Alkaline Transition

The alkaline transition is a conformational change in the native Cyt c where the Met80 is replaced by a lysine residue (probably Lys72/73/79) as axial ligand.^{204,205} The mechanism and the deprotonation process

which triggers the transition is not yet understood and the relationship of the pro-apoptotic conformation with increased peroxidase activity and the the alkaline transition in Cyt_c is not completely clear. But it was proposed, “that the alkaline conformational transition may serve as a protective mechanism against Cyt_c abnormal enhancement in peroxidase activity and adoption of the apoptotic route.” (Ying et al., 2010)²⁰⁴

11.3.2. Posttranslational modifications of Cyt_c tyrosines

The knowledge about posttranslational modification and the resulting signalling pathways of proteins in vivo is poor since the modifications get lost in the normal isolation methods.⁶⁷ Due to developments in the methodology more and more sites of posttranslational modifications are found in proteins. For example posttranslational modifications of the Cyt_c tyrosines are now known to play a regulatory role for the function of Cyt_c.

Tyrosine nitration is a result of oxidative stress, induced by different NO species.^{69,82,101,126} Upon this nitration the peroxidase function of Cyt_c was found to be increased as the Fe–Met80 bond was weakened.^{49,71,101}

Posttranslational phosphorylation on Cyt_c tyrosines was also observed. Two tyrosine phosphorylation sites have been found in bovine Cyt_c, Tyr97^{94,149,206} in bovine heart and Tyr48^{149,206} in bovine liver. It was indicated especially for the phosphorylated Tyr48, that the Fe–Met80 bond is altered and the respiratory chain is interrupted, e.g. the interaction with the CcO is inhibited.²⁰⁶ Kagan et al. suggested that phosphorylation of tyrosine in Cyt_c hinder the interactions with CL.^{67,75} It was suggested that tyrosine residues of the Cyt_c are involved in the peroxidation process of the CL and that therefore the peroxidase activity is tuned down by tyrosine phosphorylation.⁶⁷ It is noteworthy that the Tyr48 and 97 are highly conserved in eukaryotes.^{48,67} The positions of Tyr48 and 97 are depicted in Figure 12.1. All these findings hint on an important role of Cyt_c tyrosine phosphorylation as a central mechanism to regulate the functions of Cyt_c in a distinct tissue-specific manner.⁶⁷

In Cyt_c mainly the tyrosines are effected by posttranslational nitration and phosphorylation. Both modifications alter the protein structure and function but nitration only happens in stressed cells where phosphorylation also appear in normal cells.⁴⁸

12. Tyrosine Phosphomimetic-Mutations of Human Heart Cytochrome *c*

Understanding the effects of the phosphorylation of tyrosines in Cyt c , on the structure and stability of the heme, is the main goal of my work presented in the following chapter. Aiming on the elucidation of how the active site of human heart cytochrome *c* (huh Cyt c) is altered upon tyrosine phosphorylation, the tyrosines which were found to be phosphorylated in vivo (Tyr48 and 97)^{94,149,206} in bovine liver and heart respectively were altered by point mutations in huh Cyt c , since in vitro phosphorylation of distinct sites is not accomplished yet. The mutants of huh Cyt c were provided by the group of Prof. Miguel A. De la Rosa from the *Institute of Plant Biochemistry and Photosynthesis (IBVF)*, joint center of the *National Research Council Spain (CSIC)* and the *University of Seville*.

To mimic the phosphorylation tyrosine-to-glutamic acid and tyrosine-to-phenylalanine mutations in the position 48 and 97 were employed as well as a single point mutation of Tyr48 to the non canonic amino acid pCMF (para-carboxymethyl-L-phenylalanine). The different variants were used to distinguish between the effects of changing the phenolic ring to a phenyl group and to replace the ring by a charged linear amino acid as well as a combination of both. With respect to size and charge the Y48pCMF mutant is considered to be an approximation of a phosphorylated tyrosine.

12.1. Mimicking tyrosine phosphorylation?—Tyrosine mutations of Cyt c in the literature and functional data

While studies on the Y48pCMF mutant of Cyt c have not been reported, the Y48E mutant (from human⁴⁸ and bovine¹⁴⁹ heart) was considered to be an adequate candidate to mimic tyrosine phosphorylation. It is reported to exhibit a negatively shifted redox potential, impaired downstream caspase-3 activation,^{48,149} lower affinity towards CL¹⁴⁹, decreased peroxidase activity (only inducible at high CL concentrations)¹⁴⁹ and an alkaline transition pK $_a$ shifted to neutral pH values.⁴⁸ These findings fit to the experimental results of the isolated bovine heart Cyt c

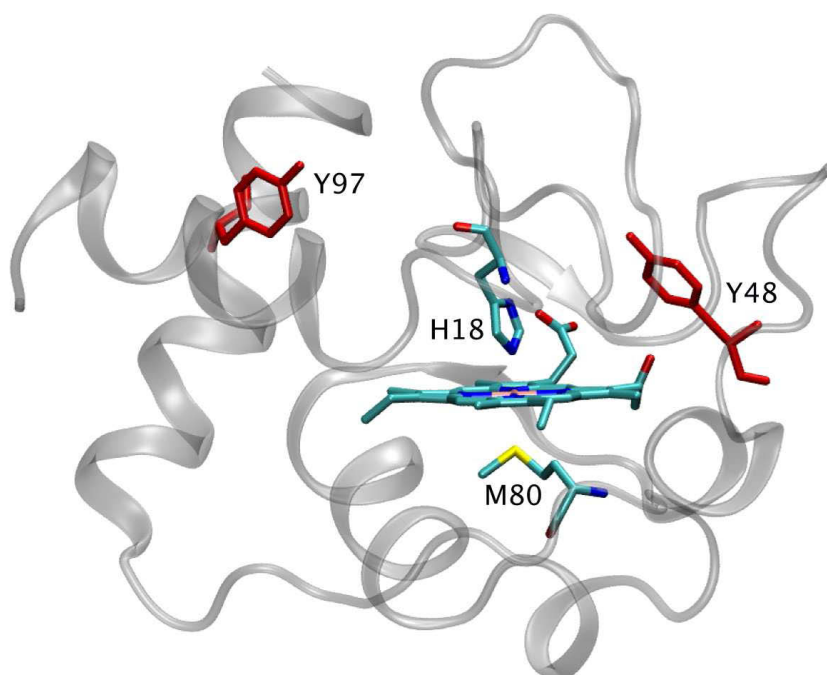


Figure 12.1.: Crystal structure of human heart cytochrome *c* with the Tyr48 and 97 depicted in red and the heme with its axial coordination in the center. Protein Data BankID code 1j3s.

that is *in vivo* phosphorylated at Tyr48 with respect to the interruption of the respiratory chain²⁰⁶ and the hindered interactions with CL.⁷⁵

The Y97E mutant was found to be less stable than the WT protein but shows similar behaviour in terms of alkaline pK_a and redox potential⁴⁸ like the WT, Y48F and Y97F mutant. Slightly lower activation of caspase-9 by the Y97E, Y48F and Y97F variants was found in comparison to the WT.⁴⁸

Functional data for the *huh* Cyt c variants were provided by the group of Prof. Miguel A. De la Rosa. All information shown below about the E and F variants and some of the data on the WT were taken from García-Heredia et al. (2011).⁴⁸ The data for the Y48pCMF variant and some of the values of the WT are yet unpublished.

Functional characterization of the Y48pCMF vs. the WT *huh* Cyt c revealed that the efficiency of the electron transfer is lower in the mutant, it shows less caspase activation, binds better to CL and shows higher

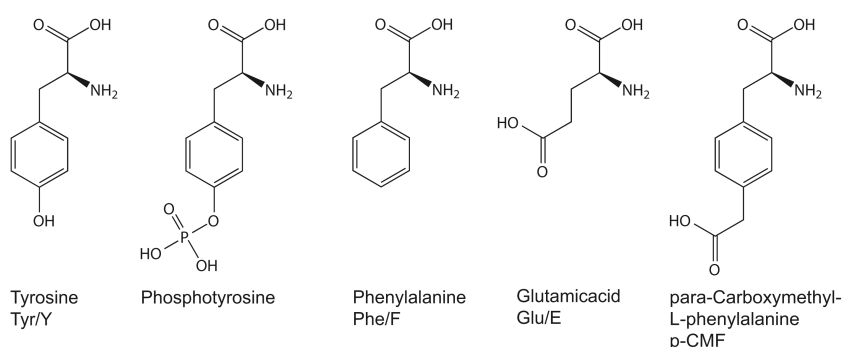


Figure 12.2.: Amino acid structures, names and abbreviations.

pH	E ⁰ (mV)				
	WT	Y48pCMF	Y48E	Y48F	Y97E
5.5	59	8			
7	57	-1	-23	33	53
8	51	-33			

Table 12.1.: Redox potentials of the provided huh Cytc variants except for the Y97F mutant. All redox potentials are given against an Ag / AgCl (3M) ref. electrode with a potential of -210 mV vs. a NHE and taken from García-Heredia et al. (2011)⁴⁸, except for the values of the Y48pCMF variant and the WT values for pH 5.5 and pH 8. These values are unpublished.

peroxidase activity (unlike the Y48E mutant), free or CL bound, than the WT protein.

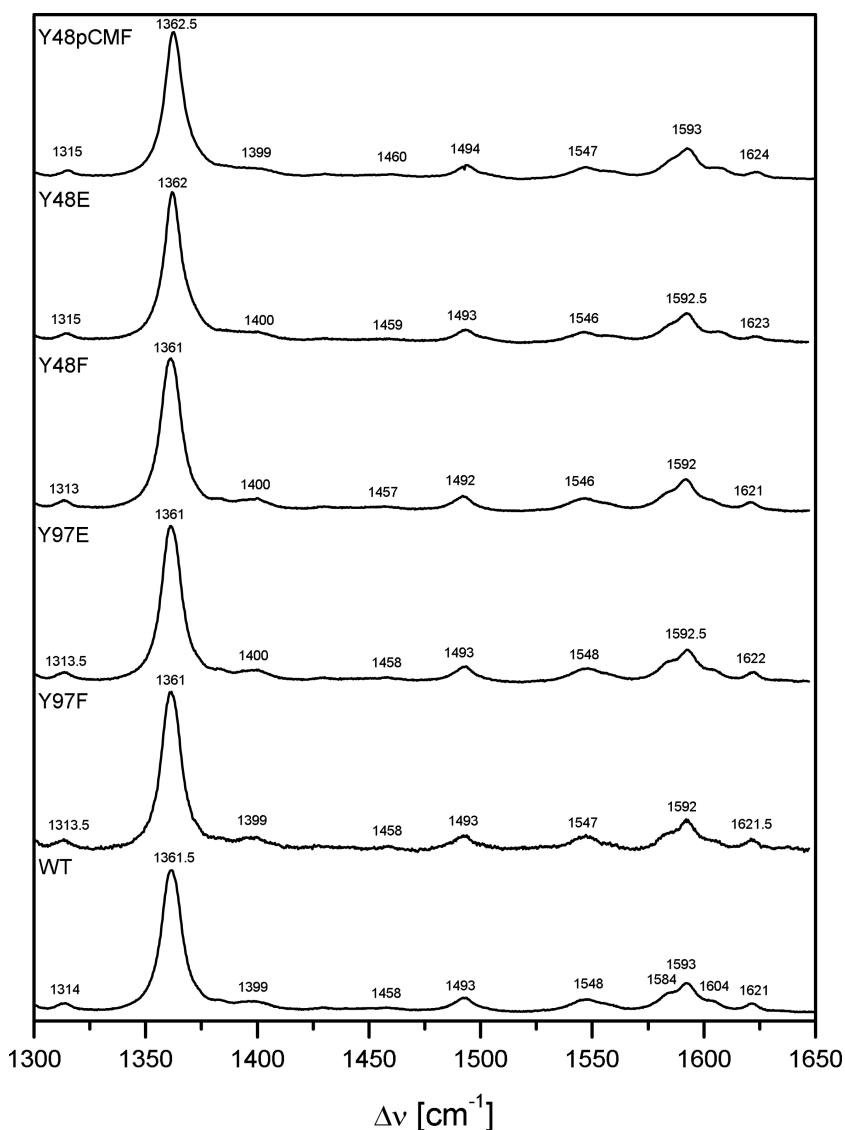
12.2. Comparison of the RR experimental results of the huh Cytc Y-variants

Resonance Raman spectra of the proteins in solution were measured with 413 nm excitation. Chemical oxidation and reduction did not always result in the pure ferric and ferrous forms of the various huh Cytc variants. For further information on the procedures see Chapter 6 on page 43. To obtain the pure spectra, the raw spectra of the “ferric” and “ferrous” species were mutually subtracted on the basis of the characteristic marker bands. In this sense, many spectra shown in this section are difference spectra of the various mutants. All band positions mentioned in the following text are those of the WT (unless noted otherwise) and all shifts in the mutant spectra refer to these band positions. In no case, there was an indication for a degradation of the sample during the RR experiment. However, some photo-reduction occurred in a few cases. The comparison of the WT and the Y48pCMF mutant will be discussed in Section 12.3 on page 116 in greater detail. The RR measurements of the WT and Y48pCMF mutant, presented in Section 12.2 and 12.3, were supported by Jana Staffa.

Alkaline Transition pK _a	
WT	9.5
Y48pCMF	6.4
Y48E	7
Y48F	10.3
Y97E	9.6

Table 12.2.: Alkaline transition pK_a for the provided huh Cytc variants except for the Y97F mutant. All values are taken from García-Heredia et al. (2011)⁴⁸ except the value of the Y48pCMF variant which is unpublished.

Figure 12.3.: RR spectra of the reduced form of all measured huf Cytc mutants and the WT at pH 7 in the oxidation and spin state fingerprint region, obtained with 413 nm excitation wavelength.



12.2.1. Reduced species

There are only very few frequency differences in the spectra of the reduced huf Cytc variants both in the high (HF) and low frequency (LF) range.

The band pattern in the HF region (Figure 12.3) of all the variants is that of a native reduced B1 6cLS species (Met–Fe–His). In the LF region (Figure 12.4), which contains the out-of-plane modes, all spectra of the reduced mutants show a very similar band pattern below 450 cm^{-1} with only one slight difference for the mutants in position Y48. While for the WT and Y97 mutants the bands at 371 cm^{-1} and 379 cm^{-1} show the same intensity, the band at 379 cm^{-1} is slightly more intense in the Y48F and more distinctly intense in the Y48E and Y48pCMF mutant of the huf Cytc. Clearly detectable differences are found in the complex band structure at around 690 cm^{-1} for the Y48E and Y48pCMF mutants.

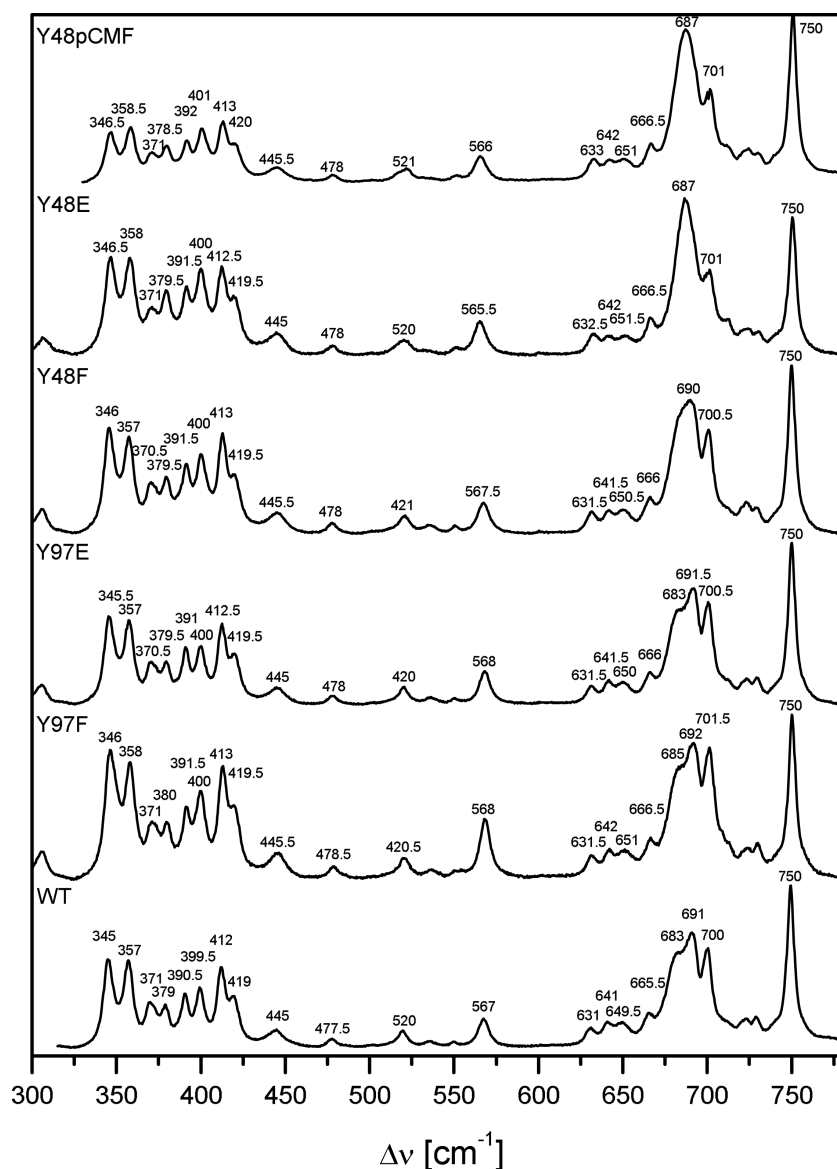


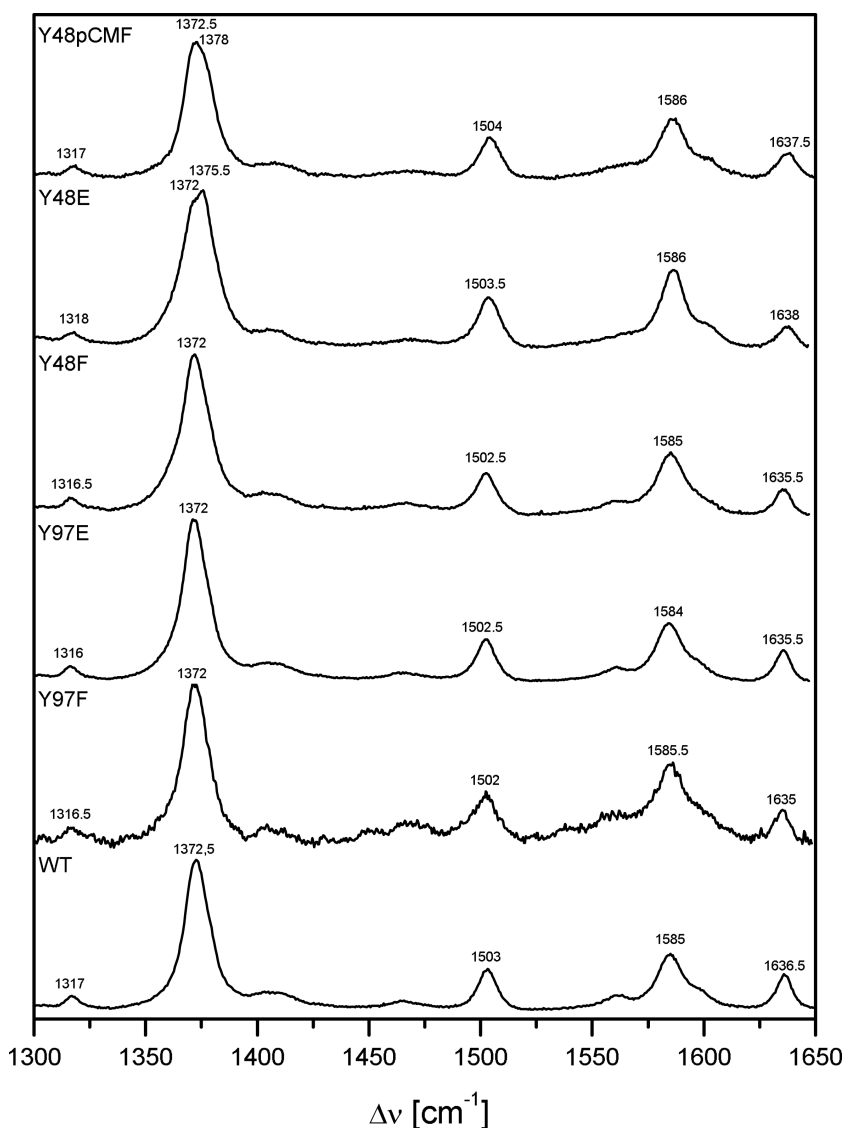
Figure 12.4: RR spectra of the reduced form of all measured heme Cytc mutants and the WT at pH 7 in the (axial) Fe ligand sensitive low frequency region, obtained with 413 nm excitation wavelength.

In the WT (and the Y97E/F and the Y48F) there is a strong band at 691 cm^{-1} with a shoulder at 683 cm^{-1} and a sharp band at 700 cm^{-1} . For the Y48E and Y48pCMF mutant we found a strong and broad band at 687 cm^{-1} and a smaller 701 cm^{-1} band than for the other variants.

12.2.2. Oxidized species

pH 7 In the HF region of the oxidized variants at pH 7 (Figure 12.5), the spectra all show similar bands at 1372 , 1503 , 1585 and 1636.5 cm^{-1} which is the band pattern of a native B1ox 6cLS Met-Fe-His coordination of the heme. In line with the low pK_a values of the alkaline transition of the Y48E ($= 7$) and the Y48pCMF ($= 6.4$) (see Table 12.2) we find an additional ν_4 -band at $1375.5/1378\text{ cm}^{-1}$ in the Y48E and Y48pCMF which is indicative of an “alkaline”-like species (as discussed below).

Figure 12.5.: RR spectra of the oxidized form of all measured huf Cytc mutants and the WT at pH 7 in the oxidation and spin state fingerprint region, obtained with 413 nm excitation wavelength.



In the LF region (Figure 12.6), the intensity ratio of the 348.5 cm^{-1} band to the band pair 397.5 cm^{-1} and 412.5 cm^{-1} changes from approximately 3:2 in the Y48F, Y97E, Y97F and the WT to 1:1.4 in Y48E and to 1:1 in Y48pCMF. Overall, the Y48E mutant at pH 7 (Figure 12.6) shows a similar spectrum to that at pH 12 (Figure 12.8) where a “alkaline”-like form is supposable dominant. In comparison the Y48pCMF spectrum at pH 7 seem to be a mixture of this “alkaline”-like form and another form, which can be identified from the HF region as the 6cLS Met–Fe–His species and is dominant in the pH 7 spectra of the other variants.

The 568 cm^{-1} band is much smaller for the Y48E and a bit smaller in the Y48pCMF than in the other mutants and the WT. Together with the finding that in the Y48F, Y97E, Y97F mutants and the WT the 702 cm^{-1} band is more intense than the 689 cm^{-1} band and that for Y48E and Y48pCMF this intensity ratio is reversed, this supports that the main spectral differences arise from different contributions of the

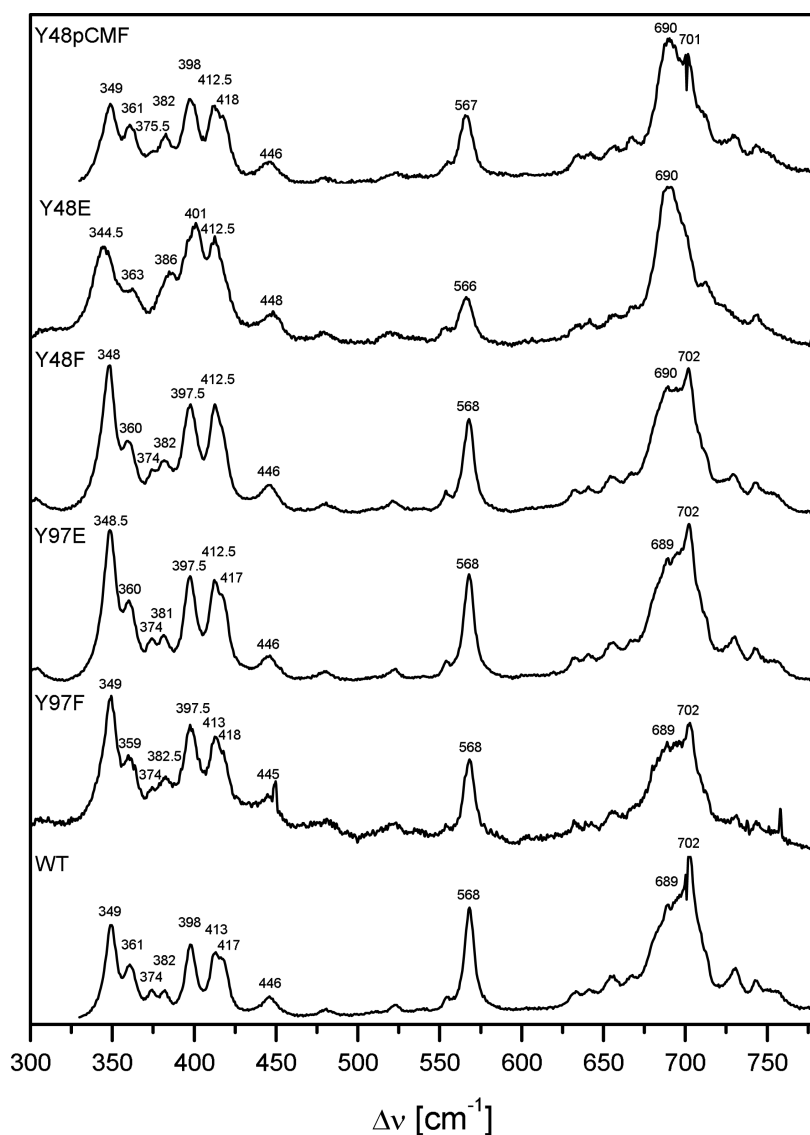
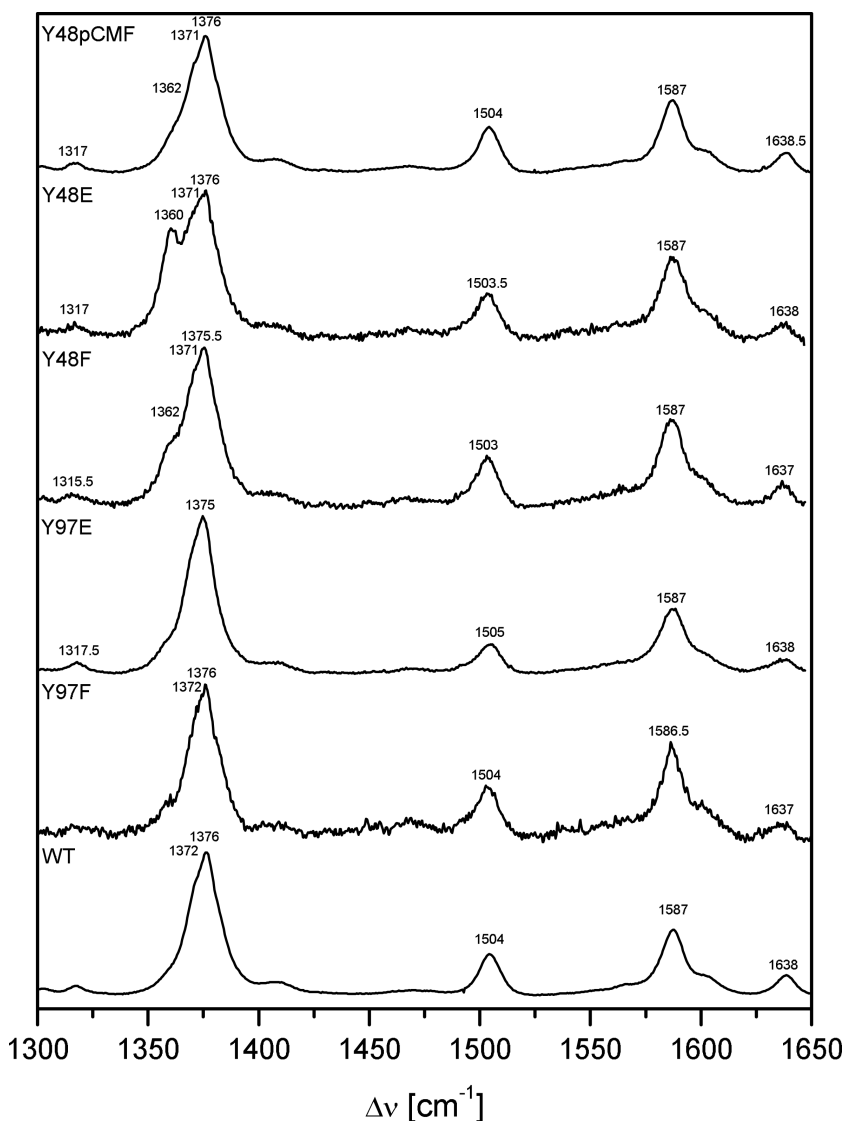


Figure 12.6.: RR spectra of the oxidized form of all measured huf Cytc mutants and the WT at pH 7 in the (axial) Fe ligand sensitive low frequency region, obtained with 413 nm excitation wavelength.

“alkaline”-like form of the heme. An intensification of the 689 cm^{-1} band in comparison to the 702 cm^{-1} band in combination with a reduced intensity of the modes between 440 and 670 cm^{-1} is reported to be an indicative of a Lys–Fe–His coordination of the heme iron.^{168,169}

pH 12 Figures 12.7 and 12.8 show the RR spectra at pH 12 in the ferric form. All variants should have underwent the alkaline transition at this pH (the pK_a values of the alkaline transition can be found in Table 12.2 on page 109), but it is unpredictable how the protein is adapting to this harsh pH. In yeast Cytc the alkaline conformation gets exchanged again to a His–Fe–OH axial coordination at a pH as high as 12. But nevertheless the Met→Lys replacement typically lead to upshifted bands in the HF-region, with a ν_4 band at $\approx 1376\text{ cm}^{-1}$ and a ν_3 band at $\approx 1505\text{ cm}^{-1}$ which can be found in all the HF spectra at pH 12. The LF spectra at

Figure 12.7.: RR spectra of the oxidized form of all measured huf Cytc mutants and the WT at pH 12 in the oxidation and spin state fingerprint region, obtained with 413 nm excitation wavelength.



pH 12 show a very unique fingerprint between 330 and 450 cm^{-1} . This pattern is typical for the alkaline form of the heme.⁴¹

In general, the overall band pattern is quite similar for all species in the HF region (Figure 12.7) and mainly show band positions that are consistent with a 6cLS species with a His–Fe–His or His–Fe–Lys (alkaline) coordination.^{101,135,145,163} However, in some of the variants there is still a considerably contribution from a reduced species reflected by the band at ca. 1362 cm^{-1} , which could not be subtracted and which nature could not simply be identified by this band. It is also obvious that the spectra consist not only of the oxidized “alkaline”-like form but of different oxidized species in varying amounts which, however, cannot be identified. An B1 6cLS species (Met–Fe–His) would be in line with the ν_4 band at 1372 cm^{-1} but also e.g. a (His⁻–Fe–Lys) or (His–Fe–OH⁻) heme species would give rise to a quite similar ν_4 band position. There

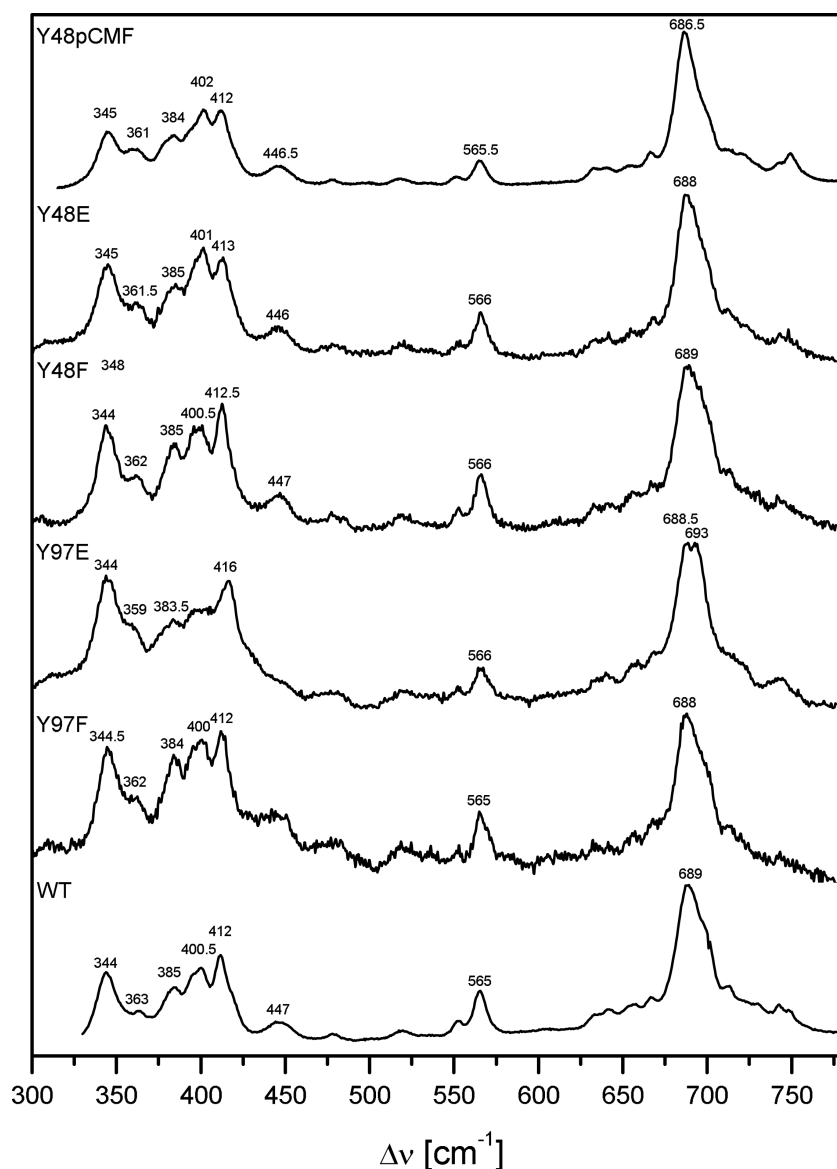


Figure 12.8.: RR spectra of the oxidized form of all measured huf Cytc mutants and the WT at pH 12 in the (axial) Fe ligand sensitive low frequency region, obtained with 413 nm excitation wavelength.

is no spectral indication that distinguishes the Y48E and/or Y48pCMF mutant spectra in the HF-region in comparison with the other variants.

In the LF region (Figure 12.8), we note again some differences for Y48E and Y48pCMF with respect to the other variants. Band intensities increase according to the bands at $384.5 < 412 < 400 \text{ cm}^{-1}$ in comparison to the others proteins where the intensity varies according to the bands at $384.5 < 400 < 412 \text{ cm}^{-1}$. For the Y97E mutant the 412 cm^{-1} band is shifted to 416 cm^{-1} , the bands at 362 and 384.5 cm^{-1} are down shifted, together with an appearance of a clear band at 693 cm^{-1} which is only present as a shoulder in the other variants. The very unique fingerprint of the alkaline form⁴¹ could be found for all variants in the LF-region between 300 and 425 cm^{-1} , with a down shifted ν_8 at about 344.5 cm^{-1} , an increased intensity of the 412 cm^{-1} band¹⁷⁰ and a reduced intensity of the modes between 440 and 670 cm^{-1} (namely the 567.5 cm^{-1} band)¹⁶⁹

in comparison to a ox B1 6cLS species (see Figure 12.6, WT). Simply the different intensities of the 384.5, 400 and 412 cm^{-1} bands in the Y48E and Y48pCMF are not consistent with the “alkaline” form which was reviewed before.⁴¹ Apart from the small differences in the LF spectra discussed above the low frequency region show no indication of other spectral contributions than the “alkaline”-form.

12.3. The Y48pCMF *huh* Cytc variant vs. the WT

As shown above, mutations in the position of Tyr48 seem to be more prone to changes in the heme structure than mutations in the position of Thy97. These changes appear especially when the phenol ring of the Tyr carries charged substituents. Changing the Tyr97 to a charged amino acid (Y97E) does not lead to RR detectable changes in comparison to the WT.

The two mutants, Y48E and Y48pCMF, where the phenol ring was substituted by a carboxylic acid (carboxymethyl group) and a carboxymethyl-phenyl ring, respectively, display some similarities in contrast to the other variants and the WT protein, even though there are also some differences between the Y48pCMF and Y48E mutant. The similarities are evidently due to the additional charge in the vicinity of the heme. The Tyr-to-Glu mutation has been reported as a phosphomimetic mutation^{48,149} but in a sterical way the pCMF group should be a better representative for a phosphotyrosine. For this reason the Y48pCMF mutant of *huh* Cytc was investigated in more detail by RR spectroscopy to study the impact of the induced mutation on the heme crevice. The experimental work was supported by Jana Staffa.

Spectra of the chemically oxidized and reduced Y48pCMF variant and the WT were recorded for pH values at 5.8, 7, 7.4 (only for oxidized Y48pCMF), 9.5 and 12 (only for oxidized variants). Reproducibility was ensured. Only three species were found in the spectra of both Cytc variants, ascribed to the reduced and oxidized B1 6cLS species and an oxidized “alkaline”-like 6cLS form. The spectra of the reduced protein were largely independent of the pH, whereas for the oxidized protein the spectra showed differences depending on the pH and the alkaline transition could be detected. As in the previous section the protein could not always completely be reduced or oxidized. To obtain the pure spectra, the raw spectra of the “ferric” and “ferrous” species were mutually subtracted on the basis of the characteristic marker bands in the HF region. This approach not always let to complete abolishment of the “unwanted” species but the comparison was much easier. The

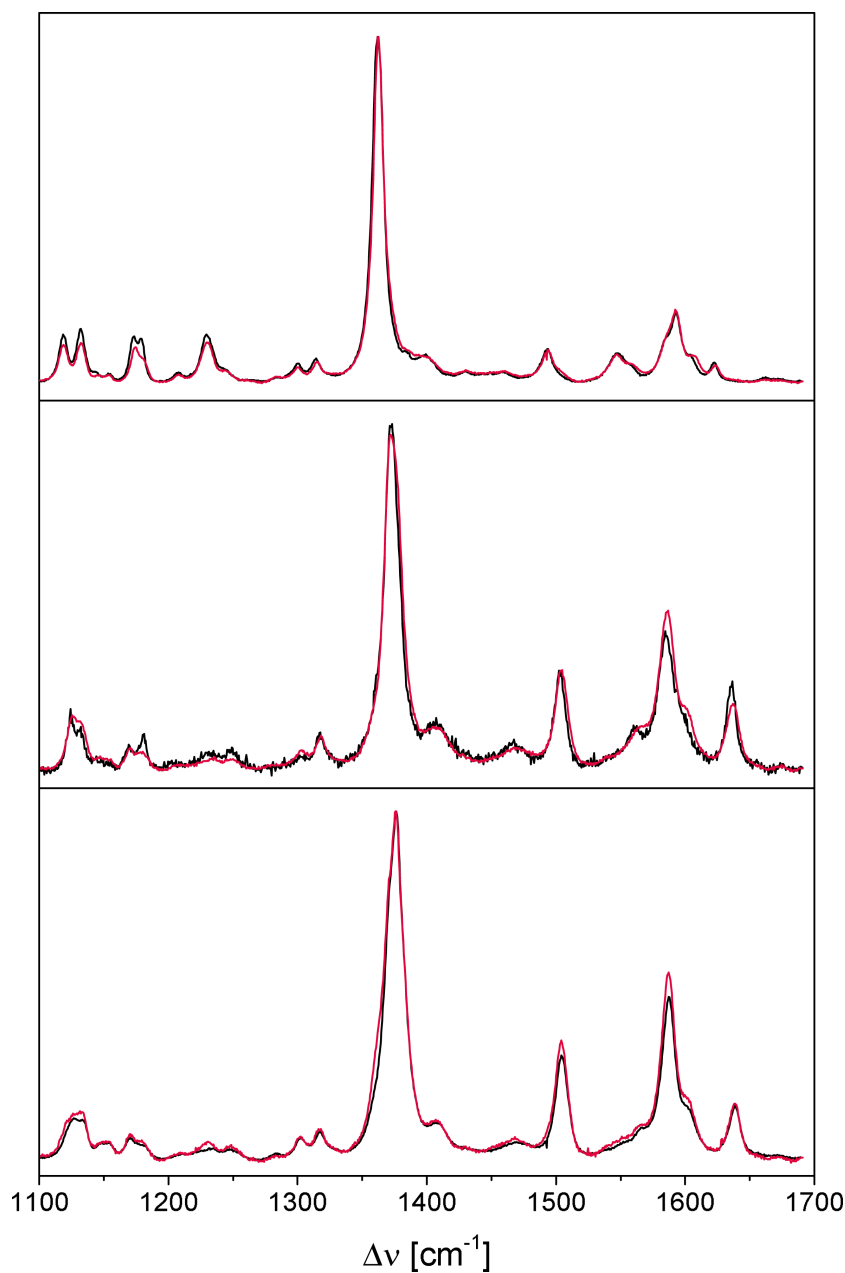
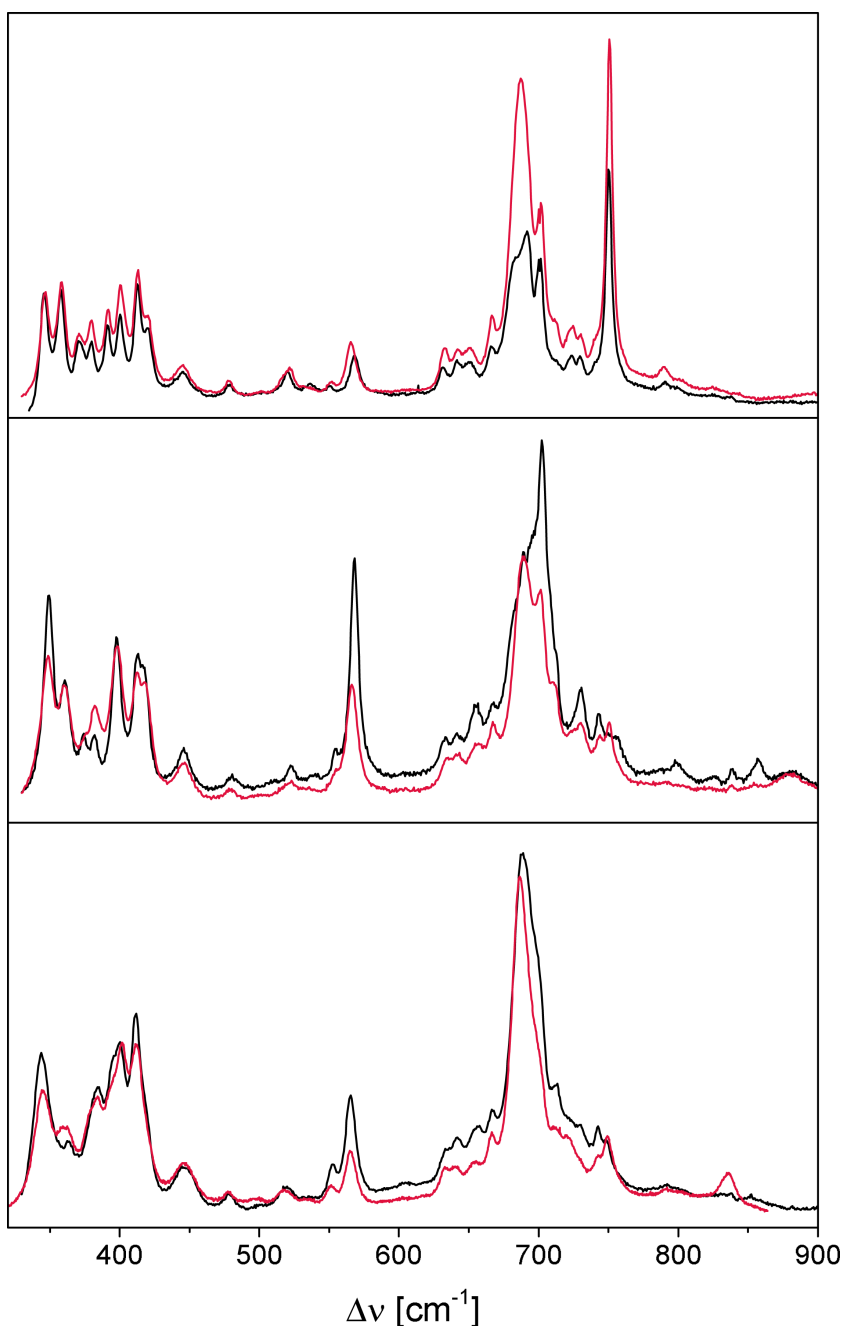


Figure 12.9.: High frequency RR spectra of the WT huf Cyt c in black and the Y48pCMF mutant in red in comparison, obtained with 413 nm excitation wavelength. Top: mainly reduced spectra of the WT and Y48pCMF at pH 7 in the B1 configuration of the heme. Middle: mainly oxidized spectra of the WT and Y48pCMF at pH 5.8 in the B1 configuration of the heme. Bottom: mainly oxidized spectra of the WT and Y48pCMF at pH 12 in the alkaline configuration of the heme.

subtraction procedure was not applied to the LF spectra since here the baseline correction and the background subtraction was not as consistent as in the HF region. Figure 12.9 and 12.10 show spectra of the Cyt c variants in different oxidation states and at different pH in the HF and LF region in comparison.

Reduced Cyt c sometimes appeared in the spectra of the oxidized Cyt c. It was either that there was not enough oxidation agent or it could be identified as photo-reduction products. The photo-reduction only occurred randomly but no sign of degradation or HS species could be detected.

Figure 12.10.: Low frequency RR spectra of the WT huf Cytc in black and the Y48pCMF mutant in red in comparison, obtained with 413 nm excitation wavelength. Top: mainly reduced spectra of the WT and Y48pCMF at pH 7 in the B1 configuration of the heme. Middle: mainly oxidized spectra of the WT at pH 7 and Y48pCMF at pH 5.8 in the B1 configuration of the heme. Bottom: mainly oxidized spectra of the WT and Y48pCMF at pH 12 in the alkaline configuration of the heme.



As discussed in the previous section there are small but clearly detectable differences in spectra of the WT and the Y48pCMF. The differences in the HF region are depicted in Figure 12.9. The spectra especially differ in the region $1100\text{--}1260\text{ cm}^{-1}$, which could be used for protein identification.

From the spectra in the LF region (Figure 12.10) recorded at pH 12 one can see that the alkaline like species of the variants are somewhat different. The differences are already shown in the previous section.

For detailed component analysis a set of three groups of Lorentzian bands in the HF region were generated for both Cytc variants independently.

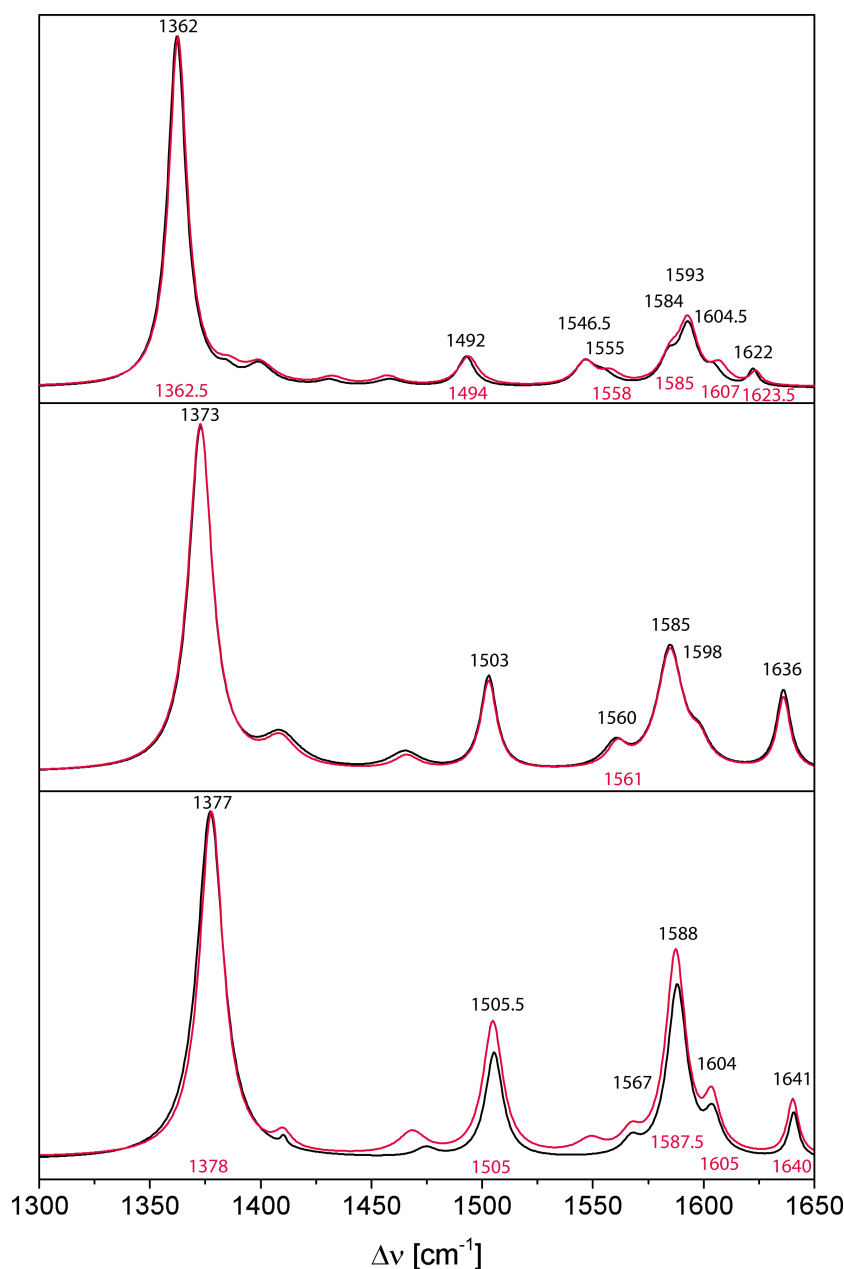


Figure 12.11.: Comparison of all component spectra, consisting of different groups of Lorentzian bands, which were necessary to rebuild all experimental RR spectra of the WT and the Y48pCMF mutant. In black the groups of bands found for the WT, in red the groups of bands found for the Y48pCMF mutant. Top: reduced B1 6cLS, middle: oxidized B1 6cLS, bottom: oxidized alkaline like bis-N 6cLS

With this three groups for each variant, it was possible, via a fitting procedure, to reconstruct all individual spectra for the different measurements of Y48pCMF mutant and the WT of huh Cyt_c. The groups for both variants differ only slightly and are depicted in Figure 12.11.

The oxidized and reduced form in huh Cyt_c which were readily identified, by band position and pattern, as the native B1 6cLS species slightly differ from the same species in hh Cyt_c. In comparison to the spectra of hh Cyt_c in Chapter 9 the band positions found for huh Cyt_c are partly upshifted by up to three wavenumbers. An upshift, especially in the core size marker region, between 1500 and 1650 cm^{-1} , is indicative of a conversion to a more planar heme in the human heart over the horse heart variant of Cyt_c.^{163,168,170} The differences between the WT and the Y48pCMF for

the B1 species in the core size marker region is marginal. The third group with the ν_4 band at $1377\text{--}1378\text{ cm}^{-1}$ was assigned to an alkaline like bis-N (Lys/His), probably His-Fe-Lys, coordinated Iron 6cLS species supported by the LF band pattern in the region of $320\text{--}430\text{ cm}^{-1}$.⁴¹

Although these three component spectra afford a satisfactory fit to the experimental spectra, the experimental data basis is too small to determine the individual component spectra with high confidence. Specifically, at high pH the residual amount of B1, albeit required for a mathematical group fit, is questionable and instead points to the involvement of another species that may bear some similarities to B1 but is of a structurally different nature.

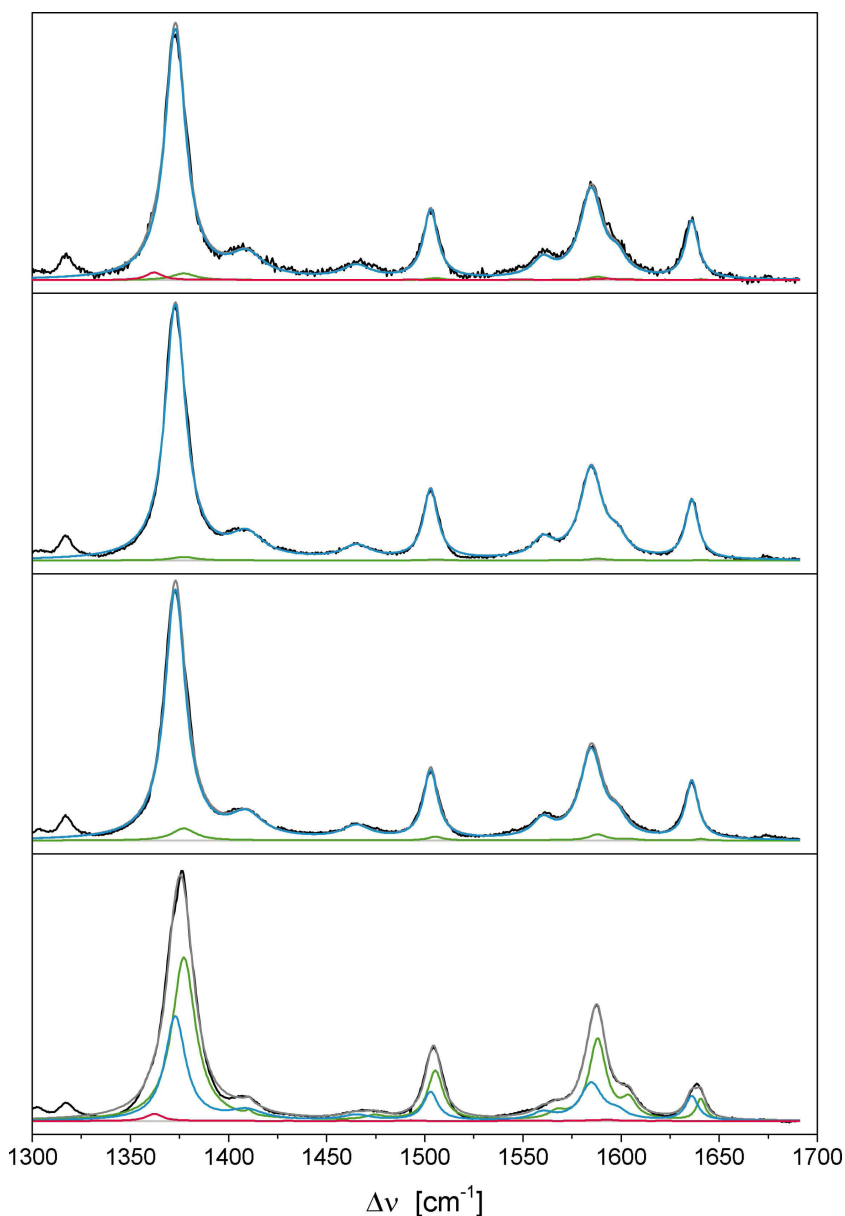


Figure 12.12.: Alkaline transition of the oxidized WT huhcc monitored by the changing spectral contribution of the B1 and alkaline conformation at different pH values. From top to bottom: pH 5.8, pH 7, pH 9.5, pH 12. In black the experimental spectra, the baseline depicted in light grey, the overall fit in grey, the reduced B1 species in red, the oxidized B1 species in blue and the alkaline species in green.

Alkaline transition The same component spectra for each variant could be used for the spectra analysis at the different pH values which implies that this bis-N coordinated 6cLS heme is unchanged with pH above the alkaline transition pK_a .⁴¹ Even though the two species found in the WT and Y48pCMF are not identical and differ especially in the LF region between 320 and 430 cm^{-1} .

Figure 12.12 and 12.13 show the oxidized spectra of the WT and the Y48pCMF at different pH values. When plotting the relative spectral

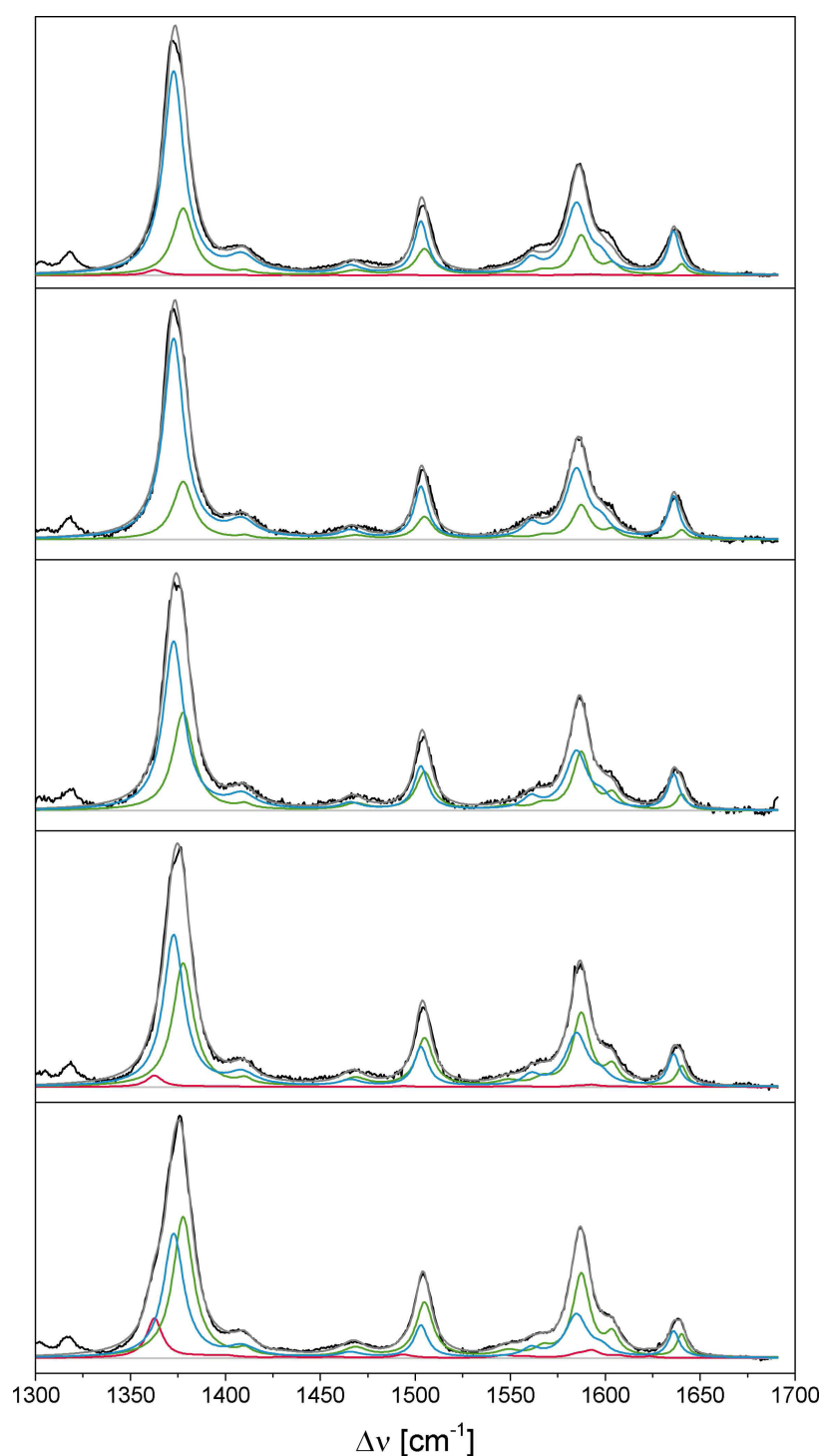
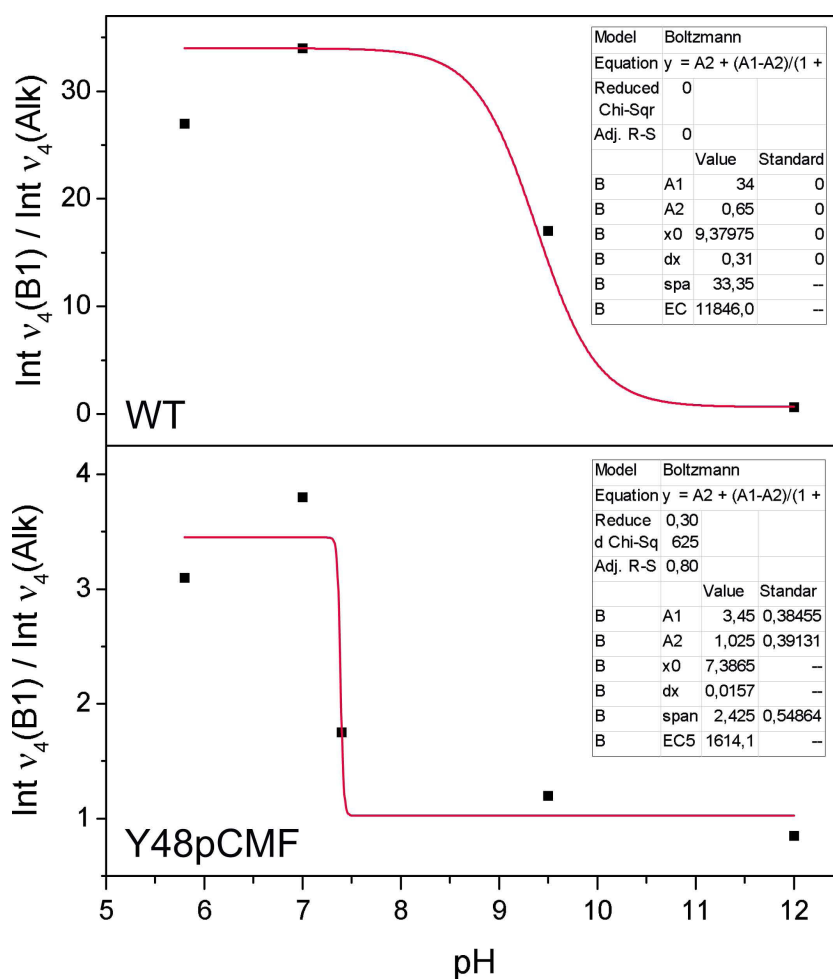


Figure 12.13.: Alkaline transition of the oxidized Y48pCMF mutant monitored by the changing spectral contribution of the B1 and alkaline conformation at different pH values. From top to bottom: pH 5.8, pH 7, pH 7.4, pH 9.5, pH 12. In black the experimental spectra, the baseline depicted in light grey, the overall fit in grey, the reduced B1 species in red, the oxidized B1 species in blue and the alkaline species in green.

Figure 12.14.: The intensity ratio of the ν_4 band of the oxidized B1 species vs. the ν_4 band of the oxidized alkaline species over the corresponding pH value as derived from Figure 12.12 for the WT and from Figure 12.13 for the Y48pCMF. The sigmoidal fit for each variant is shown in red.



contribution (intensity ratio of the corresponding ν_4) of the two different oxidized forms of both variants over the pH, one can apply a sigmoidal Boltzmann fit to the data (Figure 12.14).

With this approach the alkaline transition pK_a is determined to be at 7.4 for the Y48pCMF and at 9.4 for the WT when the underlying assumption is that the cross section of both species are the same. This values are in line with the data presented in Table 12.2 on page 109.

In the spectral analysis a considerably high proportion of the spectra is ascribed to the B1 species at high pH. As discussed above, presumably due to the harsh conditions, this is another species which show spectral similarities to the B1 species.

12.3.1. Conclusive picture of structure-property correlation in the Y48pCMF hnh Cytc?

The analysis and comparison of the RR spectra of the WT and Y48pCMF variant cannot reveal the origin of the enhanced peroxidase activity or the down shifted redox potential of the Y48pCMF mutant that are

reported above. The lowering of the redox potential by -60 mV, like for the Y48pCMF mutant, is often an indicative of an increased solvent accessibility of the heme and an opening of the heme crevice by losing the methionine as axial ligand and building a five or six coordinated high spin iron, these could also account for a higher peroxidase activity, but there is no hint in the spectra of the Y48pCMF of either of this coordination states.

12.4. Incorporation of the huh Cyt_c variants into liposomes

In Section 12.1 on page 107 it was reported that not only the peroxidase activity of the free and CL bound Y48pCMF is higher than in the WT but also the Y48pCMF binds better to CL vesicles. To analyze if the origin of this findings and the structural implications of the binding of the Y48pCMF to CL is RR detectable, I used a protocol developed in the group of Prof. Miguel A. De la Rosa (to ensure compatibility) to produce the liposomes and incorporate the WT and Y48pCMF huh Cyt_c into this vesicles containing CL. The liposomes consist of POPE (1-palmitoyl-2-oleoyl-sn-glycero-3-phosphoethanolamine) and CL (cardiolipin from bovine heart) (4:1) which are shown in Figure 12.15. The protocol can be found in Chapter 6 from page 43 of this work.

The experiments were conducted under reducing and oxidizing conditions at pH 5.8 and pH 7.4. The resulting RR spectra of the WT were identical to those of the free protein at the same pH. For the Y48pCMF only a very small difference was found; namely the ν_4 band is upshifted by about 1 cm^{-1} in the spectra of the reduced CL bound Y48pCMF mutant vs. the free one at both pH values. No other structural changes were detectable

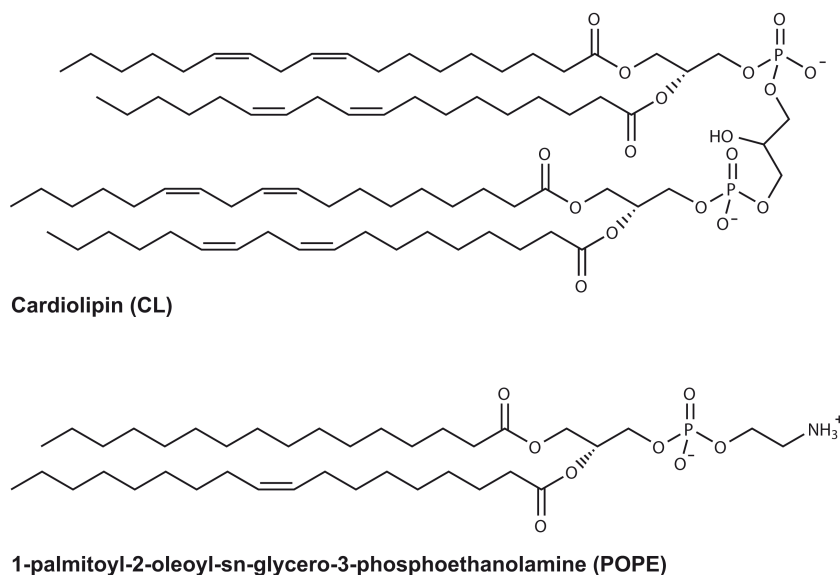


Figure 12.15.: Structures of the two phospholipids CL and POPE, used to build liposomes to incorporate WT and Y48pCMF huh Cyt_c.

in the HF and LF RR spectra upon incubation of the Cytc with the liposomes. The spectra could be fitted with the same component spectra as the free variants which made it impossible to identify and characterize CL-bound Cytc. This finding is in contradiction to literature data which show RR-spectroscopic changes upon Cytc–liposome binding^{168–170} (see also Section 11.2 on page 102).

However, an additional SEIRA experiment of Cytc with CL/POPE monolayers on the electrode under comparable conditions confirmed the binding of Cytc to CL (Jacek Kozuch, Jana Staffa and Enrico Forbig, personal communication).

Part VII.

CoFeSP—Electron Transfer and
Conformational Gating

13. Introduction of CoFeSP

13.1. The reductive acetyl-CoA pathway

Carbon is one very important energy source in cell metabolism. In the acetyl-CoA pathway of anaerobic bacteria and archaea, acetyl coenzym A is built effectively from CO_2 at consumption of adenosine triphosphate (ATP). Acetyl-CoA is then used in the citric acid circle where it gets oxidized for energy production. As shown in the scheme in Figure 13.1, a corrinoid iron-sulphur protein (CoFeSP) connects the methyl branch and the carbonyl branch of the reductive acetyl-CoA pathway, allowing the overall reduction and condensation of two molecules of CO_2 to activated acetic acid and further to biomass.^{51,119,154} This work is focused on CoFeSP and how it stays active for its central role in the acetyl-CoA pathway.

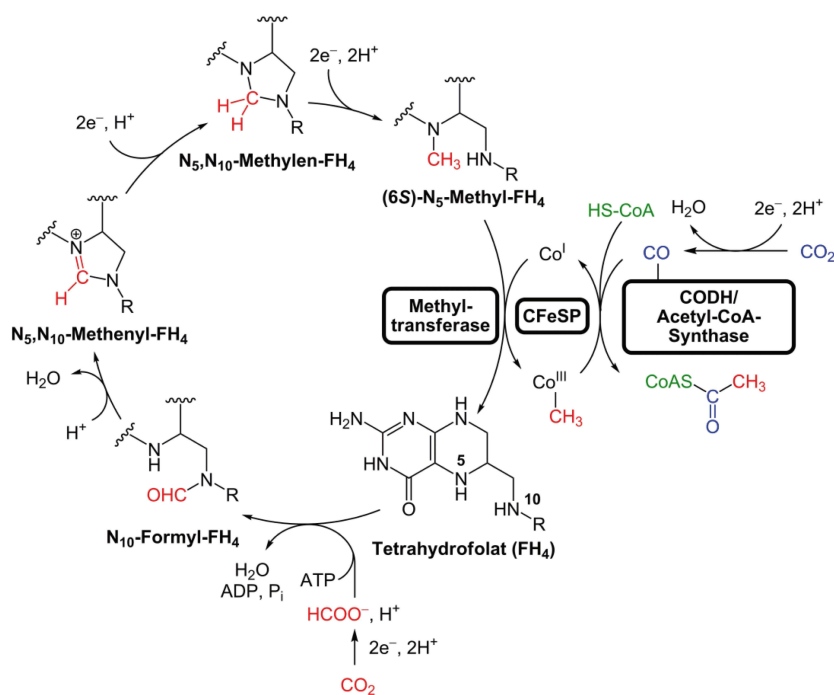
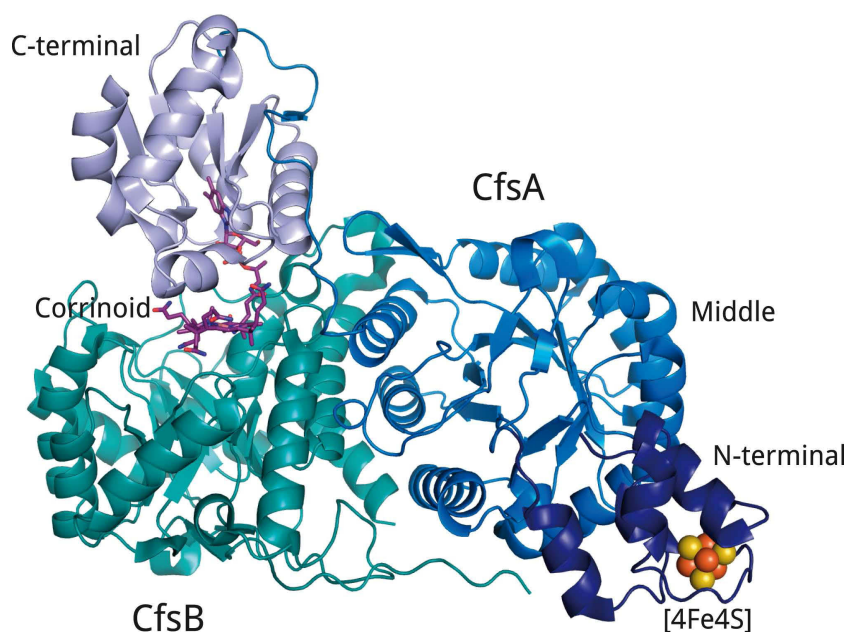


Figure 13.1.: Scheme of the reductive acetyl-CoA pathway of bacteria. Yikrazuul (2010). This picture is licensed under the Creative Commons Attribution-ShareAlike 3.0 Unported License. To view a copy of this license, visit <http://creativecommons.org/licenses/by-sa/3.0/> or send a letter to Creative Commons, 444 Castro Street, Suite 900, Mountain View, California, 94041, USA.

Figure 13.2.: Crystal structure of Co(II)FeSP with the small subunit (CfsB, cyan) and the large subunit (CfsA, blue) from the N-terminus (dark) with the [4Fe4S] cluster to the C-terminal part (light) with the cobalamin cofactor sandwiched between CfsB and the C-terminal domain of CfsA. Protein Data BankID code 2ycl.⁵¹



13.2. Structure and function of CoFeSP

Co(II)FeSP was characterized as a heterodimer (see figure 13.2) consisting of a large subunit (CfsA; 48.4 kDa) and a small subunit (CfsB; 33.9 kDa) only connected by H-bonds and electrostatic interactions.¹⁸¹ The C-terminal domain of the large subunit contains a Co β -aqua-(5,6-dimethylbenzimidazolcobamide) cofactor which is a corrin with a cobalt in the center of a cyclic system of four pyrrolic rings. It belongs to the group of cobalamins. This corrinoid cofactor is sandwiched between the subunit CfsB from the β -side and the C-terminal part of subunit CfsA from the α -side so that the periphery of the macrocycle is solvent exposed. As shown in Figure 13.3 a water molecule is bound to the cobalt as only axial ligand with a Co–O distance of 2.6 Å.⁵¹ This state with no protein ligand at the β -side of the cobalt ion is the so-called “base-off” state. On the α -side of the cobalt porphyrin plane the nearest atom is the oxygen of a threonine (Thr374) from the C-terminal domain of the CfsA subunit with a Co–O distance of 3.3 Å (also shown in Figure 13.3).^{51,181} As an additional cofactor a [4Fe4S] cluster shielded by hydrophobic amino acids is found in the N-terminal domain of the large subunit of CoFeSP.¹⁸¹ The distance of the two cofactors in the crystal structure is approximately 60 Å and the domains are quite flexible.⁵¹

The active forms of CoFeSP in the acetyl-CoA pathway are the Co(I) and Co(III)–Me states. In the Co(I)FeSP the cobalt is in the “base off” conformation like in the Co(II) state while in the Co(III)–Me state the

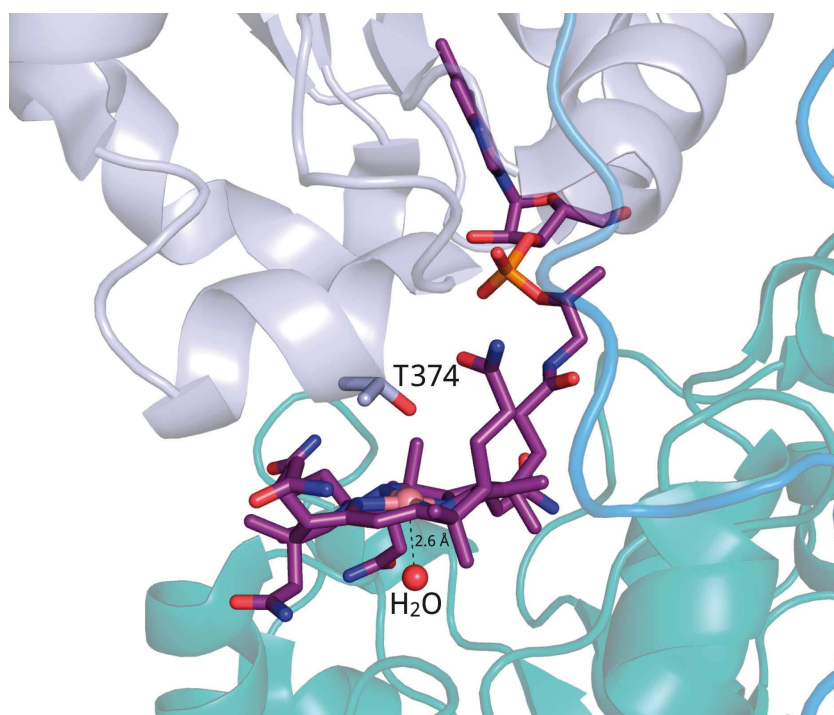


Figure 13.3.: Crystal structure of the cobalamin cofactor in Co(II)FeSP with the Thr374 of the C-terminal domain of the large subunit coordinating the cobalt from the α -side and the water depicted as red sphere in a distance of 2.6 Å coordinating the cobalt from the β -side. Protein Data BankID code 2ycl.⁵¹

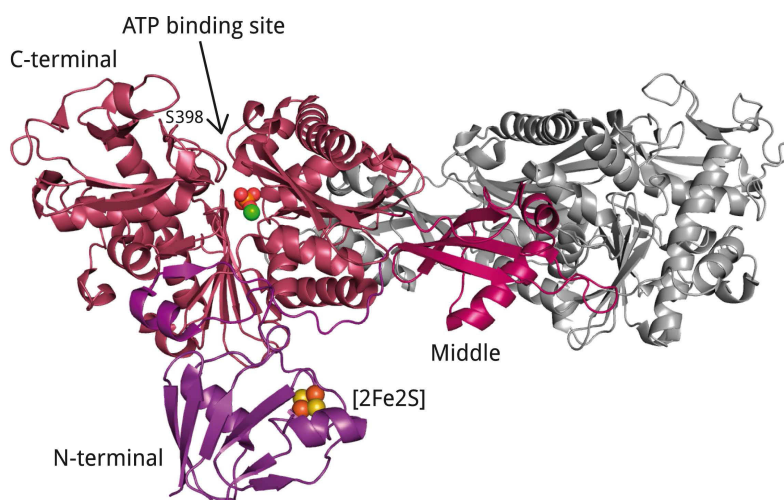
methyl group is bound to the cobalamin from the β -side so that the cofactor is in a “base-on” state. The reduction of inactive Co(II)FeSP to active Co(I)FeSP is necessary when Co(I)FeSP becomes accidentally oxidized, which happens *in vitro* after ≈ 100 methylation cycles because of the low midpoint redox potential of the Co(II)/Co(I) couple of < -500 mV.¹²⁰ The function of the [4Fe4S] cluster is still unknown but the large distance between the two cofactors makes a direct electron transfer very unlikely and therefore an active role of [4Fe4S] cluster in the reactivation process of CoFeSP can be ruled out.^{51,181}

13.3. Structure and function of RACo

An enzyme was recently discovered by Hennig et al. that accomplishes the reactivation process and was therefore named reductive activator of CoFeSP (RACo). It is encoded in an open-reading frame proximal to the structural genes of CoFeSP.⁶²

RACo belongs to the family of reductive activators for corrinoid enzymes (RACE).¹⁶⁴ It is an ATP-dependent electron transferase that is capable of transferring an electron from a redox active site with moderate redox potential to a site with low oxidation potential at the expense of ATP.²¹ Like other bacterial RACE proteins RACo contains a [2Fe2S] cluster.⁶² The active form of RACo is a homodimer. The molecular weight of a RACo monomer is 68 kDa and four structural domains can be distinguished. The N-terminal domain harbouring the [2Fe2S] cluster stands apart from

Figure 13.4.: Crystal structure of RACo (homodimer, one monomer shown in grey) with the N-terminal domain harbouring the [2Fe2S] cluster and the ATP binding site (which in the figure is occupied by a phosphate) between the C-terminal and middle domain. Protein Data BankID code 3yzz.⁶²



the rest of the molecule and is connected via a flexible linker domain to the middle domain and a large C-terminal domain.⁶² ATP binds in a cleft between the middle and the C-terminal domain. The structure of RACo is depicted in Figure 13.4.

13.4. Reactivation of CoFeSP by RACo

The activation of Co(II)FeSP requires the reduction of the Co(II) center ($E^0 \approx -510$ mV) by the [2Fe2S] center of RACo ($E^0 \approx -300$ mV), which according to the reduction potentials of the two proteins would correspond to an uphill electron transfer. The transport of an electron against a redox potential gradient could be facilitated by modulating the potential of the electron donating cofactor to increase its reducing power or by making the electron accepting cofactor a better oxidant. In either case, altering the reduction potential of a cofactor requires changes in its direct environment, e.g., the first and second coordination spheres in the case of metal containing cofactors.

As shown by Hennig et al. the formation of a complex between RACo and CoFeSP depends on the oxidation state of CoFeSP, and stable complexes have so far only been observed for Co(II)FeSP. This way the reverse thermodynamical favoured downhill electron transfer from Co(I)FeSP to Co(II)FeSP is prevented.⁶² The complex formation of CoFeSP and RACo is ATP independent but ATP than is required to break the complex (with a binding energy of $\Delta G_{bind} \approx -29$ kJ/mol) and release a reduced Co(I)FeSP.

“As the three oxidation states of the cobalamin will only differ slightly in the structure of the corrin ring, a direct interaction of RACo with the corrinoid cofactor of CoFeSP appears mandatory for the specific recognition of Co(II)–CoFeSP. The crystal structure of Co(II)–CoFeSP

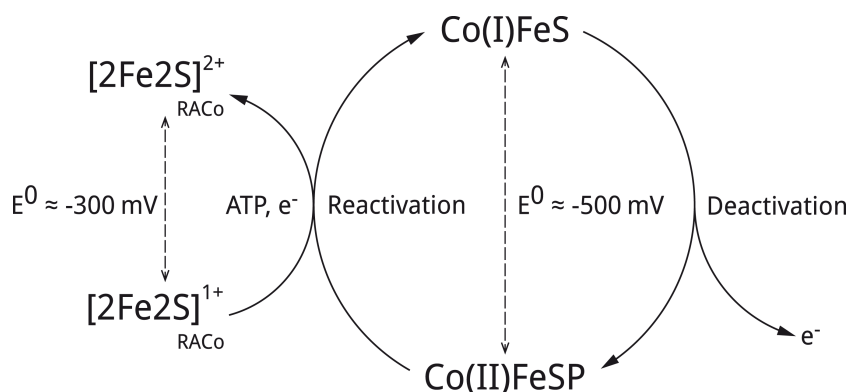


Figure 13.5.: Reactivation-scheme of CoFeSP.

shows that the corrin ring is sandwiched between the C-terminal domain of the large subunit and the small subunit with both axial coordination sites of Co shielded off by the protein matrix.^{51,181} A readout of the oxidation state appears to require a direct interaction of RACo with the corrin ring, making conformational changes of CoFeSP necessary when forming the encounter complex with RACo.” (Hennig et al., 2012)⁶² Accordingly, conformational changes at the corrinoid cofactor have to have an impact on the vibrational modes of the chromophore and thus on the resonance Raman spectra.

This work is dedicated to analyze how complex formation prepares the Co(II)FeSP–RACo complex for the energy demanding electron transfer. We used RR spectroscopy to detect specific structural changes in the cofactor environment of RACo ([2Fe2S] cluster) and Co(II)FeSP (corrinoid and [4Fe4S] cluster) induced by complex formation as well as differences between the cobalamin cofactor in Co(I)FeSP and Co(II)FeSP.

14. Conformational Gating by Complex Formation of CoFeSP and RACo—a Resonance Raman Study

This chapter is the result of a close cooperation with Sandra Hennig from the group of Holger Dobbek at the *Humboldt-Universität zu Berlin*. Most parts of it are published in Meister et al.¹¹⁹ All resonance Raman experiments were done in our laboratories by myself. All protein samples were provided by Sandra Hennig. The EPR measurements were carried out by Friedhelm Lenzian.

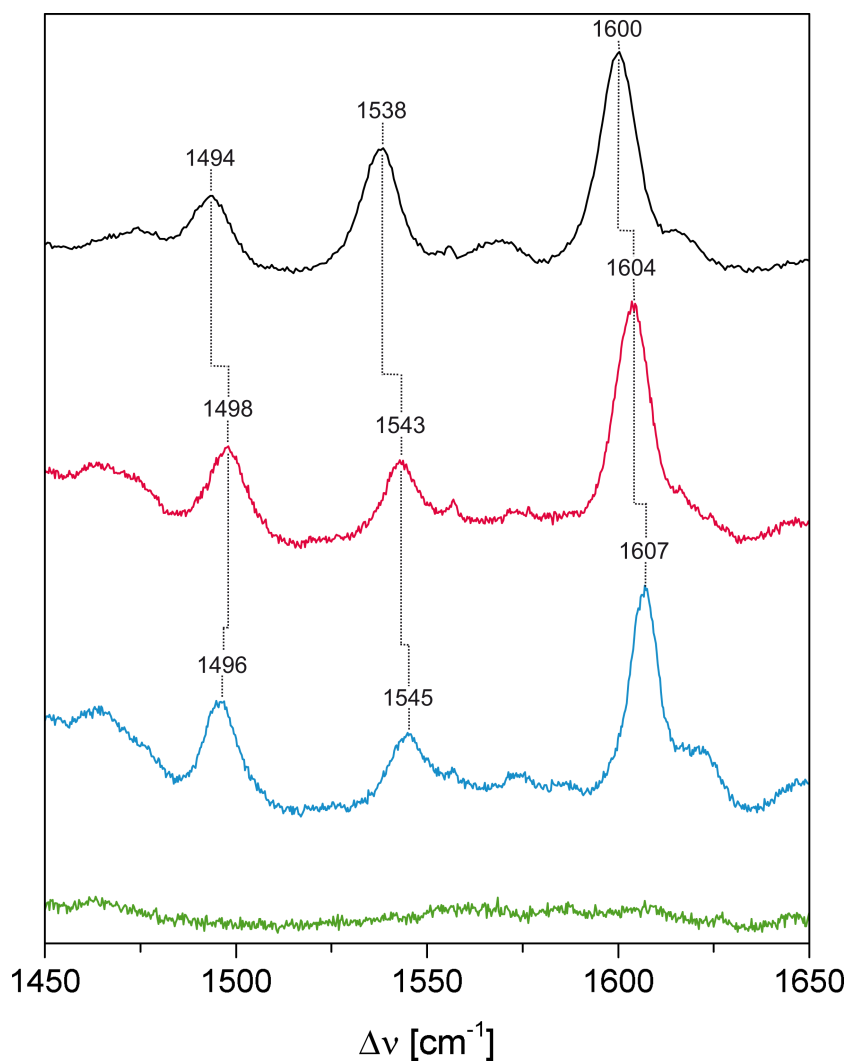


Figure 14.1.: RR spectra of Co(I)FeSP (black), Co(II)FeSP (blue), the complex of Co(II)FeSP and RACo (red) and RACo (green). The spectra, obtained with 413 nm excitation, display the frequency range of the C=C stretching modes of the corrin macrocycle.

“Adapted with permission from [W. Meister, S. E. Hennig, J. Jeoung, F. Lenzian, H. Dobbek and P. Hildebrandt, Complex Formation with the Activator RACo Affects the Corrinoid Structure of CoFeSP *Biochemistry*, **51**, 7040–7042 (2012)] Copyright (2012) American Chemical Society.”

14.1. The RR corrinoid marker region

The RR spectrum of CoFeSP, obtained with 413 nm excitation, is dominated by three bands in the region between 1400 and 1700 cm^{-1} , which can readily be attributed to the corrinoid cofactor.^{38,116,162,180} For the oxidized Co(II)FeSP state, these bands, which originate from C=C stretching modes of the corrin macrocycle, are observed at 1604, 1543, and 1498 cm^{-1} . The frequencies of these modes are sensitive to the oxidation state of the cobalt ion and undergo a small downshift of 4–5 cm^{-1} upon reduction to Co(I) by dithionite.¹¹⁶ Also, formation of a complex of Co(II)FeSP with its activator RACo is reflected by changes in the RR spectrum that are exclusively ascribed to the corrinoid because the [2Fe2S] cluster of RACo and the [4Fe4S] cluster of Co(II)FeSP

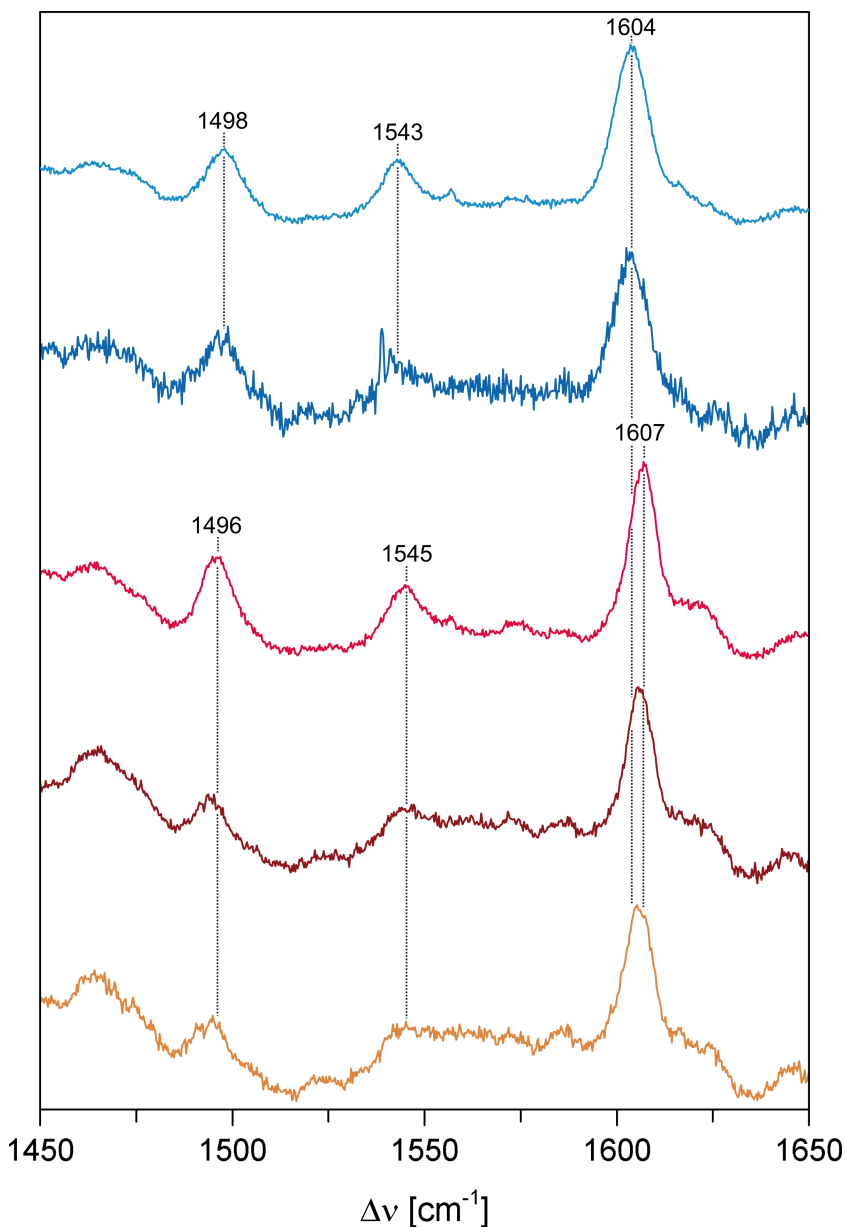


Figure 14.2.: RR spectra of Co(II)FeSP (blue), CoFe(II)SP lacking the [4Fe4S] cluster (deep blue), the complex of CoFe(II)SP and RACo (red), the complex of CoFe(II)SP and RACo without the [2Fe2S] cluster (wine red), the complex of CoFe(II)SP and RACo without the [4Fe4S] cluster (orange). The spectra, obtained with 413 nm excitation, display the frequency range of the C=C stretching modes of the corrin macrocycle.

“Adapted with permission from [W. Meister, S. E. Hennig, J. Jeoung, F. Lenzian, H. Dobbek and P. Hildebrandt, Complex Formation with the Activator RACo Affects the Corrinoid Structure of CoFeSP *Biochemistry*, **51**, 7040–7042 (2012)] Copyright (2012) American Chemical Society.”

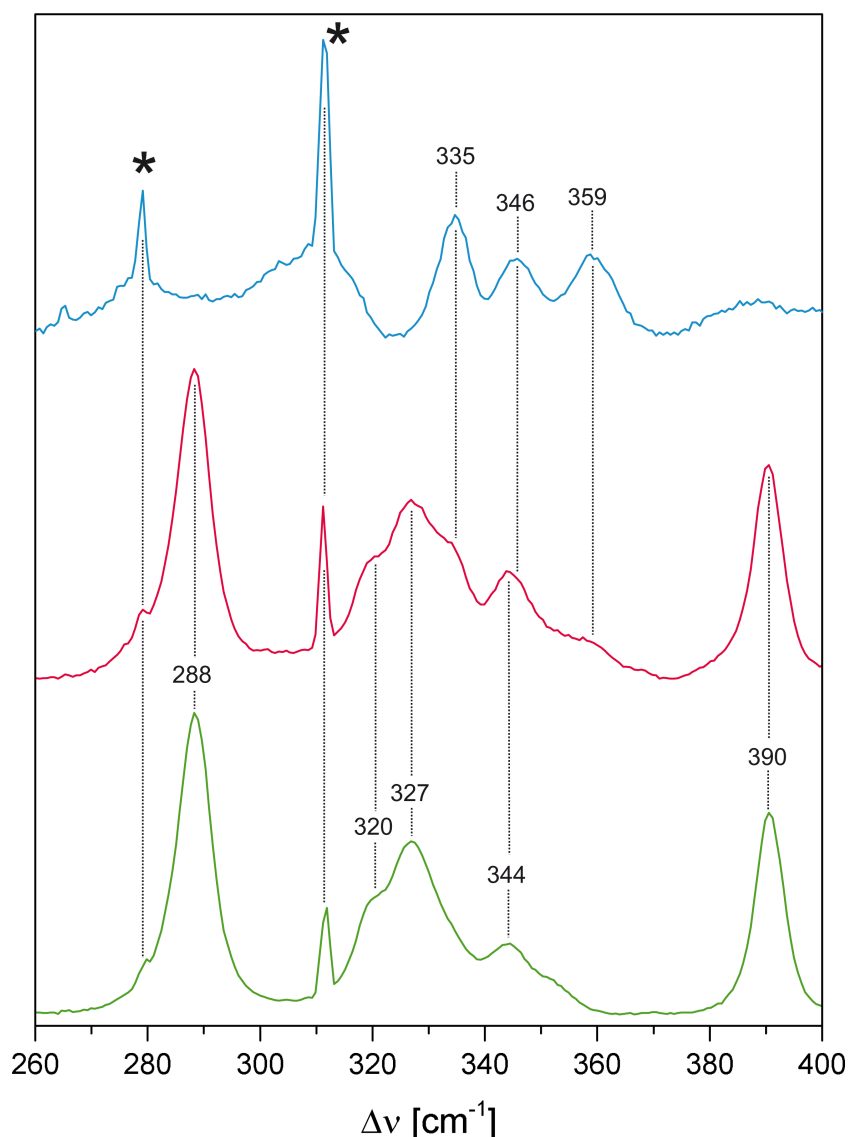


Figure 14.3.: RR spectra of Co(II)FeSP (blue), the complex of Co(II)FeSP and RACo (red), and RACo (green). The spectra, obtained with 413 nm excitation, display the frequency range of the fundamentals of the [FeS] centers. Peaks labelled with asterisks are due to non-lasing emission lines of the Kr^+ ion laser.

“Adapted with permission from [W. Meister, S. E. Hennig, J. Jeoung, F. Lenzian, H. Dobbek and P. Hildebrandt, *Complex Formation with the Activator RACo Affects the Corrinoid Structure of CoFeSP* *Biochemistry*, **51**, 7040–7042 (2012)] Copyright (2012) American Chemical Society.”

do not give rise to RR bands in this frequency range (Figure 14.1 and Figure 14.2).

Compared to the free Co(II)FeSP protein, the RACo-binding induced changes include an upshift for the most intense bands to 1607 and 1545 cm^{-1} and a 2 cm^{-1} downshift of the 1498 cm^{-1} band. In the case of the deletion mutant of CoFeSP that lacks the [4Fe4S] cluster, the complex binding constant is lowered such that the RR spectrum displays a superposition of the RR bands of the RACo-bound and the free CoFeSP protein, implying that the lack of the [4Fe4S] cluster does not affect the active site conformation of CoFeSP and the structural consequences of RACo binding. The same results are obtained for a complex of Co(II)FeSP with a deletion mutant of RACo in which the [2Fe2S] cluster has been removed. These findings indicate that the peptide segment of RACo accommodating the [2Fe2S] cluster is not involved in those interactions with Co(II)FeSP that affect the corrin structure.

14.2. The RR marker region of the [FeS] clusters

The RR bands of Co(II)FeSP in the frequency region between 250 and 400 cm^{-1} (Figure 14.3) are unambiguously attributed to the modes of the [4Fe4S] cluster because these bands are not detected in the RR spectrum of the deletion mutant lacking the [4Fe4S] cluster (Figure 14.4). Thus, there are no spectral contributions from the corrinoid cofactor in this region.

The band pattern significantly differs from that of the [2Fe2S] cluster of RACo (Figure 14.3). Furthermore, at 413 nm excitation, the resonance enhancement for the [2Fe2S] cluster is distinctly stronger such that these bands dominate the RR spectrum of the Co(II)FeSP–RACo complex whereas those of the [4Fe4S] cluster can be detected only as shoulders. To analyze the involvement of the [FeS] centers in complex formation, we have subtracted the RR spectrum either of the free Co(II)FeSP or of the free RACo from that of the complex to obtain the spectra of the bound [2Fe2S] or [4Fe4S] cluster, respectively. These spectra reveal no differences compared to the RR spectra of corresponding free proteins

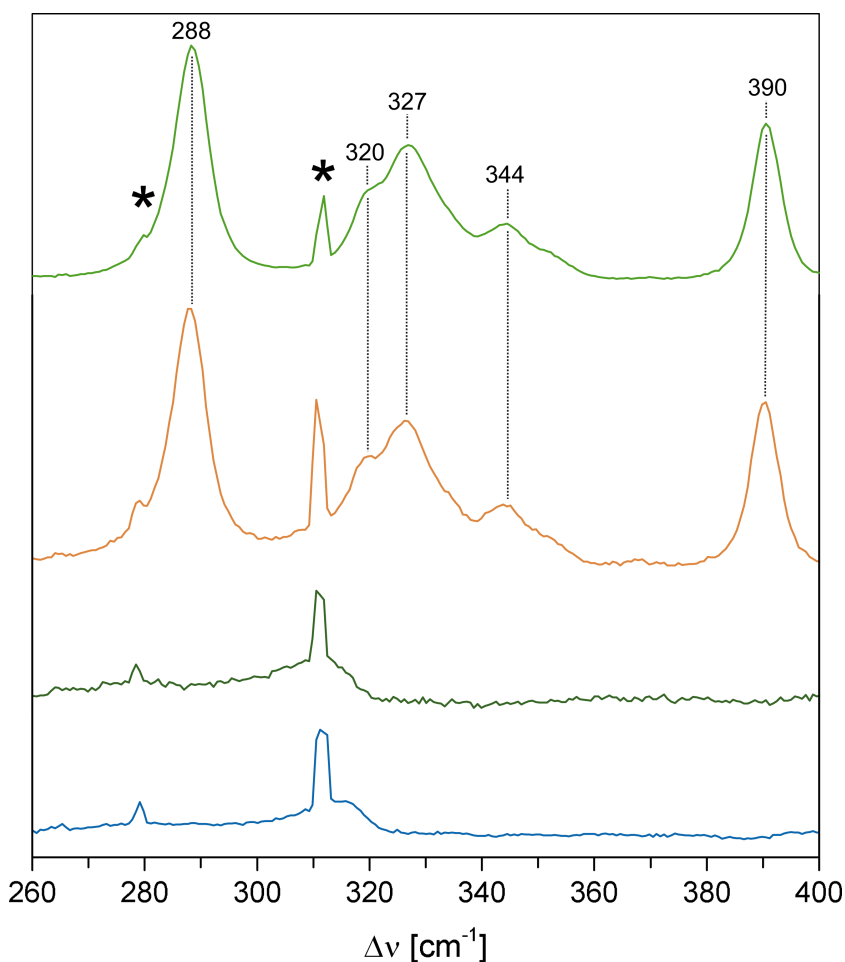


Figure 14.4.: RR spectra of the [2Fe2S] cluster containing species: RACo (green), the complex of Co(II)FeSP and RACo without the [4Fe4S] cluster (orange); species without [FeS] cluster: RACo without the [2Fe2S] cluster (deep green) and Co(II)FeSP lacking the [4Fe4S] cluster (deep blue). The spectra, obtained with 413 nm excitation, display the frequency range of the fundamentals of the [FeS] centers. Peaks labelled by asterisk are due to non-lasing emission lines of the Kr^+ ion laser.

“Adapted with permission from [W. Meister, S. E. Hennig, J. Jeoung, F. Lenzian, H. Dobbek and P. Hildebrandt, Complex Formation with the Activator RACo Affects the Corrinoid Structure of CoFeSP *Biochemistry*, **51**, 7040–7042 (2012)] Copyright (2012) American Chemical Society.”

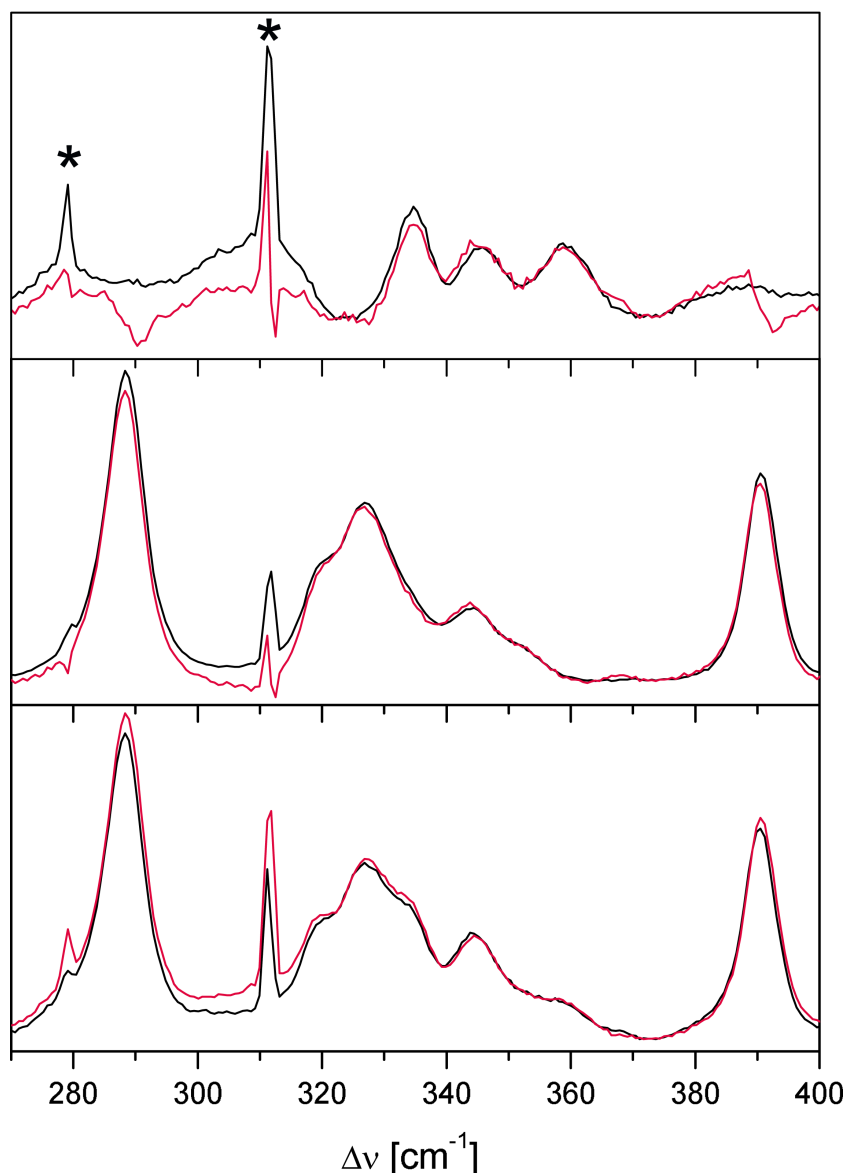


Figure 14.5.: (top) black: Co(II)FeSP, red: difference spectrum “complex–RACo”, (middle) black: RACo, red: difference spectrum “complex–Co(II)FeSP”, (bottom) black: complex, red: sum spectrum “RACo + Co(II)FeSP”. The spectra, obtained with 413 nm excitation, display the frequency range of the fundamentals of the [FeS] centers. Peaks labelled by asterisk are due to non-lasing emission lines of the Kr⁺ ion laser.

“Adapted with permission from [W. Meister, S. E. Hennig, J. Jeoung, F. Lenzian, H. Dobbek and P. Hildebrandt, *Complex Formation with the Activator RACo Affects the Corrinoid Structure of CoFeSP* *Biochemistry*, **51**, 7040–7042 (2012)] Copyright (2012) American Chemical Society.”

such that we can safely rule out (mutual) structural perturbations of the [FeS] clusters upon complex formation (Figure 14.5).

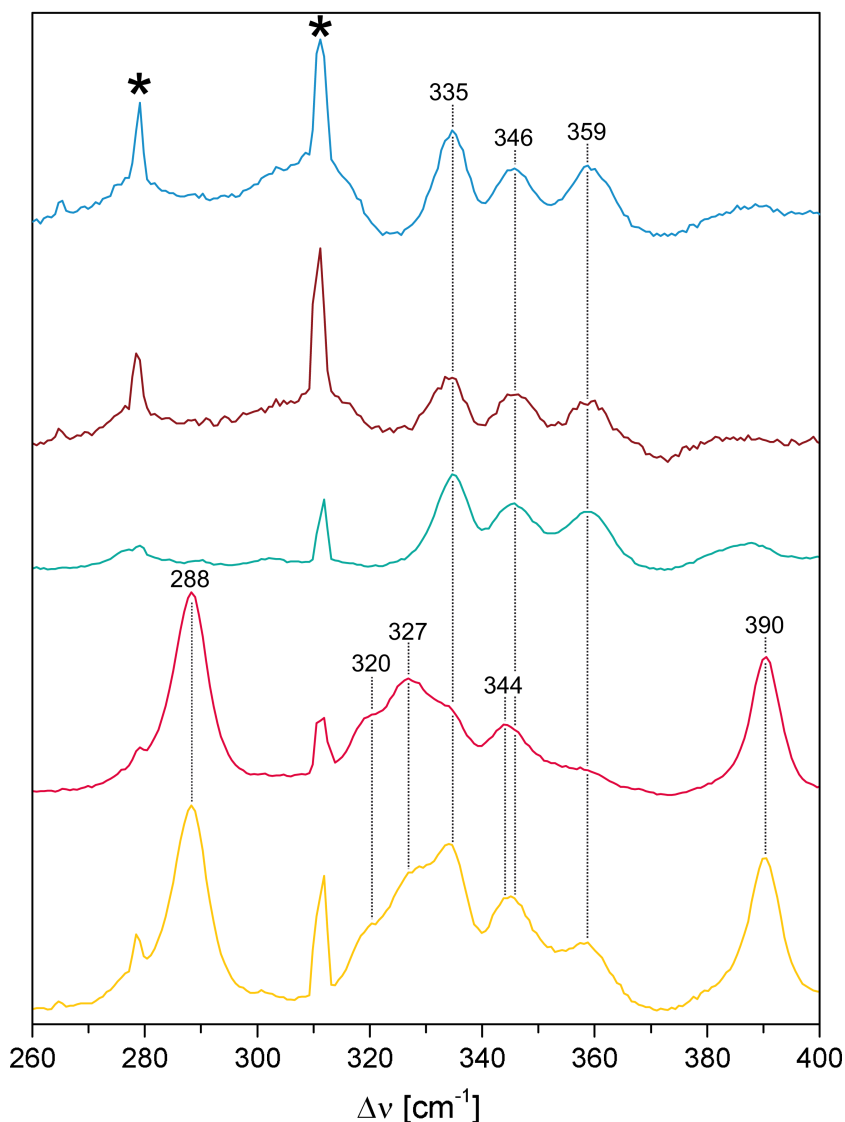
14.3. Interpretation of the RR spectra

According to the crystal structure of CoFeSP (Section 13.2), the corrinoid cofactor is located in a cleft between subunit CfsB and the C-terminal part of subunit CfsA such that the periphery of the macrocycle is solvent exposed.^{51,181} The distance from the corrinoid cofactor to the [4Fe4S] cluster is ≈ 60 Å.⁵¹ Thus, it is not surprising that the structural changes of the corrinoid due to complex formation with RACo are not influenced by the [4Fe4S] cluster.

According to our RR data, the interaction domain of RACo must be located in the C-terminal part of the protein because deletion of 100 amino

Figure 14.6.: RR spectra of the [4Fe4S] cluster containing species: Co(II)FeSP (blue), the complex of Co(II)FeSP and RACo without the [2Fe2S] cluster (brown), Co(II)FeSP without the corrinoid (turquoise); [4Fe4S] and [2Fe2S] cluster containing species: the complex of Co(II)FeSP and RACo (red), the complex of Co(II)FeSP and RACo without the corrinoid (yellow). The spectra, obtained with 413 nm excitation, display the frequency range of the fundamentals of the [FeS] centers. Peaks labelled by asterisk are due to non-lasing emission lines of the Kr⁺ ion laser.

“Adapted with permission from [W. Meister, S. E. Hennig, J. Jeoung, F. Lenzian, H. Dobbek and P. Hildebrandt, *Complex Formation with the Activator RACo Affects the Corrinoid Structure of CoFeSP Biochemistry*, **51**, 7040–7042 (2012)] Copyright (2012) American Chemical Society.”



acids at the N-terminus, harbouring the [2Fe2S] cluster, does not affect the structural consequences of complex formation on the active site of CoFeSP (Figure 14.2). The corrinoid cofactor is in a base-off configuration in the Co(II) and Co(I) oxidation states, and the cobalt ion is axially only coordinated by a water molecule (Section 13.2).^{51,181} Just according to the crystal structure of CoFeSP, there is no candidate for a protein ligand in the vicinity of the cobalt center that might replace the water ligand upon RACo binding as a possible origin for the observed changes in the RR spectrum. These changes refer to the redox state sensitive C=C stretching modes between 1490 and 1610 cm⁻¹. In analogy to previous findings for metalloporphyrins,¹⁴⁸ this redox state sensitivity may result from the translocation of electron density between the metal-centered orbitals and the antibonding molecular orbitals of the macrocycle. With the transition from Co(II) to Co(I), the increased electron density on the metal ion is partially transferred to the antibonding molecular orbitals

of the corrin, thereby weakening C=C bonds, which in turn is reflected by the observed frequency downshifts. Conversely, one would expect a transfer in the opposite direction (back-donation) for the oxidation of Co(II) to Co(III).

In fact, in an early study of the free B12 cofactor, upshifts of 4 and 10 cm^{-1} were reported for the modes at 1543 and 1604 cm^{-1} , respectively.¹¹⁶ It is now interesting to note that complex formation causes qualitatively the same frequency shifts, albeit not as large, i.e., from 1543 to 1545 cm^{-1} and from 1604 to 1607 cm^{-1} . A genuine oxidation of the Cobalt center in CoFeSP can safely be ruled out taking into account the fact that the RR spectral changes are also observed in the absence of the [FeS] centers as the only possible electron acceptors (Figure 14.2).

14.4. EPR measurements

Electron paramagnetic resonance (EPR) experiments confirm this conclusion and moreover indicate a conformational change in the axial ligand upon RACo binding (Figure 14.7). Specifically, the signal narrowing on the low field side for the CoFeSP–RACo complex points to a tightening of the ligand–Co interactions. It is therefore tempting to assume that alterations of the Co–O(aquo) bond affect the electron density in the corrin macrocycle, which in turn is reflected by the shifts in the C=C stretching frequencies. Redox-dependent complex formation requires the recognition of oxidation state specific attributes of the cofactor. As

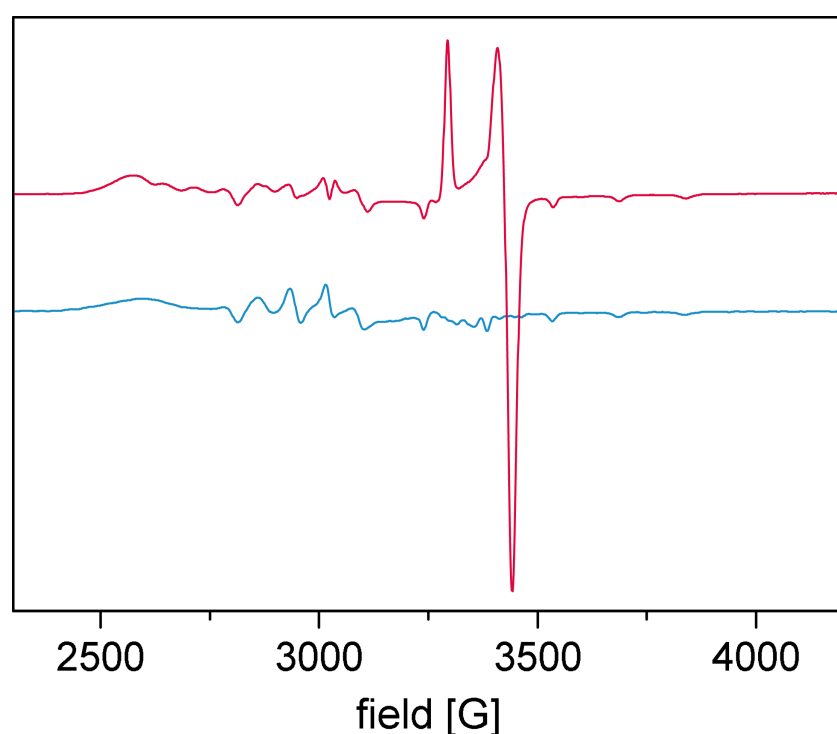


Figure 14.7.: EPR spectra of the Co(II)FeSP (blue) and the complex of Co(II)FeSP and RACo (red). The broad low-amplitude signals ranging from 2500 to 3800 G are due to the corrinoid cofactor. The sharper and better resolved signals on the low-field side of the complex indicate well-defined ligand–Co interactions in contrast to the broad and less resolved signal in the free Co(II)FeSP. The dominant signals in the spectrum of the complex originate from the [2Fe2S] cluster of RACo.

*“Adapted with permission from [W. Meister, S. E. Hennig, J. Jeoung, F. Lenzian, H. Dobbek and P. Hildebrandt, Complex Formation with the Activator RACo Affects the Corrinoid Structure of CoFeSP *Biochemistry*, 51, 7040–7042 (2012)] Copyright (2012) American Chemical Society.”*

suggested previously¹⁸¹ and confirmed by the recent crystal structure of the complex between CoFeSP and the methyltransferase from *morella thermoacetica*,⁹⁰ the corrinoid-bound C-terminal domain of CoFeSP is mobile and allows exposition of the β -side of the corrin macrocycle. It may be that in the CoFeSP–RACo complex a similar conformational change causes a displacement of the corrinoid cofactor and changes the interactions of the cobalt ion with the axial ligand, leading to the RR-detectable perturbation of the (electronic) structure of the corrin macrocycle. As a consequence, the redox potential of the corrinoid cofactor may be altered to facilitate the reduction by RACo. Note that a recent theoretical study has demonstrated that a reorientation of the water ligand may influence the electron density distribution in the Co(I) state of methyltransferases and thus tune the Co(II)/Co(I) redox potential.²¹

15. Confirmation of the Experimental Findings Through the Crystal Structure of the Complex of CoFeSP and RACo

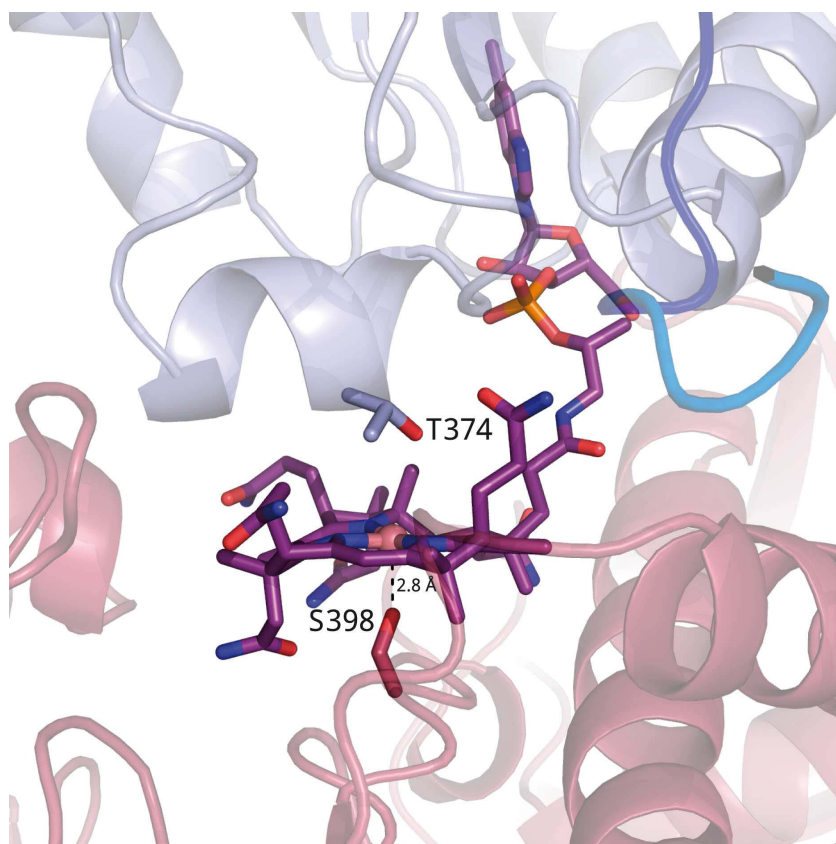
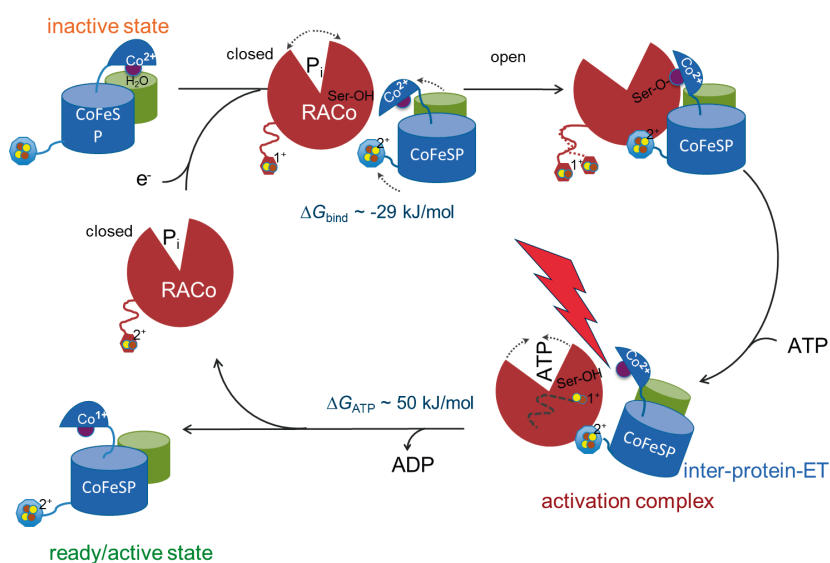


Figure 15.1.: Crystal structure of the cobalamin cofactor in the complex of CoFeSP and RACo with the Thr374 of the C-terminal domain of the big subunit of CoFeSP coordinating the cobalt from the α -side and the Ser398 of the C-terminal domain of RACo in a distance of 2.8 Å coordinating the cobalt from the β -side. The unpublished structure was solved and provided by Sandra Hennig.

In fact, the recently published crystal structure of the complex⁶¹ confirms that a serine (Ser398) residue, located in CoFeSP binding site of the C-terminal domain of the big subunit of RACo displaces the axial water-ligand of the cobalt. The Co–O(serine) distance is found to be 2.8 Å (see Figure 15.1) which is only slightly more than the Co–O(aquo) distance in the free Co(II)FeSP (see Figure 13.3 in Section 13.2). Large domain movements in both proteins are necessary to accomplish this translocation of the water by the RACo Ser398. These movements cannot be seen in the RR spectra since the direct environment of the cofactors is not altered much (except of the serine-cobalt interaction) and they are not interacting with each other. According to the crystal structure the [2Fe2S] cluster harbouring domain of RACo is not involved in complex formation and stand far apart from the interacting domains but the [4Fe4S] cluster

Figure 15.2.: Proposed reactivation mechanism of CoFeSP with RACo. The picture was provided by Holger Dobbek and is published here with his permission.



is found to stabilize the complex.⁶¹ This is in contradiction with the RR data which indicate that complex formation is possible without the [4Fe4S] cluster.

Knowing that the Ser398 of RACo displaces the water as axial ligand at the corrinoid, the interpretation of the upshifts of the 1543 and 1604 cm^{-1} RR bands as sign of strengthened C=C bonds are reasonable. It means that the electron-density at the cobalt center is further reduced upon serine binding so that the Co(II) state is stabilized in the complex which is also shown by the negatively shifted redox potential of the Co(II) in the complex.⁶¹ The lower electron-density at the cobalt lead to a backdonation of electrons from the antibonding molecule orbitals of the corrinoid macrocycle.

When comparing the the experimental data and the crystal structure, the interpretation of the EPR and RR spectra are proven to be right.

15.1. Mechanistic model for the regeneration of active CoFeSP

The RR study of CoFeSP and RACo helped to confirm a mechanistic model for the reactivation of Co(II)FeSP to Co(I)FeSP. The mechanism proposed by Hennig et al.⁶¹ is shown in Figure 15.2.

In short: The binding of RACo to the inactive Co(II)FeSP is enabled by a concerted opening movement of the ATP binding site and the CoFeSP binding site, in which the Ser398 is located. The binding of the serin to the cobalt lead to a penta-coordinated cobalt which is favoured by the Co(II). This lead to a stabilization of Co(II)FeSP. ATP provides the energy

($\Delta G_{ATP} \approx 50$ kJ/mol) to split the complex ($\Delta G_{bind} \approx -44$ kJ/mol)⁶¹ of CoFeSP and RACo. For ATP binding the conformation of RACo has to adapt a more closed conformation and the [2Fe2S] cluster moves closer to the corrinoid. With the sudden ATP binding induced closing movement of RACo, the complex is disrupted. The serine-cobalt bond is broken which lead to a four-coordinated cobalt. This conformation is favoured by the Co(I) state so that the Co(II) state is destabilized and the cobalt is easily reduced by the [2Fe2S] cluster which becomes oxidized. ADP and the active Co(I)FeSP is released and RACo enters again in a closed conformation the reactivation cycle after picking up an electron from the surrounding.

Hennig et al. could show that the cobalt in the Co(II)FeSP/RACo complex has even a more negative redox potential than the free Co(I)/Co(II) couple and that therefore a prerequisite of the reduction of the Co(II) is the complex splitting.⁶¹

Part VIII.

Concluding Discussion

Biological ET is a topic of broad interest in science. The complexity of ET reactions in biological systems is a challenge for scientists and based on the specific context very different experimental approaches are required. Depending on the system, ET can occur over a wide range of distances. The prerequisite of biological ET reactions are specific protein–protein interactions. They may involve complex recognition reactions which are associated with structural rearrangements of the partner proteins. Typically, structural changes that are linked to ET are relatively small in those proteins that serve as electron shuttles. Alternatively, larger structural changes are favoured for those proteins in which oxidation or reduction is coupled to another reaction step such as in redox enzymes.^{198,199} The proteins Cyt c and CoFeSP that were studied in this work represent examples for these two cases. Thus, an experimental method that is able to probe the ET reactions and structural changes of the metal cofactors is of particular advantage for analyzing complex biological ET reactions. These are, for example, RR and SERR spectroscopy which were employed in this work.

The surface enhancement effect used for SERR spectroscopy is based on nanostructured morphologies of the metal support. This gross roughness of the surfaces is produced by manual polishing which depends on the grain size and the pressure that is applied for this “pre”-roughening. Additionally, electrochemical roughening defines the fine structure of the surface. TR SERR spectroscopic experiments of different experimenters, presented in this work, reveal an unexpected and relatively strong “personal” effect on the ET kinetics of surface immobilized Cyt c . This “personal factor”, which has to be associated with the applied pressure since this is the only parameter that cannot precisely be controlled, evidently results in an effect on a parameter that influences the ET rates. A possible explanation is, that different pressures (depending on the physical strength) applied upon polishing lead to differing surface morphologies, which in turn influence the formation of the SAM and the SAM structure. The effective ET distances of the immobilized protein may be related to the SAM structure leading to different ET kinetics. Concomitantly, the surface enhancement may differ for different surface domains such that the SERR signals of Cyt c populations of different ET rates may be selectively enhanced.

According to R. J. P. Williams metallo-proteins involved in biological ET can be divided into two groups.^{198,199} On the one hand there are the simple wire-like electronic conductor systems. These proteins involve a rigid polypeptide fold which allows only for minimal ligand rearrangements due to a change of the charge of the metal center. Also the cofactors are

positioned inside the protein in a way that the ET distance in direction of the recognition zone is distinctly smaller than in all other directions leading to a highly selective ET route.¹⁹⁹ Examples for this systems are Cyt_c or blue copper proteins. On the other hand there are metallo-protein systems that couple the ET with other processes, such as proton movements and catalytic reactions (cytochrome *a*, cytochrome *b*, cytochrome oxidase, cytochrome *P*₄₅₀). These systems are more flexible and a considerable change in protein structure is associated with the change of the oxidation state.^{198,199} Candidates of both groups are investigated in this work. As simple ET protein, Cyt_c and its ET was investigated by SERR spectroscopy. The reactivation system of the metallo-proteins RACo and CoFeSP, investigated by RR spectroscopy, represents a system of the latter group where ET is accompanied by domain movements.

CoFeSP is a methyl transferase in the acetyl-CoA pathway of anaerobic bacteria and archaea which accidentally gets deactivated by a one electron oxidation of the cobalt center, resulting in Co(II)FeSP. The ATP dependent reductive reactivation to Co(I)FeSP is accomplished by the [2Fe2S] cluster of RACo. This process correspond to an uphill electron transfer considering the reduction potentials of the two proteins. In this work the RR spectroscopic analysis revealed the structural and electronic properties of the metal cofactors in the complex in comparison to the free RACo and the free CoFeSP in the different oxidation states. It was demonstrated that CoFeSP reduction is achieved via a conformational gating upon complex formation of Co(II)FeSP and RACo. Here, specifically the structure of the corrinoid cofactor is altered by modifying the interactions of the Co(II) center with an axial ligand. Using various deletion mutants, the potential interaction domains on the interacting proteins can be predicted which point to domain movements upon complex formation. Thus, the inter-protein ET is essentially determined by protein dynamics rather than by ET tunneling. Protein conformational changes further adjust the redox potential to allow for an efficient reductive reactivation.^{62,119}

Cyt_c exhibits two physiological functions. But only one of them is associated with a redox process, i.e. the electron transfer from complex III to complex IV in the respiratory chain. Due to its nature as an electron shuttle, no major conformational changes are expected that accompany the ET steps. This is in fact in line with the presented results. However, it was shown that protein dynamics play a critical role for the redox process. Here, a model system was used to investigate the ET of Cyt_c. Since this process occur in the mitochondrial membranes, which exhibit strong electric fields, the model system has to mimic this situation appropriately. Thus, SAMs of lipid analogues were deposited on Ag

electrodes, which functioned as redox partner and a signal amplifier for the SERR technique.⁸⁹ According to previous studies, ET of Cyt c at negatively charged SAMs or the anionic binding domain of its natural partner cytochrome c oxidase, is a three-step process including electrostatic binding, protein reorientation, and subsequently electron tunneling. In this work, engineered Cyt c variants that alter the electrostatic interactions were employed to elucidate the interplay between the individual reaction steps.^{9,89} In contrast to the WT Cyt c , where the ET occur over a narrow range of high coupling orientations, the K87C mutant, with a lysine in the proposed ET pathway exchanged by a cysteine, exhibited biphasic ET kinetics at medium and long SAM, i.e. at low electric field. Faster ET occurred upon strong coupling orientations with weak binding properties, while slower ET occurred due to low coupling orientations which exhibited stronger binding. The orientation distribution of the K87C mutant became narrower at higher electric fields, respectively shorter SAMs. Here, the good alignment of the dipole moment with the weak coupling orientations led to monophasic ET kinetics. SERR investigation of the K8C and K39C mutants supported this picture. Since the position of the mutations lie on the opposite side of the lysine binding patch, the direction and magnitude of the dipole moment was changed. The ET rates of these mutants were similar to the slow trace of the K87C mutant which hint on an ET exclusively over the BD3 over the complete range of SAM lengths. This is further supported by calculations that predict the only stable protein–SAM interactions over this binding patch. On the basis of the employed surface mutations the ET pathway in Cyt c and the role of protein reorientation was further clarified.

The ET in both systems require protein dynamics. In contrast to the large domain movements and the intramolecular structural changes in the CoFeSP/RACo system as prerequisite for ET in Cyt c protein dynamics refer to movements of the protein, i.e. rotational diffusion to reach an optimum orientation for the ET.

The model system used in this work represent a compromise between mimicking the natural environment as closely as possible and allowing for the application of highly sensitive analytical techniques. To assess how the conclusions drawn from the model systems are also valid under physiological conditions, the experiments on Cyt c , bound to SAM-coated electrodes, were extended to significantly higher ionic strengths that are close to those in cellular systems but affect the signal-to-noise ratio of the SERR spectra due to the reduced concentration of bound proteins. Nevertheless, it was possible to determine the effect of the ionic strength on the thermodynamics and kinetics of the interfacial redox process.

While the ET kinetics were slowed down at higher ionic strength the redox potential was found to be positively shifted. The positive shift of the redox potential was ascribed to the changed potential drop across the SAM and to a differential binding of the ferrous and ferric form at higher charge density in solution. Due to the shifted redox potential also the expected electric field strength was surprisingly found to be lower than at lower ionic strength, hinting on a compensatory effect of the redox potential shift which reduces consequences of electric field changes. It was shown that the slower ET kinetics were therefore not an electric field effect but the result of a change in the orientation distribution of Cyt c due to the higher ionic strength.

The second function of Cyt c , in line with the idea of R. J. P. Williams, is not restricted to electron shuttling but in fact involves structural changes of the protein. It is related to pre-apoptotic processes where Cyt c is converted to a peroxidase catalyzing the peroxidation of CL as the main component of the mitochondrial membrane. This process leads to a permeabilization of the membrane and the release of the Cyt c from the intermembrane space of the mitochondrion into the cytosol. It is thought that this change of function is a result of posttranslational phosphorylation of specific tyrosines. In this work, wild type and single tyrosine to “phosphomimetic” amino acid mutants of Cyt c were investigated by RR spectroscopy to detect potential structural changes at the redox site. However, the results do not provide a distinct and unambiguous indication for alterations of the heme center due to the modification of nearby tyrosines.

Acknowledgements

I hope that I already managed to acknowledge all people involved in the research, which I did for this thesis, in the preceding text. My sincere gratitude goes to all the people I worked with, in cooperations and in my working group, and to all the people who provided me with material, practical / scientific input, and emotional support.

Also I want to grateful acknowledge the patience of my assessors and the time they willingly spend by reviewing this work.

I thankfully want to achnowledge Prof. Dr. Christiane Nüsslein-Volhard and the CNV-Stiftung.

And Peter, without your understanding and approach to science and life this kind of work would not have been possible. It was a pleasure to work in your group.

Bibliography

- [1] M. Abe, T. Kitagawa, and Y. Kyogoku, *Resonance RAMAN-Spectra of Octaethylporphyrinato-Ni(II) and Meso-Deuterated and N-15 Substituted Derivates. 2. Normal Coordinate Analysis*, J. Chem. Phys. **69** (10), 4526–4534 (1978).
- [2] L. A. Abriata, D. Alvarez-Paggi, G. N. Ledesma, N. J. Blackburn, A. J. Vila, and D. H. Murgida, *Alternative ground states enable pathway switching in biological electron transfer*, Proc. Natl. Acad. Sci. USA **109** (43), 17348–17353 (2012).
- [3] A. C. Albrecht, *"Forbidden" Character in Allowed Electronic Transitions*, J. Phys. Chem. **33** (1), 156–169 (1960).
- [4] A. C. Albrecht, *On the Theory of Raman Intensities*, J. Phys. Chem. **34** (5), 1476–1484 (1961).
- [5] M. G. Albrecht and J. A. Creighton, *Anomalously intense Raman spectra of pyridine at a silver electrode*, J. Am. Chem. Soc. **99** (15), 5215–5217 (1977).
- [6] T. Albrecht, *Dynamik und Mechanismen der heterogenen Elektronentransferprozesse von synthetischen und natürlichen Hämproteinen*, Dissertation, Technische Universität Berlin (2003).
- [7] D. Alvarez-Paggi, D. F. Martin, P. M. DeBiase, P. Hildebrandt, M. A. Marti, and D. H. Murgida, *Molecular Basis of Coupled Protein and Electron Transfer Dynamics of Cytochrome c in Biomimetic Complexes*, J. Am. Chem. Soc. **132** (16), 5769–5778 (2010).
- [8] D. Alvarez Paggi, D. F. Martin, A. Kranich, P. Hildebrandt, M. A. Marti, and D. H. Murgida, *Computer simulation and SERR detection of cytochrome c dynamics at SAM-coated electrodes*, Electrochim. Acta **54** (22), 4963–4970 (2009).
- [9] D. Alvarez-Paggi, W. Meister, U. Kuhlmann, I. Weidinger, K. Tenger, L. Zimányi, G. Rákhely, P. Hildebrandt, and D. H. Murgida, *Disentangling Electron Tunneling and Protein Dynamics of Cytochrome c through a Rationally Designed Surface Mutation*, J. Phys. Chem. B **117** (20), 6061–6068 (2013).

- [10] F. A. Armstrong and G. S. Wilson, *Recent developments in faradaic bioelectrochemistry*, *Electrochim. Acta* **45**, 2623–2645 (2000).
- [11] P. Atkins and J. De Paula, *Physical Chemistry*, Oxford University Press, 8 rev. ed. edn. (2006).
- [12] A. Avila, B. W. Gregory, K. Niki, and T. M. Cotton, *An Electrochemical Approach to Investigate Gated Electron Transfer Using a Physiological Model System: Cytochrome c Immobilized on Carboxylic Acid-Terminated Alkanethiol Self-Assembled Monolayers on Gold Electrodes*, *J. Phys. Chem. B* **104** (12), 2759–2766 (2000).
- [13] O. Azzaroni, M. E. Vela, G. Andreasen, P. Carro, and R. C. Salvarezza, *Electrodesorption Potentials of Self-Assembled Alkanethiolate Monolayers on Ag(111) and Au(111). An Electrochemical, Scanning Tunneling Microscopy and Density Functional Theory Study*, *J. Chem. Phys. B* **106** (47), 12267–12273 (2002).
- [14] L. Banci, I. Bertini, A. Rosato, and G. Varani, *Mitochondrial cytochromes c: a comparative analysis*, *J. Biol. Inorg. Chem.* **4** (6), 824–837 (1999).
- [15] L. V. Basova, I. V. Kurnikov, L. Wang, V. B. Ritov, N. A. Belikova, I. I. Vlasova, A. A. Pacheco, D. E. Winnica, J. Peterson, H. Bayir, D. H. Waldeck, and V. E. Kagan, *Cardiolipin Switch in Mitochondria: Shutting off the Reduction of Cytochrome c and Turning on the Peroxidase Activity*, *Biochemistry* **46** (11), 3423–3434 (2007).
- [16] D. Beratan, J. Onuchic, J. Winkler, and H. Gray, *Electron-tunneling pathways in proteins*, *Science* **258** (5089), 1740–1741 (1992).
- [17] G. Berglund, G. Carlsson, A. Smith, H. Szoke, A. Henriksen, and J. Hajdu, *The catalytic pathway of horseradish peroxidase at high resolution*, *Nature* **417** (6887), 463–468 (2002).
- [18] I. Bertini, G. Cavallaro, and A. Rosato, *Cytochrome c: Occurrence and Functions*, *Chem. Rev.* **106** (1), 90–115 (2006).
- [19] J. Bolton and M. Archer, *Basic Electron-Transfer Theory*, in: G. M. James R. Bolton, Noboru Mataga (ed.), *Electron transfer in inorganic, organic, and biological systems*, American Chemical Society, no. 228 in *Advances in Chemistry*, chap. 2, 7–23 (1991).
- [20] N. J. Brewer, B. D. Beake, and G. J. Leggett, *Friction Force Microscopy of Self-Assembled Monolayers: Influence of Adsorbate Alkyl Chain Length, Terminal Group Chemistry, and Scan Velocity*,

- Langmuir **17** (6), 1970–1974 (2001).
- [21] W. Buckel, M. Hetzel, and J. Kim, *ATP-driven electron transfer in enzymatic radical reactions*, *Curr. Opin. Chem. Biol.* **8** (5), 462–467 (2004).
- [22] I. Budihardjo, H. Oliver, M. Lutter, X. Luo, and X. Wang, *Biochemical Pathways of Caspase activation during Apoptosis*, *Annu. Rev. Cell Dev. Biol.* **15** (1), 269–290 (1999).
- [23] G. W. Bushnell, G. V. Louie, and G. D. Brayer, *High-resolution three-dimensional structure of horse heart cytochrome c*, *J. Mol. Biol.* **214** (2), 585–595 (1990).
- [24] A. Campion and P. Kambhampati, *Surface-enhanced Raman scattering*, *Chem. Soc. Rev.* **27**, 241–250 (1998).
- [25] Q. Chi, J. Zhang, J. E. T. Andersen, and J. Ulstrup, *Ordered Assembly and Controlled Electron Transfer of the Blue Copper Protein Azurin at Gold (111) Single-Crystal Substrates*, *J. Phys. Chem. B* **105** (20), 4669–4679 (2001).
- [26] C. E. D. Chidsey, *Free Energy and Temperature Dependence of Electron Transfer at the Metal-Electrolyte Interface*, *Science* **251** (4996), 919–922 (1991).
- [27] R. J. Clarke, *The dipole potential of phospholipid membranes and methods for its detection*, *Adv. Coll. Interfac.* **89 - 90** (0), 263–281 (2001).
- [28] G. L. Closs, L. T. Calcaterra, N. J. Green, K. W. Penfield, and J. R. Miller, *Distance, stereoelectronic effects, and the Marcus inverted region in intramolecular electron transfer in organic radical anions*, *J. Phys. Chem.* **90** (16), 3673–3683 (1986).
- [29] K. S. Conrad and T. C. Brunold, *Spectroscopic and Computational Studies of Glutathionylcobalamin: Nature of Co-S Bonding and Comparison to Co-C Bonding in Coenzyme B12*, *Inorg. Chem.* **50** (18), 8755–8766 (2011).
- [30] D. Craig and T. Thirunamachandran, *Molecular Quantum Electrodynamics*, Dover Books on Chemistry, Dover Publications (2012).
- [31] R. S. Czernuszewicz and T. G. Spiro, *IR, Raman, and Resonance Raman Spectroscopy*, in: E. I. Solomon and A. B. P. Lever (eds.), *Methodology*, Wiley, *Inorganic Electronic Structure and Spectroscopy*, vol. 2, chap. 2 (1999).
- [32] K. L. Davis and D. H. Waldeck, *Effect of Deuterium Substitution on Electron Transfer at Cytochrome c/SAM Interfaces*, *J. Phys.*

- Chem. B **112** (39), 12498–12507 (2008).
- [33] A. Desbois, *Resonance Raman spectroscopy of c-type cytochromes*, *Biochimie* **76** (7), 693–707 (1994).
- [34] M. A. V. Devanathan, *A theory of the electrical double layer and the interpretation of differential capacity curves*, *Trans. Faraday Soc.* **50**, 373–385 (1954).
- [35] R. E. Dickerson, T. Takano, D. Eisenberg, O. B. Kallai, L. Samson, A. Cooper, and E. Margoliash, *Ferricytochrome c : I. General Features of the Horse and Bonito Proteins at 2.8 Å Resolutions*, *J. Biol. Chem.* **246** (5), 1511–1535 (1971).
- [36] P. A. M. Dirac, *The Quantum Theory of the Emission and Absorption of Radiation*, *Proc. R. Soc. London, Ser. A* **114** (767), 243–265 (1927).
- [37] W. Domcke, H. Köppel, and L. Cederbaum, *Spectroscopic effects of conical intersections of molecular potential energy surfaces*, *Mol. Phys.* **43** (4), 851–875 (1981).
- [38] S. Dong, R. Padmakumar, R. Banerjee, and T. Spiro, *Co-C bond activation in B-12-dependent enzymes: Cryogenic resonance Raman studies of methylmalonyl-coenzyme A mutase*, *J. Am. Chem. Soc.* **121** (30), 7063–7070 (1999).
- [39] S. Dong, R. Padmakumar, R. Banerjee, and T. G. Spiro, *Co-C force constants from resonance Raman spectra of alkylcobalamins: insensitivity to dimethylbenzylimidazole coordination*, *Inorg. Chim. Acta* **270** (1–2), 392–398 (1998).
- [40] S. Döpner, P. Hildebrandt, A. G. Mauk, H. Lenk, and W. Stempfle, *Analysis of vibrational spectra of multicomponent systems. Application to pH-dependent resonance Raman spectra of ferricytochrome c*, *Spectrochim. Acta A* **52** (5), 573–584 (1996).
- [41] S. Döpner, P. Hildebrandt, F. Rosell, and A. Mauk, *Alkaline conformational transitions of ferricytochrome c studied by resonance Raman spectroscopy*, *J. Am. Chem. Soc.* **120** (44), 11246–11255 (1998).
- [42] L. H. Dubois and R. G. Nuzzo, *Synthesis, Structure, and Properties of Model Organic Surfaces*, *Annu. Rev. Phys. Chem.* **43** (1), 437–463 (1992).
- [43] M. Fedurco, *Redox reactions of heme-containing metalloproteins: dynamic effects of self-assembled monolayers on thermodynamics and kinetics of cytochrome c electron-transfer reactions*, *Coord.*

- Chem. Rev. **209** (1), 263–331 (2000).
- [44] J.-J. Feng, P. Hildebrandt, and D. H. Murgida, *Silver Nanocoral Structures on Electrodes: A Suitable Platform for Protein-Based Bioelectronic Devices*, *Langmuir* **24** (5), 1583–1586 (2008).
- [45] H. O. Finklea and D. D. Hanshew, *Electron-transfer kinetics in organized thiol monolayers with attached pentaammine-(pyridine)ruthenium redox centers*, *J. Am. Chem. Soc.* **114** (9), 3173–3181 (1992).
- [46] H. O. Finklea, K. Yoon, E. Chamberlain, J. Allen, and R. Haddox, *Effect of the Metal on Electron Transfer across Self-Assembled Monolayers*, *J. Phys. Chem. B* **105** (15), 3088–3092 (2001).
- [47] M. Fleischmann, P. Hendra, and A. McQuillan, *Raman spectra of pyridine adsorbed at a silver electrode*, *Chem. Phys. Letters* **26** (2), 163–166 (1974).
- [48] J. García-Heredia, A. Díaz-Quintana, M. Salzano, M. Orzáez, E. Pérez-Payá, M. Teixeira, M. De la Rosa, and I. Díaz-Moreno, *Tyrosine phosphorylation turns alkaline transition into a biologically relevant process and makes human cytochrome c behave as an anti-apoptotic switch*, *J. Biol. Inorg. Chem.* **16**, 1155–1168 (2011).
- [49] J. M. García-Heredia, I. Díaz-Moreno, P. M. Nieto, M. Orzáez, S. Kocanis, M. Teixeira, E. Pérez-Payá, A. Díaz-Quintana, and M. A. D. la Rosa, *Nitration of tyrosine 74 prevents human cytochrome c to play a key role in apoptosis signaling by blocking caspase-9 activation*, *Biochim. Biophys. Acta* **1797** (6–7), 981–993 (2010).
- [50] E. B. Getz, M. Xiao, T. Chakrabarty, R. Cooke, and P. R. Selvin, *A Comparison between the Sulfhydryl Reductants Tris(2-carboxyethyl)phosphine and Dithiothreitol for Use in Protein Biochemistry*, *Anal. Biochem.* **273** (1), 73–80 (1999).
- [51] S. Goetzl, J.-H. Jeoung, S. E. Hennig, and H. Dobbek, *Structural Basis for Electron and Methyl-Group Transfer in a Methyltransferase System Operating in the Reductive Acetyl-CoA Pathway*, *J. Mol. Biol.* **411** (1), 96–109 (2011).
- [52] D. Gopal, G. S. Wilson, R. A. Earl, and M. A. Cusanovich, *Cytochrome c: ion binding and redox properties. Studies on ferri and ferro forms of horse, bovine, and tuna cytochrome c.*, *J. Biol. Chem.* **263** (24), 11652–11656 (1988).

- [53] S. Gosavi and R. A. Marcus, *Nonadiabatic Electron Transfer at Metal Surfaces*, *J. Phys. Chem. B* **104** (9), 2067–2072 (2000).
- [54] M. Gouterman, *Spectra of porphyrins*, *J. Mol. Spectrosc.* **6** (0), 138–163 (1961).
- [55] D. C. Grahame, *The Electrical Double Layer and the Theory of Electrocapillarity.*, *Chem. Rev.* **41** (3), 441–501 (1947).
- [56] D. C. Grahame, *Components of Charge and Potential in the Non-diffuse Region of the Electrical Double Layer: Potassium Iodide Solutions in Contact with Mercury at 25°*, *J. Am. Chem. Soc.* **80** (16), 4201–4210 (1958).
- [57] D. C. Grahame and R. Parsons, *Components of Charge and Potential in the Inner Region of the Electrical Double Layer: Aqueous Potassium Chloride Solutions in Contact with Mercury at 25°*, *J. Am. Chem. Soc.* **83** (6), 1291–1296 (1961).
- [58] H. B. Gray and J. R. Winkler, *Electron Transfer in Proteins*, *Annu. Rev. Biochem.* **65** (1), 537–561 (1996).
- [59] J. Grochol, *Raman Spectroelectrochemical Investigations of Immobilized Redox Proteins*, Dissertation, Technische Universität Berlin (2007).
- [60] J. Hazzard, G. McLendon, M. Cusanovich, and G. Tollin, *Formation of electrostatically-stabilized complex at low ionic strength inhibits interprotein electron transfer between yeast cytochrome *c* and cytochrome *c* peroxidase*, *Biochem. Biophys. Res. Commun.* **151** (1), 429–434 (1988).
- [61] S. E. Hennig, S. Goetzl, J.-H. Jeoung, M. Bommer, F. Lenzian, P. Hildebrandt, and H. Dobbek, *ATP-induced electron transfer by redox-selective partner recognition*, *Nature Communications* **5**, – (2014).
- [62] S. E. Hennig, J.-H. Jeoung, S. Goetzl, and H. Dobbek, *Redox-dependent complex formation by an ATP-dependent activator of the corrinoid/iron-sulfur protein*, *Proc. Natl. Acad. Sci. USA* **109** (14), 5235–5240 (2012).
- [63] G. Herzberg, *Electronic Spectra and Electronic Structure of Polyatomic Molecules*, no. 3 in *Molecular Spectra and Molecular Structure*, D. Van Nostrand Company, Inc. (1966).
- [64] P. Hildebrandt, *Resonance Raman Spectroscopy of Cytochrome *c**, in: R. A. Scott and A. G. Mauk (eds.), *Cytochrome *c*: A multidisciplinary approach*, University Science Books (1996).

- [65] S. Hu, I. K. Morris, J. P. Singh, K. M. Smith, and T. G. Spiro, *Complete assignment of cytochrome c resonance Raman spectra via enzymic reconstitution with isotopically labeled hemes*, *J. Am. Chem. Soc.* **115** (26), 12446–12458 (1993).
- [66] J. K. Hurley, M. Faro, T. B. Brodie, J. T. Hazzard, M. Medina, C. Gómez-Moreno, and G. Tollin, *Highly Nonproductive Complexes with Anabaena Ferredoxin at Low Ionic Strength Are Induced by Nonconservative Amino Acid Substitutions at Glu139 in Anabaena Ferredoxin:NADP+ Reductase*, *Biochemistry* **39** (45), 13695–13702 (2000).
- [67] M. Hüttemann, P. Pecina, M. Rainbolt, T. H. Sanderson, V. E. Kagan, L. Samavati, J. W. Doan, and I. Lee, *The multiple functions of cytochrome c and their regulation in life and death decisions of the mammalian cell: From respiration to apoptosis*, *Mitochondrion* **11** (3), 369–381 (2011).
- [68] Z. Iqbal, *Surface Enhancement by Sample and Substrate Preparation Techniques in Raman and Infrared Spectroscopy*, in: S. Mitra (ed.), *Sample Preparation Techniques in Analytical Chemistry*, Wiley-Interscience, chap. 10, 413–437 (2003).
- [69] H. Ischiropoulos, *Biological selectivity and functional aspects of protein tyrosine nitration*, *Biochem. Biophys. Res. Commun.* **305** (3), 776–783 (2003).
- [70] J. B. Jackson and N. J. Halas, *Surface-enhanced Raman scattering on tunable plasmonic nanoparticle substrates*, *Proc. Natl. Acad. Sci. USA* **101** (52), 17930–17935 (2004).
- [71] B. Jang and S. Han, *Biochemical properties of cytochrome c nitrated by peroxyntirite*, *Biochimie* **88** (1), 53–58 (2006).
- [72] D. L. Jeanmaire and R. P. V. Duyne, *Surface raman spectroelectrochemistry: Part I. Heterocyclic, aromatic, and aliphatic amines adsorbed on the anodized silver electrode*, *J. Electroanal. Chem.* **84** (1), 1–20 (1977).
- [73] X. Jiang and X. Wang, *Cytochrome C-mediated apoptosis*, *Annu. Rev. Biochem.* **73**, 87–106 (2004).
- [74] J. Jortner, *Temperature dependent activation energy for electron transfer between biological molecules*, *J. Phys. Chem.* **64** (12), 4860–4867 (1976).
- [75] V. E. Kagan, H. A. Bayir, N. A. Belikova, O. Kapralov, Y. Y. Tyurina, V. A. Tyurin, J. Jiang, D. A. Stoyanovsky, P. Wipf, P. M. Kochanek, J. S. Greenberger, B. Pitt, A. A. Shvedova, and

- G. Borisenko, *Cytochrome c/cardiolipin relations in mitochondria: a kiss of death*, *Free Radical Biol. Med.* **46** (11), 1439–1453 (2009).
- [76] V. E. Kagan, V. A. Tyurin, J. Jiang, Y. Y. Tyurina, V. B. Ritov, A. A. Amoscato, A. N. Osipov, N. A. Belikova, A. A. Kapralov, V. Kini, I. I. Vlasova, Q. Zhao, M. Zou, P. Di, D. A. Svistunenko, I. V. Kurnikov, and G. G. Borisenko, *Cytochrome c acts as a cardiolipin oxygenase required for release of proapoptotic factors*, *Nat. Chem. Biol.* **1** (4), 223–232 (2005).
- [77] T. Kakiuchi, H. Usui, D. Hobara, and M. Yamamoto, *Voltammetric Properties of the Reductive Desorption of Alkanethiol Self-Assembled Monolayers from a Metal Surface*, *Langmuir* **18** (13), 5231–5238 (2002).
- [78] A. E. Kasmi, J. M. Wallace, E. F. Bowden, S. M. Binet, and R. J. Linderman, *Controlling Interfacial Electron-Transfer Kinetics of Cytochrome c with Mixed Self-Assembled Monolayers*, *J. Am. Chem. Soc.* **120**, 225–226 (1998).
- [79] N. R. Kestner, J. Logan, and J. Jortner, *Thermal electron transfer reactions in polar solvents*, *J. Phys. Chem.* **78** (21), 2148–2166 (1974).
- [80] Y. C. Kim, L. A. Furchtgott, and G. Hummer, *Biological Proton Pumping in an Oscillating Electric Field*, *Phys. Rev. Lett.* **103**, 268102 (2009).
- [81] K. Kneipp, M. Moskovits, and H. Kneipp (eds.), *Surface-Enhanced Raman Scattering - Physics and Application, Topics in Applied Physics*, vol. 103, Springer Berlin Heidelberg (2006).
- [82] T. Koeck, X. Fu, S. L. Hazen, J. W. Crabb, D. J. Stuehr, and K. S. Aulak, *Rapid and Selective Oxygen-regulated Protein Tyrosine Denitration and Nitration in Mitochondria*, *J. Biol. Chem.* **279** (26), 27257–27262 (2004).
- [83] W. H. Koppenol and E. Margoliash, *The asymmetric distribution of charges on the surface of horse cytochrome c. Functional implications.*, *J. Biol. Chem.* **257** (8), 4426–4437 (1982).
- [84] W. H. Koppenol, J. D. Rush, J. D. Mills, and E. Margoliash, *The dipole moment of cytochrome c.*, *Mol. Biol. Evol.* **8** (4), 545–558 (1991).
- [85] J. Kozuch, *Structure-Function Relationships of Membrane Proteins - Spectroelectrochemical Investigation of Artificial Membranes*, Dissertation, Technische Universität Berlin (2012).

- [86] H. Kramers and W. Heisenberg, *Über die Streuung von Strahlung durch Atome*, Z. Phys. **31** (1), 681–708 (1925).
- [87] A. Kranich, *Investigations of the interfacial electron transfer of cytochrome c_6 and cytochrome c by surface-enhanced resonance Raman spectroscopy*, Dissertation, Technische Universität Berlin (2008).
- [88] A. Kranich, H. K. Ly, P. Hildebrandt, and D. H. Murgida, *Direct Observation of the Gating Step in Protein Electron Transfer: Electric-Field-Controlled Protein Dynamics*, J. Am. Chem. Soc. **130** (30), 9844–9848 (2008).
- [89] A. Kranich, H. Naumann, F. P. Molina-Heredia, H. J. Moore, T. R. Lee, S. Lecomte, M. A. de la Rosa, P. Hildebrandt, and D. H. Murgida, *Gated electron transfer of cytochrome c_6 at biomimetic interfaces: a time-resolved SERR study*, Phys. Chem. Chem. Phys. **11**, 7390–7397 (2009).
- [90] Y. Kung, N. Ando, T. I. Doukov, L. C. Blasiak, G. Bender, J. Seravalli, S. W. Ragsdale, and C. L. Drennan, *Visualizing molecular juggling within a B-12-dependent methyltransferase complex*, Nature **484** (7393), 265–269 (2012).
- [91] C. Lange and C. Hunte, *Crystal structure of the yeast cytochrome bc_1 complex with its bound substrate cytochrome c* , Proc. Natl. Acad. Sci. USA **99** (5), 2800–2805 (2002).
- [92] K. Lao, S. Franzen, M. Steffen, D. Lambright, R. Stanley, and S. G. Boxer, *Effects of applied electric fields on the quantum yields for the initial electron transfer steps in bacterial photosynthesis II. Dynamic Stark effect*, Chem. Phys. **197** (3), 259–275 (1995).
- [93] S. Lecomte, P. Hildebrandt, and T. Soulimane, *Dynamics of the heterogeneous electron-transfer reaction of cytochrome $c(552)$ from *Thermus thermophilus*. A time-resolved surface-enhanced resonance Raman spectroscopic study*, J. Phys. Chem. B **103** (45), 10053–10064 (1999).
- [94] I. Lee, A. R. Salomon, K. Yu, J. W. Doan, L. I. Grossman, and M. Hülya Bayirrttemann, *New Prospects for an Old Enzyme: Mammalian Cytochrome c Is Tyrosine-Phosphorylated in Vivo*, Biochemistry **45** (30), 9121–9128 (2006).
- [95] S. H. Lin and H. Eyring, *Study of the Franck-Condon and Herzberg-Teller Approximations*, Proc. Natl. Acad. Sci. USA **71** (10), 3802–3804 (1974).

- [96] D. J. Lockhart, C. Kirmaier, D. Holten, and S. G. Boxer, *Electric field effects on the initial electron-transfer kinetics in bacterial photosynthetic reaction centers*, *J. Phys. Chem.* **94** (18), 6987–6995 (1990).
- [97] D. A. Long, *The Raman Effect: A Unified Treatment of the Theory of Raman Scattering by Molecules*, Wiley (2002).
- [98] J. C. Love, L. A. Estroff, J. K. Kriebel, R. G. Nuzzo, and G. M. Whitesides, *Self-Assembled Monolayers of Thiolates on Metals as a Form of Nanotechnology*, *Chem. Rev.* **105** (4), 1103–1170 (2005).
- [99] H. K. Ly, M. A. Marti, D. F. Martin, D. Alvarez-Paggi, W. Meister, A. Kranich, I. M. Weidinger, P. Hildebrandt, and D. H. Murgida, *Thermal Fluctuations Determine the Electron-Transfer Rates of Cytochrome *c* in Electrostatic and Covalent Complexes*, *ChemPhysChem* **11** (6), 1225–1235 (2010).
- [100] H. K. Ly, M. Sezer, N. Wisitruangsakul, J.-J. Feng, A. Kranich, D. Millo, I. M. Weidinger, I. Zebger, D. H. Murgida, and P. Hildebrandt, *Surface-enhanced vibrational spectroscopy for probing transient interactions of proteins with biomimetic interfaces: electric field effects on structure, dynamics and function of cytochrome *c**, *FEBS J.* **278** (9), 1382–1390 (2011).
- [101] H. K. Ly, T. Utesch, I. Diaz-Moreno, J. M. García-Heredia, M. A. De La Rosa, and P. Hildebrandt, *Perturbation of the Redox Site Structure of Cytochrome *c* Variants upon Tyrosine Nitration*, *J. Phys. Chem. B* **116** (19), 5694–5702 (2012).
- [102] H. K. Ly, N. Wisitruangsakul, M. Sezer, J.-J. Feng, A. Kranich, I. M. Weidinger, I. Zebger, D. H. Murgida, and P. Hildebrandt, *Electric-field effects on the interfacial electron transfer and protein dynamics of cytochrome *c**, *J. Electroanal. Chem.* **660** (2, SI), 367–376 (2011).
- [103] K. Ly, *Application of Surface Enhanced Raman Spectroscopy to Biological Systems*, Dissertation, Technische Universität Berlin (2012).
- [104] R. Marcus, *On the Theory of Electron Transfer Reactions. VI. Unified Treatment for Homogeneous and Electrode Reactions*, *J. Chem. Phys.* **43** (2), 679–701 (1965).
- [105] R. Marcus and N. Sutin, *Electron transfers in chemistry and biology*, *Biochim. Biophys. Acta* **811** (3), 265–322 (1985).

- [106] R. A. Marcus, *Electrostatic Free Energy and Other Properties of States Having Nonequilibrium Polarization. I**, J. Chem. Phys. **24** (5), 979–989 (1956).
- [107] R. A. Marcus, *On the Theory of Oxidation-Reduction Reactions Involving Electron Transfer. I**, J. Chem. Phys. **24** (5), 966–978 (1956).
- [108] R. A. Marcus, *On the Theory of Oxidation-Reduction Reactions Involving Electron Transfer. II. Applications to Data on the Rates of Isotopic Exchange Reactions*, J. Chem. Phys. **26** (4), 867–871 (1957).
- [109] R. A. Marcus, *On the Theory of Oxidation-Reduction Reactions Involving Electron Transfer. III. Applications to Data on the Rates of Organic Redox Reactions*, J. Chem. Phys. **26** (4), 872–877 (1957).
- [110] R. A. Marcus, *Exchange reactions and electron transfer reactions including isotopic exchange. Theory of oxidation-reduction reactions involving electron transfer. Part 4.-A statistical-mechanical basis for treating contributions from solvent, ligands, and inert salt*, Discuss. Faraday Soc. **29**, 21–31 (1960).
- [111] R. A. Marcus, *On the Theory of Oxidation-Reduction Reactions Involving Electron Transfer. V. Comparison and Properties of Electrochemical and Chemical Rate Constants*, J. Phys. Chem. **67** (4), 853–857 (1963).
- [112] R. A. Marcus, *Chemical and Electrochemical Electron-Transfer Theory*, Annu. Rev. Phys. Chem. **15** (1), 155–196 (1964).
- [113] R. A. Marcus, *Theory of Electron Transfer Reaction Rates of Solvated Electrons*, J. Chem. Phys. **43** (10), 3477–3489 (1965).
- [114] R. A. Marcus, *Electron transfer reactions in chemistry theory and experiment*, J. Electroanal. Chem. **438** (1–2), 251–259 (1997).
- [115] R. Margalit and A. Schejter, *Cytochrome c: A Thermodynamic Study of the Relationships among Oxidation State, Ion-Binding and Structural Parameters 1. The Effects of Temperature, pH and Electrostatic Media on the Standard Redox Potential of Cytochrome c*, Eur. J. Biochem **32** (3), 492–499 (1973).
- [116] E. Mayer, D. J. Gardiner, and R. E. Hester, *Resonance Raman spectra of vitamin B12 and some cobalt corrinoid derivatives*, J. Chem. Soc., Faraday Trans. 2 **69**, 1350–1358 (1973).

- [117] G. McLendon, *Long-distance electron transfer in proteins and model systems*, *Acc. Chem. Res.* **21** (4), 160–167 (1988).
- [118] W. Meister, *SERR spektroskopische Untersuchungen zum Elektronentransfer des immobilisierten Cytochrom c*, Diplomarbeit, Technische Universität Berlin (2008).
- [119] W. Meister, S. E. Hennig, J.-H. Jeoung, F. Lenzian, H. Dobbek, and P. Hildebrandt, *Complex Formation with the Activator RACo Affects the Corrinoid Structure of CoFeSP*, *Biochemistry* **51** (36), 7040–7042 (2012).
- [120] S. Menon and S. Ragsdale, *The role of an iron-sulfur cluster in an enzymatic methylation reaction - Methylation of CO dehydrogenase/acetyl-CoA synthase by the methylated corrinoid iron-sulfur protein*, *J. Biol. Chem.* **274** (17), 11513–11518 (1999).
- [121] H. Michel, *Cytochrome c Oxidase: Catalytic Cycle and Mechanisms of Proton Pumping-A Discussion*, *Biochemistry* **38** (46), 15129–15140 (1999).
- [122] H. Michel, J. Behr, A. Harrenga, and A. Kannt, *Cytochrome C oxidase: Structure and spectroscopy*, *Annu. Rev. Biophys. Biomol. Struct.* **27**, 329–356 (1998).
- [123] G. Mie, *Beiträge zur Optik trüber Medien, speziell kolloidaler Metallösungen*, *Annalen der Physik* **330** (3), 377–445 (1908).
- [124] J. R. Miller, J. V. Beitz, and R. K. Huddleston, *Effect of free energy on rates of electron transfer between molecules*, *J. Am. Chem. Soc.* **106** (18), 5057–5068 (1984).
- [125] M. F. Molinas, A. De Candia, S. H. Szajnman, J. B. Rodriguez, M. Marti, M. Pereira, M. Teixeira, S. Todorovic, and D. H. Murgida, *Electron transfer dynamics of Rhodothermus marinus caa3 cytochrome c domains on biomimetic films*, *Phys. Chem. Chem. Phys.* **13**, 18088–18098 (2011).
- [126] H. P. Monteiro, R. J. Arai, and L. R. Travassos, *Protein tyrosine phosphorylation and protein tyrosine nitration in redox signaling*, *Antioxidants & Redox Signaling* **10** (5), 843–889 (2008).
- [127] G. R. Moore and G. W. Pettigrew, *Cytochromes c. Evolutionary, Structural and Physicochemical Aspects*, Springer-Verlag Berlin Heidelberg (1990).
- [128] C. Moser, J. Keske, K. Warncke, R. Farid, and P. Dutton, *Nature of biological electron transfer*, *Nature* **355** (6363), 796–802 (1992).

- [129] M. Moskovits, *Surface roughness and the enhanced intensity of Raman scattering by molecules adsorbed on metals*, J. Chem. Phys. **69** (9), 4159–4161 (1978).
- [130] M. Moskovits, *Surface-enhanced spectroscopy*, Rev. Mod. Phys. **57** (3), 783–826 (1985).
- [131] M. Moskovits, *Surface-enhanced Raman spectroscopy: a brief retrospective*, J. Raman Spectrosc. **36** (6–7), 485–496 (2005).
- [132] D. Murgida and P. Hildebrandt, *Surface-Enhanced Vibrational Spectroelectrochemistry: Electric-Field Effects on Redox and Redox-Coupled Processes of Heme Proteins*, in: K. Kneipp, M. Moskovits, and H. Kneipp (eds.), *Surface-Enhanced Raman Scattering - Physics and Applications*, Springer Berlin Heidelberg, *Topics in Applied Physics*, vol. 103, 313–334 (2006).
- [133] D. H. Murgida and P. Hildebrandt, *Heterogeneous electron transfer of cytochrome c on coated silver electrodes. Electric field effects on structure and redox potential*, J. Phys. Chem. B **105** (8), 1578–1586 (2001).
- [134] D. H. Murgida and P. Hildebrandt, *Proton-Coupled Electron Transfer of Cytochrome c*, J. Am. Chem. Soc. **123** (17), 4062–4068 (2001).
- [135] D. H. Murgida and P. Hildebrandt, *Electron-Transfer Processes of Cytochrome c at Interfaces. New Insights by Surface-Enhanced Resonance Raman Spectroscopy*, Acc. Chem. Res. **37** (11), 854–861 (2004).
- [136] D. H. Murgida and P. Hildebrandt, *Redox and redox-coupled processes of heme proteins and enzymes at electrochemical interfaces*, Phys. Chem. Chem. Phys. **7**, 3773–3784 (2005).
- [137] D. H. Murgida and P. Hildebrandt, *Disentangling interfacial redox processes of proteins by SERR spectroscopy*, Chem. Soc. Rev. **37**, 937–945 (2008).
- [138] T. M. Nahir and E. F. Bowden, *The distribution of standard rate constants for electron transfer between thiol-modified gold electrodes and adsorbed cytochrome c*, J. Electroanal. Chem. **410** (1), 9–13 (1996).
- [139] T. M. Nahir, R. A. Clark, and E. F. Bowden, *Linear-Sweep Voltammetry of Irreversible Electron Transfer in Surface-Confined Species Using the Marcus Theory*, Anal. Chem. **66** (15), 2595–2598 (1994).

- [140] I. Nantes, A. Faljoni-Alario, A. Vercesi, K. Santos, and E. Bechara, *Liposome effect on the cytochrome c-catalyzed peroxidation of carbonyl substrates to triplet species*, *Free Radical Biol. Med.* **25** (4–5), 546–553 (1998).
- [141] H. Naumann, *The NpSR11 photocycle and its dependence on the electric field - a combined quantum chemical and Raman spectroscopic study*, Dissertation, Technische Universität Berlin (2009).
- [142] K. Niki, W. R. Hardy, M. G. Hill, H. Li, J. R. Sprinkle, E. Margoliash, K. Fujita, R. Tanimura, N. Nakamura, H. Ohno, J. H. Richards, and H. B. Gray, *Coupling to Lysine-13 Promotes Electron Tunneling through Carboxylate-Terminated Alkanethiol Self-Assembled Monolayers to Cytochrome c*, *J. Phys. Chem. B* **107** (37), 9947–9949 (2003).
- [143] K. Niki, J. R. Sprinkle, and E. Margoliash, *Intermolecular biological electron transfer: an electrochemical approach*, *Bioelectrochemistry* **55** (1–2), 37–40 (2002).
- [144] S. Oellerich, S. Lecomte, M. Paternostre, T. Heimbürg, and P. Hildebrandt, *Peripheral and Integral Binding of Cytochrome c to Phospholipids Vesicles*, *J. Phys. Chem. B* **108** (12), 3871–3878 (2004).
- [145] S. Oellerich, H. Wackerbarth, and P. Hildebrandt, *Spectroscopic characterization of nonnative conformational states of cytochrome c*, *J. Phys. Chem. B* **106** (25), 6566–6580 (2002).
- [146] S. Oellerich, H. Wackerbarth, and P. Hildebrandt, *Conformational equilibria and dynamics of cytochrome c induced by binding of sodium dodecyl sulfate monomers and micelles*, *Eur. Biophys. J.* **32**, 599–613 (2003).
- [147] Y.-L. P. Ow, D. R. Green, Z. Hao, and T. W. Mak, *Cytochrome c: functions beyond respiration*, *Nat. Rev. Mol. Cell. Biol.* **9** (7), 532–542 (2008).
- [148] N. Parthasarathi, C. Hansen, S. Yamaguchi, and T. Spiro, *Metalloporphyrin Core Size Resonance Raman Marker Bands Revisited - Implication for the Interpretation of Hemoglobin Photoproduct Raman Frequencies*, *J. Am. Chem. Soc.* **109** (13), 3865–3871 (1987).
- [149] P. Pecina, G. G. Borisenko, N. A. Belikova, Y. Y. Tyurina, A. Pecinova, I. Lee, A. K. Samhan-Arias, K. Przyklenk, V. E. Kagan, and M. Hüttemann, *Phosphomimetic Substitution of Cytochrome c Tyrosine 48 Decreases Respiration and Binding to Cardiolipin*

- and Abolishes Ability to Trigger Downstream Caspase Activation*, *Biochemistry* **49** (31), 6705–6714 (2010).
- [150] H. Pelletier and J. Kraut, *Crystal structure of a complex between electron transfer partners, cytochrome c peroxidase and cytochrome c*, *Science* **258** (5089), 1748–1755 (1992).
- [151] J. Petrovic, R. A. Clark, H. Yue, D. H. Waldeck, and E. F. Bowden, *Impact of Surface Immobilization and Solution Ionic Strength on the Formal Potential of Immobilized Cytochrome c*, *Langmuir* **21** (14), 6308–6316 (2005).
- [152] G. W. Pettigrew and G. R. Moore, *Cytochromes c. Biological Aspects*, Springer-Verlag Berlin Heidelberg (1987).
- [153] M. Pudlak and R. Pincak, *Influence of the electric field on the electron transport in photosynthetic reaction centers*, *Eur. Phys. J. E* **34** (3), 1–8 (2011).
- [154] S. W. Ragsdale and E. Pierce, *Acetogenesis and the Wood–Ljungdahl pathway of CO₂ fixation*, *Biochim. Biophys. Acta* **1784** (12), 1873–1898 (2008).
- [155] B. Rai, P. Sathish, C. P. Malhotra, Pradip, and K. G. Ayappa, *Molecular Dynamic Simulations of Self-Assembled Alkylthiolate Monolayers on an Au(111) Surface*, *Langmuir* **20** (8), 3138–3144 (2004).
- [156] C. V. Raman, *A Change of Wave-length in Light Scattering*, *Nature* **121**, 619–619 (1928).
- [157] C. V. Raman and K. S. Krishnan, *A New Type of Secondary Radiation*, *Nature* **121**, 501–502 (1928).
- [158] L. Rayleigh, *XXXIV. On the transmission of light through an atmosphere containing small particles in suspension, and on the origin of the blue of the sky*, *Philos. Mag. Series 5* **47** (287), 375–384 (1899).
- [159] R. Renner, *Zur Theorie der Wechselwirkung zwischen Elektronen- und Kernbewegung bei dreiatomigen, stabförmigen Molekülen*, *Z. Phys.* **92** (3-4), 172–193 (1934).
- [160] V. A. Roberts and M. E. Pique, *Definition of the Interaction Domain for Cytochrome con Cytochrome c Oxidase: III. PREDICTION OF THE DOCKED COMPLEX BY A COMPLETE, SYSTEMATIC SEARCH*, *J. Biol. Chem.* **274** (53), 38051–38060 (1999).

- [161] S. Sadeghi, F. Valetti, C. Cunha, M. Romao, C. Soares, and G. Giarlardi, *Ionic strength dependence of the non-physiological electron transfer between flavodoxin and cytochrome c(553) from D-vulgaris*, *J. Biol. Inorg. Chem* **5** (6), 730–737 (2000).
- [162] S. Salama and T. Spiro, *Visible and Near-Ultraviolet Resonance Raman-Spectra of photolabile Vitamin-B12 derivatives with rapid-flow technique*, *J. Raman Spectrosc.* **6** (2), 57–60 (1977).
- [163] E. Santoni, S. Scatragli, F. Sinibaldi, L. Fiorucci, R. Santucci, and G. Smulevich, *A model for the misfolded bis-His intermediate of cytochrome c: the 1-56 N-fragment*, *J. Inorg. Biochem.* **98** (6), 1067–1077 (2004).
- [164] A. Schilhabel, S. Studenik, M. Voedisch, S. Kreher, B. Schlott, A. Y. Pierik, and G. Diekert, *The Ether-Cleaving Methyltransferase System of the Strict Anaerobe Acetobacterium dehalogenans: Analysis and Expression of the Encoding Genes*, *J. Bacteriol.* **191** (2), 588–599 (2009).
- [165] F. Schreiber, *Self-assembled monolayers: from 'simple' model systems to biofunctionalized interfaces*, *J. Phys.: Condens. Matter* **16** (28), R881 (2004).
- [166] R. A. Scott and A. G. Mauk (eds.), *Cytochrome c: A multidisciplinary approach*, University Science Books (1996).
- [167] F. Siebert and P. Hildebrandt, *Vibrational Spectroscopy in Life Science, Tutorials in Biophysics*, vol. 3, Wiley-VCH (2007).
- [168] F. Sinibaldi, E. Droghetti, F. Polticelli, M. C. Piro, D. D. Pierro, T. Ferri, G. Smulevich, and R. Santucci, *The effects of ATP and sodium chloride on the cytochrome c-cardiolipin interaction: The contrasting behavior of the horse heart and yeast proteins*, *J. Inorg. Biochem.* **105** (11), 1365–1372 (2011).
- [169] F. Sinibaldi, B. Howes, M. Piro, F. Polticelli, C. Bombelli, T. Ferri, M. Coletta, G. Smulevich, and R. Santucci, *Extended cardiolipin anchorage to cytochrome c: a model for protein-mitochondrial membrane binding*, *J. Biol. Inorg. Chem.* **15**, 689–700 (2010).
- [170] F. Sinibaldi, B. D. Howes, E. Droghetti, F. Polticelli, M. C. Piro, D. Di Pierro, L. Fiorucci, M. Coletta, G. Smulevich, and R. Santucci, *Role of Lysines in Cytochrome c-Cardiolipin Interaction*, *Biochemistry* **52** (26), 4578–4588 (2013).
- [171] J. F. Smalley, S. W. Feldberg, C. E. D. Chidsey, M. R. Linford, M. D. Newton, and Y.-P. Liu, *The Kinetics of Electron Transfer Through Ferrocene-Terminated Alkanethiol Monolayers on Gold*,

- J. Phys. Chem. **99** (35), 13141–13149 (1995).
- [172] A. Smekal, *Zur Quantentheorie der Dispersion*, *Naturwissenschaften* **11** (43), 873–875 (1923).
- [173] C. P. Smith and H. S. White, *Theory of the interfacial potential distribution and reversible voltammetric response of electrodes coated with electroactive molecular films*, *Anal. Chem.* **64** (20), 2398–2405 (1992).
- [174] G. Smulevich and T. G. Spiro, *Surface enhanced Raman spectroscopic evidence that adsorption on silver particles can denature heme proteins*, *J. Phys. Chem.* **89** (24), 5168–5173 (1985).
- [175] T. G. Spiro, *Resonance Raman spectroscopy. New structure probe for biological chromophores*, *Acc. Chem. Res.* **7** (10), 339–344 (1974).
- [176] T. G. Spiro, *Resonance Raman Spectroscopy as a Probe of Heme Protein Structure and Dynamics*, in: C. B. Anfinsen, J. T. Edsall, and F. M. Richards (eds.), *Advances in Protein Chemistry*, Academic Press, vol. 37, 111–159 (1985).
- [177] T. G. Spiro and T. C. Streckas, *Resonance Raman Spectra of Hemoglobin and Cytochrome c: Inverse Polarization and Vibronic Scattering*, *Proc. Natl. Acad. Sci. USA* **69** (9), 2622–2626 (1972).
- [178] T. G. Spiro and T. C. Streckas, *Resonance Raman spectra of heme proteins. Effects of oxidation and spin state*, *J. Am. Chem. Soc.* **96** (2), 338–345 (1974).
- [179] O. Stern, *Theory of the electrolytic double layer*, *Z. Elektrochem.* **30**, 508–516 (1924). Deutsche Bunsen Gesellschaft, June 1924, Gottingen, Germany.
- [180] T. A. Stich, J. Seravalli, S. Venkatesh Rao, T. G. Spiro, S. W. Ragsdale, and T. C. Brunold, *Spectroscopic Studies of the Corrinoid/Iron-Sulfur Protein from Moorella thermoacetica*, *J. Am. Chem. Soc.* **128** (15), 5010–5020 (2006).
- [181] T. Svetlitchnaia, V. Svetlitchnyi, O. Meyer, and H. Dobbek, *Structural insights into methyltransfer reactions of a corrinoid iron-sulfur protein involved in acetyl-CoA synthesis*, *Proc. Natl. Acad. Sci. USA* **103** (39), 14331–14336 (2006).
- [182] S. W. G. Tait and D. R. Green, *Mitochondria and cell death: outer membrane permeabilization and beyond*, *Nat. Rev. Mol. Cell. Biol.* **11** (9), 621–632 (2010).

- [183] T. Takano and R. E. Dickerson, *Conformation change of cytochrome c: I. Ferrocycytochrome c structure refined at 1.5 Å resolution*, *J. Mol. Biol.* **153** (1), 79–94 (1981).
- [184] T. Takano and R. E. Dickerson, *Conformation change of cytochrome c: II. Ferricytochrome c refinement at 1.8 Å and comparison with the ferrocycytochrome structure*, *J. Mol. Biol.* **153** (1), 95–115 (1981).
- [185] J. Tang and A. C. Albrecht, *Studies in Raman Intensity Theory*, *J. Chem. Phys.* **49** (3), 1144–1154 (1968).
- [186] K. Tenger, P. Khoroshyy, K. L. Kovács, L. Zimányi, and G. Rákhely, *Improved system for heterologous expression of cytochrome c mutants in Escherichia coli.*, *Acta Biol. Hung.* **58**, 23–35 (2007).
- [187] K. Tenger, P. Khoroshyy, G. Rákhely, and L. Zimányi, *Maturation of a eukaryotic cytochrome c in the cytoplasm of Escherichia coli without the assistance by a dedicated biogenesis apparatus*, *J. Bioenerg. Biomembr.* **42** (2), 125–133 (2010).
- [188] N. Thornberry and Y. Lazebnik, *Caspases: Enemies within*, *Science* **281** (5381), 1312–1316 (1998).
- [189] Z.-Q. Tian, B. Ren, and D.-Y. Wu, *Surface-Enhanced Raman Scattering: From Noble to Transition Metals and from Rough Surfaces to Ordered Nanostructures*, *J. Phys. Chem. B* **106** (37), 9463–9483 (2002).
- [190] T. Tsukihara, H. Aoyama, E. Yamashita, T. Tomizaki, H. Yamaguchi, K. Shinzawa-Itoh, R. Nakashima, R. Yaono, and S. Yoshikawa, *Structures of metal sites of oxidized bovine heart cytochrome c oxidase at 2.8 Å*, *Science* **269** (5227), 1069–1074 (1995).
- [191] J. Ulstrup and J. Jortner, *The effect of intramolecular quantum modes on free energy relationships for electron transfer reactions*, *J. Chem. Phys.* **63** (10), 4358–4368 (1975).
- [192] N. V. Venkataraman, S. Zürcher, and N. D. Spencer, *Order and Composition of Methyl-Carboxyl and Methyl-Hydroxyl Surface-Chemical Gradients*, *Langmuir* **22** (9), 4184–4189 (2006).
- [193] H. Wackerbarth, D. Murgida, S. Oellerich, S. Döpner, L. Rivas, and P. Hildebrandt, *Dynamics and mechanism of the electron transfer process of cytochrome c probed by resonance Raman and surface enhanced resonance Raman spectroscopy*, *J. Mol. Struct.* **563–564** (0), 51–59 (2001).

- [194] W. L. Wallace and A. J. Bard, *Electrogenerated chemiluminescence. 35. Temperature dependence of the ECL efficiency of tris(2,2'-bipyridine)ruthidium(2+) in acetonitrile and evidence for very high excited state yields from electron transfer reactions*, J. Phys. Chem. **83** (10), 1350–1357 (1979).
- [195] K. Wang, Y. Zhen, R. Sadoski, S. Grinnell, L. Geren, S. Ferguson-Miller, B. Durham, and F. Millett, *Definition of the Interaction Domain for Cytochrome *c* Cytochrome *c* Oxidase: II. Rapid Kinetic Analysis of Electron Transfer from Cytochrome *c* to Rhodobacter Sphaeroides cytochrome Oxidase surface Mutants*, J. Biol. Chem. **274** (53), 38042–38050 (1999).
- [196] A. Warshel and P. Dauber, *Calculations of resonance Raman spectra of conjugated molecules*, J. Chem. Phys. **66** (12), 5477–5488 (1977).
- [197] J. Wei, H. Liu, D. E. Khoshtariya, H. Yamamoto, A. Dick, and D. H. Waldeck, *Electron-Transfer Dynamics of Cytochrome *C*: A Change in the Reaction Mechanism with Distance*, Angew. Chem. Int. Ed. **41** (24), 4700–4703 (2002).
- [198] R. J. P. Williams, *The Energetics and Dynamics of Metallo-Proteins*, Z. Phys. Chem. **269** (2), 387–402 (1988).
- [199] R. J. P. Williams, *Overview of Biological Electron Transfer*, in: M. K. Johnson, R. B. King, D. M. Kurtz Jr., C. Kutal, M. L. Norton, and R. A. Scott (eds.), *Electron Transfer in Biology and the Solid State*, American Chemical Society, *Inorganic Compounds with Unusual Properties*, vol. 226, chap. 1, 3–23 (1989).
- [200] B. Willner, E. Katz, and I. Willner, *Electrical contacting of redox proteins by nanotechnological means*, Curr. Opin. Biotechnol. **17** (6), 589–596 (2006).
- [201] E. Wilson, J. Decius, and P. Cross, *Molecular Vibrations: The Theory of Infrared and Raman Vibrational Spectra*, McGraw-Hill (1955).
- [202] J. Xu and E. Bowden, *Determination of the orientation of adsorbed cytochrome *c* on carboxyalkanethiol self-assembled monolayers by in situ differential modification*, J. Am. Chem. Soc. **128** (21), 6813–6822 (2006).
- [203] J. Xu, H. Li, and Y. Zhang, *Relationship between electronic tunneling coefficient and electrode potential investigated by using self-assembled alkanethiol monolayers on gold electrodes*, J. Phys. Chem. **97** (44), 11497–11500 (1993).

- [204] T. Ying, Z.-H. Wang, F. Zhong, X. Tan, and Z.-X. Huang, *Distinct mechanisms for the pro-apoptotic conformational transition and alkaline transition in cytochrome c*, *Chem. Commun.* **46**, 3541–3543 (2010).
- [205] T. Ying, F. Zhong, J. Xie, Y. Feng, Z.-H. Wang, Z.-X. Huang, and X. Tan, *Evolutionary alkaline transition in human cytochrome c*, *J. Bioenerg. Biomembr.* **41**, 251–257 (2009).
- [206] H. Yu, I. Lee, A. R. Salomon, K. Yu, and M. Hüttemann, *Mammalian liver cytochrome c is tyrosine-48 phosphorylated in vivo, inhibiting mitochondrial respiration*, *Biochim. Biophys. Acta* **1777**, 1066–1071 (2008).
- [207] H. Yue, D. Khoshtariya, D. H. Waldeck, J. Grochol, P. Hildebrandt, and D. H. Murgida, *On the Electron Transfer Mechanism Between Cytochrome c and Metal Electrodes. Evidence for Dynamic Control at Short Distances*, *J. Phys. Chem. B* **110** (40), 19906–19913 (2006).